MAX-PLANCK-INSTITUT FÜR QUANTENOPTIK

Coherent manipulation of ultracold atoms with microwave near-fields

Pascal Alexander Böhi

Coherent manipulation of ultracold atoms with microwave near-fields

Dissertation
submitted to the Faculty of Physics
of the Ludwig-Maximilians-Universität
München

by
Pascal Alexander Böhi
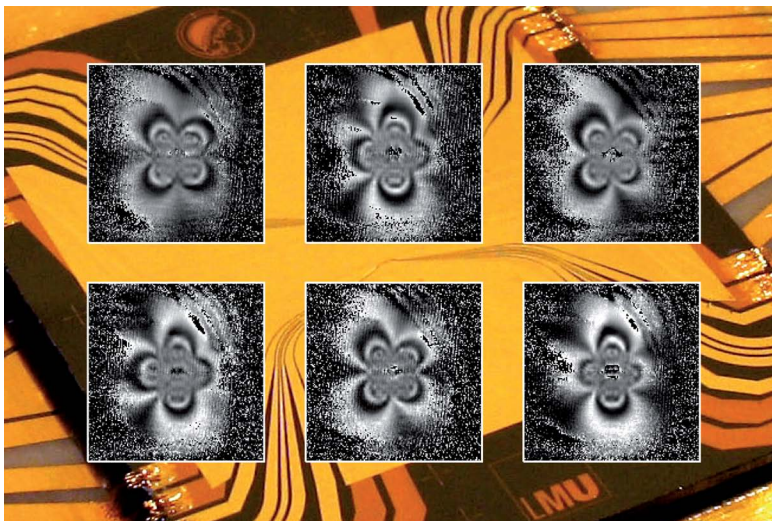
München, July 9, 2010

meinen Eltern

Zusammenfassung

Der spektakuläre Fortschritt auf dem Gebiet der ultrakalten Quantengase beruht auf der Kontrolle von internen- und Bewegungs-Quantenzuständen sowie Kollisions-Wechselwirkungen. Atomchips ermöglichen solche Kontrolle von Quantensystemen in kompakten, robusten und skalierbaren Aufbauten.

In dieser Dissertation berichte ich über Experimente auf einem Atomchip mit integrierten Wellenleitern, deren Mikrowellen-Nahfelder als eine neue Methode zur kohärenten Manipulation von ultrakaltem Rubidium verwendet werden.

Mikrowellen-Nahfeldpotentiale vereinen die Flexibilität und Vielseitigkeit von optischen Fallen mit der Robustheit und Konfigurierbarkeit von statischen Mikrofallen. Die Mikrowellenpotentiale hängen vom internen atomaren Hyperfeinzustand ab, was wir für die zustandsselektive Aufspaltung von Bose-Einstein Kondensaten verwenden. Wir demonstrieren erstmalig die kombinierte kohärente Manipulation von internen- und Bewegungs-Zuständen in einem Atominterferometer auf einem Atomchip, mit Kennzeichnung der Interferometerarme durch interne Hyperfeinzustände. Weiter verwenden wir die Nahfeld-Potentiale um via zustandsabhängiger Kollisions-Wechselwirkungen *gequetschte* Spin-Zustände für die Quanten-Metrologie herzustellen. Ausserdem existieren sehr vielversprechende Vorschläge, mittels dieser Potentiale ein Quanten-Phasengatter zu realisieren.

Das Vermessen von Mikrowellen-Feldern ist bedeutsam für die Entwicklung von Mikrowellen-Komponenten sowie in der Wissenschaft, z.B. zur Vermessung der Feld-Homogenität in den Wechselwirkungs-Regionen einer Atomuhr.

Wir haben eine Technik entwickelt, die Wolken von ultrakalten Atomen als empfindliche, abstimmbare, und nichtinvasive Sonden für das Abbilden von Mikrowellen-Feldverteilungen mit einer räumlichen Auflösung im Mikrometerbereich benutzt. Die Mikrowellenmagnetfeld-Komponenten treiben Rabi-Oszillationen zwischen atomaren Hyperfeinzuständen, deren Resonanzbedingung mittels eines statischen Magnetfelds abgestimmt werden kann. Das Auslesen geschieht mit zustandsselektiver Absorptionsabbildung. Eine quantitative Auswertung ist einfach und es ist möglich die Verteilung der verschiedenen Polarisationskomponenten sowie Phasen des Mikrowellenmagnetfelds zu rekonstruieren. Die Mikrowellen-Nahfeldverteilung um einen der Wellenleiter auf dem Atomchip wird vermessen und die damit korrespondierende Stromverteilung auf dem Wellenleiter wird rekonstruiert. Für unsere experimentellen Parameter können wir Amplituden des Mikrowellenmagnetfelds von bis zu 2×10^{-4} G messen.

Die vorgestellten Experimente sind Basis für die Realisierung transportabler, auf Verschränkung basierender Quanten-Interferometer, Quanten-Phasengatter und eines neuen Verfahrens zur Charakterisierung von Mikrowellen-Feldverteilungen.

Abstract

The spectacular progress in the field of ultracold quantum gases is intimately connected with the availability of sophisticated techniques for quantum-level control of internal states, motional states, and collisional interactions. Atom chips provide such control in compact, robust, and scalable setups, which makes them attractive for both applications and fundamental studies.

In this thesis I report on experiments that use a new method for coherent manipulation of ultracold atoms. The method is based on microwave near-fields, provided by a waveguide structure that is fully integrated on an atom chip. We generate microwave near-field potentials that combine the versatility of optical traps with the robustness and tailorability of static magnetic microtraps. These potentials depend on the internal atomic state, and we use them for state-selective splitting of Rb Bose-Einstein condensates. We show for the first time combined coherent manipulation of internal and motional states on an atom chip, realizing a trapped-atom interferometer with internal state labeling of the interferometer paths. Moreover, we use microwave near-field potentials for the preparation of spin-squeezed states for quantum-enhanced metrology through controlling state-dependent collisional interactions. In addition, very promising proposals exist for the implementation of a quantum phase gate using these potentials.

Measuring microwave fields is important for engineering of microwave devices as well as in science, e.g. to characterize the field homogeneity in the interaction regions of an atomic clock. We develop a novel technique that uses clouds of uncondensed ultracold atoms as sensitive, tunable and non-invasive probes for microwave field imaging with micrometer spatial resolution. The microwave magnetic field components drive Rabi oscillations on atomic hyperfine transitions whose frequency can be tuned with a static magnetic field. Readout is accomplished using state-selective absorption imaging. Quantitative data extraction is simple and it is possible to reconstruct the amplitudes and phases of the different microwave magnetic field components. While we demonstrate 2D imaging, an extension to 3D imaging is straightforward. We use the method to determine the microwave near-field distribution around the on-chip waveguide and reconstruct the corresponding current distribution. For our experimental parameters, the method provides a microwave magnetic field sensitivity of $\sim 2 \times 10^{-4}$ G, which can even be improved further with variants discussed.

The experiments presented in this thesis open the path for the realization of portable quantum-enhanced interferometer devices, the implementation of a quantum phase gate as well as for a new generation of microwave field sensors.

Contents

CONTENTS

CONTENTS

Introduction

Ultracold neutral bosonic atoms are an ideal system to study quantum effects. They can be cooled relatively easily to ultra low temperatures, where quantum effects such as Bose-Einstein condensation [1] become relevant. The atoms are isolated amazingly well from the environment by levitating them either in a magnetic [2] or optical [3] trapping potential inside a UHV vacuum chamber. Furthermore, most relevant atomic species have an internal hyperfine structure which can be manipulated in the experiment, and which is well protected from the environment. For quantum information processing, for example, internal quantum states represent qubits, while coherent atomic motion in combination with collisions can be used to generate entanglement.

On an "atom chip" [4, 5, 6, 7], magnetic trapping potentials are generated by currents on wires that are microfabricated on a chip substrate. In the near-field of the wires, complex and tight potentials can be generated, which can vary on a micrometer lengthscale, realizing e.g. a magnetic conveyor belt for atoms [8]. Atom chips combine the excellent coherence properties of ultracold neutral atoms [9] with a compact, robust and scalable setup through microfabrication [10, 11], realizing a versatile "quantum laboratory on a microchip". Atom chips have already been used to investigate the coherence of internal hyperfine states [9], to study cavity quantum electrodynamics [12], low-dimensional quantum gases [13], magnetic lattices [14] and atom interferometry [15, 16, 17, 18, 19, 20, 21]. Atoms on atom chips have been used as probes for atom-surface interactions [22, 23], the Meissner effect [24], electric and magnetic field distributions [25, 26, 27], and thermal magnetic near-field noise [28, 29]. Chip-based atom clocks are currently being developed [9, 30, 31], portable setups have already been built [32, 33] and key components are now commercially available.[1]

However, a severe limitation of atom chips is that techniques to generate entanglement have not been experimentally available so far. The controlled generation of entanglement is currently of great interest in the field of ultracold atoms, both because a better understanding of this puzzling fea-

---

[1] www.coldquanta.com

5

ture of quantum mechanics is desired, and because it may form the basis of future technologies such as quantum information processing [34], quantum simulations [35], and quantum-enhanced metrology [36, 37, 38, 39]. Several proposals for the on-chip generation of entanglement for individual atoms [40, 41, 42, 43, 44] and ensembles [45, 46] exist. An essential ingredient of many of these proposals is a hyperfine-state dependent potential [43, 46] that allows one to condition interactions on the internal state, resulting in entanglement. In the work presented in this thesis, we realize such a potential for the first time on an atom chip [21] and use it to generate entangled states of a BEC [47].

We are working with ^{87}Rb, which has two hyperfine levels $|F = 1, m_F = -1\rangle \equiv |1\rangle$ and $|F = 2, m_F = 1\rangle \equiv |2\rangle$ (the *qubit* or *clock states*) which are magnetically trappable and which have the same magnetic moment, making their energy difference insensitive to magnetic field fluctuations to first order [48].[2] For the robust state pair $|1\rangle$ and $|2\rangle$, a combination of static electric and magnetic fields can not provide state selective potentials for entanglement generation [43]. Optical traps are also impractical because if operated at a detuning which is large compared to the hyperfine splitting, the differential potential is only weak, whereas at a detuning comparable to the hyperfine splitting, the differential potential can become strong, but problems with decoherence due to photon scattering arise [43]. Furthermore, the integration of optical components on an atom chip is a non-trivial task.

The solution is to use microwave potentials [49, 50], which can be made state-selective via microwave frequency and polarization. Spontaneous decay is negligible and they can be tailored on a μm scale using the strong microwave near-field dependence around a waveguide structure [51] fully integrated on an atom chip. Microwave near-fields can be extremely strong: When microwave trapping with far-field radiation was demonstrated in 1994 [50], a cavity with a circulating microwave power of several hundreds of kilowatts was used to reach a resonant Rabi frequency of up to $|\Omega_{\text{far-f.}}/2\pi| = 36$ MHz. In the near-field of the micron-sized waveguide integrated on our atom chip, we measure a Rabi frequency $|\Omega_{\text{near-f.}}/2\pi| \sim 1$ MHz with only ~ 10 mW microwave power at a distance of 8.5 μm from the on-chip waveguide. In addition, the achievable gradients in the near-field $|\nabla\Omega_{\text{near-f.}}|$ can be orders of magnitude stronger than achievable in the far-field.

State-dependent microwave potentials allow us to adjust the spatial wave function overlap of states $|1\rangle$ and $|2\rangle$. This enables the realization of a trapped-atom interferometer with internal-state labeling of the interferome-

---

[2]The energy difference between two states is the quantity that is measured e.g. in an atomic clock.

ter arms [52, 21], paving the way to portable atom interferometric sensors [53, 54], as well as the controlled generation of multi-particle entanglement in the form of spin-squeezed states [46, 47] and entangling quantum gates [43].

This thesis

I report on the design and fabrication of a novel atom chip with micron-sized integrated microwave guiding structures, which exhibit strong microwave near-field gradients. We develop a sensitive, tunable and non-invasive method to measure and reconstruct a microwave magnetic field distribution using clouds of uncondensed ultracold atoms [55, 56]. We use it to characterize the microwave near-field distribution of the waveguide on our atom chip. Furthermore, we use the state-selective microwave potentials for the implementation of a trapped-atom interferometer with internal state labeling of the interferometer arms, realizing for the first time combined coherent manipulation of internal and motional states on an atom chip [21]. We apply the state-selective potentials for the production of spin-squeezed states [46], where we measure a spin noise reduction of $-3.7 \pm 0.4\,\mathrm{dB}$ ($-2.5 \pm 0.6\,\mathrm{dB}$ *useful* squeezing) [47], which implies four-partite entanglement between the condensate atoms [57].

Microwave field imaging. − Today, Monolithic Microwave Integrated Circuits (MMICs) are of great importance in science and technology. Function and failure analysis is of crucial importance for the design of MMICs as well as for simulation verification [58]. External port measurements (e.g. using a network analyzer) offer only limited insight. The microwave near-field distribution on the device gives much more information, enabling specific improvement. We develop a non-invasive method to characterize a microwave near-field distribution using clouds of non-degenerate ultracold atoms [55, 56], which works by releasing a cloud of atoms to free fall, and using the microwave near-field to drive resonant Rabi oscillations on different hyperfine transitions, which can be detected using state-selective absorption imaging [48]. Since the microwave field can be probed on a relatively large region of interest at once, this method is time efficient. Moreover, the distribution of the microwave magnetic field components and their phases can be fully reconstructed.

We use this method to characterize the microwave near-field distribution of the on-chip waveguide and reconstruct the current distribution on the waveguide wires by comparing the measured microwave field distribution to simulations.

For our experimental parameters, this imaging technique provides a microwave magnetic field sensitivity down to 2×10^{-4} G at a spatial microwave field resolution of $s = 8 \, \mu$m. With variants presented, the microwave magnetic field sensitivity could be increased to 5×10^{-9} G, which is comparable to the DC magnetic field sensitivity reached with SQUIDs, but at a much higher spatial resolution [27]. While we demonstrate 2-dimensional imaging, an extension to 3D imaging slice-by-slice is straight forward.

Trapped-atom interferometry. − In a second set of experiments, we use microwave near-fields for state-selective splitting of mesoscopic Bose-Einstein condensates (BECs) containing about 400 atoms. We measure the coherence of the splitting process by implementing a trapped-atom interferometer with internal state labeling of the interferometer arms [21]. This demonstrates for the first time combined coherent control of internal and motional states on an atom chip. Internal-state labeling of the interferometer arms allows for convenient interferometer readout because interference fringes do not have to be resolved spatially. Instead, only the numbers of atoms in the two states have to be measured, which can be done with high accuracy.

Atom interferometry holds great promise for the detection of inertial effects like acceleration, rotation and gravitation [59]. The intrinsic sensitivity of atom interferometers e.g. to rotations is about eleven orders of magnitude higher than that of optical interferometers, assuming equal particle flux [60]. In combination with the compactness of atom chip setups, this holds great promise for real-life applications of atom interferometers, e.g. for resource exploration [61] or for precision measurements in space.

The scalability through microfabrication makes quantum information processing on atom chips particularly attractive. The reported experiments demonstrate a key ingredient for the implementation of a chip-based controlled phase gate for single atoms [43].

Production of spin-squeezed states. − The state-selective potentials can be used to tune interactions in a state-dependent way for atoms such as ^{87}Rb that do not have convenient Feshbach resonances [21]. Controlling the wave function overlap of states $|1\rangle$ and $|2\rangle$ in a two-component condensate allows for the generation of spin-squeezed states [46], as has been shown in one of our recent experiments [47]. These states are useful for quantum metrology to surpass the *standard quantum limit* of interferometric measurement [39].

Organization of chapters

The **first chapter** gives an introduction to atom chips. I describe magnetic trapping on atom chips, present our robust *clock* or *qubit* states and give a review of Bose-Einstein condensation. Special emphasis is placed on two-component BECs and the origin of our state-selective microwave potentials.

The **second chapter** introduces our atom chip with integrated microwave structures. I describe the design of the waveguide structures, the atom chip fabrication, and its DC and microwave characterization.

The **third chapter** lines out our experimental setup, with special focus on the vacuum system, the magnetic μ-metal shielding, the DC, RF and microwave sources, and the experimental control and data acquisition system. I give a brief description of the production of mesoscopic BECs and describe a first set of experiments, where we show that large Rabi frequencies and gradients can be obtained in the microwave near-field.

The **fourth chapter** shows a first set of main results of this thesis, where I describe the new microwave field imaging method that we developed. I present its theory, describe two methods for quantitative data extraction and use it to characterize the microwave near-field distribution around the coplanar waveguide on our chip. The sensitivity of this method is estimated, and variants for increasing the microwave sensitivity and the spatial resolution are discussed.

The **fifth chapter** presents a second set of main results, where we demonstrate the state-selectivity of the microwave near-field potentials and where we show full coherent control of internal and motional wave functions by implementing a trapped-atom interferometer with internal state labeling. I discuss several sources of noise in our experiment and elaborate on the role of mean-field effects in the splitting experiments.

The **sixth chapter** presents the application of the state-dependent potentials for the on-chip generation of multi-particle entanglement. I briefly describe an experiment where we produce and characterize spin squeezed states with two-component BECs. Furthermore, I line out how our state-selective potentials could be used for the on-chip implementation of a controlled phase gate for single atoms.

Contributions to publications

- *Coherent manipulation of Bose-Einstein condensates with state-dependent microwave potentials on an atom chip*
  P. Böhi, M. F. Riedel, J. Hoffrogge, J. Reichel, T. W. Hänsch, and P. Treutlein
  Nature Physics **5**, 592-597 (2009).

- *Atom-chip-based generation of entanglement for quantum metrology*
  M. F. Riedel, P. Böhi, Y. Li, T. W. Hänsch, A. Sinatra, and P. Treutlein
  Nature **464**, 1170-1173 (2010).

- *Imaging of microwave fields using ultracold atoms*
  P. Böhi, M. F. Riedel, T. W. Hänsch, and P. Treutlein
  Appl. Phys. Lett. **97**, 051101 (2010)

- *Method and device for sensing microwave magnetic field polarization components*
  P. Böhi, M. F. Riedel, T. W. Hänsch and P. Treutlein
  U.S. patent pending.

Chapter 1

Atom chips and coherent manipulation of ultracold atoms

The magnetic potentials for the first magnetic atom traps were produced by macroscopic coils. While magnetic fields produced in such a way allow for the creation of large trapping volumes, the tailorability of the potentials is only very limited. This is due to the fact that the magnetic fields can only vary on a length scale comparable to the distance of the atoms to the field generating devices and the size of them. This poses limitations on achievable gradients. Complex potential landscapes e.g. forming a micron-sized beam splitter are not readily implementable. On atom chips on the other hand, the atoms are at just some μm distance from the current-carrying wires that create the magnetic fields. This allows the realization of much higher gradients. There is great flexibility in the arrangement of the wires on the chip, such that complex geometries can be implemented. Using microfabricated multi-layer wire structures on an atom chip, nearly arbitrary potential configurations can be implemented. Therefore, atom chips bring the scalability and versatility of microfabrication to the world of atomic physics and quantum optics.

In the following, I will present the basic theory relevant for trapping neutral ^{87}Rb atoms in chip traps. I discuss the production and properties of two-component Bose-Einstein condensates (BECs), before state-selective microwave potentials are described. For further information on chip traps, the reader is also referred to some recent atom chip review articles [62, 5, 6, 7].
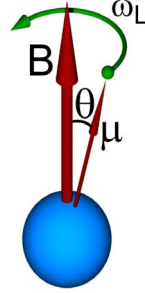
Figure 1.1.1: Illustration of an atom with magnetic moment $\boldsymbol{\mu}$ in a static magnetic field $\mathbf{B}$. The atomic magnetic moment $\boldsymbol{\mu}$ is precessing around $\mathbf{B}$ at the Larmor frequency ω_L. The angle θ between $\mathbf{B}$ and $\boldsymbol{\mu}$ is constant.

1.1 Magnetic trapping

Early experiments on trapping of neutral atoms with magnetic fields were reported in 1985 [2]. Soon after that, the density and the number of trapped atoms was improved by many orders of magnitude using superconducting traps and different loading schemes [1, 63, 64, 65]. Since then, magnetic traps became the every day workhorses in cold atoms experiments. The basics of magnetic trapping is presented in the following.

The potential energy $E_{\mathrm{B}}(\mathbf{r})$ of a neutral atom with magnetic moment $\boldsymbol{\mu}$ in a static magnetic field $\mathbf{B}(\mathbf{r})$ is given by

$$E_B(\mathbf{r}) = -\boldsymbol{\mu} \cdot \mathbf{B}(\mathbf{r}). \tag{1.1.1}$$

The magnetic moment $\boldsymbol{\mu}$ is precessing around $\mathbf{B}(\mathbf{r})$ (see Figure 1.1.1) at the Larmor frequency

$$\omega_L(\mathbf{r}) = \frac{\mu B(\mathbf{r})}{\hbar}. \tag{1.1.2}$$

This precession stabilizes the projection $\boldsymbol{\mu} \cdot \mathbf{B}(\mathbf{r})$. Classically, $\boldsymbol{\mu}$ can have any orientation relative to $\mathbf{B}(\mathbf{r})$. Quantum mechanically, the projection of $\boldsymbol{\mu}$ onto $\mathbf{B}(\mathbf{r})$ has discrete values given by the quantum number m_F of the z-component of the total angular momentum operator $\mathbf{F} = \mathbf{I} + \mathbf{J}$, where $\mathbf{I}$ is the nuclear-spin operator and $\mathbf{J}$ the operator for the total angular momentum of the electron. Therefore atoms in a magnetic field $\mathbf{B}(\mathbf{r})$ have a potential energy

$$E_{\mathrm{B}}(r) = \mu_B g_F m_F \left| \mathbf{B}(\mathbf{r}) \right|, \tag{1.1.3}$$
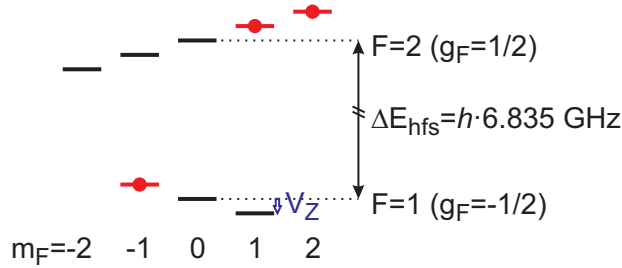
Figure 1.1.2: Hyperfine term scheme of the $5^2S_{1/2}$ ground state of ^{87}Rb in a static magnetic field B. The Zeeman shift between the different m_F levels is given by $V_Z = \frac{\mu_B B}{2}$. Weak-field seeking states - states with $g_F m_F > 0$ - are indicated in red.

with μ_B the Bohr magneton and g_F the Landé g-factor (see Figure 1.1.2). The formula above is valid as long as $E_B \ll \Delta E_{\text{hfs}}$, with ΔE_{hfs} the hyperfine splitting. The Landé factor g_F is given by [66]

$$
\begin{aligned}
g_F &= g_J \frac{F(F+1) - I(I+1) + J(J+1)}{2F(F+1)} \\
&\quad + g_I \frac{F(F+1) + I(I+1) - J(J+1)}{2F(F+1)} \\
&\approx g_J \frac{F(F+1) - I(I+1) + J(J+1)}{2F(F+1)}.
\end{aligned}
\tag{1.1.4}
$$

The approximation above neglects the nuclear term, which would only be a correction of the order of 0.1%.

An inhomogeneous magnetic field exerts a force on atoms with a finite magnetic moment μ. The force is given by

$$
\mathbf{F}(\mathbf{r}) = -\nabla E_B(r) = -\mu_B g_F m_F \nabla |\mathbf{B}(\mathbf{r})|.
\tag{1.1.5}
$$

Atoms with $g_F m_F > 0$ (weak field seeking states) are attracted to regions of lower magnetic fields while for $g_F m_F < 0$ (strong field seeking states) atoms get accelerated towards regions of high magnetic field. According to Wing's theorem [67], in free space a magnetic field cannot have a local maximum, but a local minimum. Therefore only atoms with $g_F m_F > 0$ can be trapped in static magnetic traps.[1]

An atom moving in a magnetic trap experiences a magnetic field $\mathbf{B}$ that is changing in direction and magnitude over time. For m_F to stay constant

---

[1]Atoms in a strong field seeking state can be "trapped" along Kepler guides [68].

during movement of the atoms in the trap, the change of the direction of the magnetic field $\theta(t)$ has to be slow compared to the Larmor precession frequency ω_L of the magnetic moment $\boldsymbol{\mu}$:

$$\frac{d\theta}{dt} \ll \omega_L = \frac{\mu B}{\hbar} \tag{1.1.6}$$

An upper bound for $\frac{d\theta}{dt}$ is the trap frequency. A change in $g_F m_F$ is called (Majorana) spin flip. If $m_F g_F \leq 0$, then the atom is lost from the trap, because for $g_F m_F = 0$ the atom sees no magnetic trapping potential and for $g_F m_F < 0$ the formerly attractive potential becomes repulsive. Therefore, one has to avoid regions of vanishing magnetic field in an atom trap when designing it.

A trap is implemented by realizing a spatially varying magnetic field landscape $\mathbf{B}(\mathbf{r})$. In the following, some magnetic trap field configurations are presented.

1.2 Quadrupole and Ioffe-Pritchard traps

The traps used in our experiment can be divided into two classes: Quadrupole traps, which have a vanishing magnetic field in the trap center, and Ioffe-Pritchard traps, where the magnetic field at the bottom of the trap is finite [6].

1.2.1 Quadrupole traps

In a quadrupole trap, the magnetic field vanishes at the trap minimum. The magnetic field around the minimum can be approximated by a linear function

$$\mathbf{B} = B'_x x \mathbf{e_x} + B'_y y \mathbf{e_y} + B'_z z \mathbf{e_z}. \tag{1.2.1}$$

Maxwell's equations require $B'_x + B'_y + B'_z = 0$. Quadrupole traps suffer from trap loss due to Majorana spin flips near the trap center. For clouds which are relatively hot, the atoms spend most of the time away from the zero crossing of the magnetic field, and the spin flip loss is only weak. In our experiment, a quadrupole magnetic field configuration is used during the magneto-optical trap (MOT) stage.

1.2.2 Ioffe-Pritchard traps

The lowest-order (and therefore tightest) trap which can have a nonzero field in the minimum is a harmonic trap [1]. A magnetic trap with non-vanishing

bias field along x has an axial field $B_x = B_0 + B'' \frac{x^2}{2}$. Applying Maxwell's equations and assuming axial symmetry, the trapping field has the form [1]

$$\mathbf{B} = B_0 \begin{pmatrix} 1 \\ 0 \\ 0 \end{pmatrix} + B' \begin{pmatrix} 0 \\ -y \\ z \end{pmatrix} + \frac{B''}{2} \begin{pmatrix} x^2 - \frac{1}{2}(y^2 + z^2) \\ -xy \\ -xz \end{pmatrix}. \qquad (1.2.2)$$

The magnetic field around the trap center, expanded up to second order can be written as [1]

$$B(\mathbf{r}) \approx B_0 + \frac{B''}{2}x^2 + \frac{1}{2}\left(\frac{B'^2}{B_0} - \frac{B''}{2}\right)\left(y^2 + z^2\right). \qquad (1.2.3)$$

This results in harmonic confinement of atoms with magnetic moment $\mu = \mu_B g_F m_F$ and mass m with axial (radial) trap frequencies ω_x ($\omega_\perp$) [69]

$$\omega_x = \sqrt{\frac{\mu}{m}B''}, \qquad \omega_\perp = \sqrt{\frac{\mu}{m}\left(\frac{B'^2}{B_0} - \frac{B''}{2}\right)}. \qquad (1.2.4)$$

This trap configuration was first proposed and demonstrated for atom trapping by Pritchard [63, 70, 1]. It is similar to the configuration discussed by Ioffe for plasma confinement in the 1960s [1].

1.3   Static magnetic traps on atom chips

There are various possibilities to generate magnetic potentials on atom chips. Among those are current conducting wires [7], permanent magnets [71] and superconducting circuits [72]. On our atom chip we use normal conducting wire structures made out of gold, that have been patterned using photo lithography. The following describes the trapping principles using on-chip wires.

1.3.1   Wire guide

If a wire carries a current I, a circular magnetic field around that wire is created (see illustration on Figure 1.3.1). In the following we will assume the wire to be infinitely thin. The superposition of wire's magnetic field with an homogeneous, external magnetic field $\mathbf{B}_e$, oriented perpendicular to the wire, leads to a region of vanishing magnetic field, at a distance of

$$z_0 = \frac{\mu_0 I}{2\pi B_e}. \qquad (1.3.1)$$
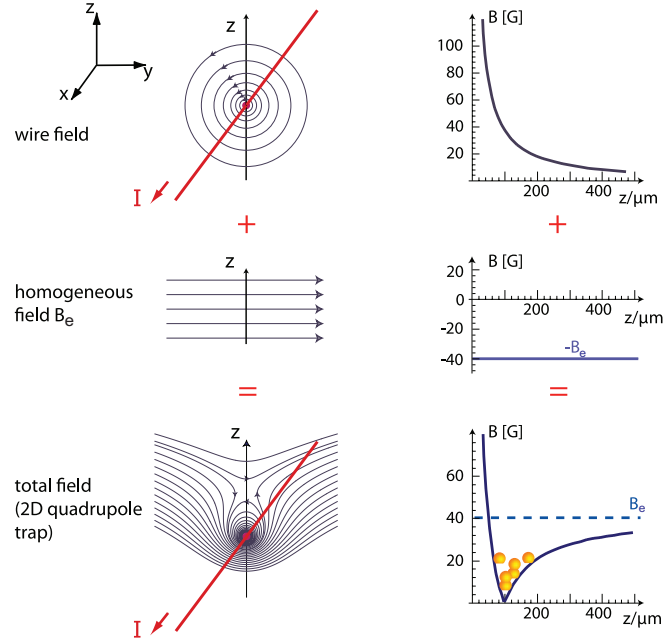
Figure 1.3.1: Wire guide trapping potential. The trapping potential is generated by the superposition of the magnetic field from a straight wire, biased by a current I and an external, homogeneous magnetic field $\mathbf{B}_e$, which is oriented perpendicular to the wire. At a distance $z_0 = \frac{\mu_0 I}{2\pi B_e}$ the magnetic fields compensate each other, forming a two dimensional quadrupole trap in the yz-plane. Weak-field seeking atoms can be trapped in two dimensions, but are not confined along x. The figure is adapted from [6].

Since the geometry is translational invariant along the direction of the wire, the region of vanishing magnetic field is also a line along that direction. Near that magnetic field minimum line, the transverse magnetic field is well approximated by a two-dimensional quadrupole field with gradient $B' = -\frac{\mu_0 I}{2\pi z_0^2}$.

The wires used in our experiment are not infinitely thin and free standing, but have a rectangular cross section (thickness t, width w), and are fabricated on a substrate. For distances d from that wire, with $d \gg w\,, t$, the magnetic field around the wire is well approximated by that of an infinitely thin wire.

Weak-field seeking atoms in such a magnetic potential are trapped in two dimensions, but are free to move in the direction along the wire. Three dimensional confinement can be achieved either by bending the ends of the wire or by crossing the wire with an additional wire (the so called *dimple trap*). Both configurations are discussed in the following.

16
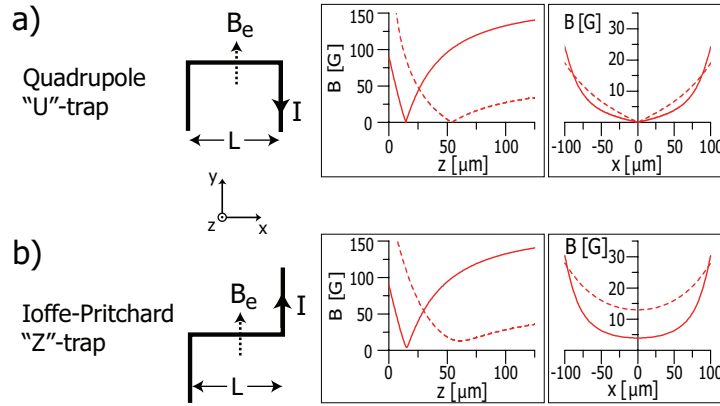
Figure 1.3.2: Wire configuration for a quadrupole (a) and a Ioffe-Pritchard trap (b). While the "U"-shaped wire configuration in (a) results in a trap minimum with vanishing magnetic field, wires shaped like a "Z" (b) result in a magnetic field configuration with finite magnetic field at the trap center. For this calculation, length $L = 250\,\mu$m, wire-width $w = 50\,\mu$m and $I = 2$ A. The bias-field along y is $B_e = 54$ G (dashed lines) and 162 G (solid lines). The Figure is adapted from [6].

1.3.2   U / Z shaped wire

Three dimensional trapping can be provided by bending the wire ends at right angles to form either a "U" or a "Z" (see Figure 1.3.2). In both cases, the magnetic fields from the currents in the input leads provide axial confinement, while the central part of the wire generates radial confinement.

For the case of a "U", the magnetic fields from the input leads compensate each other at $x = 0$, thereby forming a three dimensional quadrupole potential with field zero at $x = 0$, $y > 0$ and $z \approx z_0$.

In the case of a "Z", the magnetic fields from the input leads do not compensate each other, leading to a finite field in the trap center at $x = 0$. The trapping potential is a three-dimensional Ioffe-Pritchard potential.

1.3.3   Dimple trap

A very versatile Ioffe-Pritchard trap configuration is the dimple trap above a wire crossing (see Figure 1.3.3). The wire along x with current I_0 together with $B_{e,y}$ produce a two-dimensional quadrupole field in the yz-plane, with minimum at $z = z_0$, $y = 0$, and no longitudinal confinement along x. A longitudinal magnetic field $B_{e,x}$ together with a current I_1 along y removes the field zero and provides longitudinal confinement. For sufficiently small $I_1 \ll I_0$, the transverse confinement is nearly unchanged and the dimple trap
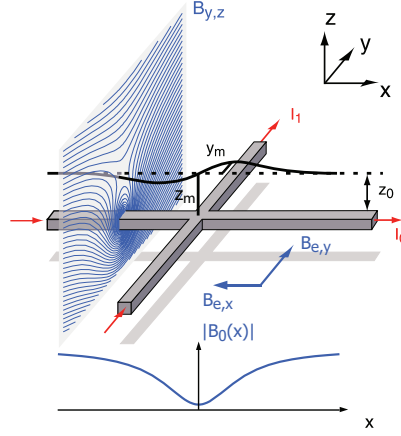
Figure 1.3.3: Dimple trap above a wire crossing. The magnetic field of the current I_0 together with the homogeneous magnetic field $B_{e,y}$ creates a 2d quadrupole potential in the yz-plane, where the atoms are not confined along x. The superposition of the magnetic field from I_1 together with the bias field $B_{e,x}$ modulates the magnetic field along the x-axis and provides three dimensional confinement. Typically $I_1 \ll I_0$, for which the symmetry of the 2d quadrupole is only weakly distorted. Larger values twist the quadrupole guide as indicated. The Figure is adapted from [62].

minimum is located at $z_{\text{dimple}} \approx z_0$ and $y_{\text{dimple}} = 0$. The trap frequencies can be approximated by [69]

$$\omega_x = \sqrt{\frac{\mu}{m}\frac{\mu_0 I_1}{\pi z_0^3}} \quad \text{and} \quad \omega_\perp = \sqrt{\frac{\mu}{m}\frac{\mu_0^2 I_0^2}{4\pi^2 z_0^4 |B_{e,x} + \mu_0 I_1/2\pi z_0|}}. \tag{1.3.2}$$

Larger ratios of $\frac{I_1}{I_0}$ lead to a displacement and twisting of the trap as illustrated in Figure 1.3.3.

The dimple trap constitutes a building block for adjustable, more complex trap geometries like multi well configurations [43] or arrays of atom traps.

1.4 Breit-Rabi formula

The magnetically trappable hyperfine states $|F = 1, m_F = -1\rangle \equiv |1\rangle$ and $|F = 2, m_F = 1\rangle \equiv |2\rangle$ (the *clock-states*) have nearly identical magnetic moments μ and therefore are very promising for the on-chip implementation of an atomic clock [9, 30, 31] and as qubit basis states for quantum information processing (QIP) [43]. In the following I describe their energy difference ΔE and differential magnetic moment $\Delta\mu$ as a function of the external magnetic field B.

The formula (1.1.3) on page 12 is the result of a perturbative calculation of E_B using eigenstates $|F, m_F\rangle$ of the operator $\mathbf{F} = \mathbf{J} + \mathbf{I}$. For stronger magnetic fields, the ground state $5^2\mathrm{S}_{1/2}$ of $^{87}\mathrm{Rb}$ is more accurately described by the *Breit-Rabi* Hamiltonian [73, 66]:

$$H = A_{\mathrm{hfs}}\mathbf{I} \cdot \mathbf{J} + \mu_B B(g_J J_z + g_I I_z). \qquad (1.4.1)$$

Even though $\left|\frac{g_I}{g_J}\right| \approx 10^{-3}$, the coupling of $\mathbf{I}$ to the magnetic field B is not completely negligible, especially for spectroscopic experiments. In general, the eigenstates of Eq. (1.4.1) have to be determined by numerical diagonalization of the Hamiltonian. An analytical formula exists for the ground state manifold of a D transition, the Breit-Rabi formula [66]

$$E_{F,m_F} = -\frac{\Delta E_{\mathrm{hfs}}}{2(2I+1)} + g_I \mu_B m_F \pm \frac{\Delta E_{\mathrm{hfs}}}{2}\left(1 + \frac{4m_F \beta}{2I+1} + \beta^2\right)^{1/2}, \quad (1.4.2)$$

where $\Delta E_{\mathrm{hfs}} = A_{\mathrm{hfs}}(I + \frac{1}{2})$ is the hyperfine splitting and $\beta = \frac{(g_J - g_I)\mu_B B}{\Delta E_{\mathrm{hfs}}}$, see Appendix B for numerical values. $m_F = m_I \pm m_J$ (the $\pm$ sign is the same as in Eq. (1.4.2)).

The Breit-Rabi eigenenergies as a function of the magnetic field are illustrated in Figure 1.4.1. At a magnetic field of $B_\lozenge = 3.229\,\mathrm{G}$, the clock-states $|1\rangle$ and $|2\rangle$ have to first order a constant differential Energy $\Delta E = E_{2,1} - E_{1,-1} = h \cdot 6.834678113\,\mathrm{GHz}$ as a function of $(B - B_\lozenge)$, and therefore they share the same magnetic moment μ. The differential magnetic moment between $|1\rangle$ and $|2\rangle$ is given by $\frac{\partial(\Delta E)}{\partial B} = \Delta\mu_{1,-1}^{2,1} = 2h \cdot 431\,\frac{\mathrm{Hz}}{\mathrm{G}^2} \cdot (B - B_\lozenge) + \mathcal{O}(B^2)$ [74]. The common magnetic moment for $|1\rangle$ and $|2\rangle$ maximizes the coherence time in the presence of magnetic field fluctuations.

For strong magnetic fields, where the interaction with the magnetic field dominates the hyperfine interaction, we enter the Paschen-Back regime, where $\mathbf{I}$ and $\mathbf{J}$ couple independently to B.

1.5 Bose-Einstein condensation

Bose-Einstein condensation, which is the macroscopic occupation of a single-particle quantum state of motion, has opened up the possibility to explore quantum phenomena on a macroscopic scale. The achievement of Bose-Einstein condensation on an atom chip [75] has significantly lowered the technical complexity required to produce this fascinating state of matter, and portable devices have already been implemented [32]. Using a chip trap makes it possible to realize much more complex potentials. Furthermore, the
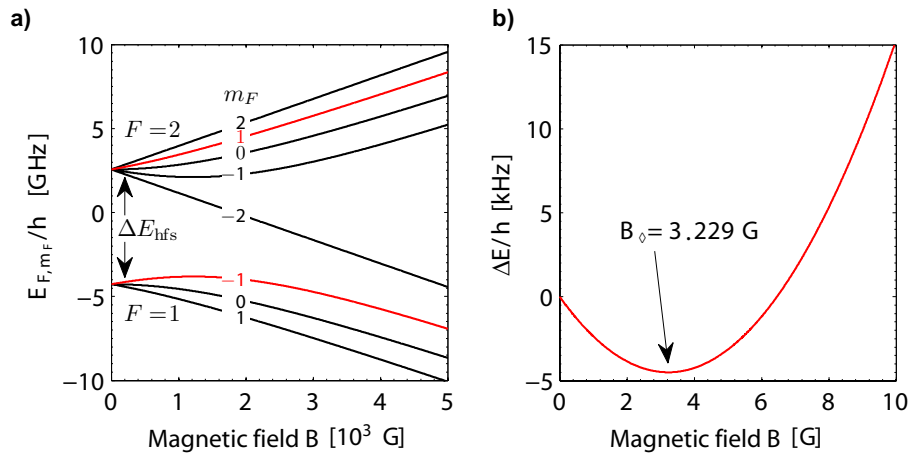
Figure 1.4.1: Energy of the hyperfine levels as a function of the static magnetic field B. (a) The energy of the different $|F, m_F\rangle$ sublevels for the $5^2\mathrm{S}_{1/2}$ ground state of $^{87}\mathrm{Rb}$ for values of B of up to $5 \times 10^3\,\mathrm{G} = 0.5\,\mathrm{T}$. The *clock-states* $|1, -1\rangle \equiv |1\rangle$ and $|2, 1\rangle \equiv |2\rangle$ are indicated in red. The slope shows that for high and low values of B, different hyperfine levels are magnetically trappable (i.e. those with positive slope). (b) Energy difference between $|1\rangle$ and $|2\rangle$ (with an offset of 6.834682610 GHz substracted) as a function of B. At the *sweetspot* $B_\diamond$=3.229 G, both states have a vanishing first order differential Zeeman shift. The Figure has been taken from [69].

chip can also constitute an interface between the Bose-Einstein condensate (BEC) and different types of (quantum) technology such as superconducting structures [76, 24, 72], optical single atom detectors [12], (reconfigurable) permanent magnetic structures [77], and nanomechanical resonators [78] to name just a few.

Bose-Einstein condensation occurs in thermal equilibrium, when entropy is maximized by putting a macroscopic population of bosonic atoms into the ground state of the system.[2] Since only atoms in an excited state contribute to the entropy, their contribution is maximized by forming a BEC in the ground state and distributing the remaining energy between the atoms which are not in the ground state of the trap [1]. A BEC is simply formed by lowering the temperature of the sample below the critical temperature T_c. Condensate growth is governed by bosonic stimulation [79], very similar to the stimulated emission in a laser.

In the case of non-interacting particles, the critical temperature T_c, the temperature at which condensation starts, for the case of a harmonic trap with trap frequencies ω_x, ω_y and ω_z, and $\omega_{ho} = (\omega_x \omega_y \omega_z)^{1/3}$, is given by [80]

$$T_c = 0.94 \cdot \frac{\hbar \omega_{ho} N^{1/3}}{k_B}, \tag{1.5.1}$$

where the prefactor is obtained in the limit $N \gg 1$. Corrections of the formula above for the case of finite N can be found in [81]. For a given number of atoms N at temperature $T \leq T_c$, the number of atoms N_0 in the ground state is given by

$$N_0(T) = N \left(1 - \frac{T^3}{T_c^3} \right). \tag{1.5.2}$$

In the following, we assume that the BEC is fully condensed (i.e. $N_0 \approx N$), which is justified, since in our experiment, typically $T \ll T_c$. In the non-interacting case, the wave function Ψ_N of the condensate can be written as the product of N single particle wave functions $\phi(\mathbf{r})$

$$\Psi_N(\mathbf{r}_1, \mathbf{r}_2, .., \mathbf{r}_N) = \prod_{i=1..N} \phi(\mathbf{r}_i) \tag{1.5.3}$$

The wave function $\phi(\mathbf{r})$ is the single particle ground state wave function of the confining potential, with $\int d\mathbf{r} \, |\phi(\mathbf{r})|^2 = 1$, and the condensate order parameter $\Psi(\mathbf{r}) = \sqrt{N} \cdot \phi(\mathbf{r})$.

---

[2]Real ultracold gas systems are only metastable and decay on a timescale which is typically much longer than the thermalization time.

In a real condensate however, in general interactions between the atoms are not negligible. In a cold, dilute gas of ^{87}Rb atoms, the interaction is dominated by elastic binary collisions at low energy which are characterized by a single parameter, the s-wave scattering length a_s [82]. For ^{87}Rb atoms, $a_s > 0$ and the interaction is repulsive. In a mean-field description, the energy of the interacting system with $N \gg 1$ (neglecting terms $\propto \frac{1}{N}$) is given by the functional [80]

$$E(\phi) = N \cdot \int d\mathbf{r} \left[\frac{\hbar^2}{2m} |\nabla\phi(\mathbf{r})|^2 + V(\mathbf{r}) |\phi(\mathbf{r})|^2 + \frac{gN}{2} |\phi(\mathbf{r})|^4 \right], \qquad (1.5.4)$$

where the coupling constant g is related to the s-wave scattering length a_s through

$$g = \frac{4\pi\hbar^2 a_s}{m}. \qquad (1.5.5)$$

An equation for the wave function $\phi(\mathbf{r})$ can be obtained by minimizing $E(\phi)$ with respect to ϕ subject to the condition of normalization $\int d\mathbf{r}\, |\phi(\mathbf{r})|^2 = 1$ being obeyed. This leads to the stationary Gross-Pitaevskii equation

$$\left(-\frac{\hbar^2}{2m} \nabla^2 + V_{\text{ext}}(\mathbf{r}) + gN |\phi(\mathbf{r})|^2 \right) \phi(\mathbf{r}) = \mu_{\text{c}} \phi(\mathbf{r}), \qquad (1.5.6)$$

where interactions between the atoms are described by the nonlinear mean-field term. Solving the above equation gives the single-particle wave function $\phi(\mathbf{r})$ and the chemical potential μ_{c}. For non-interacting particles μ_{c} is equal to the energy per particle ϵ - but in the interacting case, it is the energy of adding another particle. In the mean-field description, quantum depletion, which is an admixture of excited states, is neglected. In the Bogoliubov theory, the quantum depletion is $\frac{8}{3\pi^{1/2}} \sqrt{na_s^3}$, which is typically less than 1% for alkali condensates [1].

Dynamics in condensates (neglecting dissipation) is described by the time-dependent version of the Gross-Pitaevskii equation [83]

$$i\hbar \frac{\partial}{\partial t} \phi(\mathbf{r}, t) = \left(-\frac{\hbar^2}{2m} \nabla^2 + V_{\text{ext}}(\mathbf{r}) + gN |\phi(\mathbf{r}, t)|^2 \right) \phi(\mathbf{r}, t). \qquad (1.5.7)$$

1.5.1 Non-interacting case

In the case of non-interacting atoms, $g = a_s = 0$, and $\phi(\mathbf{r})$ is a Gaussian function given by [82]

$$\phi(\mathbf{r}) = \left(\frac{m\omega_{\text{ho}}}{\pi\hbar} \right)^{\frac{3}{4}} \cdot \exp\left(-\frac{m}{2\hbar} \left(\sum_{j=x,y,z} \omega_j j^2 \right) \right). \qquad (1.5.8)$$

The extension a_{ho} of the ground state wave function $\phi(\mathbf{r})$ is

$$a_{\mathrm{ho}} = \sqrt{\frac{\hbar}{m\omega_{\mathrm{ho}}}} \tag{1.5.9}$$

and is independent of the number of atoms N.

1.5.2 Thomas-Fermi approximation

In many experimental situations of atoms with repulsive interaction, the kinetic energy term in Eq. (1.5.6) is much smaller than the potential or interaction energy, except very close to the edge of the condensate. Neglecting the kinetic energy term from the Gross-Pitaevskii equation, gives the atom density distribution

$$n(\mathbf{r}) = N \left|\phi(\mathrm{r})\right|^2 = \frac{1}{g}\left[\mu - V_{\mathrm{ext}}(\mathbf{r})\right] \tag{1.5.10}$$

in the region where the right hand side is positive, and $n(\mathbf{r}) = 0$ outside this region [80]. The boundary of the cloud is therefore given by $V_{\mathrm{ext}}(\mathbf{r}) = \mu$. In the case of a harmonic trap, the condensate has a parabolic density profile [1]

$$n_c(\mathbf{r}) = \frac{15}{8\pi} \frac{N m^{\frac{3}{2}} \omega_x \omega_y \omega_z}{(2\mu_c)^{\frac{3}{2}}} \max\left(1 - \sum_{i=x,y,z} \frac{i^2}{R_i^2}, 0\right), \tag{1.5.11}$$

with $R_i = \sqrt{2\mu_c/m\omega_i^2}$ the Thomas-Fermi radii, where the condensate density goes to zero.

1.5.3 Intermediate regime

In the experiments presented in Chapter 5, we prepare condensates containing between 400 to 1000 atoms. Our experiment trap has axial (radial) trap frequencies of $f_x = 109\,\mathrm{Hz}$ ($f_\perp = 500\,\mathrm{Hz}$), which for 400 (1000) atoms gives a chemical potential $\mu_c = h \cdot 890\,\mathrm{Hz}$ ($h \cdot 1150\,\mathrm{Hz}$) [84]. Therefore, with our experimental parameters we are neither in the non-interacting case ($\mu_c \ll h \cdot f_i$) nor in the Thomas-Fermi regime ($\mu_c \gg h \cdot f_i$). Formulas interpolating between both regimes can be found in [84, 85].

1.6 Two-photon transition

Coherent transitions between the clock-states $|1\rangle$ and $|2\rangle$ require a two-photon drive, because they differ by two units of angular momentum. Such

a two-photon drive can consist of a microwave at frequency ω_{mw}, blue detuned by Δ with respect to $|1, -1\rangle \leftrightarrow |2, 0\rangle$ and a radio-frequency at ω_{rf} which is red detuned relative to the transition $|2, 0\rangle \leftrightarrow |2, 1\rangle$ such that $(E_{2,1} - E_{1,-1} + E_{\mathrm{ls}})/\hbar = \omega_{\mathrm{mw}} + \omega_{\mathrm{rf}}$ (see Figure 1.6.1). E_{ls} denotes the level-shift between the clock-states due to the off-resonant microwave, and in the limit of large detuning is given by $E_{\mathrm{ls}} = V_{\mathrm{mw}}^{2,1} - V_{\mathrm{mw}}^{1,-1}$, see Section 1.8.1. The level-shift arises due to the AC-Zeeman effect of the microwave and scales linearly with the applied microwave power (see Section 1.8). Various transitions contribute to E_{ls} due to the different microwave polarization components that are present. The radio frequency also causes similar level shifts, but for a linearly polarized radio frequency (as used in our experiment), the shifts of $|1\rangle$ and $|2\rangle$ are identical [69], and can therefore be neglected in this consideration.

When the resonant Rabi frequencies Ω_{mw} and Ω_{rf} are much smaller than the detuning ($|\Omega_{\mathrm{mw}}|^2$ and $|\Omega_{\mathrm{rf}}|^2 \ll \Delta^2$), then the population of the intermediate state $|2, 0\rangle$ is very small and the three-level system can be treated as an effective two-level system with a two-photon Rabi frequency [86]

$$\Omega_{\mathrm{2P}} = \frac{\Omega_{\mathrm{mw}}\Omega_{\mathrm{rf}}}{2\Delta}. \tag{1.6.1}$$

The two-photon pulse duration dt_{2P} should be short compared to the characteristic trap times $\frac{2\pi}{\omega_i}$ in order to prevent any undesired density evolution during the pulses.

1.7 Two-component BECs

The first binary mixture of BECs has been demonstrated in [87]. They produced two overlapping ^{87}Rb BECs in the hyperfine states $|1, -1\rangle$ and $|2, 2\rangle$ by sympathetic cooling of the atoms in $|2, 2\rangle$ with the atoms in state $|1, -1\rangle$. As a result of the different magnetic moments, the clouds were not overlapping completely due to different trapping potentials in combination with the gravitational sag. Furthermore, there was no fixed and repeatable phase relation between both condensates.

Ultracold clouds and condensates in a coherent superposition of states $|1\rangle$ and $|2\rangle$, prepared using the two-photon transition as described in the previous section, have been studied extensively by the Cornell group, where they measured atomic coherence properties [88], studied effects of elastic collisional interactions [48, 74], observed component separation [89], measured cooling due to decoherence in a partially condensed system [90] and spin waves [91].
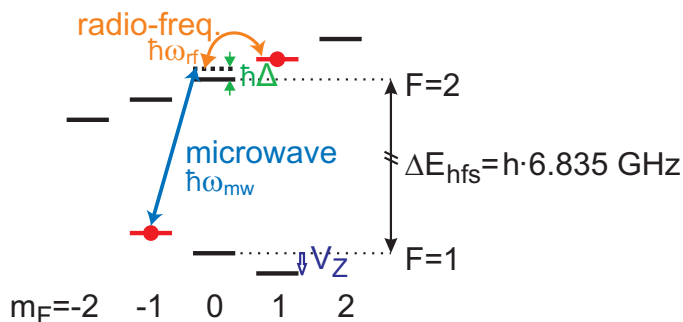
Figure 1.6.1: Two-photon transition between the hyperfine states $|1, -1\rangle \equiv |1\rangle$ and $|2, 1\rangle \equiv |2\rangle$ of the ^{87}Rb ground-state. The transition is the result of a blue detuned microwave (detuning Δ) at frequency ω_{mw} with respect to the transition $|1, -1\rangle \leftrightarrow |2, 0\rangle$ and a red detuned radio-frequency field at frequency ω_{rf}. If $|\Omega_{\text{mw}}|^2$ and $|\Omega_{\text{rf}}|^2 \ll |\Delta|^2$ then the system can be seen as an effective two-level system. The level-shift E_{ls} due to the off-resonant microwave field is not shown. For our experimental parameters, E_{ls} is on the order of some $h \cdot 10$ kHz, depending on the values of the microwave power P_{mw} and intermediate state detuning Δ.

In our experiment we initially condense the atoms in state $|1\rangle$. Under influence of a resonant Rabi drive of duration dt_{2P}, the state of the initially single-component BEC changes according to [92]

$$\prod_{i=1..N} \phi_1(\mathbf{r}_i) \quad \rightarrow \quad \prod_{i=1..N} \left\{ \cos[\tfrac{1}{2}\,|\Omega_{\text{2P}}|\,dt_{\text{2P}}]\phi_1(\mathbf{r_i}) + ie^{-i\alpha}\sin[\tfrac{1}{2}\,|\Omega_{\text{2P}}|\,dt_{\text{2P}}]\phi_2(\mathbf{r_i}) \right\}$$
$$= \Psi_{2c}, \tag{1.7.1}$$

where ϕ_1 (ϕ_2) is the spatial mode function of state $|1\rangle$ ($|2\rangle$). For a sufficiently fast two-photon pulse, $\phi_1 \equiv \phi_2$ immediately after the pulse. Using this method it is possible to prepare any desired superposition of both states with a well defined, relative phase $ie^{-i\alpha}$, where $\Omega_{\text{2P}} = |\Omega_{\text{2P}}|\,e^{i\alpha}$. Both involved states $|1\rangle$ and $|2\rangle$ have the same magnetic moments and therefore both components see identical confining potentials. Furthermore, the common magnetic moment preserves coherence in the presence of magnetic field fluctuations.

Measuring the number of atoms N_1 (N_2) in states $|1\rangle$ ($|2\rangle$) of Ψ_{2c}, we get a binomial distribution with mean value $\overline{N}_1 = p_1 \cdot N$, ($\overline{N}_2 = N - \overline{N}_1$) and widths $\sigma_1 = \sigma_2 = \sqrt{N \cdot p_1(1 - p_1)}$, where $p_1 = \cos^2[\tfrac{1}{2}\,|\Omega_{\text{2P}}|\,dt_{\text{2P}}]$. For large values of N, the distribution of N_1 (N_2) is essentially peaked at $\overline{N}_1$ ($\overline{N}_2$). In

a mean-field description, we can approximate Ψ_{2c} by

$$\tilde{\Psi}_{2c}(\mathbf{r}) = \sqrt{N_1} \cdot \phi_1(\mathbf{r}) + ie^{-i\alpha}\sqrt{N_2} \cdot \phi_2(\mathbf{r}) = \Psi_1(\mathbf{r}) + ie^{-i\alpha}\Psi_2(\mathbf{r}). \quad (1.7.2)$$

Notice that the approximation made in Eq. (1.7.2) neglects certain physical effects. The superposition of different atom numbers in both states in Eq. (1.7.1) in the presence of interactions also leads to a phase spreading, called *phase diffusion* [93]. This can be used to create entanglement and spin squeezed states, as we have shown in our experiment, see Section 6.1 and [47].

1.7.1 Time evolution of a two-component BEC

In a two-component BEC, where both states experience the same potential and the Rabi coupling between both states is turned off ($\Omega_{2P} = 0$), there are three important quantities which characterize the evolution of the system: The self-repulsion for each of the states and the mutual repulsion between them [94]. Both condensate components are initially prepared with identical density distributions since typically $dt_{2P} \ll \frac{2\pi}{\omega_i}$. This constitutes the starting point from which the condensate mean-field wave functions Ψ_1 (Ψ_2) evolve and redistribute themselves. The evolution of the binary-component system, including release from the trap, is governed by a pair of coupled Gross-Pitaevskii equations for the condensate wave functions Ψ_i (again for $N_i \gg 1$ and thereby neglecting terms $\propto \frac{1}{N_i}$) [89]

$$i\hbar\frac{\partial\Psi_i(\mathbf{r},t)}{\partial t} = \left(-\frac{\hbar^2}{2m}\nabla^2 + V_{\text{ext}}(\mathbf{r}) + U_{ii}\left|\Psi_i(\mathbf{r},t)\right|^2 + U_{ij}\left|\Psi_j(\mathbf{r},t)\right|^2\right)\Psi_i(\mathbf{r},t),$$
$$(1.7.3)$$

where $i, j = 1, 2$ ($i \neq j$), the mean-field potentials $U_{ij} = \frac{4\pi\hbar^2 a_{ij}}{m}$, and m the mass of a ^{87}Rb atom. The different measured scattering lengths are $a_{11} = 100.40\,a_0$, $a_{12} = 97.66\,a_0$ and $a_{22} = 95.00\,a_0$ [95]. Due to their similarity, the total density distribution $n_T(\mathbf{r}) = |\Psi_1(\mathbf{r})|^2 + |\Psi_2(\mathbf{r})|^2$ will not change significantly from its original value during the redistribution of the wave functions, but the effect on the equilibrium distribution of the different components may be profound [89]: Since $a_{12}^2 > a_{11}a_{22}$ the condensate is unstable to component separation [80]. It has been theoretically predicted and experimentally verified that the energetic minimum for a large atom number N is reached when the state $|2\rangle$ resides in the trap center, surrounded by a shell of state $|1\rangle$. This arrangement is energetically favored because the state with the higher scattering length forms a lower density shell around the higher density state with the smaller scattering length [89, 95].
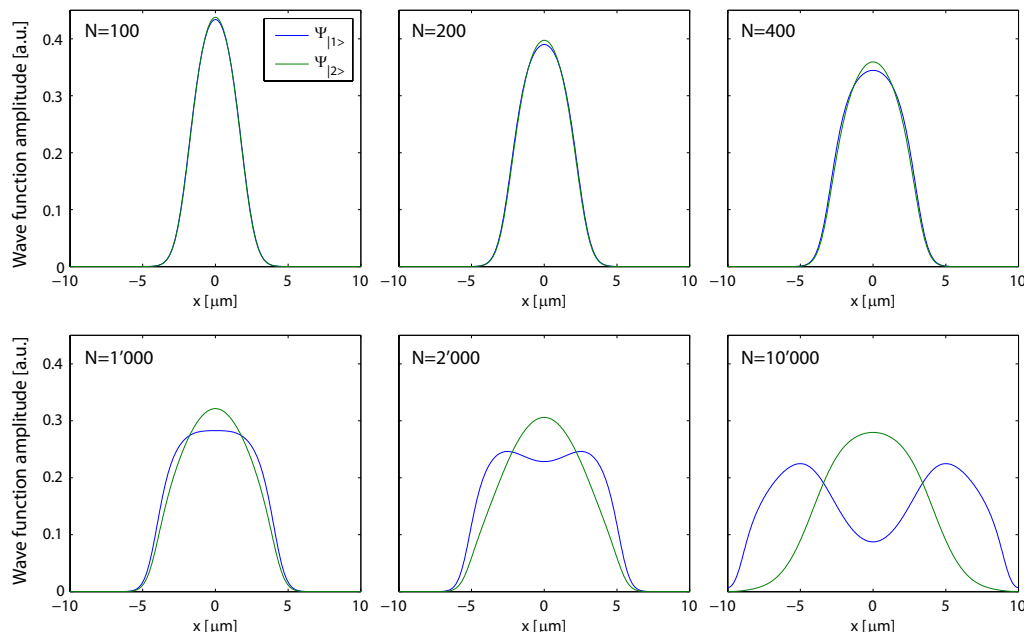
Figure 1.7.1: Simulated normalized 1D ground-state mode functions Ψ_1 and Ψ_2 along x of a two-component BEC in an equal superposition of states $|1\rangle$ and $|2\rangle$ for our experiment trap parameters and different atom numbers N. The description is given in the main text.

In Figure 1.7.1 we show the normalized ground-state mode functions Ψ_1 and Ψ_2 along x of a two-component BEC in an equal superposition of states $|1\rangle$ and $|2\rangle$ for different atom numbers N, calculated for our experiment trap parameters of Chapter 5 ($f_x = 109\,\text{Hz}$, $f_\perp = 500\,\text{Hz}$) using a 1D Gross-Pitaevskii (GP) solver written by Philipp Treutlein. In this simulation, we assume that the condensate is in the ground state of the transverse harmonic trapping potential. As the total atom number N increases, the overlap of both ground state mode functions decreases because of the difference in the intra- and inter-species scattering lengths. For the atom numbers $N = 400$ used in our experiments described in Chapter 5 we find that component separation is negligible, which is also confirmed by a 3D GP simulation by Li Yun and Alice Sinatra from Paris.

Pulses on the two-photon transition lead to a change of the population in the respective states with different scattering lengths, on a time scale typically much faster than the characteristic trap times $\frac{2\pi}{\omega_i}$. A change in the internal state population is accompanied by a sudden change in the mean-field energy. This can lead to oscillatory spatial behavior of the condensate wave functions as in [48, 95]. Again, for our atom numbers this is negligible.

The presence of a binary mixture of states in a condensate has also implications on trap loss, as will be detailed in the following section.

1.7.2   Trap loss in a two-component BEC

In the following, I describe sources for loss of atoms in chip traps. This imposes limitations e.g. on the duration of interferometric measurements.

Loss of magnetically trapped atoms can be caused by collisions with background gas atoms, which have a relatively high kinetic energy, or by inelastic collisions between the trapped atoms. The loss of atoms of a magnetically trapped, single-component condensate is described by the rate equation [69]

$$
\begin{aligned}
\frac{dN}{dt} &= -\gamma_{\mathrm{bg}} \int n(\mathbf{r})d^3\mathbf{r} - K \int n^2(\mathbf{r})d^3\mathbf{r} - L \int n^3(\mathbf{r})d^3\mathbf{r} + \mathcal{O}(n^4), \\
\leftrightarrow \frac{1}{N}\frac{dN}{dt} &= -\gamma_{\mathrm{bg}} - K \left\langle n \right\rangle - L \left\langle n^2 \right\rangle.
\end{aligned}
\tag{1.7.4}
$$

In this equation the coefficient γ_{bg} describes the loss arising from collisions with the residual background gas in the vacuum chamber, which is proportional to the background gas pressure. The second term describes inelastic two-body collisions between the trapped atoms, and the last term describes three-body recombination, where two atoms form a molecule and the kinetic energy is carried away by the molecule and the atom, satisfying energy and momentum conservation.

Inelastic two-body collisions   Inelastic two-body collisions are the result of two effects: Spin-exchange processes and magnetic dipole-dipole interactions [80]. For transitions, which are not forbidden by angular momentum selection rules, spin-exchange rates dominate by far over dipole-dipole interactions. An allowed spin-exchange process is e.g. $|2,1\rangle + |2,1\rangle \rightarrow |2,0\rangle + |2,2\rangle$, which conserves total m_F. The rate constant $K_{|2,1\rangle} \equiv K_2$ has recently been measured to be $K_2 = 1.194(19) \times 10^{-13}\,\mathrm{cm^3 s^{-1}}$ [95].

For states $|1,-1\rangle$ and $|2,2\rangle$, spin-exchange collisions are forbidden by angular moment selection rules [80]. They can make transitions via the magnetic dipole-dipole interaction at much lower rates.

Three-body collisions   Three-body loss puts stringent limits on achievable densities in atom traps. Typically both the molecule and the remaining atom are lost from the trap. For state $|1,-1\rangle$ the rate constant has been measured to be $L_{|1,-1\rangle} = L_1 = 5.8(19) \times 10^{-30}\mathrm{cm^6 s^{-1}}$ [96].

For a thermal ensemble, the constants for two- and three-body losses have to be multiplied by a quantum statistical factor of 2! and 3!, respectively,

which appears due to bosonic bunching. These have been verified experimentally. This constitutes an affirmation of the second order coherence in a condensate, as opposed to the classical case [96].

Loss in a two-component condensate Aforementioned loss rates are only valid when there is only one single condensate component. A condensate in a superposition of different hyperfine states is subjected to additional loss channels due to collisions between the different states. For a condensate in a superposition of states $|1\rangle$ and $|2\rangle$, the dominant contributions to collisional loss is described by (assuming perfect spatial overlap between the two components) [69]

$$\frac{1}{N_1}\frac{dN_1}{dt} = -\gamma_{\rm bg} - K_{12}\langle n_2 \rangle - L_1 \left\langle n_1^2 \right\rangle, \tag{1.7.5}$$

$$\frac{1}{N_2}\frac{dN_2}{dt} = -\gamma_{\rm bg} - K_{12}\langle n_1 \rangle - K_2 \langle n_2 \rangle, \tag{1.7.6}$$

with N_i and n_i the expectation values for numbers and densities of atoms in states $|i\rangle$. The rate constants for a BEC are L_1, K_2 as above and $K_{12} = 0.780(19) \times 10^{-13}\,{\rm cm}^3{\rm s}^{-1}$ [95].

1.8 State-dependent microwave potentials

Many interesting effects can be studied with state-dependent potentials, including atom interferometry with internal state labeling [52], entanglement through state-selective collisions [43, 97] and spin squeezing [47]. Atom interferometry (see [53] and Chapter 5) allows a precise measurement e.g. of inertial [98, 60] and surface forces. Compared with optical interferometry, atoms have an intrinsic sensitivity e.g. to rotation, which is increased by the ratio of their rest energy to the energy of the photon, typically about ten orders of magnitude higher [59, 53, 60].

A combination of static magnetic and electric fields (as considered in [40, 99]) is not capable of providing a differential potential for the robust pair $|1\rangle$ and $|2\rangle$. This is because the magnetic moments and electrostatic polarizabilities are equal for both states [43]. Optical dipole traps are also not practical because if operated at a detuning from the D_1 or D_2 transition much larger than the hyperfine splitting of ^{87}Rb, the differential potential is relatively weak. If an optical dipole trap is operated at a detuning comparable to the hyperfine splitting, the differential potential can be made strong, but spontaneous scattering of photons becomes strong, which causes decoherence, heating and loss of the atoms in the trap [43]. A further disadvantage of

optical potentials is that while it is possible to integrate optical components on an atom chip [12, 15, 100, 101, 102], it is hard to implement tailor-made potentials, which are non-periodic.

We have established a new technique to generate state dependent potentials on an atom chip using microwave near-fields. It combines the flexibility of optical dipole potentials with the stability and tailorability of static magnetic microtraps.

Trapping of neutral atoms using far-field microwave radiation has first been proposed in [49] and the first experimental realization was reported in [50]. Microwave potentials arise by a similar effect as optical dipole traps, but while optical potentials are generated by the AC Stark effect [1], microwave potentials arise via the AC Zeeman effect. For microwaves, decoherence rates due to spontaneous emission are negligible and the state-selectivity can be adjusted via microwave frequency and polarization.

In the following, I describe the origin of microwave potentials for ground-state ^{87}Rb atoms. While I start with the assumption of the microwave field being a classical field, a quantum treatment can be found in [69, 103]. Here and in the rest of this thesis the Larmor frequency ω_L is given by $\omega_L = \frac{\mu_B B}{2\hbar}$.

Consider a ^{87}Rb atom in the $5^2\mathrm{S}_{1/2}$ ground state at fixed coordinate $\mathbf{r}$. The atom interacts with the local static magnetic field $\mathbf{B}_0$ and the (classical) real-valued microwave magnetic field $\mathbf{B}_{\mathrm{mw}}(t) = \frac{1}{2}\left[\hat{\mathbf{B}}_{\mathrm{mw}}e^{i\omega t} + \hat{\mathbf{B}}_{\mathrm{mw}}^* e^{-i\omega t}\right]$, with $\hat{\mathbf{B}}_{\mathrm{mw}}$ a complex phasor. The atomic hyperfine states are described by the Hamiltonian[3]

$$H = (\hbar\omega_{\mathrm{hfs}}/2)\mathbf{I} \cdot \mathbf{J} + \mu_B(g_J\mathbf{J} + g_I\mathbf{I}) \cdot (\mathbf{B}_0 + \mathbf{B}_{\mathrm{mw}}(t)). \qquad (1.8.1)$$

The first term describes the hyperfine coupling between the total electron spin $\mathbf{J}$ and the nuclear spin $\mathbf{I}$. The second term is the coupling of the static and microwave magnetic field to $\mathbf{J}$ and $\mathbf{I}$. For high precision simulations yielding a comparison to spectroscopic measurements, all the terms have to be taken into account. For our purpose, a number of approximations can be made:

- We neglect the coupling of $\mathbf{I}$ to the magnetic fields because $\left|\frac{g_I}{g_J}\right| \approx 5 \times 10^{-4}$.

- We treat the coupling of $\mathbf{J}$ to $\mathbf{B}_0$ perturbatively because $\mu_B B_0 \ll \hbar\omega_{\mathrm{hfs}}$ ($\omega_{\mathrm{hfs}} = \Delta E_{\mathrm{hfs}}/\hbar$).

---

[3]The electric field of the microwave has not to be considered, because the energy shift is common mode for $F = 1$ and $F = 2$. [66]

- We transfer to a frame rotating at frequency ω and make the rotating-wave approximation, which is valid because $\mu_B B_{\mathrm{mw}}, \hbar \Delta_0 \ll \hbar \omega$, with $\Delta_0 = \omega - \omega_{\mathrm{hfs}}$.

With these approximations, we express H in the basis $|F, m_F\rangle$, with the quantization axis along $\mathbf{B}_0$:

$$
\begin{aligned}
H \approx & \sum_{m_2} \left(-\tfrac{1}{2}\hbar\Delta_0 + \hbar\omega_L m_2 \right) |2, m_2\rangle\langle 2, m_2| \\
& + \sum_{m_1} \left(\tfrac{1}{2}\hbar\Delta_0 - \hbar\omega_L m_1 \right) |1, m_1\rangle\langle 1, m_1| \\
& + \sum_{m_1, m_2} \left(\tfrac{1}{2}\hbar\Omega_{1,m_1}^{2,m_2} |2, m_2\rangle\langle 1, m_1| + \mathrm{c.c.} \right),
\end{aligned}
\tag{1.8.2}
$$

where we have approximated $g_J \approx 2$. The microwave couples the transition $|1, m_1\rangle \leftrightarrow |2, m_2\rangle$ with Rabi frequency

$$
\Omega_{1,m_1}^{2,m_2} = \left(\frac{2\mu_B}{\hbar} \right) \langle 2, m_2 | \hat{\mathbf{B}}_{\mathrm{mw}} \cdot \mathbf{J} | 1, m_1 \rangle
\tag{1.8.3}
$$

and detuning

$$
\Delta_{1,m_1}^{2,m_2} = \Delta_0 - (m_2 + m_1)\omega_L.
\tag{1.8.4}
$$

In our simulations, we numerically diagonalize the Hamiltonian of Eq. (1.8.2). The eigenstates are the *dressed states* $|D\rangle$, which are shown in Figure 1.8.1.

An anti-crossing emerges whenever Δ_{1,m_1}^{2,m_2} vanishes and Ω_{1,m_1}^{2,m_2} is simultaneously non-zero. In the vicinity of an anti-crossing, the dressed eigenstates are mainly a superposition of the states that anti-cross. Accordingly, the energy difference between both dressed eigenstates near an anti-crossing in a two-level approximation can be written as [103]:

$$
E_+ - E_- \approx \hbar \sqrt{ \left| \Omega_{1,m_1}^{2,m_2} \right|^2 + \left| \Delta_{1,m_1}^{2,m_2} \right|^2 }.
\tag{1.8.5}
$$

Consequently, the energy difference between the dressed states on resonance is given by $\hbar \left| \Omega_{1,m_1}^{2,m_2} \right|$.

In Figure 1.8.2 I show $E(D)$ as a function of $B_{\mathrm{mw}} = |\mathbf{B}_{\mathrm{mw}}|$ for the experimental parameters of Chapter 5, i.e. $B_0 = 3.23\,\mathrm{G}$ and microwave frequency ω which is blue detuned by $\delta \equiv \Delta_{1,-1}^{2,-1} = 2\pi \times 600\,\mathrm{kHz}$ with respect to the transition $|1, -1\rangle \to |2, -1\rangle$ ($\Delta_0 = -2\omega_L + 2\pi \times 600\,\mathrm{kHz}$). One can see that for small values of B_{mw} the energy of state $|1, -1\rangle$ is shifted much more than that of $|2, 1\rangle$.
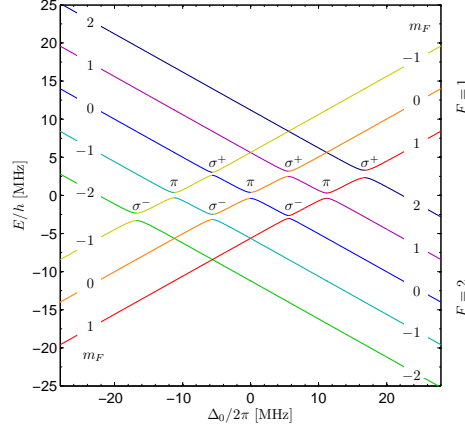
Figure 1.8.1: Dressed states energies $E(D)$ as a function of Δ_0. $B_0 = 8\,\mathrm{G}$, $\hat{\mathbf{B}}_{\mathrm{mw}} = \frac{1}{\sqrt{3}}(1,1,1)\,\mathrm{G}$. The line colors indicate the dominant hyperfine state in the dressed state. The figure has been taken from [69].
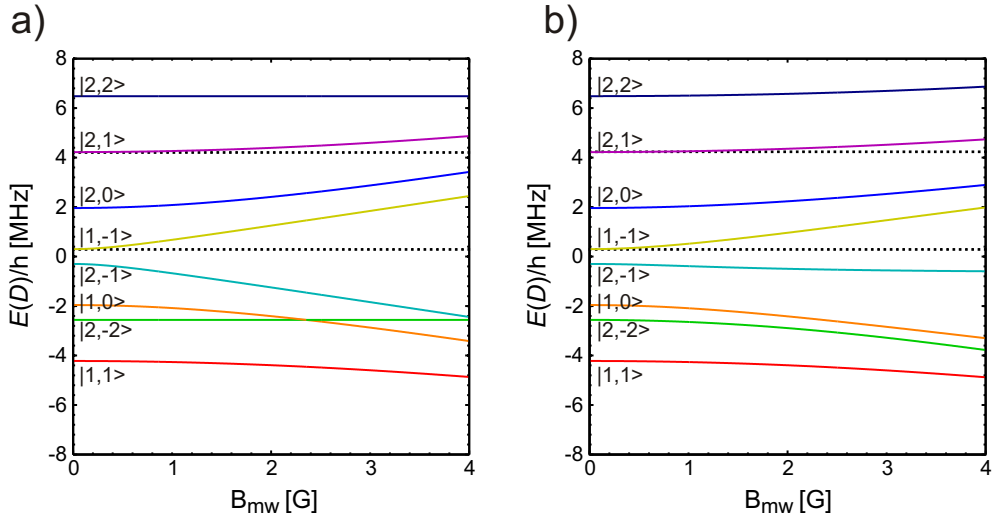
Figure 1.8.2: $E(D)$ as a function of $|\mathbf{B}_{\mathrm{mw}}|$ for $B_0 = 3.23\,\mathrm{G}$ along x and microwave frequency ω which is blue detuned by $\delta = 2\pi \times 600\,\mathrm{kHz}$ with respect to the transition $|1,-1\rangle \rightarrow |2,-1\rangle$ ($\Delta_0 = -2\omega_L + 2\pi \times 600\,\mathrm{kHz}$) for (a) $\mathbf{B}_{\mathrm{mw}} = (1,0,0)$ (a π-polarized microwave) and (b) $\mathbf{B}_{\mathrm{mw}} = (1,1,1)/\sqrt{3}$. For small values of B_{mw} the energy of state $|1,-1\rangle$ is shifted much more than that of $|2,1\rangle$.

1.8.1 Limit of large detuning

In the case of a far-detuned microwave, where $\left|\Omega_{1,m_1}^{2,m_2}\right|^2 \ll \left|\Delta_{1,m_1}^{2,m_2}\right|^2$ for all m_1, m_2, each eigenstate $|D\rangle$ consists essentially of a $|F, m_F\rangle$ of the unperturbed system. The admixture of other states is of order $\Omega_{1,m_1}^{2,m_2}/2\Delta_{1,m_1}^{2,m_2} \ll 1$ [69]. In this regime, the energy for an eigenstate $|D\rangle \approx |F, m_F\rangle$ can be written as

$$E(D) \approx E_0^F + V_Z^{F,m_F} + V_{\mathrm{mw}}^{F,m_F}. \tag{1.8.6}$$

Here V_Z^{F,m_F} is the static Zeeman shift and V_{mw}^{F,m_F} is the microwave potential due to the AC Zeeman shift given for $F = 1$ by [43]

$$V_{\mathrm{mw}}^{1,m_1} = \frac{\hbar}{4} \sum_{m_2} \frac{\left|\Omega_{1,m_1}^{2,m_2}\right|^2}{\Delta_{1,m_1}^{2,m_2}}, \tag{1.8.7}$$

and for the $F = 2$ manifold by

$$V_{\mathrm{mw}}^{2,m_2} = -\frac{\hbar}{4} \sum_{m_1} \frac{\left|\Omega_{1,m_1}^{2,m_2}\right|^2}{\Delta_{1,m_1}^{2,m_2}}. \tag{1.8.8}$$

The state-selectivity in the limit of far detuning can clearly be seen by comparing Eq. (1.8.7) with Eq. (1.8.8). Working in the limit of large detuning is advantageous, since the admixture of other states $\propto \Omega_{1,m_1}^{2,m_2}/2\Delta_{1,m_1}^{2,m_2}$ can be made small. This is important for good coherence since the admixed states typically have a different magnetic moment $\tilde{\mu}$ which leads to an increased sensitivity to magnetic field fluctuations.

Chapter 2

A microwave atom chip

In the experiments reported in this thesis, we employ a newly developed atom chip, which combines wires for static magnetic trapping with integrated microwave waveguide structures (see photograph on Figure 2.0.1). This chapter covers the design of the chip as well as its fabrication and characterization.

The design of the chip fulfills a number of requirements. In order to be able to produce BECs we need to have an on-chip mirror for the mirror-MOT as well as wires for magnetic trapping, which can withstand the high current densities required to compress the magnetic trap for efficient evaporative cooling. We need micron sized waveguide structures on the chip that exhibit strong near-field gradients (for state-dependent microwave potentials that vary on a μm scale) and the feasibility to superimpose microwave and DC currents on the same wires, where the latter are used for static magnetic trapping. To avoid electrical contact between the waveguide and wires for magnetic trapping, the chip must contain two layers of metalization. We need substrates with high thermal conductivity to prevent overheating of the on-chip wires. Furthermore, the chip substrate has to be compatible with microwave structures (i.e. not cause high losses). Last but not least, we need good optical access to the chip for optical imaging.

In the following, I give an overview of microwave waveguide basics and introduce the coplanar waveguide (CPW) structure, which we chose to integrate on the atom chip. I will cover the field distribution around the CPW, which determines the potentials seen by the atoms, and which allows to create microwave potentials that vary on a micrometer scale. Thereafter, I describe how we design, simulate and characterize microwave test structures fabricated in the design process. Finally, I will cover the fabrication of the atom chip and then conclude this chapter with its DC and microwave characterization.

.
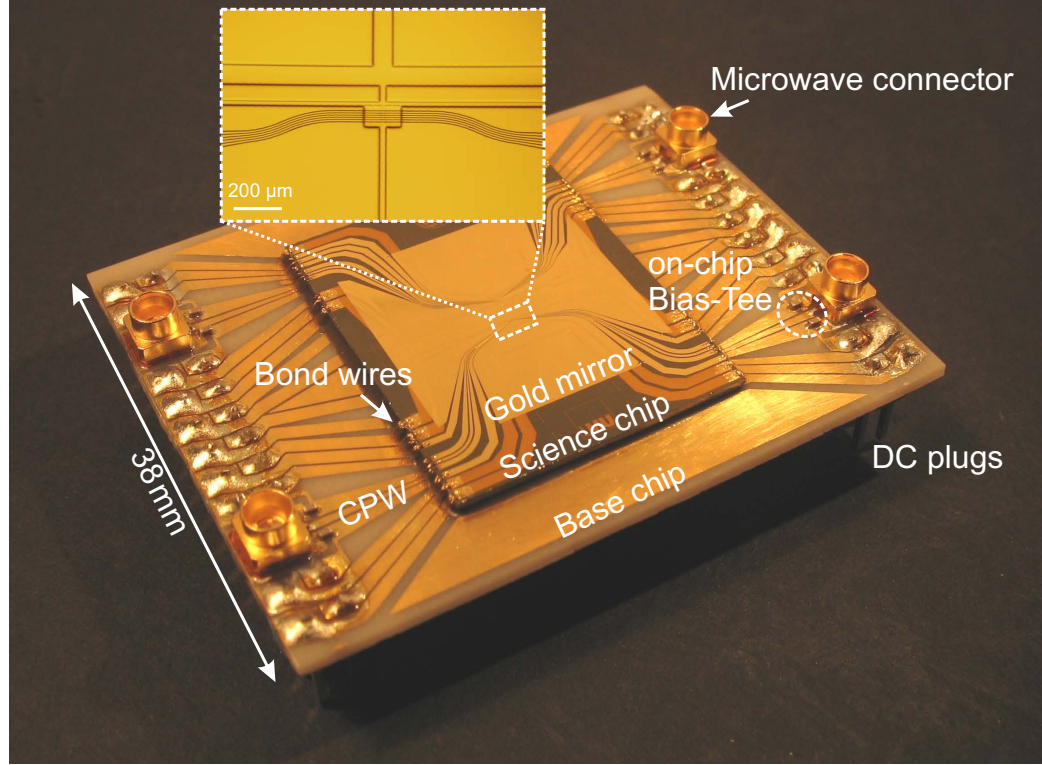
Figure 2.0.1: Overview of our atom chip. The atom chip consists of three chips, the base chip, the science chip and a spacer chip between the two. These are glued to each other. The base chip consists of a $800\,\mu$m thick AlN substrate with $12\,\mu$m thick gold wires, which are used for the last MOT stage. The base chip constitutes a wall of the vacuum system, seals it, and provides electrical feed through to the vacuum, including DC and microwave contacts for the science chip. Both, the science and the spacer chip consist of a $525\,\mu$m thick high-resistivity Si substrate, oxidized with a $20\,$nm SiO_2 insulation layer. While the spacer chip contains no metallic structures, the science chip has two layers of metalization, separated by a $6\,\mu$m thin poly-imide layer. While the wires on the lower layer are used for static magnetic trapping only, the wires on the upper layer carry DC currents for static trapping as well as microwave currents for the state-selective microwave potentials. Furthermore, the upper metalization layer contains gold mirrors for the mirror-MOT. The atom chip package is water cooled on its backside (shown in Figure 2.2.6).

2.1 Microwave design

It is well known that in the far-field of an electromagnetic radiation source, focusing to much below a wavelength is impossible (known as the Abbe-Rayleigh diffraction limit). Accordingly, structuring microwave potentials on a μm scale in the far-field of a microwave source at $\nu_{\mathrm{mw}} = 6.8\,\mathrm{GHz}$ is impossible because the (vacuum) wavelength $\lambda_{\mathrm{mw}} = \frac{c}{\nu_{\mathrm{mw}}} \approx 4.4\,\mathrm{cm}$. This limitation can be overcome by going to the near-field of a microwave guiding structure; at a distance $d \ll \lambda_{\mathrm{mw}}$. In the near-field region, the microwave magnetic fields created by the microwave currents on the waveguide structure have the same position dependence as magnetic fields created by DC currents on the same wires [104]. Therefore, in the near-field, the relevant length scale for achievable field gradients is not a function of λ_{mw}, but of the lateral extent of the microwave guiding structure $s + 2w$ (see Figure 2.1.1) and the distance d to the waveguide structures, which allows the realization of much stronger gradients than achievable in the far-field (see Section 3.9).

There exist several planar waveguide geometries which can be integrated on an atom chip. We chose to integrate coplanar waveguides (CPWs) onto our atom chip, a waveguide structure that has first been described by C.P. Wen [105]. A CPW in its ideal form consists of an infinitely thin conducting strip (the *signal wire*) with two semi-infinite ground conductors on a surface of an infinitely thick dielectric substrate [106]. In practice, CPW grounds always have a finite extent g and the substrate has a finite thickness or is even a multi-layer dielectric (see schematic on Figure 2.1.1).

CPWs are well suited for integration on an atom chip, because they are uniplanar in construction (all structures are on the same side of the substrate), no *via holes* [107] are needed, and they can be tapered without change in the characteristic impedance [108]. Knowledge of the microwave field distribution around the CPW is important because it determines the microwave potential for the atoms. In the following, the basic theory of CPWs, microwave propagation and the near-fields around them will be presented.

2.1.1 Coplanar waveguide theory

For ideal, translationally invariant transmission lines with perfect conductors, that are in addition completely surrounded by a uniform dielectric medium, the principal wave that can exist on the transmission line is a TEM wave [51], where the electric and magnetic fields for an electromagnetic wave traveling
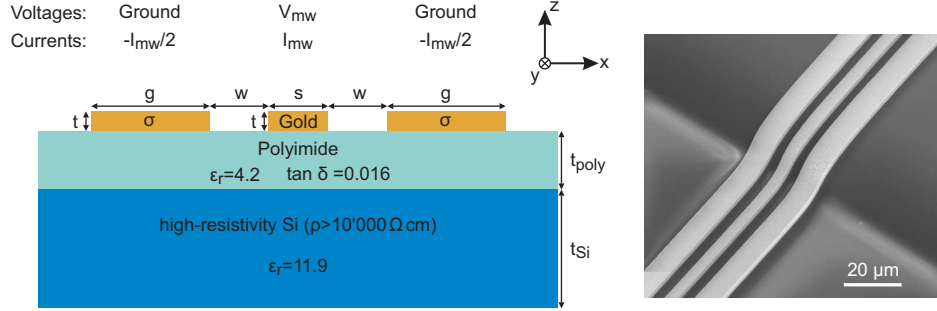
Figure 2.1.1: (Left) Schematic drawing of a CPW structure that is integrated on our atom chip. The thicknesses are $t_{\mathrm{poly}} \approx 6\,\mu\mathrm{m}$ and $t_{\mathrm{Si}} = 525\,\mu\mathrm{m}$. The conductivity of gold is $\sigma = 4.5 \times 10^7\,\Omega^{-1}\mathrm{m}^{-1}$ at room temperature. The voltages and currents indicated correspond to that of an ideal CPW mode. (Right) Exemplary microfabricated CPW structure (here, $t = 800\,\mathrm{nm}$).

along y are given by

$$\mathbf{E}(\mathbf{r}, t) = \mathrm{Re}\left[\mathbf{E}(x, z)\exp(i\omega t - \gamma y)\right], \tag{2.1.1}$$

$$\mathbf{B}(\mathbf{r}, t) = \mathrm{Re}\left[\mathbf{B}(x, z)\exp(i\omega t - \gamma y)\right]. \tag{2.1.2}$$

TEM waves are convenient because the distribution of the transverse fields can be calculated by combining computationally cheap 2D electro- and magnetostatic analyses.

Conductor loss In micrometer sized transmission lines, conductor loss plays an important role [109]. A finite conductivity σ not only leads to attenuation but also changes the current distribution within the wire via the skin effect [104], which affects the electromagnetic field within and around the wire. For gold and $\omega = 2\pi \times 6.8$ GHz, the skin depth $\delta_{\mathrm{skin}} = \sqrt{2/\omega\mu_0\sigma} = 0.9\,\mu\mathrm{m}$ is comparable to the dimensions of the micron sized structures on our chip (see Section 2.1.3).

Planar transmission lines, like a CPW, where the dielectric does not fill the complete surrounding, and/or where the conductors have only finite conductivity (see Figure 2.1.1) do not support true TEM waves. There are longitudinal field components at the dielectric-air interface as well as inside the conductors of finite conductivity σ. In the low-frequency limit, where $\lambda_{\mathrm{mw}}/(s + 2w) \gg 1$ and for weak conductor losses, the dominant mode of propagation is very similar to the true TEM case, i.e. the longitudinal field components are much smaller than the transverse [110]. These are called *quasi-TEM* modes [51]. Typically the condition

$$\lambda_{\mathrm{mw}}/(s + 2w) > 10 \tag{2.1.3}$$

a)   b)

GND V_0 GND $-V_0$ GND V_0
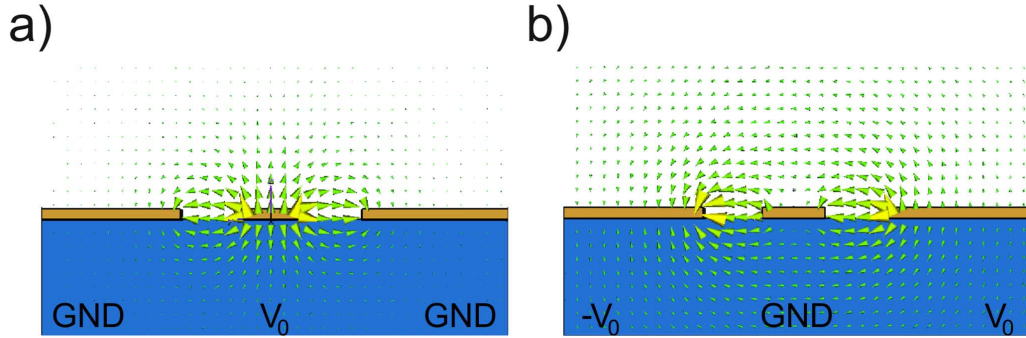
Figure 2.1.2: Visualization of the electric field distribution $\mathbf{E}(x,z)$ of the two modes supported by CPW structures. The modes are called (a) the *CPW mode* and (b) the *slotline* or *odd mode*. In our experiment, any coupling of power from the CPW mode to the slotline mode is undesired. The potentials of the CPW wires are indicated on the bottom. The figure has been adapted from [111].

is sufficient to guarantee quasi-TEM behavior [109].

Since a CPW consists of three wires, it has two eigenmodes, the *CPW* and the *slotline mode* (see Figure 2.1.2). We excite only the CPW mode (by pulling both grounds to the same potential), but discontinuities in the CPW geometry can couple power from the CPW mode to the slotline mode. This could be avoided by equilibrating the potential between both grounds by properly spaced conductive bridges [112, 113], but this is incompatible with the DC currents on the CPW grounds as required on our chip. We carefully designed and tested the structures on our chip to minimize such coupling between modes.

The electric and magnetic field distribution $\mathbf{E}(\mathbf{r})$ and $\mathbf{B}(\mathbf{r})$ around a waveguide can in general be computed with a computationally very expensive full-wave 3D simulation, using software packages like *HFSS*[1] or *Yatpac*.[2] If the condition for quasi-TEM behavior is satisfied (Eq. (2.1.3)), then for a piece of transmission line with constant cross section, the fields $\mathbf{E}(x,z)$ and $\mathbf{B}(x,z)$ can be calculated using a 2D quasistatic simulation that takes conductor loss into account, as described in [109, 69, 114].[3] Both methods yield a field distribution which takes the current distribution in the wires into account, that is strongly influenced by the skin effect [104].

At distances d from the waveguide, with $d \gg s, w$, and t, the simulation

---

[1]From Ansoft, www.ansoft.com

[2]www.yatpac.org

[3]If conductor loss is negligible, then a static simulation is sufficient.
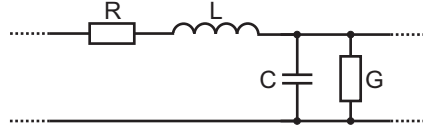
Figure 2.1.3: Equivalent circuit for a piece of transmission line with constant cross section. The parameters R, L, C and G (all defined per unit length) are defined as integrals of $\mathbf{E}(x,z)$ and $\mathbf{B}(x,z)$. From these parameters, the complex propagation constant γ and the complex characteristic impedance Z_c can be calculated. While for typical waveguides $G \ll \omega C$, for micron sized structures R and ωL can be of comparable magnitude.

can be simplified even further to a static simulation, where the waveguide currents are approximated by homogeneous currents that flow on infinitely thin waveguide wires, and $\mathbf{B}(x,z)$ is calculated via the law of Biot-Savart.

In many cases, where the structure is not translational invariant (therefore a 2D quasistatic or static analysis is inappropriate) and full-wave 3D simulations are too expensive, one can use 3D planar simulations using software packages like *Sonnet*[4] or *Microwave Office*.[5] Their outputs are S-parameters [115] and current distributions on infinitely thin layers. The corresponding microwave magnetic near-field distribution can be calculated from the current distribution again using the law of Biot-Savart.

Equivalent circuit model A piece of a transmission line with constant cross-section, where the (quasi)-TEM condition is fulfilled (Eq. (2.1.3)), can be related to an equivalent circuit model [109] (see Figure 2.1.3), which is very helpful for intuition. Such a circuit contains the series resistance R, inductance L, capacitance C and shunt conductance G, which are all defined per unit length of the transmission line. These parameters are defined as integrals of $\mathbf{E}(x,z)$ and $\mathbf{B}(x,z)$ [51], and we calculate them using $\mathbf{E}(x,z)$ and $\mathbf{B}(x,z)$ from a quasi-static simulation. From these, the parameters which describe the wave propagation on the transmission line can be derived:

$$Z_c = \sqrt{\frac{R + i\omega L}{G + i\omega C}}, \tag{2.1.4}$$

$$\gamma = \alpha + i\beta = \sqrt{(R + i\omega L)(G + i\omega C)}. \tag{2.1.5}$$

$Z_c = \frac{V_{\mathrm{mw}}}{I_{\mathrm{mw}}}$ is called the characteristic impedance, and is in general complex. A complex-valued Z_c leads to a phase shift between electric and magnetic

---

[4]www.sonnetsoftware.com

[5]From AWR, www.awrcorp.com

fields, but this does not influence the microwave potential for the atoms. Changes of Z_c along the transmission line lead to mismatch loss (reflections). The quantity γ is the propagation constant, which contains α quantifying microwave attenuation and $\beta = \frac{2\pi}{\lambda_{\mathrm{mw}}}$ with λ_{mw} the wavelength of the guided wave. In a lot of cases, for the calculation of Z_c and γ it is not necessary to perform a numerical simulation. For most regimes, approximate analytical formulas exist [109], which yield useful results. A helpful tool for estimates is the program *TX-Line*.[6]

Scaling   For an ideal CPW with perfect conductors, Z_c is only a function of $\frac{s}{s+2w}$ [69, 108] and therefore the idealized CPW can be tapered without change in Z_c by scaling s and w by a common factor. For a real CPW, the same is approximately true.

2.1.2   Designing the microwave chip

In designing the microwave chip, it is important to keep reflections, microwave attenuation and coupling of power from the even to the odd mode at tolerable levels, in order to get the desired field distribution and field strength at the position of the atoms. Discontinuities along a CPW can cause such undesired behavior. Since discontinuities cannot be fully avoided, they have to be designed carefully to minimize unwanted effects. Furthermore, a substrate has to be chosen which does not cause strong microwave losses.

We chose a hybrid aproach, where we simulated test structures using quasi-static simulations and Sonnet, and compared the simulations to measurements on fabricated test structures, which we characterized on a probe station[7] (see Figure 2.1.4) using a vector network analyzer[8] together with high-frequency probes,[9] see below. In this way we identified suitable subcircuits for the atom chip.

For the design of the final chip, we used our experience gained with the test structures. We simulated the outer regions of the CPW with quasi-static simulations (i.e. for the calculation of Z_c such that there are no jumps in impedance), while the central part of the CPW was simulated using Sonnet.
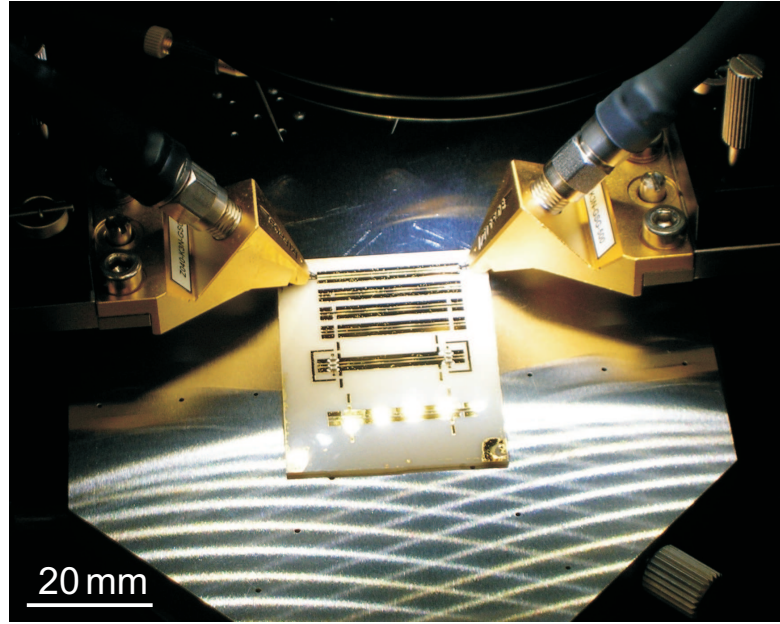
Figure 2.1.4: A test-chip with relatively large CPW structures fabricated on an AlN substrate, under test on our probe station. The lowest two circuits contain on-chip Bias-Tee structures. To characterize the microwave properties of such a structure, we use a vector network analyzer (VNA) which generates a microwave signal at variable frequency (up to 8.5 GHz). This is fed onto one port of the structure using high-frequency probes. The reflected and transmitted signal is evaluated by the VNA, which calculates the frequency-dependent scattering matrix S_{ij}.

Design and characterization of sub-circuits

The following structures, which we analyzed using test chips, were included in the final chip design:

- On-chip Bias-Tees, used to superimpose microwave and DC currents on the CPW wires. The DC currents constitute dimple trap currents, as described in Section 1.3. For the CPW signal wire, a commercially available, external coaxial Bias-Tee[10] is used. For the CPW grounds we want individual control of the static currents on the CPW ground wires. Since such an external split-ground Bias-Tee is not available, we developed an on-chip Bias-Tee for the CPW grounds, which together with its performance is shown in Figure 2.1.5.

- Wire bonds, which connect the CPW on the base chip with the one on the science chip.

- Bends of the CPW.

- Tapering of the CPW. In the center of the chip, the CPW has to have μm sized wires which results in strong near-field gradients. At the edges of the chip, it is technically much more straight forward to connect a millimeter sized CPW than a microns sized structure. In between, the CPW has to be tapered without changing the characteristic impedance Z_c too abruptly[11] (which otherwise would cause reflections). A microns sized CPW causes considerable microwave loss, limiting the power reaching the chip center, therefore the tiny part of the CPW should not be longer than necessary.

- Crossing of metallic structures, which are in the lower layer of the science chip. The CPW crosses wires on the lower layer which are separated by a insulating polyimide layer with thickness $t_{\text{Poly}} \approx 6\,\mu$m (see Figure 2.1.6). The layer thickness t_{Poly} is comparable to $s + 2w$ in the center. As a result, fringing fields induce currents into the lower layer structure which themselves create microwave magnetic fields.

---

[6]From AWR, web.awrcorp.com

[7]Süss Microtech Prober PM5 HF

[8]Agilent E5071B

[9]Süss Microtech Z-Probe 40K3N, 500 μm pitch

[10]UMCC BT-S000-HS

[11]In the final chip Z_c changes smoothly from $|Z_c| = 50\,\Omega$ at the edge of the science chip to $|Z_c| = 70\,\Omega$ and $|Z_c| = 80\,\Omega$ in the chip center, respectively, see Section 2.1.3.

- We tested the compatibility of several substrate materials with microwave circuits. AlN as well as high-resistivity silicon ($\rho > 10^4\,\Omega\mathrm{cm}$) have been identified as suitable materials for our microwave circuits (i.e. do not cause excessive microwave loss).

As examples, the measured characteristics for the on-chip Bias-Tee (Figure 2.1.5) and for a CPW test structure crossing a wire (Figure 2.1.6) are shown.

The microwave potential seen by the atoms depends on the distribution of the microwave magnetic field $\mathbf{B}(\mathbf{r})$, which itself depends on microwave currents, including currents induced in the lower layer of metalization. The influence of induced microwave currents on $\mathbf{B}(\mathbf{r})$ had to be estimated numerically. F. Peretti and G. Csaba from the Lugli-Group at the TU Munich performed an HFSS full-wave 3D simulation of a test structure, where a micron-sized, tapered CPW crosses a $50\,\mu\mathrm{m}$ broad wire in the lower layer, separated by $\approx 4\,\mu\mathrm{m}$ of polyimide (see Figure 2.1.6a). The impedance changes from $|Z_c| = 50\,\Omega$ at the edge of the chip to $|Z_c| = 80\,\Omega$ in the center. The results of their calculation are the $\mathbf{E}(\mathbf{r})$ and $\mathbf{B}(\mathbf{r})$ field distributions as well as the S-parameters. We compare the simulated S-parameters with HFSS to a simulation with Sonnet as well as to measurements on the same structure. The results are shown in Figure 2.1.6b. We find good qualitative agreement for the reflective S-parameters, while the simulations underestimate losses. Furthermore, we compare the HFSS-simulated $\mathbf{B}(\mathbf{r})$ distribution[12] with a quasi-static simulation. We find that distortions of the microwave field are small as long as $s + 2w$ is not much larger than the thickness of the polyimide between both layers of metalization. In this case, the fields from the full-wave 3D simulations agree reasonably well with quasi-static simulations [69].

2.1.3 Microwave structures on the atom chip

Here I present the microwave structures on our chip. We have decided to integrate two separate microwave structures, which are shown in Figure 2.1.7. One structure consists of a single CPW, with dimensions in the center of the chip $s = g = 6\,\mu\mathrm{m}$ and $w = 3\,\mu\mathrm{m}$. The other structure consists of two shorted CPWs, placed next to each other. The dimensions in the chip center are $s = g = 2.5\,\mu\mathrm{m}$, $w = 2\,\mu\mathrm{m}$. The thickness of both structures is $t = 1\,\mu\mathrm{m}$. At the position of the short, we get an anti-node in the microwave current I_mw, and therefore an antinode of $\mathbf{B}(\mathbf{r})$. This ensures a maximum potential seen by the atoms. The modulation of $\mathbf{B}(\mathbf{r})$ over the small extent of the atom cloud due to the standing wave is negligible.

---

[12]The simulated area has a side length of $25\,\mu\mathrm{m}$
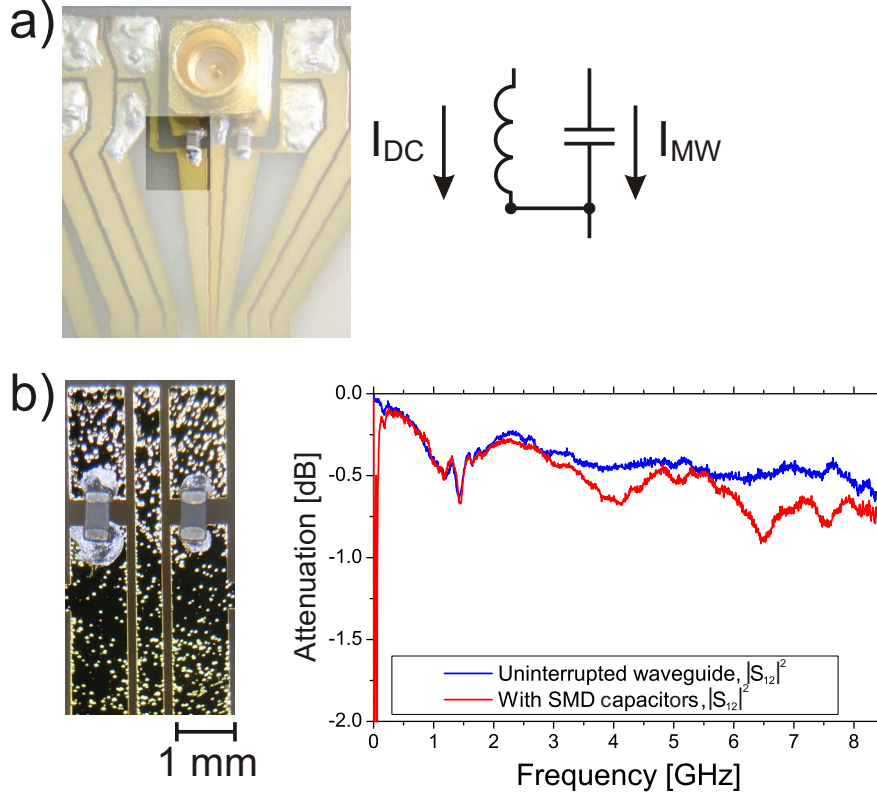
Figure 2.1.5: On-chip Bias-Tee and its performance. (a) Picture of a Bias-Tee on the base chip for one of the CPW grounds, consisting of a 100 pF SMD capacitor. On the right, the schematic circuit is shown. Microwaves are injected via a Mini-SMP plug. (b) Picture of a test-structure and its transmission characteristic (red) and as comparison (blue) the measurement of a translational invariant CPW, without capacitors. Note that the Bias-Tee structure has again two SMD capacitors on the other end of the CPW. The Bias-Tee leads to additional losses of about 0.5 dB at 6.8 GHz. On the photograph, the CPW shows some bubble-like notches, which sometimes appear when using an old electroplating bath in the fabrication. These bubbles are not expected to modify the microwave propagation characteristics, because their extent is much less than λ_{mw}. On the experiment chip, we have no such bubbles.
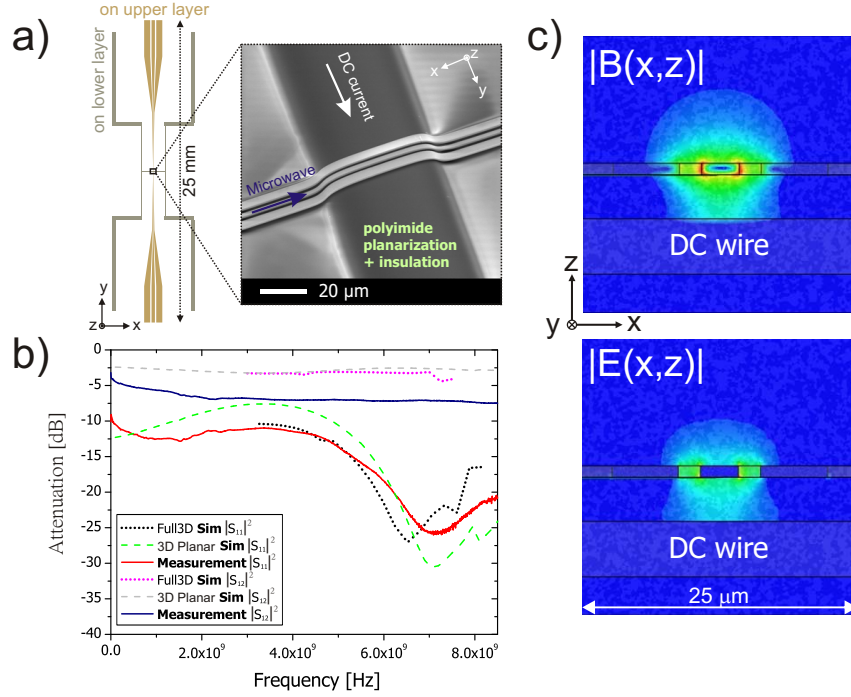
Figure 2.1.6: Comparison between measurement and numerical simulations. (a) Illustration of the examined test structure. A CPW structure (800 nm thick gold) is deposited on a $4\,\mu$m thick layer of polyimide. Below the polyimide, we have a 50 μm broad DC wire crossing the center of the CPW. (b) Comparison between the measured S-parameters and simulations, either full-wave 3D simulations using the package HFSS or 3D planar simulations using Sonnet. We find good agreement in the reflection characteristics. (c) Field distribution in the center of the CPW, extracted from the HFSS simulation.

Since t is comparable to the skin depth of $\delta_{\mathrm{skin}} = 0.9$ μm at $\omega = 2\pi \times$ 6.8 GHz (see Section 2.1.1), microwave electromagnetic fields are not screened from the inside of the conductors and microwave currents flow in the whole cross section of the wires [43].

The characteristic impedance of the CPWs changes smoothly from $|Z_c| = 50\,\Omega$ on the base chip and on the edge of the science chip to $|Z_c| = 70\,\Omega$ ($|Z_c| = 80\,\Omega$) in the center of the single (double) CPW structure.

The chip design is shown in detail in Appendix A.
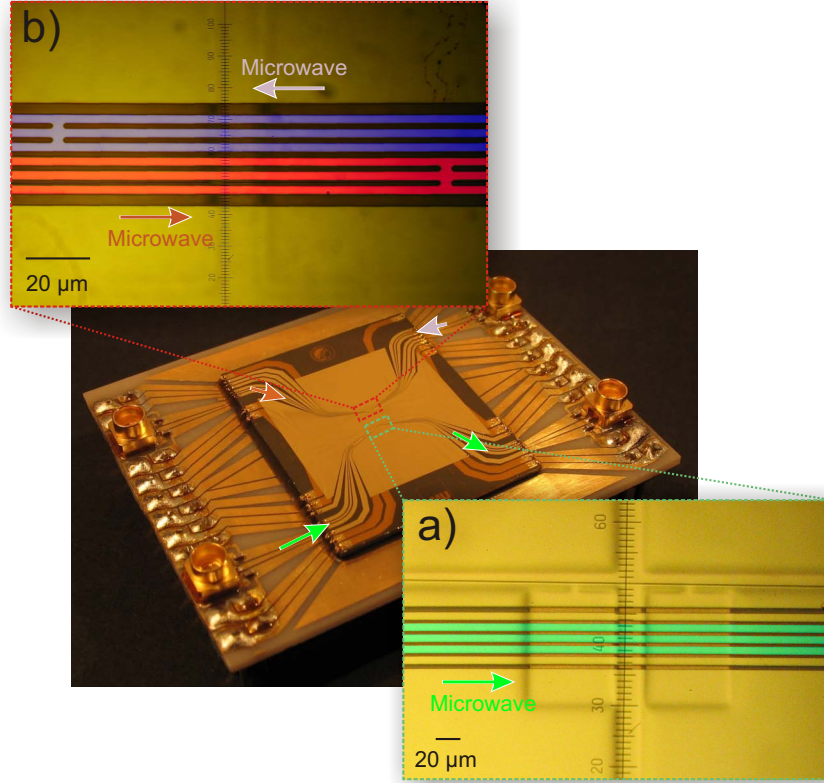
Figure 2.1.7: Microscope images of the two waveguide structures integrated on our atom chip. The single CPW structure (a) is the one used in the experiments reported in this thesis. The structure consists of five wires, out of which the three center ones form the CPW (highlighted in green), where microwave and DC currents are superimposed. The two lateral wires are DC wires which can be used for static trapping. The second structure (b), the double CPW structure, consists of two CPWs next to each other (highlighted in red and blue). Both waveguides of the double CPW structure are shorted, which creates a standing microwave, with an antinode in I_{mw} (and therefore B) at the position of the short, close to the static trap for the atoms. A schematic overview can be found in Appendix A.
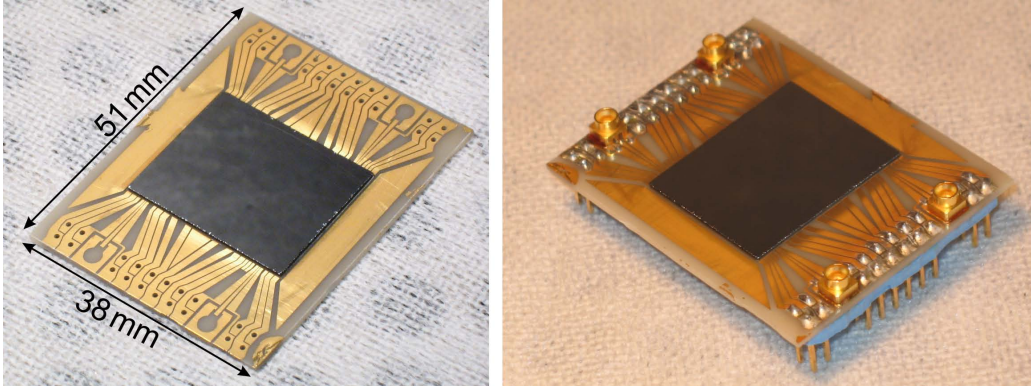
Figure 2.2.1: Photographs of the base chip. (Left) base chip with the Si spacer chip glued on top. The 40 laser drilled holes can be recognized. The U-shaped wires for the last MOT stage are hidden below the spacer chip. (Right) Picture of the same base chip, after the mini-SMP plugs and the male DC connectors have been soldered to the base chip using In-Pb solder.

2.2 Fabrication

Now I give a short description of the fabrication and characterization of the atom chip that was built and used in this thesis. For a detailed fabrication recipe, the reader is referred to [69].

The chip was microfabricated in the clean room facility of Prof. Kotthaus. I am very grateful for generously being allowed to use the equipment in his clean room.

Our atom chip (shown on Figure 2.0.1) consists of three sub-chips: The base chip, a spacer chip and the science chip. The base chip seals the vacuum and provides electrical feed through to the science chip inside the vacuum. It contains relatively thick ($12\,\mu$m) and broad (up to $1\,$mm) wires which are used in the last MOT phase, the MOT close to the chip surface, with currents of up to $10\,$A. The spacer chip ensures that the science chip is above the solder joints (see right part of Figure 2.2.1) and the glue meniscus between the base chip and the Pyrex glass cell (see later), which would otherwise obstruct the absorption imaging beam at grazing incidence. The science chip contains wires used for magnetic trapping and microwave manipulation of the ultracold atoms.

2.2.1 Base chip

The base chip (see Figure 2.2.1) is fabricated on a 800 μm thick AlN substrate, a non-toxic ceramic which has a relatively high thermal conductivity

of $180\,\mathrm{WK^{-1}m^{-1}}$ [6]. The AlN ceramic is mechanically more stable than Si, and therefore provides stability to the chip package. Its relatively rough surface inhibits using it for the magnetic trapping structures on the science chip. The substrate contains 40 laser drilled holes with radii of 300 μm each,[13] which are used for DC electrical contacting the base chip from the back. The laser drilling produces Al droplets, which are distributed all over the substrate. Before further processing, these droplets had to be removed by a combination of cleaning with a fiberglass brush, ultrasonic acetone baths and piranha etch.[14] After cleaning of the substrate, the chip structure is fabricated by electroplating (see schematic on Figure 2.2.2). First, we deposit in a UHV e-beam evaporation chamber a 3 nm Ti adhesion layer, followed by a 50 nm gold seed layer. Then a 8 μm thick layer of photoresist (ma-P 1240 from micro resist technology) is spun on. This photoresist layer is then photolithographically structured using a foil mask.[15] The exposed gold seed layer is subsequently electroplated to a thickness of 12 μm.[16] The "overplating" of 12 μm gold in 8 μm deep trenches is uncritical for the relatively wide wire structures on the base chip. Subsequently, the photoresist structure is removed using acetone and piranha etch. Then, the unplated seed-layer (including the Ti adhesion layer) is removed by dipping the chip for 1 minute into aqua regia.[17] In this step, also the electroplated gold structures are thinned by $\sim 100\,\mathrm{nm}$.

We glue the spacer chip on the base chip, using the heat conductive glue H77S from Epo-Tek, which is carefully outgassed under vacuum conditions before application in order to prevent any virtual leaks. Furthermore, we take care to apply only a thin layer in order to get good thermal contact between the base and the spacer chip, such that dissipated heat is transported efficiently to the water cooled base chip to avoid thermal damage of the chip. The spacer chip is a high-resistivity Si substrate[18] like the one for the science chip. The spacer chip touches some bond wires as well as wires and feed lines on the base chip. Since we want to avoid any cross-talk between the wires in order to be able to define the currents on the 10^{-5} level, the

---

[13]The holes in the AlN substrate have been laser drilled by A.L.L. Lasertechnik GmbH, München

[14]Piranha etch is a highly reactive mix of sulfuric acid and hydrogen peroxide. We use a mixture of 96% H_2SO_4 and 33% H_2O_2 in the volume ratio of 4:1. CAUTION! *Never* increase H_2O_2 concentration beyond 3:1 and *never* bring piranha etch in contact with organic solvents; this would result in an explosion.

[15]From Zitzmann GmbH, Eching. The masks have a resolution of 16'000 DPI.

[16]Using an ammoniumsulfite-gold solution from Metakem.

[17]Aqua regia is a mixture of water, hydrochloric acid and nitric acid with volume ratios $H_2O : 32\%\,HCL : 65\%\,HNO_3 = 1 : 3 : 1$. It dissolves Au as well as Ti.

[18]Float-zone Si in (100) orientation from Topsil.

a) evaporate gold
seed layer

b) spin on
photoresist

c) UV exposure

d) develop
photoresist

e) electroplate gold

+ U −

Ti/Pt anode

Au$^+$

ammoniumsulfite-
gold-solution

f) remove
photoresist

g) gold etch to
remove seed layer
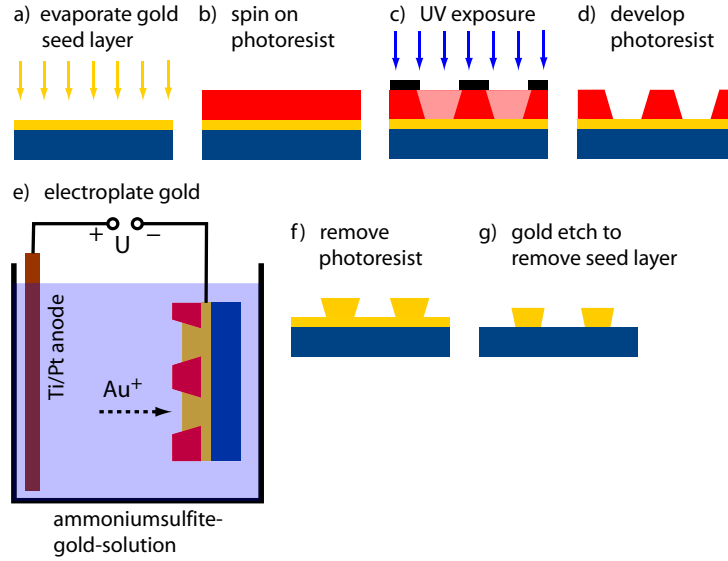
Figure 2.2.2: Schematic illustration of the fabrication process for the electroplated structures. Electroplating allows time and material efficient production of relatively thick structures. The process steps are explained in the main text. The Figure has been taken from [69].

spacer has to be highly isolating. Neither does the 2 nm native SiO_2 layer provide enough isolation, nor does the bulk resistivity of the high-resistivity Si, where $\rho \sim 10^4\,\Omega$cm. Therefore, we oxidize a 20 nm layer of SiO_2 by thermal oxidation at 1100 °C. The substrates oxidized in this way exhibit a measured DC resistivity $> 40\,\text{M}\Omega$. Since the thermal conductivity of SiO_2 ($1.5\,\text{WK}^{-1}\text{m}^{-1}$) is much lower than that of Si ($150\,\text{WK}^{-1}\text{m}^{-1}$), the insulating layer should not be grown any thicker than necessary [11].

In the next step, socket adapters with a pitch of 2.54 mm are trimmed and their pins are insert into the laser drilled holes, from the back of the chip (see the right part of Figure 2.2.1). The plugs are mechanically fixed using the glue Epo-Tek 353ND. For electrical contacting of the SMD capacitors, mini-SMP jacks[19] as well as the DC pins, we use the indium solder reflow paste Indalloy 204.[20] Indalloy 204 has a melting point of 170°C and consists of 70% In and 30% Pb. After the solder paste is applied, we put the chip on an aluminum block[21] with temperature monitoring, and heat the block on a hotplate at a ramp speed of 10°C per minute to a temperature of 200°C,

---

[19]from Rosenberger GmbH

[20]from "Indium Corporation".

[21]The glued plugs prevent good thermal contact between the chip and the hotplate if directly placed on it.

hold the temperature steady for about 30 s, until we slowly ramp down the temperature again (-10°C per minute).

Before using Indalloy solder pastes, we tried to solder with conventional Sn based reflow pastes or conducting epoxies like H20F from Epo-Tek. It turned out that soldering gold conductors with Sn pastes does not work because the paste completely dissolves the gold stripe [116], establishing no electrical contact. Furthermore, there seem to be issues with Sn based solder getting brittle when dissolving gold. Using conductive, silver-filled epoxy glues like H20F from Epo-Tek works on a short time scale, but it turned out that electrical contact worsens with time (on the order of weeks) by at least a factor of 10. It turns out to be a well-known problem, which is attributed to an incompatibility of silver-filled glues with Sn, which is contained in the DC pins as well as in the SMD solder pads.[22]

2.2.2 Science chip

The science chip consists of the same, very smooth oxidized Si substrate as the spacer chip (see above). The chip accommodates two layers of metalization. The lower layer is fabricated by the same procedure as described above for the base chip, except that the spin coated photoresist has only a thickness of 6.5 μm, we use a higher resolution chrome mask[23] for lithography and the structures are electroplated to a thickness of only 5 μm (see Figure 2.2.3a). The wires exhibit a very low r.m.s. surface roughness of 15 nm (measured for a 7 μm thick wire [69]). Smooth wire surfaces and edges are important in order to prevent magnetic potential corrugations [117].

Before fabricating the upper layer of metalization, we have to deposit an isolating film in between to prevent wires in the upper layer from being short circuit by the ones in the lower layer. We chose polyimide, which provides good insulation and is compatible with a UHV environment. We apply 3 consecutive layers of polyimide. After each spin-on of the liquid polyimide solution,[24] we perform a hard-bake at 350°C in a nitrogen atmosphere. After the hard-bake, each layer has a thickness of $\approx 2\,\mu$m. Baked polyimide is highly resistant to chemicals like acetone, aqua regia and even piranha etch, but not to oxygen plasma. The polyimide does not only provide insulation, but it also smoothens out the underlying bumpy structure. Using multiple layers of polyimide, the planarization improves with each additional layer. This smoothing is important since the gold mirror for the mirror-MOT (which

---

[22]According to Epo-Tek, tin-oxide passivates the Ag particles contained in the glue, which degrades the electrical contact.

[23]From Delta Mask, the mask is produced with a laser spot size of 0.8 μm

[24]Polyimide PI 2562 and adhesion promoter VM651, both from HD MicroSystems.
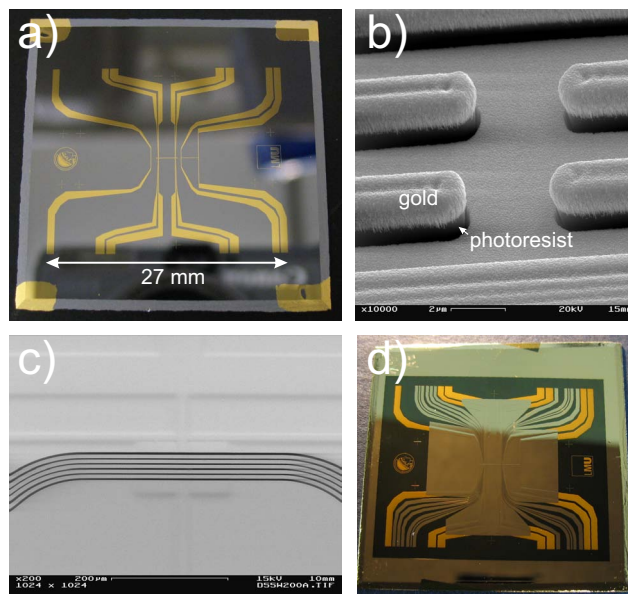
Figure 2.2.3: Overview of the different progress steps in the fabrication of the science chip. (a) Picture of the chip after the fabrication of the lower metalization layer, whose wires are used for magnetic trapping. (b) SEM pictures of the upper gold layer before and (c) after the lift-off step. (d) Photograph of the chip after lift-off, before trimming the chip with a diamond sawing blade.

is deposited on top of the polyimide), should be as flat as possible and because there should be no bumps in the CPW. At the same time the polyimide layer should not be too thick because the thermal heat conductivity of polyimide is about three orders of magnitude lower than that of Si.

For the metallic structures on the upper layer, on top of the polyimide, we apply a lift-off metalization technique (see schematic in Figure 2.2.4). We first apply and photolithographically pattern a photoresist film, onto which we evaporate gold. Gold that is deposited onto photoresist is subsequently removed together with the resist in an acetone bath.

We spin on $1.6\,\mu$m image reversal photoresist.[25] An image reversal resist allows to create an undercut in the photoresist structures (the undercut is faintly visible in Figure 2.2.3b). An undercut of the photoresist avoids direct contact between the gold on the polyimide and that on the photoresist, and therefore enables the removal of the gold in the lift-off step. The resist is first exposed for a few seconds to UV light through a chrome mask with the inverted structure (Figure 2.2.4a). Due to the small light dose, the photoresist is not fully exposed down to the bottom over the whole area, which leads to the undercut and the contrast is not diminished by any back scattered light.

The next step is the image reversal bake (Figure 2.2.4b) on a hotplate at a temperature of 120°C. In that step the exposed resist cross-links and thereby makes itself insoluble to the developer and to any further exposure. In the next step, the whole chip is exposed to UV light (Figure 2.2.4c), which renders the previously unexposed areas soluble in the developer. These areas are then removed by the developer in the subsequent step (Figure 2.2.4d). After a further cleaning step in oxygen plasma, the chip is ready for gold coating.

The chip is locked in the UHV e-beam evaporation chamber, where we first deposit $3\,$nm of Ti adhesion layer followed by $1\,\mu$m of evaporated gold (Figure 2.2.4e). The gold is grown at a rate of $0.03-0.04\,$nm/s, the whole gold evaporation takes more than 7 hours. The evaporated gold exhibits a very smooth surface, which is essential for the on-chip gold mirrors. The resulting surface roughness has been measured to be $3\,$nm r.m.s. [69].

After locking out the chip from the UHV chamber, we put it into a glass with acetone. After some minutes, the remaining photoresist dissolves and the gold peels off (Figure 2.2.4f). The chip now looks as in Figure 2.2.3d.

The last step is to cut away the unnecessary part of the Si substrate. Therefore we coat the chip with a thick layer of photoresist (ma-P 1240), which serves as a protection layer, and trim the Si substrate with a diamond saw blade at 20'000 RPM. Furthermore, we scratch off some of the

---

[25] AZ 5214 E from Clariant
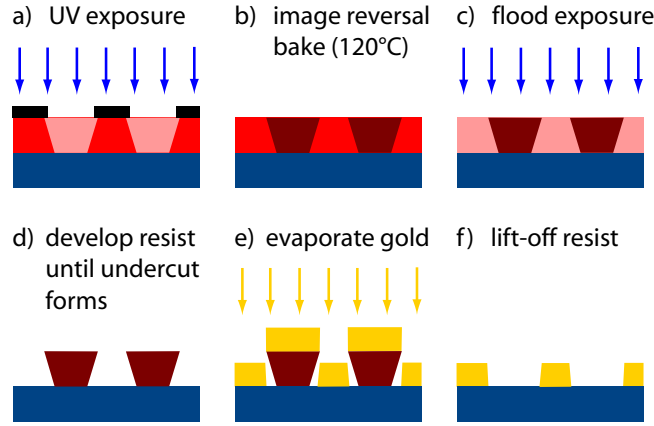
Figure 2.2.4: Illustration of the lift-off process, which is used for the upper layer of the science chip. The individual steps are explained in the main text. The Figure has been taken from [69].

polyimide, for electrical contacting of the wires on the lower layer, using a scalpel. Finally, we again remove the protective resist layer using acetone.

2.2.3 Combining base and science chip

The last step in the fabrication of the atom chip is to glue the base and the science chips together, and to establish electrical contact between them.

The science chip is glued to the spacer chip on the base chip using out-gassed H77S. As it is the case of gluing the spacer chip, we take care to use as little glue as possible in order to get good thermal contact with the spacer chip.

For electrical contact between the base chip and the science chip, we apply up to 15 gold bond wires per contact pad (see Figure 2.2.5). Using test chips it turned out that using more bonds and crossing the individual bond wires is beneficial for the microwave transmission characteristics. Furthermore, in order to prevent charges being accumulated on the three gold mirrors on the chip, we also use one bond wire each to contact them with wires on the upper metalization layer.

2.2.4 Glass cell

Finally, we glue the chip to a Pyrex cell.[26] The Pyrex cell has an inner edge length of 30 mm, and is anti-reflection coated for 780 nm at the outside.

---

[26]Hellma 704.027-BF, without label.
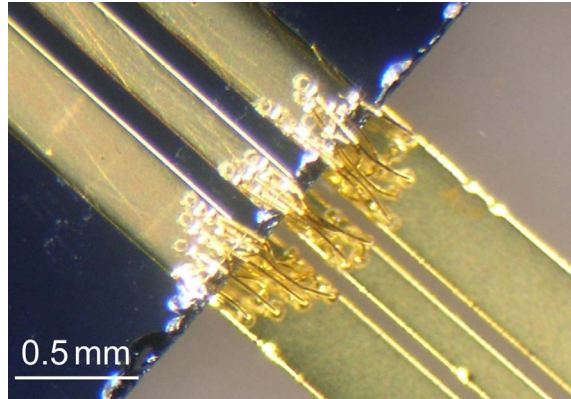
Figure 2.2.5: Close-up of wire bonds on a test chip. The same kind of wire bonds is used for the actual chip. The individual gold wires have a diameter of $25\,\mu$m each. Each wire can typically withstand a DC current of 800 mA.
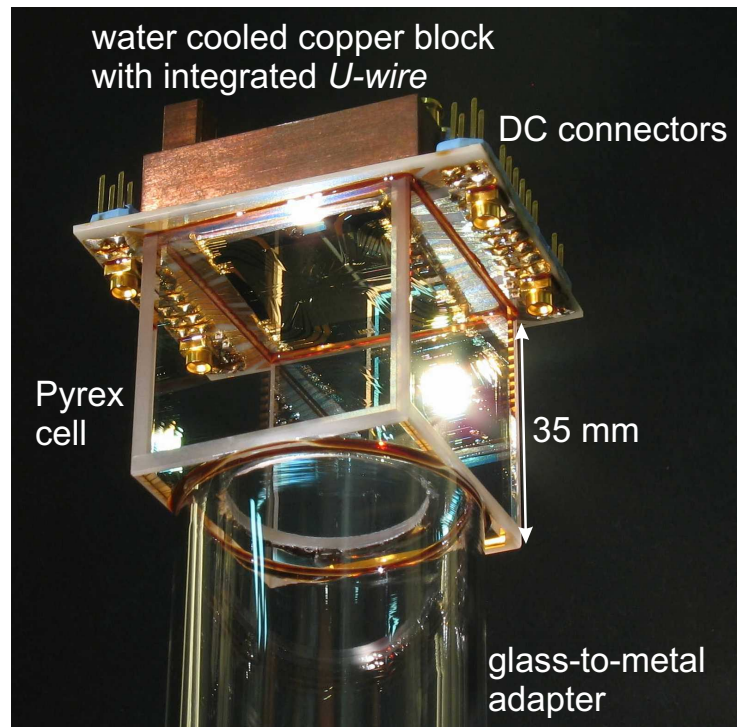
Figure 2.2.6: The atom chip is glued to the Pyrex cell, which is connected to the glass-to-metal adapter, that is attached to the stainless steel vacuum chamber. On top of the atom chip, the water-cooled copper block with integrated *U-wire* conductor can be seen, which is used to create the quadrupole magnetic field configuration for the MOT.

The inner edges are beveled, to prevent a big glue meniscus, which could disturb optical access. Before attaching the chip to the Pyrex cell, we drill a hole with a diameter of 23 mm through the bottom of the Pyrex cell and glue the cell to a glass-to-metal adapter (see Figure 2.2.6) using outgassed, vacuum-compatible Epo-Tek 353ND. We follow an optimized curing schedule, which reduces stress due to the glue and the different expansion coefficients of Pyrex and glass. After applying the glue, we wait two days for the glue to shrink while still being viscous, before we perform the final curing. In the final curing, the whole cell assembly is slowly heated during 1.5 h to a final temperature of 150°C. After curing at this temperature for one hour, we slowly ramp the temperature down again.

For gluing the Pyrex cell to the chip, we follow the same procedure as before. The Pyrex cell is rotated by an angle of 3° relative to the chip edges such that reflected laser beams do not overlap, which would otherwise cause interference fringes on absorption images.

The glue joint between the base chip and the Pyrex cell also transverses the CPWs on the base chip. This leads to a local change in the CPW impedance which causes reflections. We examine this effect using a test chip and find that the presence of one glue joint on the base chip leads to a decrease in CPW power transmission by 0.18 dB and an increase in the reflected power by about the same amount. This means that there is no significant absorption by the glue joint.

2.3 DC and MW characterization of the science chip

Resistive heating of a chip wire in combination with its thermal contact to the substrate limits the maximum current the wire can withstand. A current flowing in a wire heats it up and thereby increases its resistivity, which again increases resistive power dissipation. The wire will eventually find its thermal equilibrium, or "burn". Power dissipation at microwave frequencies not only depends on the total current but also on the current density distribution $j(x, z)$ in the cross section of the wire, which is strongly influenced by the skin effect [104].

In the following, I present DC and microwave characterizations of some of the science chip wires.[27] During all these measurements, the chip is placed on the metal chuck of our probe station. The relatively high heat capacity of the chuck "simulates" the water-cooled heat sink on the back of the atom chip built into the experiment. The dominant cooling mechanism for the wires is heat conduction to the substrate [11]. Therefore, the results of the measurements below, which are carried out at ambient pressure, are also valid for a vacuum environment.

DC characterization   Knowledge of the (maximum) DC current density j_{max} a wire can withstand is important because the confinement for the atoms scales with j [11].

We send DC current pulses through the respective wires and measure the voltage drop across them. We apply currents at a duty-cycle of $\sim 30\%$ (3 s on, 7 s off), which is a typical atom chip DC wire duty cycle. In Figure 2.3.2, the results of two upper layer wires and a thin wire on the lower metalization layer on the science chip are shown.

The measurements show that the wires on the upper layer can carry a current density of at least $2.8 \times 10^{10} \, \mathrm{A/m^2}$, while the wires below the polyimide can endure at least $5.5 \times 10^{10} \, \mathrm{A/m^2}$.[28] Using the measured increase in resistivity, it is possible to estimate the temperature change of the respective wire. Assuming that the increase in resistance of the signal wire of the double CPW structure (see Figures 2.3.1 and 2.3.2a) is only due to heating of the central part with cross section $1 \, \mu\mathrm{m} \times 2.5 \, \mu\mathrm{m}$ and length $240 \, \mu\mathrm{m}$, we get a temperature change $\Delta T = 450°\mathrm{C}$. This value overestimates the actual ΔT because it neglects heating of the wire leads. In the actual experiments,

---

[27]The tested chip is identical to the one built into the experiment.

[28]In [69] it is reported that a very much comparable wire on the lower layer of a two-layer chip burns at $j_{\mathrm{max}} = 6 \times 10^{10} \, \mathrm{A/m^2}$.
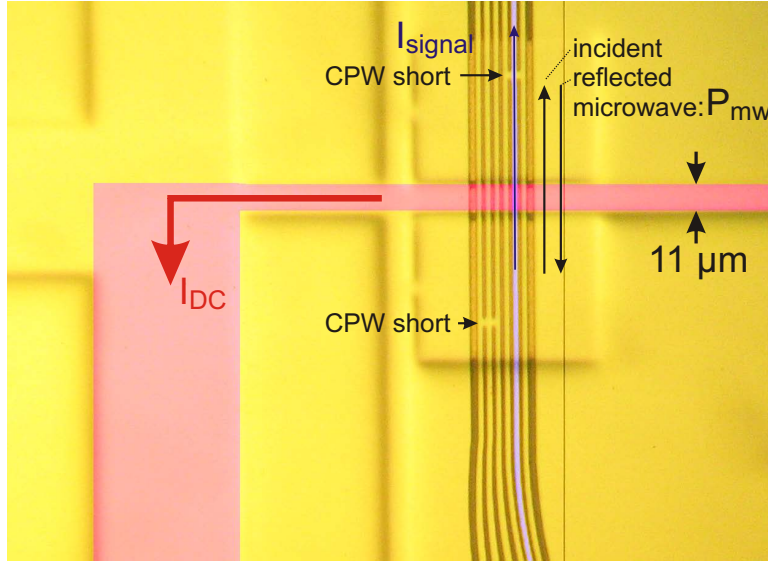
Figure 2.3.1: Illustration of the double CPW wires used in the current tests. The wire with I_{DC} is a wire on the lower layer (cross section $11\,\mu\text{m} \times 5\,\mu\text{m}$), while the one with I_{signal} (cross section $2.5\,\mu\text{m} \times 1\,\mu\text{m}$) is located on the upper layer. For microwave tests, an incident microwave ($\omega = 2\pi \times 6.8\,\text{GHz}$) is reflected at the CPW short and forms a standing wave with a periodicity of $1.4\,\text{cm}$, a factor 50 longer than the length of the central part of the CPW. The microwave current forms an antinode at the position of the short.

we stay well below the maximum currents applied in the tests described here (cf. Section 3.8).

Microwave characterization Here I present a characterization of the on-chip microwave structures on the science chip (i.e. before gluing it to the base chip) by performing S-parameter measurements. In Chapter 4 a more sophisticated characterization of the microwave near-field is presented where atoms are used as probes.

We measure the frequency dependent microwave S-parameter characteristics of one of the fabricated science chips using the network analyzer. The results are shown in Figure 2.3.3. For the case of the single CPW structure, due to the symmetry we infer from the transmission measurements an attenuation of $-2.15\,\text{dB}$ from the edge to the center of the chip. Furthermore, the flatness of the transmitted signal is an indication that there is no significant standing wave present on the chip. In the case of the double CPW structure, from the reflected signal we infer a microwave attenuation of $-2.65\,\text{dB}$ from the corner of the chip to its center. For both structures, we find the attenu-
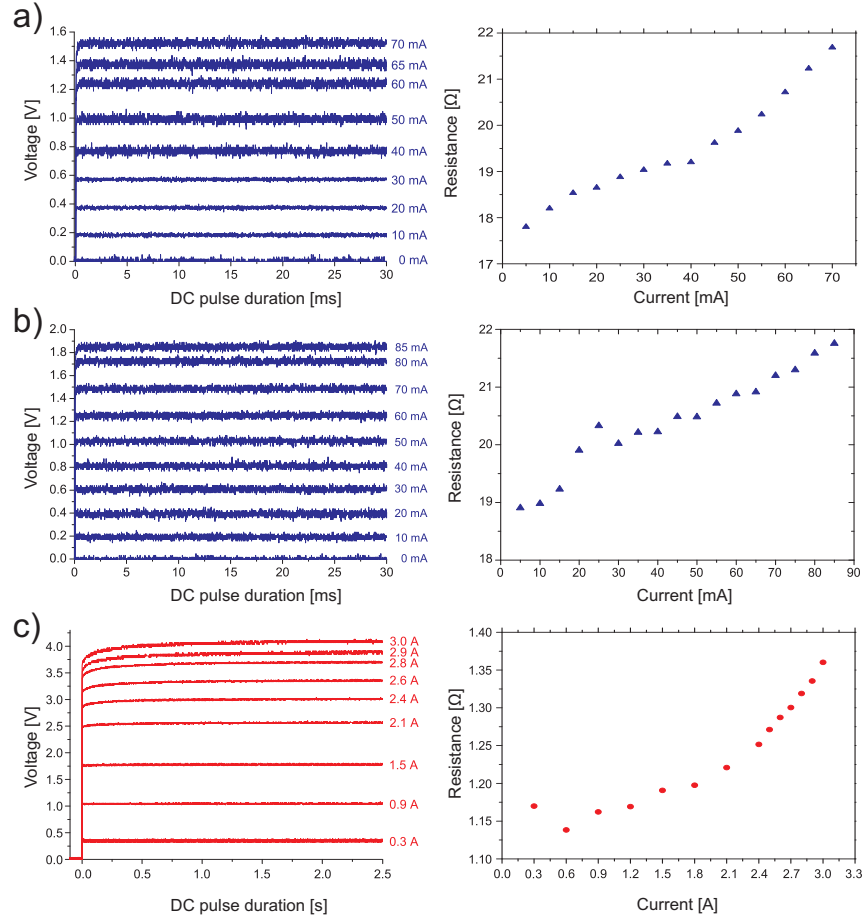
Figure 2.3.2: Results from the DC characterization of some science chip wires. We push a variable DC current through some of the chip wires and record the voltage drop (left). From the steady state voltage drop, the wire resistivity (right) is extracted. The change in resistivity indicates the temperature change of the wire. Measurements include the approximately constant resistance of the cables of $0.3\,\Omega$. (a) Current through the smallest wire on the upper layer with a cross section of $2.5\,\mu\mathrm{m} \times 1\,\mu\mathrm{m}$, highlighted in blue on Figure 2.3.1 (current I_signal). Due to the tiny heat capacity, and small total power dissipation, which does not change the substrate temperature significantly, the steady state is reached within some ms. (b) Signal wire of the single CPW structure, see Figure 2.1.7a, with cross section $6\,\mu\mathrm{m} \times 1\,\mu\mathrm{m}$ (current I_s in Figure 3.8.1). Compared with (a), the slope of the resistance differs by a factor $\approx \frac{1}{2}$. (c) Measurement for the narrowest wire on the lower layer, highlighted in pink on Figure 2.3.1 (current I_DC), with minimal cross-section $11\,\mu\mathrm{m} \times 5\,\mu\mathrm{m}$. For this wire, it takes about 2 s to reach a steady state resistance. We attribute this long time scale to heating of the substrate. The maximum current density tested on this wire is $j_\mathrm{max} = 5.5 \times 10^{10}\,\mathrm{A/m^2}$, which caused no damage.
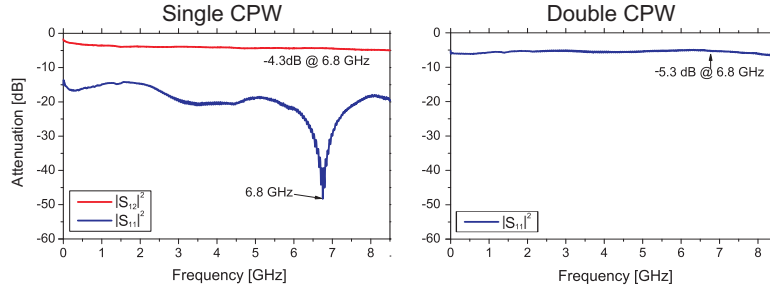
Figure 2.3.3: Microwave transmission and reflection characteristics of the single and double CPW structures. For the single CPW structure, we have a transmission of -4.3 dB at 6.8 GHz. The reflected signal shows that there is a resonance at 6.8 GHz, but since there is no significant modulation of the transmitted signal, there is no indication of any experimentally relevant standing wave. For the double CPW structure, we have the inverse situation. We have a reflection of -5.3 dB at 6.8 GHz. The high reflectivity is expected as a result of the CPW short. A transmission is not given because the wires after the short do not form a CPW anymore. These characteristics are measured in the dark, because the presence of light modifies the transmission as well as the reflection characteristics through excitation of electron-hole pairs in the substrate. The effects of the probes and cables have been calibrated out.

ation increase slightly with growing values of the microwave power P_{mw} (see Figure 2.3.4). Measurements were performed without illumination, because the presence of light increases the microwave attenuation through excitation of electron-hole pairs in the Si semiconductor substrate.

We test the chip for the maximum microwave power the structures can withstand. We find that for both structures, we can feed at least 26 dBm (400 mW) onto the CPW, without damaging it (in this chapter, microwave power readings correspond to the power at the corner of the science chip). This corresponds to an incident r.m.s. microwave current $I_{\mathrm{mw,rms}} = 90\,\mathrm{mA}$ at the corner of the chip ($|Z_{c,\mathrm{corner}}| = 50\,\Omega$) or an incident $I_{\mathrm{mw,rms}} = 59\,\mathrm{mA}$ in the center of the chip ($|Z_{c,\mathrm{center}}| = 70\,\Omega$) for the single CPW structure. In the center of the double CPW structure ($|Z_{c,\mathrm{center}}| = 80\,\Omega$), we have a standing wave antinode with an amplitude of $104\,\mathrm{mA}$. The measurements were performed at a 10% duty-cycle; 500 ms on, 4500 ms off. Again, in the experiment we stay well below these power levels.

Power dissipation and microwave attenuation   We also examine the influence of DC currents on microwave characteristics. We find that by increasing I_{DC} and/or P_{mw}, we get increased microwave loss (see Figure 2.3.4a,

61
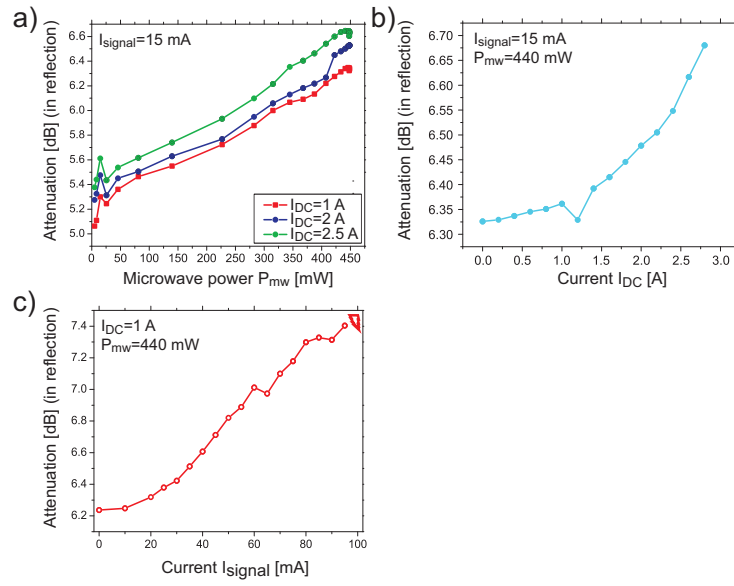
Figure 2.3.4: Influence of DC currents I_{DC}, I_{signal} and microwave power P_{mw} on microwave attenuation characteristics. We use the double CPW structure, and record the attenuation of the reflected microwave at fixed frequency $\omega = 2\pi \times 6.8\,\text{GHz}$. We find that by increasing the microwave power P_{mw} in a), as well as by increasing I_{DC} in b), or by increasing I_{signal} in c), the microwave attenuation increases. In (c), at $I_{signal} = 99\,\text{mA}$ the wire burns.

2.3.4b). The same is also true for the DC current I_{signal} (Figure 2.3.4c). We attribute the dependence of microwave attenuation on DC currents purely to thermal effects. At simultaneous application of $I_{\text{signal}} = 99\,\text{mA}$, $P_{\text{mw}} = 440\,\text{mW}$, and $I_{\text{DC}} = 1\,\text{A}$, the limit of the signal wire is reached, and it burns in the very center.

Chapter 3

Setup and preparation of mesoscopic BECs

In this chapter, the experimental setup is presented. It covers the equipment used for quick cycle and highly reproducible production of mesoscopic BECs, containing down to 100 atoms or less; this includes a vacuum and laser system, low-noise current sources as well as a magnetic μ-metal shielding. Furthermore, the microwave and RF setup for the coherent manipulation of atoms with state dependent microwave potentials is covered, which is essential for the experiments presented in Chapter 5. This chapter also gives a description of the experimental control and the low-noise imaging system, which allows the detection of spin-squeezed states (see Chapter 6). I conclude this chapter with a first set of experiments, where the microwave near-field around the single CPW structure is characterized with trapped condensates.

3.1   Chip, coils & vacuum

The optically accessible part of the vacuum system is the glass cell (see Figure 2.2.6 in the previous chapter). The glass cell with the atom chip is surrounded by three pairs of Helmholtz coils, as can be seen in the overview in Figure 3.0.1 and the close-up in Figure 3.1.1. The coil cage is water cooled to prevent thermal drifts and air convection. The flange of the glass-to-metal transition is attached to our vacuum system (Figure 3.1.2), which has a base pressure of 5×10^{-10} mbar. The vacuum is maintained by a 40 l/s ion pump[1] and a Ti-sublimation pump, and the background gas pressure is measured

---

[1]VacIon Plus 40 Diode
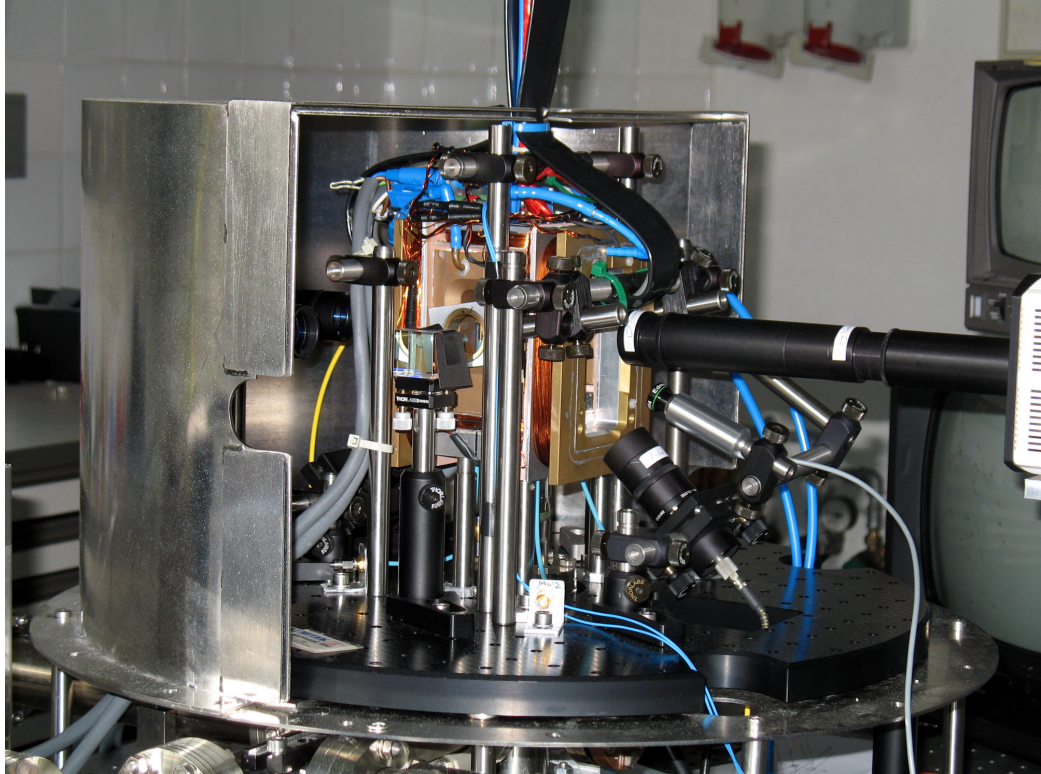
Figure 3.0.1: The atom chip setup. The magnetic μ-metal shield is partly opened. The atom chip and the glass cell is surrounded by three pairs of water-cooled Helmholtz coils. Attached to the back of the chip is a water cooled copper block with an integrated U-wire that is used for the creation of the quadrupole field for the MOT and which provides cooling to the chip. Laser light is fed to outcouplers via optical single-mode fibers. The objective and a part of the camera for imaging on the y-axis are visible on the right part. The μ-metal shielding has a diameter of about 50 cm.

Cable for on-chip DC currents

Coil cage

RF antenna

Microwave horn

Imaging beam outcoupler

Horizontal MOT outcoupler
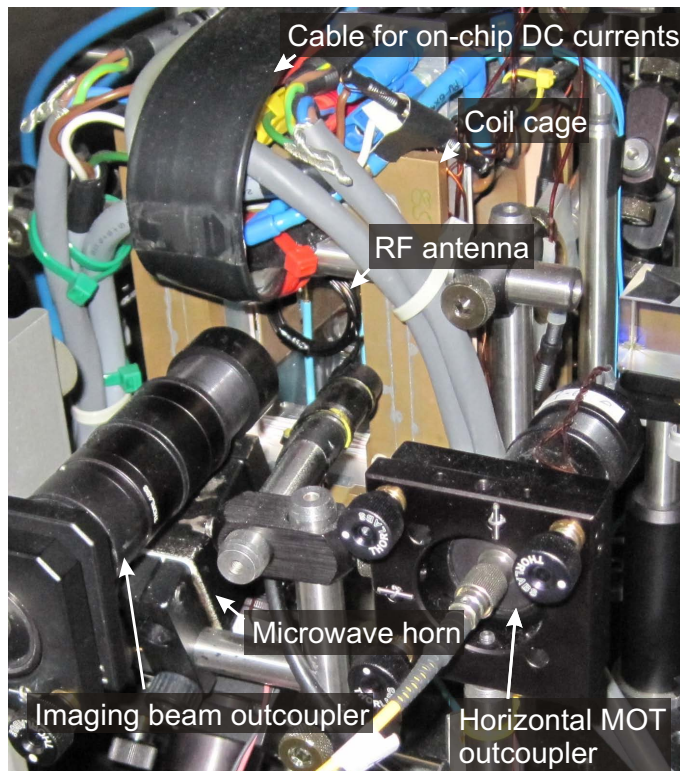
Figure 3.1.1: Close-up of the chip setup. The atom chip and the glass cell are surrounded by the coil cage.

using an ion gauge.[2] During the experiments, the ion gauge is switched off, because its emitted infrared radiation is visible on the camera.

The vacuum system consists of a single chamber, where the loading of the magneto-optical trap (MOT) with ^{87}Rb atoms from the background gas is done at the same location as the subsequent forced evaporative cooling to quantum degeneracy. While fast loading of the MOT requires a relatively high background gas pressure, collisions with the background gas shorten the magnetic trap life times. This is unfavorable for subsequent efficient forced evaporative cooling. The essential condition for evaporative cooling is a long lifetime of the atomic sample compared to the thermalization time [1]. In magnetic microtraps, the solution is to increase the inter-atomic collision rate during evaporative cooling by compressing the magnetic traps, and relaxing the trap after condensation to decrease loss due to inelastic collisions between trapped atoms in the experiment trap. In this way, we achieve 1-body loss dominated trap lifetimes, measured with a sample initially prepared as a BEC of about 4.5 s. This is indeed at least a factor of 20 lower than what can be achieved in a two-chamber setup [118], but is fully sufficient for our experiments.

3.1.1 Rubidium source

As a source for ^{87}Rb atoms, we have integrated three rubidium dispensers into the vacuum system (see Figure 3.1.2). Two dispensers[3] contain a rubidium-chromate and a redox agent. In addition, we have integrated a third dispenser,[4] which contains a rubidium-indium alloy. The dispensers are point-welded to a wire which is connected to the internal ports of an electrical vacuum feed through (see Figure 3.1.2). Release of atomic ^{87}Rb is controlled via the current that is sent through the dispenser.[5] The current is at a few hundred mA above the threshold, at which the release of ^{87}Rb starts. In all experiments reported in this thesis, always the same SAES dispenser is used. When running the experiment, the dispenser is running continuously at a constant current level $I_{\text{Disp}} = 3.75\,\text{A}$. A modulation of the current would cause atom number drifts and seems not to be compatible with the short experimental cycle time desired. The option of modulating the rubidium background pressure using light-induced atomic desorption (LIAD) as e.g. in [119] seems to be unfavorable, because this would also lead to drifts in the total atom number.

---

[2]Leybold Ionivac IE514 Extraktor

[3]SAES Getters RB/NF/3,4/12FT10+10

[4]Alvatec AS-RbIn-5-F

[5]Release of ^{87}Rb is always accompanied by emission of other unwanted contaminants.
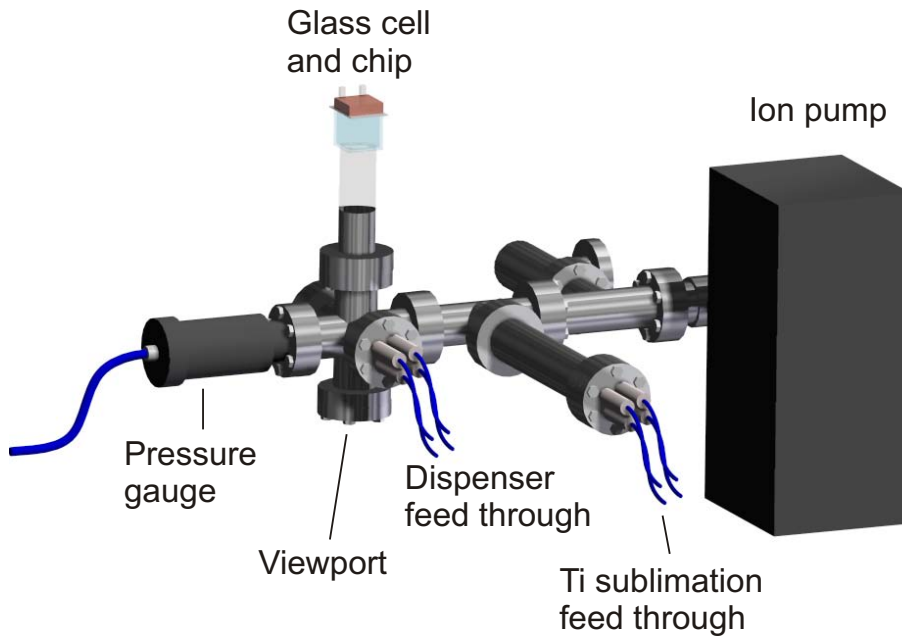
Figure 3.1.2: Overview of our compact vacuum system. It contains electrical feed throughs for the Ti sublimation pump as well as for the dispensers. The glass cell and the chip are flanged to the top port of a six-way cross. On top of the chip, there is the water-cooled copper block with a "U"-shaped wire for the MOT, which can withstand currents > 60 A. On the opposite port of the six-way cross, there is a viewport for a camera used to observe the fluorescence from the MOT.
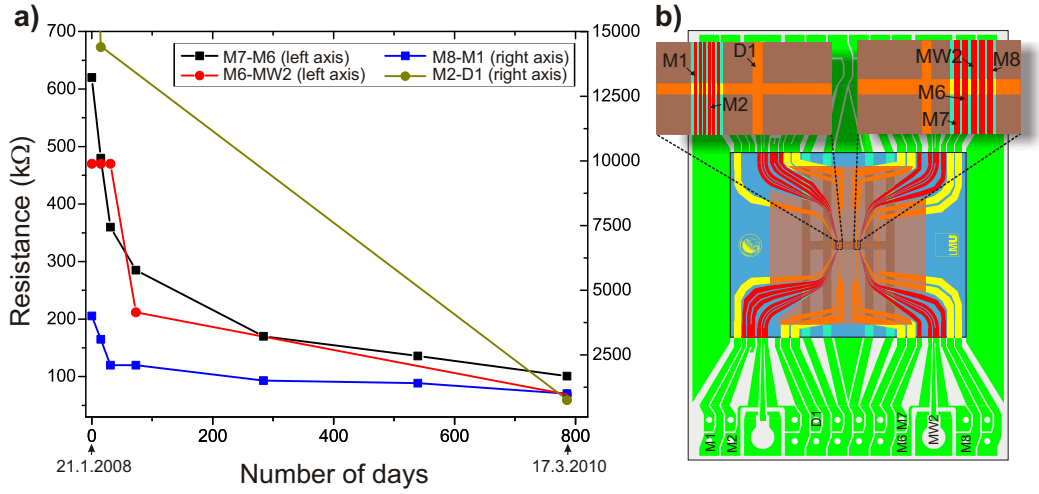
Figure 3.1.3: Change of resistivity between some of the on-chip wires indicated in (b) as a function of time. (a) The first measurement of the resistivity was taken after about 7 months of operation with the atom chip, about 3 months after the first BEC. It seems that the decrease in resistivity is slowly saturating. (b) Schematic of our atom chip with the wires from (a) indicated. Wires on the base chip are drawn in green, those in the lower layer of the science chip are yellow, while wires on the upper layer are colored in red (see Appendix A for a enlarged version).

Rubidium has a very high probability of sticking to a surface. As a result, the pressure gauge, which is located at another port of the six-way cross (see Figure 3.1.2), does not adequately measure the ^{87}Rb pressure inside the glass cell [120].

Rubidium deposition on the chip When the atom chip was built into the setup, we measured a DC resistance $> 40\,\text{M}\Omega$ between all wires on the science chip as well as between the wires on the base chip. We measure a decrease of the insulation between the wires as a function of time, as shown in Figure 3.1.3. We attribute this to rubidium, which is adsorbed on the surface of the chip and slowly creates a conducting layer on the atom chip. We have not yet tried whether the resistivity can be recovered by using a LIAD technique, since the lowest resistivity $(65\,k\Omega)$ is still a factor of 4000 above the resistivity of the signal wire of the single CPW structure, measured from one end of the chip to the other.
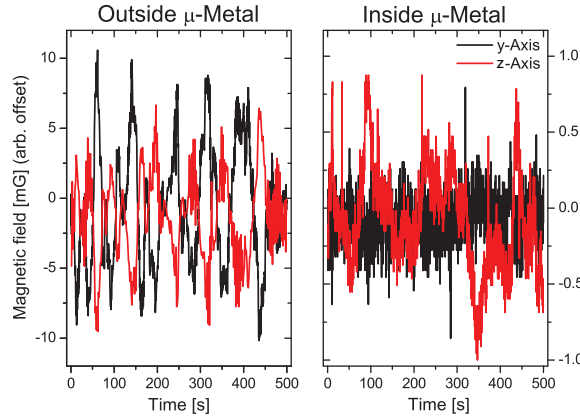
Figure 3.2.1: Measurement of the magnetic field fluctuations in our lab. Measured magnetic field fluctuations on the two axes with the highest amplitude outside the μ-metal (left) and inside the magnetic field shield (right), both measured with a flux gate (Bartington MAG03-MC70). One can clearly recognize that the shielding factor is not the same on both axes at the position of measurement, which is some centimeters away from the position of the atoms. The main contribution to the slow drifts of the magnetic field is due to the nearby subway line.

3.2 Magnetic shielding

The stability of the (static) magnetic field is important for two main reasons: Firstly, magnetic field fluctuations inhibit the preparation of a reproducible atom number through forced evaporative cooling, as the final atom number is very sensitive on the magnetic field, because it influences the trap bottom. Secondly, magnetic field fluctuations limit the coherence time between states $|1\rangle$ and $|2\rangle$ in general [69], and especially when using microwave potentials, because then the dressed states have a differential magnetic moment [21, 47].

Therefore, we have put a magnetic shielding[6] around our experiment. Without magnetic shielding, we measure peak-to-peak fluctuations of the magnetic field of up to 33 mG, which is mostly caused by the nearby subway line. The magnetic field changes on a minute time-scale. Inside the magnetic shielding, we measure total peak-to-peak magnetic field fluctuations of up to 2.6 mG (225 μG r.m.s.), see Figure 3.2.1.

A side effect of the magnetic shield is that its interior acts as a microwave resonator. We find, that by moving parts like e.g. the camera tubus inside the μ-metal, even by only some mm, the microwave field strength radiated from the horn and measured with the atoms changes substantially.

---

[6]Single-layer μ-metal shielding from Sekels GmbH

3.3 Microwave and radio-frequency setup

3.3.1 Microwave for on-chip CPW

We create state-selective potentials for states $|1\rangle$ and $|2\rangle$ by coupling an off-resonant microwave into the CPW. In the limit of large detuning $\left|\Omega_{1,m_1}^{2,m_2}\right|^2 \ll \left|\Delta_{1,m_1}^{2,m_2}\right|^2$ for all m_1, m_2, the differential potential between $|1\rangle$ and $|2\rangle$ depends linearly on the microwave power P_{mw} (see Section 1.8.1). Therefore, to minimize dephasing between $|1\rangle$ and $|2\rangle$ we need high stability and reproducibility of P_{mw}.

The microwave power for the on-chip waveguide is generated by an amplified Agilent 8257D microwave generator, whose output is amplitude stabilized using a feedback loop with a 20 dB directional coupler and an Agilent 8471E microwave detector (see Figure 3.3.1). We measure a relative long-term drift in P_{mw} of $< 5 \times 10^{-4}$ peak-to-peak if we set the amplitude modulation (AM) input to a constant level by the experiment control. For frequency stability, the microwave generator's internal clock is phase-locked to a 10 MHz Oscilloquartz OCXO 8607-BM reference.

The transmission through the atom chip (including the base chip) is attenuated by $\sim 6\,\mathrm{dB}$ at $6.8\,\mathrm{GHz}$ (see Figure 3.3.2). We find that the relative drift of the power launched into the chip is the same as that of the transmitted power. This indicates that there is no significant long-term drift of the CPWs transmission properties.

3.3.2 Microwave and radio-frequency for state preparation

Microwave and radio-frequency fields irradiated to the atoms for internal state preparation should be as homogeneous as possible to prevent Rabi frequency gradients across the clouds.

Microwave

The microwave for the state-preparation is generated by a second Agilent 8257D microwave generator. It is also phase-locked to the Oscilloquartz OCXO 8607-BM. Its output is fed through a circulator and a switch[7] and is amplified using a 4 W amplifier.[8] We measure a relative long-term stability

---

[7]Miteq N147BDM2
[8]AML 48P4201-4W

cable to CPW
max. 120 mW

power monitoring

DC current
Bias-Tee
UMCC BT-S000-HS

microwave detector
Agilent 8471E

absorptive

switch

circulator
AEROTEK
H15-1FFF

circulator
AEROTEK
H15-1FFF

20 dB dir. coupler
Pulsar CS20-10-435/1 Miteq N147BDM2

Microwave gen.
Agilent 8257D

AM in   ALC in   MW Out

50 Ω termination

from experimental
control

att.

32 dB amp.
AML 218P3203

20 dB dir. coupler
Pulsar CS20-10-435/1

microwave detector
Agilent 8471E
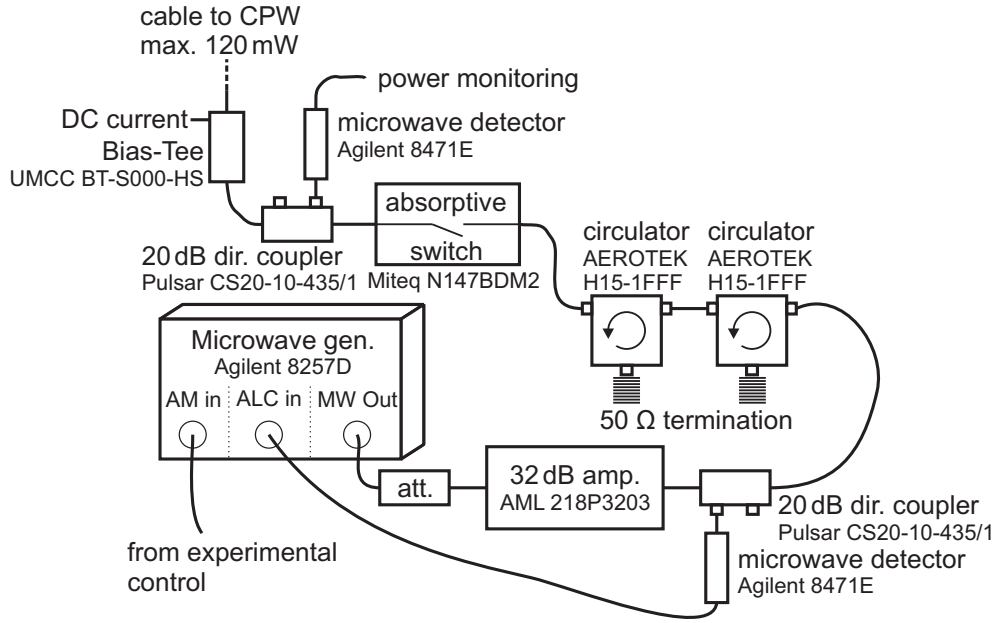
Figure 3.3.1: Sketch of the microwave power stabilization circuit. The microwave generator's output is running cw. It is attenuated, such that the generators maximum output (+14 dBm) saturates the 32 dB amplifier. 1% of the amplified microwave power is fed back to the generator's ALC ("automatic leveling control") input to stabilize the output power. The ALC bandwidth is set to 100 kHz. Even though the microwave switch (rise/fall-time < 300 ns) is an absorptive switch, we need 2 circulators until we see no effect of the switch on the power stabilization. From this chapter on to the end of this thesis, microwave power values P_{mw} correspond to the power measured at the second directional coupler.
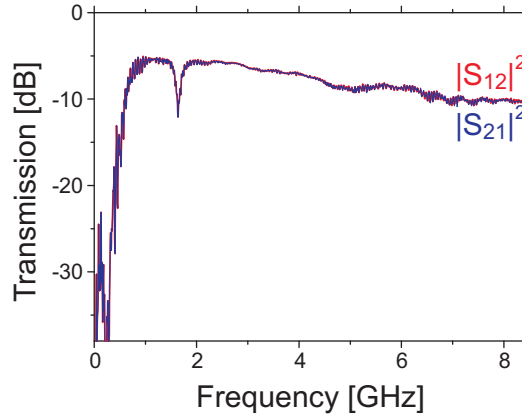
Figure 3.3.2: Measurement of the microwave transmission characteristics of the single CPW structure including cables. We measure a damping of 10 dB at 6.8 GHz from one end to the other, including the cables which contribute 4 dB. $|S_{12}|^2$ and $|S_{21}|^2$ are equal, as it is expected in absence of non-linearities. Due to symmetry, we expect an attenuation of 5 dB from one end of the cable to the chip center.

of the pulse-area after the amplifier of 2×10^{-3}. The output of the amplifier is then fed to the microwave horn shown in Figure 3.1.1. The horn irradiates the atom chip with a relatively homogeneous, linearly polarized microwave, whose AC magnetic field is approximately perpendicular to the static magnetic field in the trap center. However, the presence of the structured chip surface causes microwave near-field variations, see Section 4.4.

Radio-frequency

The radio-frequency for the two-photon drive is generated by an Agilent 33250A function generator. It is phase-locked to the same 10 MHz reference as the microwave generators. The output is then fed through a switch[9] and is amplified by an amplifier[10] to up to 2 W. We measure a relative long-term stability of the pulse area of 1×10^{-3}. The output of the amplifier is then fed to the radio-frequency antenna indicated on Figure 3.1.1. The same generator is also used for the first two (of three) forced evaporative cooling ramps.

---

[9]Mini-circuits ZASWA-2-50DR
[10]Mini-circuits ZHL-1-2W
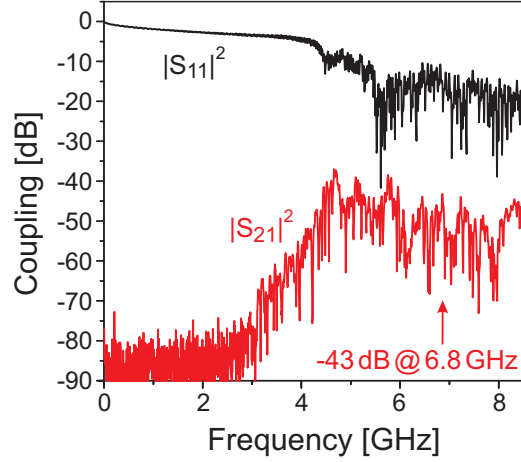
Figure 3.3.3: Coupling between the microwave horn and the on-chip CPW. Using a network analyzer, a variable microwave frequency is sent to the microwave horn, and the signal picked up by the single CPW structure is measured. $|S_{21}|^2$ is the transmitted signal picked up by the CPW and $|S_{11}|^2$ is the signal reflected by the microwave horn due to impedance mismatch. The data includes about 4 dB attenuation from the cables to the horn and from the CPW to the network analyzer. The data is taken with the magnetic shield closed.

Coupling between the horn and the CPW

We find a finite coupling between the microwave horn and the on-chip CPW. Using a network analyzer, we shine in a microwave of variable frequency through the horn to the chip and measure the signal picked up by the CPW. The measurement is shown in Figure 3.3.3. The consequence is a degraded microwave horn field homogeneity near the CPW, which leads to dephasing of Rabi oscillations, see Figure 5.1.1a. In Section 4.4 we find that the microwave field inhomogeneities near the CPW cannot be explained purely by the coupling between the horn and the on-chip waveguide.

3.4 Current sources

For the critical chip wire currents on the lower layer of the science chip, where the stability is very important,[11] we use ultra-stable, bipolar current sources, which have been developed in our group [121]. These current sources have a maximum output current (voltage) $I_{\max} = \pm 3\,\mathrm{A}$ ($V_{\max} = \pm 10\,\mathrm{V}$), and

---

[11] As opposed to currents e.g. in the MOT phase or the first magnetic trap
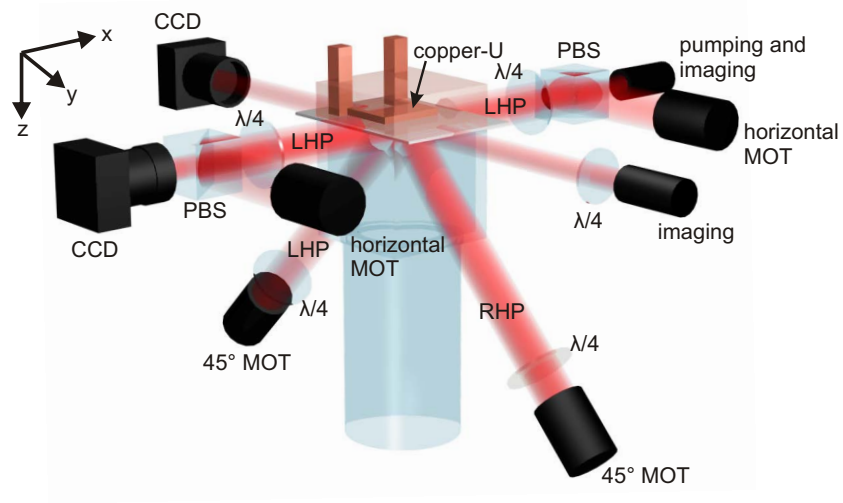
Figure 3.5.1: Illustration of the optical beam paths for cooling, optical pumping and imaging. The beams from the 45° MOT outcouplers are reflected at the upper metalization layer on the science chip. The polarizations of the beams with respect to their propagation directions are indicated, where RHP (LHP) stands for right-hand-side (left-hand-side) circular polarization. The current through the copper-U, that is glued on the back of the atom chip, together with homogeneous external fields create the quadrupole magnetic field for the MOT.

exhibit an r.m.s. current noise $\Delta I / |I_{\mathrm{max}}| = 5 \times 10^{-6}$ in a frequency band of 0.3 Hz - 200 kHz. The current drifts within an hour by less than $10^{-5} |I_{\mathrm{max}}|$ peak-to-peak. The sources can switch currents within $15 \, \mu s$ (10%-90%) for typical loads of some Ohms.

For the coils, we use sources with similar characteristics, but with $I_{\mathrm{max}} = \pm 5 \, \mathrm{A}$ and which are optimized for inductive loads. These sources can switch the currents in the coils in less than 1 ms.

For DC currents in the upper layer of the science chip, we use commercial current sources.[12] These bipolar sources have a maximum output current (voltage) of $I_{\mathrm{max}} = \pm 20 \, \mathrm{mA}$ ($V_{\mathrm{max}} = \pm 10 \, \mathrm{V}$). They exhibit a relative drift of $\Delta I / |I| \leq 6 \times 10^{-5}$ within 500 s. We measured an r.m.s. current noise $\Delta I / |I_{\mathrm{max}}| = 1.2 \times 10^{-5}$ in a frequency band of 3 Hz - 230 kHz.
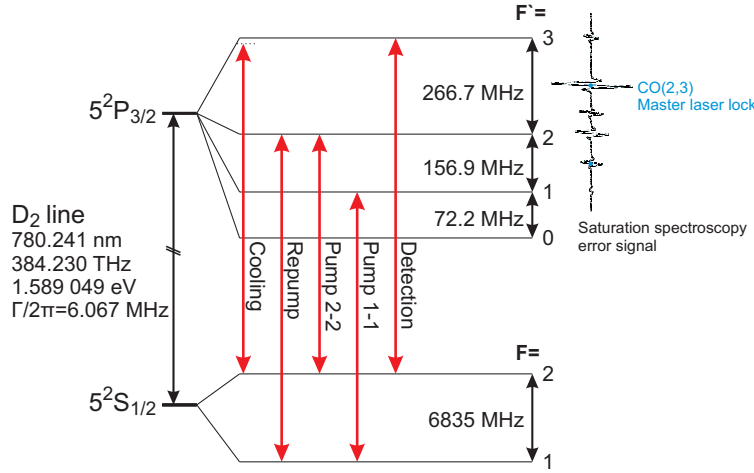
Figure 3.5.2: ^{87}Rb term scheme and overview of the laser frequencies used in the experiment. The MOT cooling light frequency is detuned by -2Γ with respect to the resonance $F = 2 \rightarrow F' = 3$, the light for the molasses cooling is detuned by -13Γ. The lock point for the master laser is indicated in blue in the saturation spectroscopy error signal on the upper right. The spectroscopic error signal has been taken from [122].

3.5   Laser system

Laser light for cooling of atoms in the mirror MOT [4] and molasses, optical pumping, and imaging of the atoms is generated by three diode lasers,[13] which emit light near the D$_2$ line of ^{87}Rb ($\lambda = 780$ nm). The relevant laser frequencies which are derived from the diode lasers using acousto-optic modulators (AOMs) are indicated in Figure 3.5.2. The laser light after the AOMs is coupled into polarization maintaining single-mode fibers and is guided to outcouplers near the glass cell. Here I will only give a short overview of the laser system. A more detailed description can be found in [121].

Cooling laser   Cooling in the MOT and in the optical molasses is performed on the transition $F = 2 \leftrightarrow F' = 3$. The laser light required is generated by two lasers in master-slave configuration. The master laser is a grating stabilized diode laser in Littrow configuration [123], which is frequency locked using Doppler-free saturation spectroscopy on the crossover-resonance $F = 2 \rightarrow F' = \mathrm{CO}(2,3)$ (see Figure 3.5.2). The laser light is frequency shifted in a double-pass AOM by $2 \times \left(110\,\mathrm{MHz} + \frac{\Delta}{2}\right)$, before it is

---

[12]BCS 002/10 from HighFinesse GmbH.
[13]with Sharp GH0781JA2C laser diodes, $P_{\mathrm{max}} = 120$ mW.

injected into the slave diode laser. This locks the frequency of the slave laser to the incident laser frequency. The slave laser light passes another AOM,[14] which shifts the light frequency by -86.65 MHz, before it is split and fed into four polarization maintaining fibers leading to the outcouplers for the mirror-MOT (see Figure 3.5.1).

The MOT laser light frequency can be shifted from the resonance $F = 2 \to F' = 3$ by up to $\Delta = -16\Gamma/2\pi$ to the red and $\Delta = 7\Gamma/2\pi$ to the blue, with the slave diode laser still being injection locked. The light for the MOT is detuned by $\Delta = -2\Gamma/2\pi$, while during the molasses phase, $\Delta = -13\Gamma/2\pi$.

Repump laser   During the MOT and molasses phase, atoms can be pumped off-resonantly by the cooling light to the $F = 1$ ground state. To bring the atoms back to the cooling cycle, we use *repump* laser light, which is resonant with the transition $F = 1 \to F' = 2$. This light is generated by a second grating stabilized diode laser, which is locked on the transition $F = 1 \to F' = \mathrm{CO}(1, 2)$ (cf. Figure 3.5.2), which is then frequency shifted on resonance with the atomic transition $F = 1 \to F' = 2$ by an AOM at frequency 78.5 MHz. This light beam is superimposed to the cooling light in both 45° mirror-MOT outcouplers.

The repump laser light is not only used for cooling, but also for state-selective absorption imaging, see in Section 3.7.1 below.

Pump lasers   We use the combination two left-hand circularly polarized beams resonant with the transitions $F = 2 \to F' = 2$ (*2-2-pump*) and $F = 1 \to F' = 1$ (*1-1-pump*) to transfer the atoms to the magnetically trappable state $|1, -1\rangle$ after molasses cooling. Both beams are superimposed into a separate optical single-mode fiber (*pump fiber*), whose light at the other end is superimposed with one of the horizontal MOT beams (cf. Figure 3.5.1).

2-2-pump laser   The 2-2-pump beam is taken directly from the master diode laser, before the double-pass AOM. The light has to be shifted by -133.5 MHz. Since the AOM used here works efficiently only up to 90 MHz, the laser is frequency shifted in a double-pass AOM configuration by $2 \times -66.75\,\mathrm{MHz}$.

1-1-pump laser   The 1-1-pump is derived from the repump diode laser, and is frequency shifted using an AOM by -78.5 MHz, before it is coupled into the pump beam fiber.

---

[14]This AOM is also used for laser power modulation and fast switching

Detection laser   The detection laser is resonant with $F = 2 \rightarrow F' = 3$ and is taken from the MOT laser beam. The detection laser is either coupled into a separate single-mode fiber for imaging along the y axis or into the pump fiber for imaging along x.

Our laser system is very stable - as long as the air condition keeps the temperature steady, the laser system can be operated for days without re-locking.

3.6   Experiment control

The experiment is controlled by a computer equipped with 4 National Instruments digital/analog cards ($2\times$PCI-6733, $1\times$PCI-6723 and $1\times$PCIe-6259) as well as a GPIB adapter. In total, we have 20 analog 16bit, 32 analog 13bit and 48 digital ports. All analog-out channels show high frequency *glitches* at the beginning of each sample.[15] Amplitudes and durations of these glitches are shown in the table below, measured at a sampling frequency of 100 kHz. Furthermore, I show the expected maximum voltage drifts during 24 h for an output voltage of 10 V, calculated according to the specs of the cards.

card	drift within 24 h [mV]	glitch amplitude [mV]	glitch duration [μs]
PCI-6733 ($8\times$16bit, 8 digital)	1.4	5	2
PCIe-6259 ($4\times$16bit, 32 digital)	2.1	10	1
PCI-6723 ($32\times$13bit)	10	100	2

On some critical channels, we filter the glitches with a low-pass filter.

The experimental control software is based on *goodTime*, a program written by Jakob Reichel. I extended it by implementing the following features: Syntax highlighting and a virtual oscilloscope (see Figure 3.6.1), relocking to the 50 Hz power net frequency, as well as inter-process communication with the camera software for triggering and parameter transmission via Microsoft's DCOM interface.[16] We are working with a sample interval of $10\,\mu$s.

---

[15]These glitches are documented.

[16]Using DCOM (Distributed Component Object Model), the process to communicate with can be on the same computer as well as on any computer reachable via the network. In our case, the camera control software runs on a different computer than the experimental control software.

Shorter intervals needed for the Ramsey sequence are generated using a SRS DG535 delay generator, triggered by goodTime.

Syntax highlighting and virtual oscilloscope Syntax highlighting in combination with code folding facilitates reading and writing of code enormously (see Figure 3.6.1a). The syntax highlighting class built into goodTime is based on the *Scintilla* library.[17]

The idea behind the virtual oscilloscope (see Figure 3.6.1b) is as follows: It turns out that in the daily lab work debugging of the experimental control code is done more efficiently (and much more often successfully) by checking the relevant analog/digital channels with an oscilloscope rather than by analyzing the code of the sequence. Since our oscilloscopes have only up to four channels, and setting up a measurement takes some time, a graphical preview of arbitrarily many chosen output channels should facilitate sequence examination and debugging.

3.7   Data acquisition

3.7.1   State-selective absorption imaging

We take our experimental data using state-selective resonant absorption imaging [1], where a σ^- polarized laser pulse (duration $dt_{\mathrm{im}} = 40\,\mu\mathrm{s}$), resonant with the cycling transition $F = 2$, $m_F = -2 \rightarrow F' = 3$, $m_{F'} = -3$, is shone through the atom cloud and the shadow cast by the atoms is imaged with a CCD camera. We use an Andor iKon-M DU934N-BR-DD camera, which contains a back-illuminated, deep depletion CCD chip, that exhibits a quantum efficiency of $q = 0.90$ at $\lambda = 780\,\mathrm{nm}$ and Temperature $-80°$C. Two thirds of the CCD are shadowed by a razor blade, and are only used as a storage area. We start with two laser pulses which image the different hyperfine states. The first laser pulse projects the atoms which are in a superposition of the hyperfine states $|1\rangle$ and $|2\rangle$, onto the $F = 2$ manifold and images the atoms in $F = 2$. After the image is taken, the charges accumulated in the illuminated area of the CCD are moved into the shadowed area, which takes $dt_{\mathrm{move}} = 1.6\,\mathrm{ms}$. During dt_{move}, atoms in $F = 2$ fly out of the depth of focus of the imaging system due to the photon recoil momentum transferred by the imaging pulse. Subsequently, a 20 μs repumping pulse pumps the atoms from $F = 1$ to $F = 2$, which are then imaged as in the first pulse. Subsequently, the charges of the second exposure are also shifted into the shadowed region, before a last exposure without atoms is performed.

---

[17]www.scintilla.org
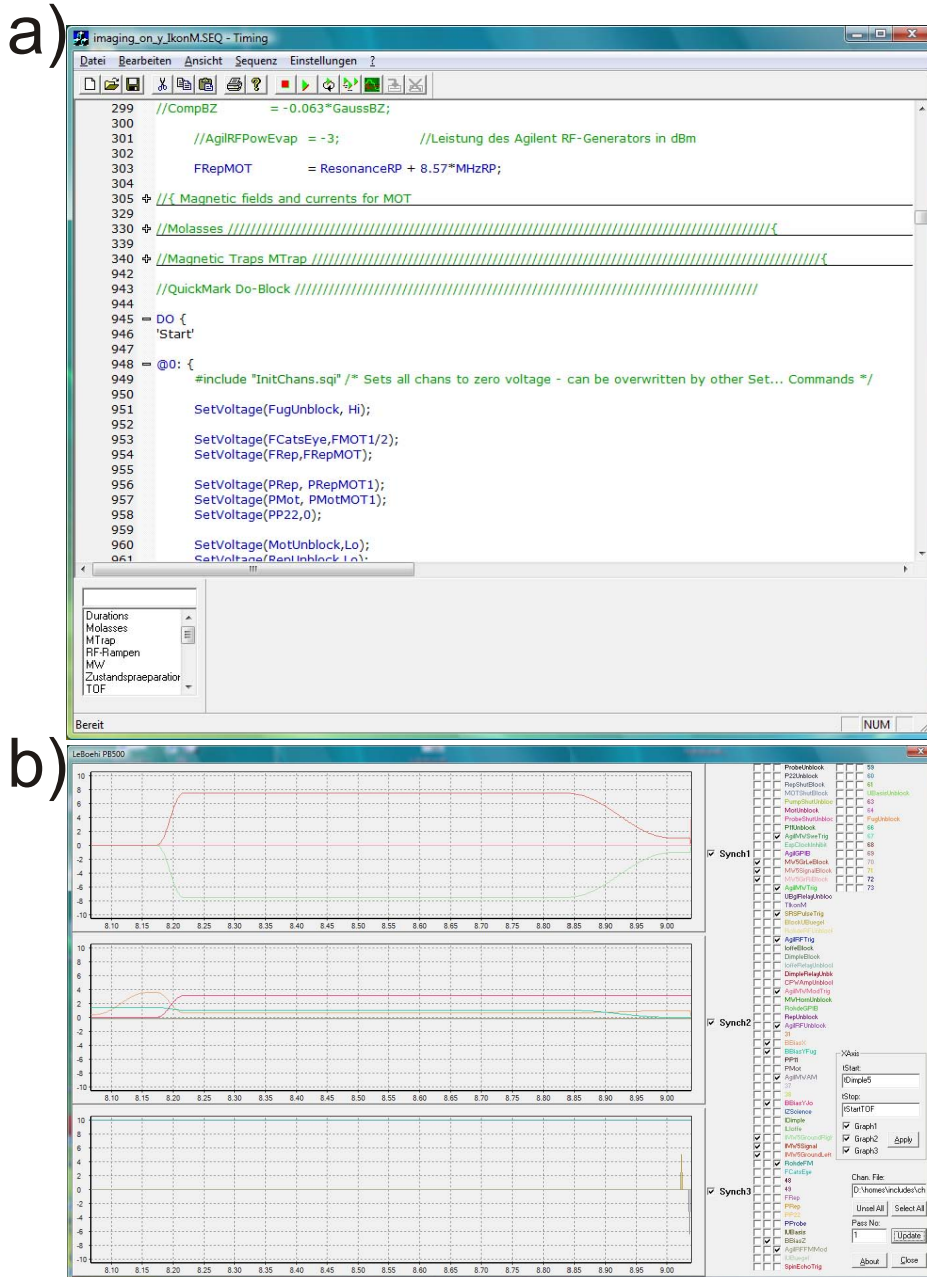
Figure 3.6.1: Screen shot of our experimental control software goodTime. (a) Main user interface of goodTime, with syntax highlighting and code folding. (b) The virtual oscilloscope shows a preview of the output on the respective channels. This can facilitate debugging a lot.
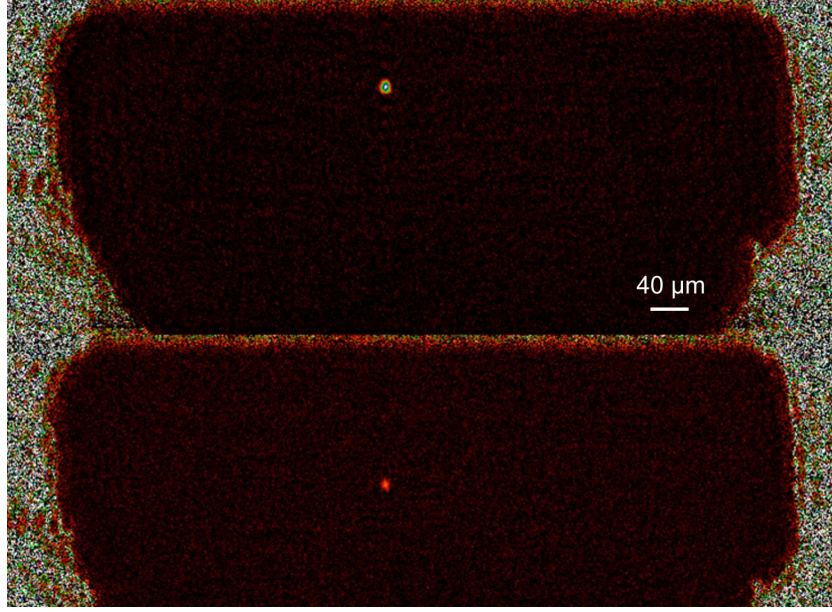
Figure 3.7.1: State-selective absorption image of a BEC prepared in a superposition of $|1\rangle$ and $|2\rangle$ (top: $F = 2$, bottom: $F = 1$) with about 1000 atoms in total ($F = 2 : N_2 \sim 800$ atoms, $F = 1 : N_1 \sim 200$ atoms). We detect the number of atoms in each hyperfine manifold with an r.m.s. imaging noise of 10 atoms, which is dominated by photonic shot noise. The time between both absorption images in $F = 2$ and $F = 1$ is 1.6 ms; the atoms in $F = 2$ are imaged after 4 ms time-of-flight (TOF), while the atoms in $F = 1$ are imaged after 5.6 ms of free fall. The resolution of our imaging system is $s_{\mathrm{opt}} = 4\,\mu$m.

After that, the mechanical shutter of the camera closes, and the accumulated charges of the two *absorption images* and from the *reference image* on the chip are read out to the camera count bitmaps $n_{\text{abs},F=2}(x,y)$, $n_{\text{abs},F=1}(x,y)$ and $n_{\text{ref}}(x,y)$. Furthermore, we take about once a day a picture without a laser pulse, $n_{\text{dark}}(x,y)$, which measures background light and camera dark current.

The spatial atomic density distribution in the manifolds $F = 1$ and $F = 2$, $N_{F=i}(x,y)$, can then be calculated according to [124]

$$N_{F=i}(x,y) = \frac{A}{\sigma_{\text{eff}}} \ln\left(\frac{n_{\text{ref}}(x,y) - n_{\text{dark}}(x,y)}{n_{\text{abs},F=i}(x,y) - n_{\text{dark}}(x,y)}\right) + \frac{2}{\Gamma dt_{\text{im}}qg}\left(n_{\text{ref}} - n_{\text{abs},F=i}\right),$$

(3.7.1)

where $A = (l_{\text{pixel}} \cdot \alpha_{\text{mag}})^2$ is the pixel area in the object plane (l_{pixel} is the pixel period on the CCD chip and α_{mag} is the magnification of the imaging system), $\Gamma = 2\pi \times 6.067$ MHz is the natural line width of the D$_2$-line, q is the quantum efficiency and g the gain of the camera, and $\sigma_{\text{eff}} = \epsilon\sigma_0$ with $\sigma_0 = 3\lambda^2/2\pi$ is the resonant cross-section for a two-level atom. ϵ adjusts the effective scattering cross section σ_{eff}, and is calibrated following [124] to $\epsilon = 0.90$, such that the measured atom number is independent of the imaging intensity I. The factor ϵ takes into account the effects of pumping the atoms to the cycling transition as well as imperfect imaging light polarization. The product $q \cdot g$ can be calculated from a measurement of photonic shot noise (we take the measurement $g = 1.11$ from the camera manufacturer).

Measurement of the number of atoms both in $F = 1$ and $F = 2$ in a single shot allows to take out fluctuations in the total atom number preparation.

Imaging noise We image the atoms with an imaging beam intensity $I \approx I_{\text{sat}}$, where I_{sat} is the saturation intensity, because this provides us the best signal to noise ratio.[18]

When imaging typical BECs containing 1000 atoms after a time-of-flight of 4 ms, the photonic shot noise on the camera over the image area of the BEC leads to an atom number uncertainty of 10 atoms r.m.s. on the absorption images for each hyperfine manifold.

When imaging clouds in a superposition of states $|1\rangle$ and $|2\rangle$, with N_1 and N_2 the number of detected atoms in states $|1\rangle$ and $|2\rangle$ and σ_1 (σ_2) the imaging noise for state $|1\rangle$ ($|2\rangle$), the r.m.s. imaging noise σ_{norm} of the normalized atom

---

[18]Ed Marti (UC Berkeley), private communication.

number[19] $N_{1(2),\mathrm{norm}} = \frac{N_{1(2)}}{N_1+N_2}(\overline{N}_1 + \overline{N}_2)$ is given by

$$\sigma_{\mathrm{norm}} = \frac{\sqrt{\overline{N}_1^2\sigma_2^2 + \overline{N}_2^2\sigma_1^2}}{(\overline{N}_1 + \overline{N}_2)} \qquad (3.7.2)$$

For mean atom numbers $\overline{N}_1 = \overline{N}_2 = 500$, we get $\sigma_{\mathrm{norm}} = \frac{10}{\sqrt{2}} \approx 7.1$. This is substantially below projection noise $\sigma_{\mathrm{proj}} = \sqrt{\overline{N}_1 \cdot \overline{N}_2/(\overline{N}_1 + \overline{N}_2)} = 15.8$. This in turn allows the detection and characterization of entangled states like spin-squeezed states using our imaging system [47].

3.7.2 Camera control

For camera control and data processing, I wrote a MATLAB-GUI based program called *MatCam*. The main advantage of a MATLAB based program is that modifying, extending and debugging can be done with great ease, without having to restart or even recompile the program after each modification. MatCam camera drivers have to implement a simple interface, and have to be provided as a Win32-DLL file. Currently, I have implemented camera drivers for 5 different camera types. Furthermore, MatCam also provides a simple interface for user-defined m-file based fitting routines.

MatCam communicates with goodTime via the already mentioned DCOM interface. It takes parameters from the experimental control software, e.g. for proper atom number calculation (i.e. dt_{im} from Eq. (3.7.1)) as well as any chosen parameter. All transmitted parameters as well as extracted values (e.g. the number of atoms, or the extracted temperature) are logged to text-files, which can be imported into any analysis software. Furthermore, MatCam comes with a reanalysis function, which allows to reanalyze previous scans.

3.8 Production of mesoscopic BECs

In this section, I briefly sketch the procedure for the production of mesoscopic BECs in state $|1\rangle$, which constitute the starting point for the experiments described in the following section and Chapter 5. For a detailed treatise of laser cooling and Bose-Einstein condensation in chip traps, see [125, 126].

MOT and optical molasses   Atoms are collected and cooled from the background gas by the mirror-MOT and a subsequent optical molasses phase

---

[19]The normalized atom number takes out the relatively small fluctuations in the total number of prepared atoms.
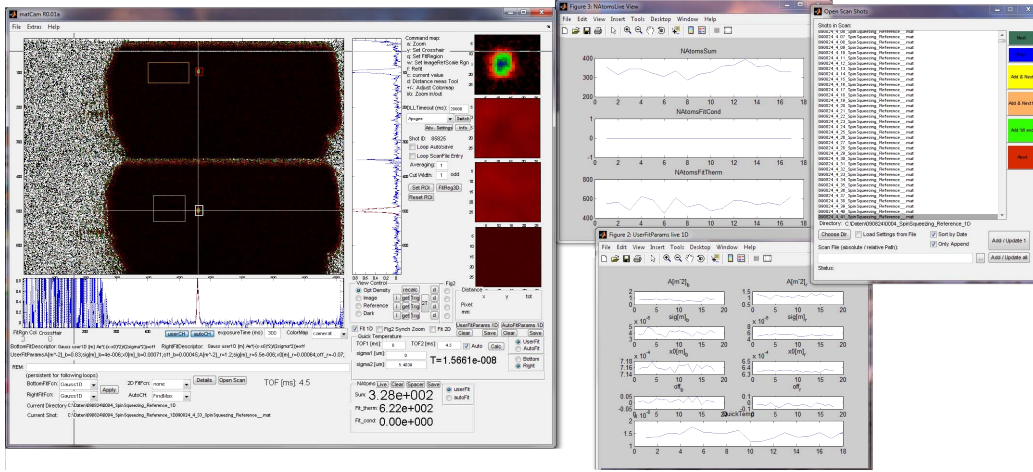
Figure 3.7.2: Screen shot of MatCam with its primarily used tool windows.

as described in [69], except that we do not modulate the background pressure with a LIAD technique. At the end of the molasses phase, we end up with an atomic ensemble of about 6×10^6 atoms at a temperature of $7\,\mu\text{K}$. Due to the wire gaps and bumps of the on-chip mirrors (see Figure 2.0.1 and Chapter A) the MOT has some fuzzy structure, which turned out to be no problem for subsequent loading of the magnetic traps.

Optical pumping Before switching on the magnetic traps, we have to optically pump the atoms into a magnetically trappable hyperfine state. We do this by shining in a $400\,\mu\text{s}$ pulse of 1-1-pump and 2-2-pump laser light which is σ^- polarized with respect to the magnetic field of 2 G. This transfers the atoms with high efficiency into the magnetically trappable hyperfine state $|1\rangle$. The optical pumping increases the temperature of the cloud to $11\,\mu\text{K}$.

Magnetic trapping and evaporative cooling The first magnetic trap ("Z-Ioffe"), a Ioffe-Pritchard trap with a relatively large trapping volume that is formed by a "Z"-shaped wire on the lower layer of the chip ($I_Z = 2.65\,\text{A}$, see Figure 3.8.1a and Table 3.1), is switched on and captures about 4.5×10^6 atoms. This trap is then compressed adiabatically to increase the elastic collision rate (which is a prerequisite for fast evaporative cooling) and the temperature of the cloud is lowered by a first RF evaporation ramp, such that the remaining precooled cloud ($\approx 1 \times 10^6$ atoms) fits into the next trap. We then ramp the atoms adiabatically into the next, more elongated "Long-Ioffe" trap ($I_{LZ} = 630$ mA, on the lower chip layer), followed by smooth turning on of the "Dimple-1" trap (current $I_{D1}=350$ mA, lower chip layer).

There we perform another RF evaporation ramp, such that we empty the
"plateau" of this dimple trap (see Figure 3.8.1b), and end up with a cloud of
30'000 atoms at a temperature close to but still above T_c. Subsequently, we
crossfade from the dimple trap created by I_{D1} to a little more relaxed one
("Dimple-2") created by DC currents on the single-CPW wires where each
of the three CPW wires carries a current of 15 mA (total current I_{D2}=2 ×
15 mA − 15 mA=15 mA, see Table 3.1).[20] In this dimple trap we perform a
last step of RF evaporative cooling (see Figure 3.8.2), such that we end up
with quasi pure condensates containing up to 5'000 atoms. The prepared
atom numbers in the BEC is highly reproducible (see Figure 3.8.3). Then,
we ramp the condensate during 150 ms into the experiment trap, which is
created by currents on the Long-Ioffe and CPW wires. This ramp is adiabatic
to avoid excitations in the BEC.

We could also create condensates directly in the "Dimple-1" trap, but
then we would have to transfer the condensate from a dimple trap created
by current I_{D1} to the experiment trap created by DC currents on the CPW
wires, which not only involves ramping of currents but also switching of a
current source at the risk of creating excitations in the condensate. Per-
forming the second RF evaporation directly in the trap "Dimple-2" is not
an option because the achievable trap volumes are too small because of the
limited DC current capabilities of the CPW wires.

We measure the trap bottom as the stop frequency of the last RF evap-
oration ramp at which the trap is emptied to 1.4130 MHz (including some
10 kHz due to RF power broadening), corresponding to a magnetic field
B_0=2.019 G in the trap center (we simulate $B_0 = 1.89$ G, see Table 3.1). To
produce BECs with 400 atoms, we have to stop the RF-evaporation 3.3 kHz
above the trap bottom. This agrees well with the calculated chemical poten-
tial μ_c=3.7 kHz for a BEC of 400 atoms in the condensation trap (f_x=200 Hz,
$f_\perp$=2100 Hz) [84].

---

[20]This choice of currents on the CPW wires has historic reasons as one of the current
sources was originally connected in the wrong way. Since condensation works well in this
configuration, we did not change it.
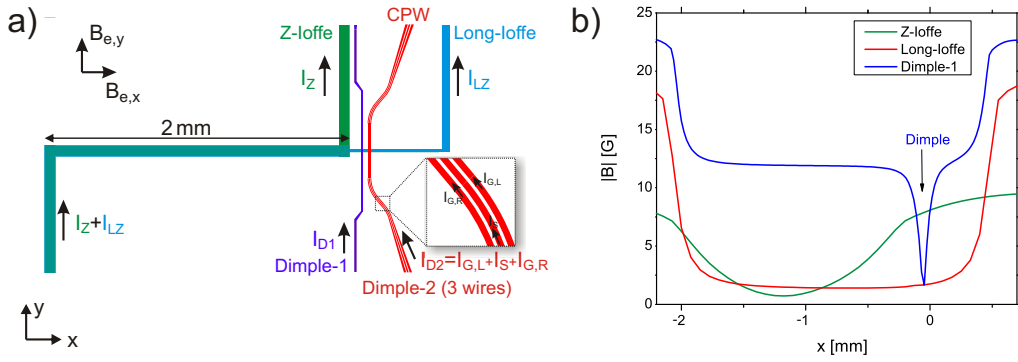
Figure 3.8.1: Illustration of the science chip wires for static magnetic trapping and the magnetic field configurations they create in the experiment. (a) Geometry of the relevant on-chip wires together with their currents (the arrow indicates the current direction, see Appendix A for more details). All wires, except for the "Dimple-2" wires are located on the lower layer of the science chip. The smallest widths of the "Z-Ioffe", "Long-Ioffe" and "Dimple-1" wires are 50 μm, 17 μm and 10 μm respectively. "Left" and "Right" in $I_{G,L}$ and $I_{G,R}$ corresponds to the nomenclature in the experiment control code. (b) Magnetic fields in the different traps on a cut along x through the trap minimum ($x = y = 0$ is at the intersection of the middle "Dimple-2" and "Long-Ioffe" wire). One can clearly recognize the plateau of the "Dimple-1" trap, which is emptied during the second RF evaporation, such that the cooled cloud accumulates in the dimple.

Step	Δt [ms]	I_Z	I_{LZ}	I_{D1} [A]	$I_{\text{G.L}}$	I_{S}	$I_{\text{G,R}}$ [mA]	$B_{e,x}$	$B_{e,y}$ [G]	d [μm]	f_1	f_2	f_3 [Hz]	B_0 [G]	ν_{RF} [MHz]
Z-Ioffe1	2	2.65	0	0	0	0	0	0	12	400	24	180	220	1.90	
ramp	200	↓	0	0	0	0	0	↓	↓						
Z-Ioffe2	500	2.5	0	0	0	0	0	1.4	55	76	16	3820	3870	1.85	50→17.5
ramp	10	↓	0	0	0	0	0	1.4	↓						
Z-Ioffe3	5	0.63	0	0	0	0	0	1.4	20	47	7	2120	2140	1.47	
ramp	100	↓	↓	0	0	0	0	1.4	20						
Long-Ioffe	1	0	0.63	0	0	0	0	1.4	20	53	17	2280	2320	1.55	
ramp	100	0	0.63	↓	0	0	0	↓	20						
Dimple-1	1000	0	0.63	-0.35	0	0	0	12	20	51	460	3800	3900	0.793	19→1.8
ramp	50	0	0.63	↓	↓	↓	↓	↓	20						
Dimple-2	600	0	0.63	0	-15	-15	15	2.3	20	53	200	2100	2100	1.89	2→1.4
ramp	150	0	↓	0	↓	↓	↓	↓	↓						
ExpTrap	~15	0	0.13	0	-2	-2	2	3.3	5.2	44	109	500	500	3.23	

Table 3.1: Sequence of traps created with the wires in Figure 3.8.1. *ExpTrap* is the trap that is used for the experiments in Chapter 5 and Section 6.1. Durations Δt, trap frequencies f_i, distances of the trap centers from the chip surface d, magnetic fields in the trap center B_0 and the frequencies ν_{RF} of the RF evaporative cooling ramps are shown in the table. Arrows indicate smooth ramps from the start to the end values. Numbers given for f_i, B_0 and d have been calculated (except for *ExpTrap*, for which these values have been measured).
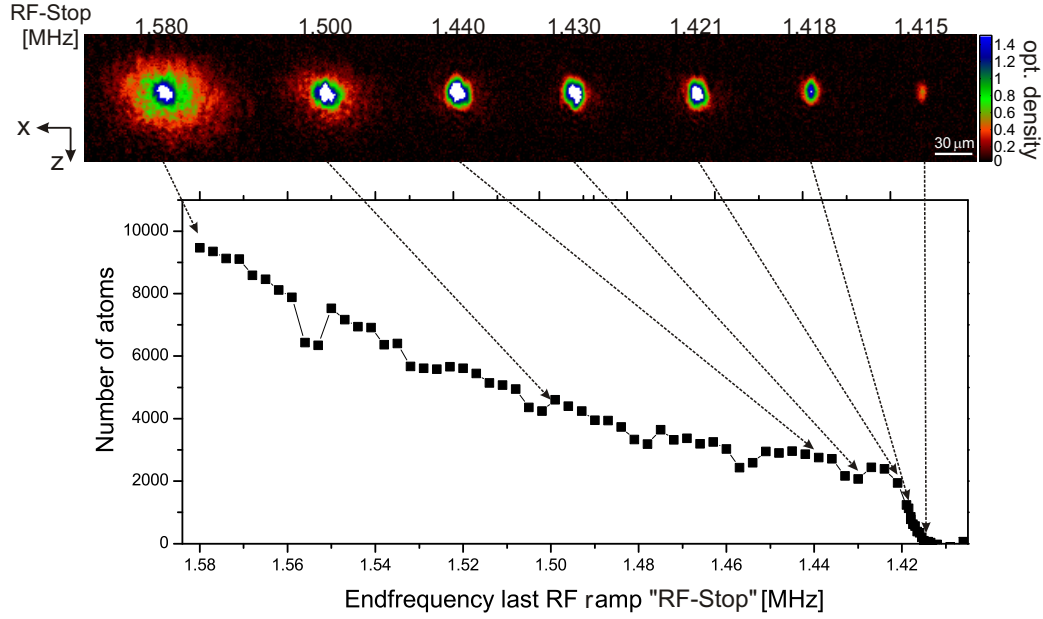
Figure 3.8.2: Bose-Einstein condensation through RF evaporative cooling. The lower part of the figure shows the number of atoms for different values of the end frequency of the last RF ramp. In this set of measurements we produce "pure" BECs with about 2000 atoms without discernible thermal fraction. The upper part shows the optical density of the clouds after a time-of-flight of 7.7 ms. The condensed component is only slightly elongated because the atoms are released from a relaxed detection trap ($f_x = 40$ Hz, $f_\perp = 130$ Hz).
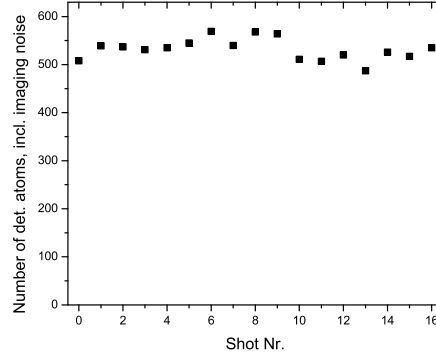
Figure 3.8.3: Stability of the atom number preparation in a BEC. We repeatably prepare a mesoscopic BEC by cutting with the RF-ramp for condensation deep into the BEC. We end up with a condensate containing 533±22 atoms (including imaging noise of about 10 atoms r.m.s.). This exceptional stability is only possible with the magnetic μ-metal shield.

3.9 Atoms in the CPW near-field

In this section, I report on a first set of measurements, which characterize the microwave near-field around the single CPW structure. We ramp a condensate containing 3000 atoms to different traps at different positions and drive resonant single-photon Rabi oscillations on the σ_-, π and σ_+ transition using the CPW. The static magnetic field B_0 in the trap center is approximately oriented along x. We find very high microwave magnetic field gradients, and measure Rabi oscillation frequencies $|\Omega/2\pi|$ reaching nearly 1 MHz for $P_{\mathrm{mw}} = 25\,\mathrm{mW}$ (see Figure 3.9.1). We compare the measured Rabi frequencies with a static simulation for an ideal CPW mode (assuming homogeneous microwave currents I_{mw} on the signal wire and $-I_{\mathrm{mw}}/2$ on each of both grounds), and find rough agreement. The observed Rabi oscillations are quickly damped out, which is caused by the strong field gradient across the extent of the atom cloud.

The high microwave near-field strength can be illustrated by comparing our measured Rabi frequencies $|\Omega/2\pi| \sim 1$ MHz for about 8 mW microwave power reaching the chip center with the first microwave trapping experiments [50], where they reached $|\Omega/2\pi| = 36$ MHz inside a microwave cavity with a circulating microwave power of several hundreds of kilowatts.

For a thorough comparison between measurement and simulation, the microwave field at many more trap positions should have been measured, which is a very time-consuming task. In the following chapter, I will present a more sophisticated and parallelized method for measuring a microwave near-field distribution and compare it to simulations.
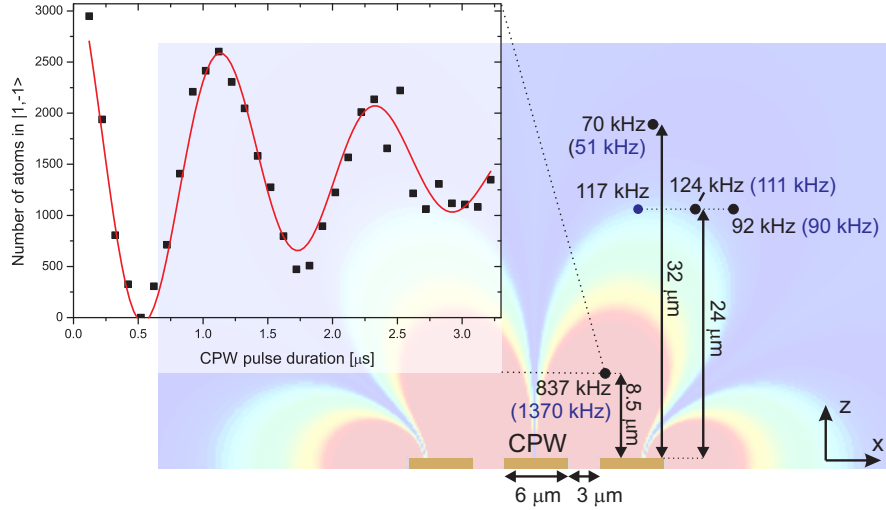
Figure 3.9.1: Measurement of the resonant Rabi frequencies $|\Omega/2\pi|$ at different trap positions. We prepare a BEC containing 3000 atoms in different traps (the calculated trap positions are indicated by the filled circles). In the traps, the static magnetic field is approximately along x. We launch a resonant microwave at frequency $\omega = \omega_-$ ($P_{\mathrm{mw}} = 25\,\mathrm{mW}$) into the single CPW structure and observe resonant Rabi oscillations between states $|1,-1\rangle$ and $|2,-2\rangle$ (see inset). The Rabi oscillations are highly damped because of microwave field gradients across the BEC. The measured Rabi frequencies $|\Omega/2\pi|$ for different trap positions are indicated in black next to the trap. A static simulation of an ideal CPW mode (semi-transparent background) is adjusted by scaling the microwave current amplitude I_{mw}, such that the measured frequency at the trap indicated by the blue filled circle is equal to the measured one (117 kHz). Numbers given in blue correspond to the Rabi frequencies extracted from the simulation. We find rough agreement between measurements and the simulation.

Chapter 4

Imaging of microwave fields using ultracold atoms

When we started using the on-chip CPW structure, we were curious about its microwave near-field distribution, and how well the distribution agrees with what is expected from simulations. First tests, where we measured the microwave Rabi frequency at some points in the CPW near-field with trapped condensates (see Section 3.9) showed some discrepancy between measurements and static simulations, in which we assume a homogeneous CPW mode current distribution on infinitely thin waveguide wires, see Section 2.1.1. Furthermore, the displacement of the atoms observed when applying the state dependent microwave potentials (see next chapter) was not reproduced very well by the simulation. One way to clarify the incongruity would have been to map out the whole microwave near-field with trapped condensates. Recording the whole CPW near-field in that way would have been very time consuming: Each trap has to be simulated, and at least one of the microwave resonance frequencies for the different polarizations has to be adjusted experimentally,[1] since the simulation typically does not predict the magnetic field in the trap center and thereby the transition frequencies sufficiently accurately.

Measuring a microwave near-field distribution of a device is not only relevant for atom chips, but it is also of interest for a broader microwave engineering community. Today, Monolithic Microwave Integrated Circuits (MMICs) are of great importance in science [21, 127] and technology. In particular, they constitute key building blocks of today's communication technology [128]. Function and failure analysis is of crucial importance for the design of MMICs

---

[1] As soon as the resonance frequency for one polarization component is found experimentally, the Zeeman shift is known and the other resonance frequencies can be calculated.
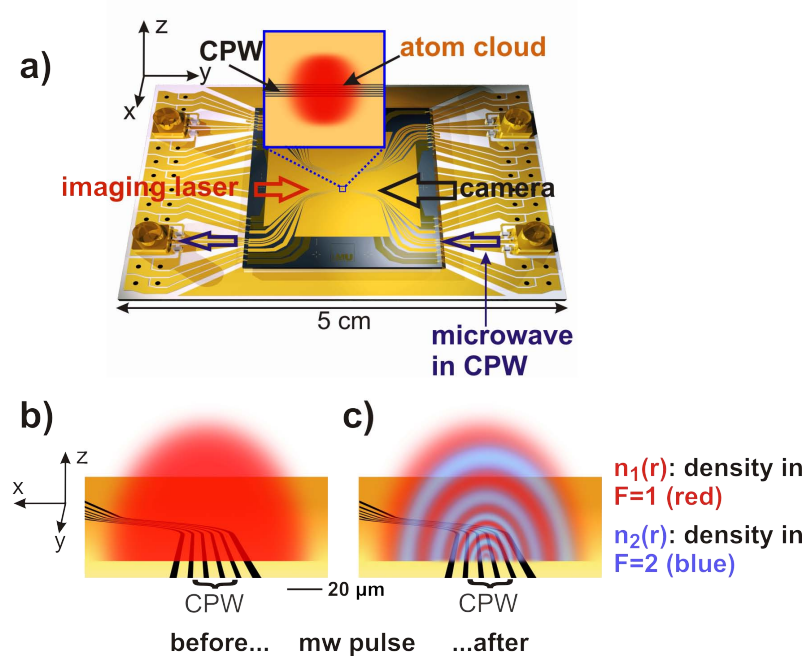
Figure 4.0.1: Illustration of the working principle of the microwave field imaging technique. The description is given in the main text.

as well as for simulation verification [129, 58]. External port measurements (e.g. using a network analyzer) offer only limited insight. The microwave near-field distribution on the device gives much more information, enabling specific improvement. Therefore, different methods have been developed to measure the spatial distribution of microwave near-fields. These methods include electron beam testing [130], photo-emissive probing [130], photo-excitation testing [130], internal and external electro-optic sensing [130, 131], charge density probing [130], electric force microscopy [130, 129], the capacitive coupling method [130], SQUID microscopy [132], modulated scattering probing [133] as well as various pickup devices [134, 135, 136, 137]. All these methods use diverse physical effects to measure the microwave near-field distribution. However, these methods have in common that they use a scanning technique to measure the field distribution point-by-point, which can be a quite time consuming task.

We conceived and implemented a different, parallelized way of mapping out a microwave near-field distribution. It works in the following way: we move a trapped thermal cloud of atoms close to the microwave structure to be characterized. Then the trap is switched off and the atoms are released to free fall. During a hold-off time dt_{ho}, the cloud drops due to gravity and
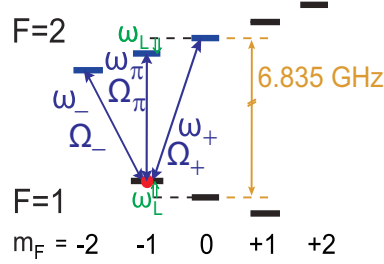
Figure 4.0.2: Ground state hyperfine levels of ^{87}Rb atoms in a static magnetic field. Initially, the atoms are trapped in state $|F, m_F\rangle = |1, -1\rangle$. The three relevant transitions $|1, -1\rangle \leftrightarrow |2, m_2\rangle$, $(m_2 = -2, -1, 0)$ are indicated. The corresponding transition frequencies ω_γ $(\gamma = -, \pi, +)$ are split by ω_L due to the Zeeman Effect. The resonant Rabi frequencies Ω_γ are also indicated.

expands due to its thermal velocity spread, filling the region to be imaged (Figure 4.0.1a+b). We maintain a homogeneous static magnetic field $\mathbf{B}_0$. It provides the quantization axis and splits the hyperfine transition frequencies ω_γ, $(\gamma = -, \pi, +)$ by ω_L, see Figure 4.0.2. A microwave signal on the CPW is subsequently switched on for a duration dt_{mw} (typically some tens of μs). We select one of the transitions by setting the microwave frequency to $\omega = \omega_\gamma$. The microwave magnetic field couples to the atomic magnetic moment and drives Rabi oscillations at frequency $|\Omega_\gamma(\mathbf{r})|$ on the resonant transition, with $|\Omega_\gamma(\mathbf{r})| \propto B_\gamma(\mathbf{r})$, where $B_\gamma(\mathbf{r})$ is the microwave magnetic field polarization component at spatial position $\mathbf{r}$, that drives the transition ω_γ.

After the resonant microwave pulse, a spatial distribution of atomic populations in $F = 1$ and $F = 2$ results, see Figure 4.0.1c. The probability to detect an atom at position $\mathbf{r}$ in $F = 2$ is

$$p_2(\mathbf{r}) \equiv \frac{n_2(\mathbf{r})}{n_1(\mathbf{r}) + n_2(\mathbf{r})} = \sin^2\left[\tfrac{1}{2} |\Omega_\gamma(\mathbf{r})| \, dt_{\mathrm{mw}}\right]. \tag{4.0.1}$$

Here, $n_1(\mathbf{r})$ ($n_2(\mathbf{r})$) is the density of atoms in $F = 1$ ($F = 2$), which can be measured using state-selective absorption imaging [48]. An overview of $p_2(\mathbf{r})$ arising from the different polarization components around our single CPW structure is shown in Figure 4.0.3.

From $p_2(\mathbf{r})$ we can reconstruct $|\Omega_\gamma(\mathbf{r})|$ and thus the spatial distribution of the resonant microwave magnetic field polarization component $B_\gamma(\mathbf{r})$, as shown in Section 4.2 below. In the following section, we derive the relation between $|\Omega_\gamma|$ and B_γ, and show how the relative phases between the microwave polarization components can be reconstructed.
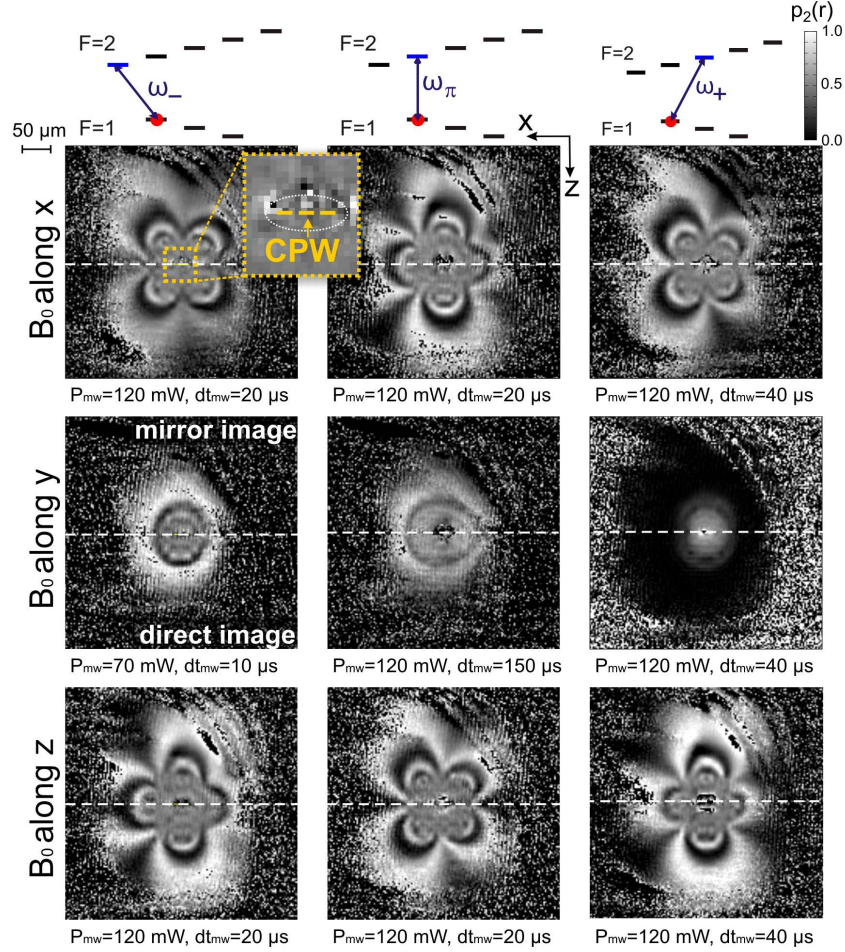
Figure 4.0.3: Imaging of microwave magnetic field components near the single CPW structure. The images show the measured probability $p_2(\mathbf{r})$ to find an atom in $F = 2$ after applying the microwave pulse, see Eq. (4.0.1). Columns correspond to measurements on the three different transitions ω_γ, rows to three different orientations of $\mathbf{B}_0$. The imaging beam is reflected from the chip surface at an angle of $2°$. As a result, on each picture, the direct image and its reflection on the chip surface are visible. The dashed line separates the two. Due to distortions of the imaging beam caused by the CPW, no atoms are visible in the center. The microwave power launched into the CPW, P_{mw}, and the microwave pulse duration dt_{mw} are indicated. dt_{ho} varies between $1 - 2\,\text{ms}$. The noise on the image periphery corresponds to regions without atoms. Images are averaged over several experimental runs (15 to 130).

4.1 Theory

4.1.1 Rabi frequencies Ω_γ

We derive the Rabi frequencies [86] for the resonant coupling of ground state hyperfine levels of ^{87}Rb with a microwave field. In the following, we consider an atom in a weak static magnetic field $\mathbf{B}_0$, so that the Zeeman splitting $\omega_L = \mu_B B_0/2\hbar$ is small compared to the zero-field splitting of $\omega_0 \simeq 2\pi \times 6.8$ GHz between the two hyperfine states $F = 1$ and $F = 2$ of the $5^2 S_{1/2}$ electronic ground state of ^{87}Rb. The atom is initially prepared in the hyperfine sublevel $|F, m_F\rangle = |1, -1\rangle$, and the microwave frequency ω is equal to one of the ω_γ. The real-valued microwave magnetic field at position $\mathbf{r} = (x, y, z)$ in the fixed Cartesian laboratory coordinate system is $\mathbf{B}(\mathbf{r}, t) = \frac{1}{2}\left[\hat{\mathbf{B}}(\mathbf{r})e^{-i\omega t} + \hat{\mathbf{B}}^\star(\mathbf{r})e^{i\omega t}\right]$ with the complex phasor

$$\hat{\mathbf{B}}(\mathbf{r}) \equiv \begin{pmatrix} \hat{B}_x(\mathbf{r})e^{-i\phi_x(\mathbf{r})} \\ \hat{B}_y(\mathbf{r})e^{-i\phi_y(\mathbf{r})} \\ \hat{B}_z(\mathbf{r})e^{-i\phi_z(\mathbf{r})} \end{pmatrix}.$$

Here, we have chosen $\hat{B}_i(\mathbf{r})$, $\phi_i(\mathbf{r}) \in \mathbb{R}_{\geq 0}$, $(i = x, y, z)$.

In the following, we consider a fixed position in space and suppress the dependence of $B_i(\mathbf{r})$ and $\phi_i(\mathbf{r})$ on $\mathbf{r}$ to simplify notation. We apply a homogeneous static magnetic field $\mathbf{B}_0$. For a given $\mathbf{B}_0$, we choose a new Cartesian coordinate system (x', y', z') with the z'-axis pointing along $\mathbf{B_0}$, which defines the quantization axis for the atomic states $|F, m_F\rangle$. In this new coordinate system, the microwave magnetic field phasor is given by

$$\hat{\mathbf{B}} \equiv \begin{pmatrix} \hat{B}_{x'}e^{-i\phi_{x'}} \\ \hat{B}_{y'}e^{-i\phi_{y'}} \\ \hat{B}_{z'}e^{-i\phi_{z'}} \end{pmatrix}.$$

The microwave magnetic field couples to the magnetic moment of the electron spin of the atom. The coupling to the nuclear magnetic moment is neglected, because it is three orders of magnitude smaller than the electron magnetic moment. The Rabi frequency on the hyperfine transition $|1, m_1\rangle \leftrightarrow |2, m_2\rangle$ is given by

$$\Omega_{1,m_1}^{2,m_2} = \frac{2\mu_B}{\hbar}\langle 2, m_2|\hat{\mathbf{B}} \cdot \mathbf{J}|1, m_1\rangle, \tag{4.1.1}$$

with $\mathbf{J} = (J_{x'}, J_{y'}, J_{z'})$ the electron spin operator. Using $J_\pm = J_{x'} \pm iJ_{y'}$ we

can write

$$
\begin{aligned}
\hat{\mathbf{B}} \cdot \mathbf{J} &= \hat{B}_{x'} e^{-i\phi_{x'}} J_{x'} + \hat{B}_{y'} e^{-i\phi_{y'}} J_{y'} + \hat{B}_{z'} e^{-i\phi_{z'}} J_{z'} \\
&= \tfrac{1}{2} \left(\hat{B}_{x'} e^{-i\phi_{x'}} - i\hat{B}_{y'} e^{-i\phi_{y'}} \right) J_+ + \tfrac{1}{2} \left(\hat{B}_{x'} e^{-i\phi_{x'}} + i\hat{B}_{y'} e^{-i\phi_{y'}} \right) J_- \\
&\quad + \hat{B}_{z'} e^{-i\phi_{z'}} J_{z'}.
\end{aligned} \tag{4.1.2}
$$

Evaluating the matrix elements for the three transitions connecting to $|1,-1\rangle$ (see Appendix C), we obtain the Rabi frequencies:

$$
\begin{aligned}
\underline{\Omega_-} &\equiv \Omega^{2,-2}_{1,-1} = \frac{2\mu_B}{\hbar} \langle 2,-2| \frac{1}{2} \left(\hat{B}_{x'} e^{-i\phi_{x'}} + i\hat{B}_{y'} e^{-i\phi_{y'}} \right) J_- |1,-1\rangle \\
&= \underline{-e^{-i\phi_-} \cdot \sqrt{3} \cdot \frac{\mu_B}{\hbar} \hat{B}_-}, \tag{4.1.3}
\end{aligned}
$$

$$
\begin{aligned}
\underline{\Omega_\pi} &\equiv \Omega^{2,-1}_{1,-1} = \frac{2\mu_B}{\hbar} \langle 2,-1| \hat{B}_{z'} e^{-i\phi_{z'}} J_{z'} |1,-1\rangle \\
&= \underline{-e^{-i\phi_\pi} \cdot \sqrt{\frac{3}{4}} \cdot \frac{\mu_B}{\hbar} \hat{B}_\pi}, \tag{4.1.4}
\end{aligned}
$$

$$
\begin{aligned}
\underline{\Omega_+} &\equiv \Omega^{2,0}_{1,-1} = \frac{2\mu_B}{\hbar} \langle 2,0| \frac{1}{2} \left(\hat{B}_{x'} e^{-i\phi_{x'}} - i\hat{B}_{y'} e^{-i\phi_{y'}} \right) J_+ |1,-1\rangle \\
&= \underline{e^{-i\phi_+} \cdot \sqrt{\frac{1}{2}} \cdot \frac{\mu_B}{\hbar} \hat{B}_+}, \tag{4.1.5}
\end{aligned}
$$

where the following definitions are used

$$
\begin{aligned}
\hat{B}_- e^{-i\phi_-} &:= \tfrac{1}{2} \left(\hat{B}_{x'} e^{-i\phi_{x'}} + i\hat{B}_{y'} e^{-i\phi_{y'}} \right), \tag{4.1.6} \\
\hat{B}_\pi e^{-i\phi_\pi} &:= \hat{B}_{z'} e^{-i\phi_{z'}}, \tag{4.1.7} \\
\hat{B}_+ e^{-i\phi_+} &:= \tfrac{1}{2} \left(\hat{B}_{x'} e^{-i\phi_{x'}} - i\hat{B}_{y'} e^{-i\phi_{y'}} \right), \tag{4.1.8}
\end{aligned}
$$

with $\hat{B}_\gamma, \phi_\gamma \in \mathbb{R}_{\geq 0}$, ($\gamma = -, \pi, +$). We note that Ω_π is proportional to the projection of $\hat{\mathbf{B}}$ onto $\mathbf{B}_0$, while $\Omega_{+(-)}$ is proportional to the right (left) handed circular polarization component in the plane perpendicular to $\mathbf{B}_0$.

In the experiment, we choose a sufficiently strong static field B_0 so that $\omega_L \gg \Omega_\gamma$. Furthermore, we choose the microwave frequency resonant with one of the transitions, $\omega = \omega_\gamma$. In this way, Rabi oscillations are induced only on the resonant transition in a given run of the experiment, which allows us to selectively image the individual microwave magnetic field components $\hat{B}_\gamma$. The extraction of the field components from absorption images is described, in Section 4.2 below.

98

4.1.2 Reconstruction of the microwave magnetic field

The amplitudes $\hat{B}_x$, $\hat{B}_y$, and $\hat{B}_z$ of the Cartesian components of $\hat{\mathbf{B}}$ in laboratory coordinates can be easily determined by measuring $|\Omega_\pi|$ with the quantization axis $\mathbf{B}_0/B_0$ pointing along x, y, and z, respectively. In the following, the upper index indicates the direction of the quantization axis in laboratory coordinates, e.g. Ω_-^y ($\hat{B}_-^y$) means Ω_- ($\hat{B}_-$) for $\mathbf{B}_0$ pointing along the y-axis.

To reconstruct the relative phases $(\phi_y - \phi_x)$ and $(\phi_z - \phi_x)$ between the Cartesian components of $\hat{\mathbf{B}}$, we also measure the amplitudes of the circularly polarized components $\hat{B}_+^x$, $\hat{B}_-^x$, $\hat{B}_+^y$, $\hat{B}_-^y$, $\hat{B}_+^z$, and $\hat{B}_-^z$. Having measured these components, we can reconstruct the relative phases according to the following recipe.

$\mathbf{B}_0$ **along** x We choose a coordinate system with z' along x, resulting from the following coordinate transformation:

$$\boxed{\begin{aligned} x' &= -z \\ y' &= y \\ z' &= x \end{aligned}}$$

In this rotated coordinate system, the microwave magnetic field phasor reads

$$\hat{\mathbf{B}} \equiv \begin{pmatrix} \hat{B}_{x'} e^{-i\phi_{x'}} \\ \hat{B}_{y'} e^{-i\phi_{y'}} \\ \hat{B}_{z'} e^{-i\phi_{z'}} \end{pmatrix} = \begin{pmatrix} -\hat{B}_z e^{-i\phi_z} \\ \hat{B}_y e^{-i\phi_y} \\ \hat{B}_x e^{-i\phi_x} \end{pmatrix}.$$

From this we obtain:

$$\boxed{\begin{array}{ccc|ccc} \hat{B}_{x'} &=& \hat{B}_z & \phi_{x'} &=& \phi_z + \pi \\ \hat{B}_{y'} &=& \hat{B}_y & \phi_{y'} &=& \phi_y \\ \hat{B}_{z'} &=& \hat{B}_x & \phi_{z'} &=& \phi_x \end{array}}$$

Using Eqs. (4.1.6) and (4.1.8), we calculate

$$\hat{B}_+^2 - \hat{B}_-^2 = -\hat{B}_{x'} \hat{B}_{y'} \sin(\phi_{y'} - \phi_{x'}). \tag{4.1.9}$$

By insertion of the coordinate transformation and using Eqs. (4.1.3) - (4.1.5), we obtain

$$\sin(\phi_z - \phi_y) = \frac{\hbar}{4\mu_B^2 \hat{B}_z \hat{B}_y} \left(\frac{4}{3} |\Omega_-^x|^2 - 8|\Omega_+^x|^2 \right) = \frac{1}{\hbar \hat{B}_y \hat{B}_z} \left((\hat{B}_-^x)^2 - (\hat{B}_+^x)^2 \right). \tag{4.1.10}$$

B$_0$ along y   A similar calculation as before yields

$$\sin\left(\phi_x - \phi_z\right) = \frac{\hbar}{4\mu_B^2 \hat{B}_x \hat{B}_z} \left(\frac{4}{3}|\Omega_-^y| - 8|\Omega_+^y|^2\right) = \frac{1}{\hbar \hat{B}_x \hat{B}_z}\left((\hat{B}_-^y)^2 - (\hat{B}_+^y)^2\right).$$
(4.1.11)

B$_0$ along z   In this case, we obtain

$$\sin\left(\phi_y - \phi_x\right) = \frac{\hbar}{4\mu_B^2 \hat{B}_x \hat{B}_y} \left(\frac{4}{3}|\Omega_-^z| - 8|\Omega_+^z|^2\right) = \frac{1}{\hbar \hat{B}_x \hat{B}_y}\left((\hat{B}_-^z)^2 - (\hat{B}_+^z)^2\right).$$
(4.1.12)

All quantities on the right hand sides of Eqs. (4.1.10) - (4.1.12) can be measured. From Eqs. (4.1.10) - (4.1.12), the relative phases $(\phi_y - \phi_x)$ and $(\phi_z - \phi_x)$ can be determined. The solution is unique except for the very degenerate case where $\sin\left(\phi_x - \phi_z\right) = \sin\left(\phi_y - \phi_x\right) = \sin\left(\phi_z - \phi_y\right) = 0$. In this case, there are 4 solutions which cannot be distinguished. The absolute microwave phase distribution can be reconstructed using an interferometric method as described in Section 4.5 below.

4.2   Data extraction methods

In the beginning of this chapter, I discussed that the spatial probability $p_2(\mathbf{r})$ of finding an atom at position $\mathbf{r}$ in state $F = 2$ can be measured. From $p_2(\mathbf{r})$, we can calculate $|\Omega_\gamma(\mathbf{r})|$ by inverting Eq. (4.0.1) unambiguously only if $|\Omega_\gamma(\mathbf{r})|\, dt_{\mathrm{mw}} \leq \pi$ everywhere. For $|\Omega_\gamma(\mathbf{r})|\, dt_{\mathrm{mw}} > \pi$, there is no unique solution (see Figure 4.2.1b). We have developed two methods, the *ray-tracing method* and the *movie method*, to determine $|\Omega_\gamma(\mathbf{r})|$ uniquely.

4.2.1   Ray-tracing method

In the ray-tracing method, the calculation of $|\Omega_\gamma(\mathbf{r})|$ up to an offset $n{\cdot}2\pi/dt_{\mathrm{mw}}$ depends on whether $p_2(\mathbf{r})$ is on the falling or rising slope with respect to P_{mw} (with dt_{mw} fixed) or dt_{mw} (with P_{mw} fixed), see illustration in Figure 4.2.1. The calculation works in the following way: On the image of $p_2(\mathbf{r})$, we send rays from the image periphery (where $|\Omega_\gamma|\, dt_{\mathrm{mw}} \ll 1$ and $n = 0$) through the point of interest $\mathbf{r}$ to the center of the microwave structure (where $|\Omega_\gamma|$ is maximal). We count the number of minima and maxima of $p_2(\mathbf{r})$ encountered on the ray. Each time the ray passes a maximum plus a minimum, n increases by one. If on the way from the periphery to the point $\mathbf{r}$ the last extremum was a maximum, we are on a falling slope, otherwise we are on a rising one.
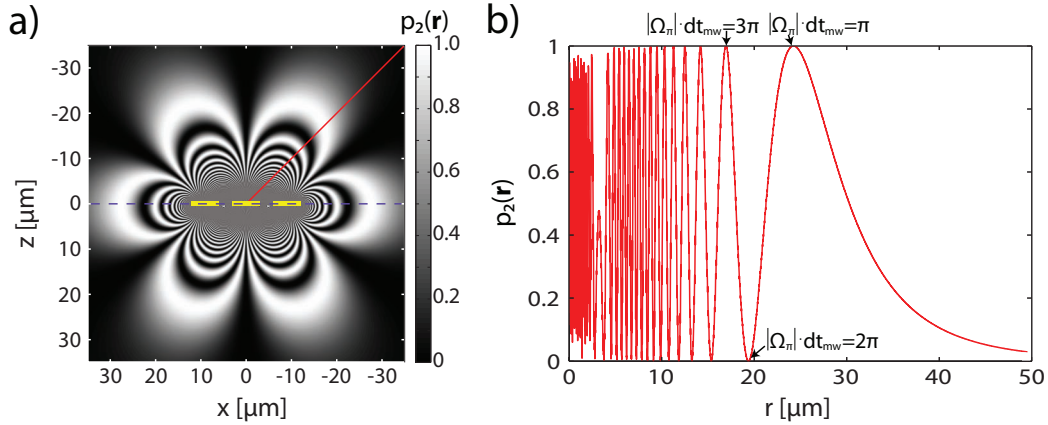
Figure 4.2.1: Illustration of the ray-tracing method. (a) Simulation of the distribution $p_2(\mathbf{r})$ around the CPW (indicated in yellow, calculated with a static simulation for a perfect CPW mode on the waveguide wires) for $\mathbf{B}_0$ along z and $\omega = \omega_\pi$. The simulation shows what corresponds to the direct image (below) as well as the mirror image on the chip (above). The blue dashed line separates the two (cf. Figure 4.0.3). A sample ray (see text) is indicated in red. (b) $p_2(\mathbf{r})$ on the ray indicated in a). $r = 0$ corresponds to the center of the CPW structure. By inverting Eq. (4.0.1), $|\Omega_\pi|$ cannot be calculated unambiguously. By counting the numbers of minima and maxima on the ray (counted from outside, where $|\Omega_\pi(r)| \cdot dt_{\mathrm{mw}} \ll 1$) and by tracking the slope on the ray, $|\Omega_\pi(r)|$ can be calculated uniquely, see main text. The small peak around $r = 4\,\mu\mathrm{m}$ is caused by the ray being tangent to an isopotential line of $p_2(\mathbf{r})$.

We calculate for the case of a rising slope:

$$|\Omega_\gamma(\mathbf{r})|_{\mathrm{rising}} = \frac{2}{dt_{\mathrm{mw}}} \arcsin\left(\sqrt{p_2(\mathbf{r})}\right) + n\frac{2\pi}{dt_{\mathrm{mw}}}, \tag{4.2.1}$$

whereas in the case of a falling slope

$$|\Omega_\gamma(\mathbf{r})|_{\mathrm{falling}} = (n+1)\frac{2\pi}{dt_{\mathrm{mw}}} - \frac{2}{dt_{\mathrm{mw}}} \cdot \arcsin\left(\sqrt{p_2(\mathbf{r})}\right). \tag{4.2.2}$$

The ray-tracing process is illustrated in Figure 4.2.2.
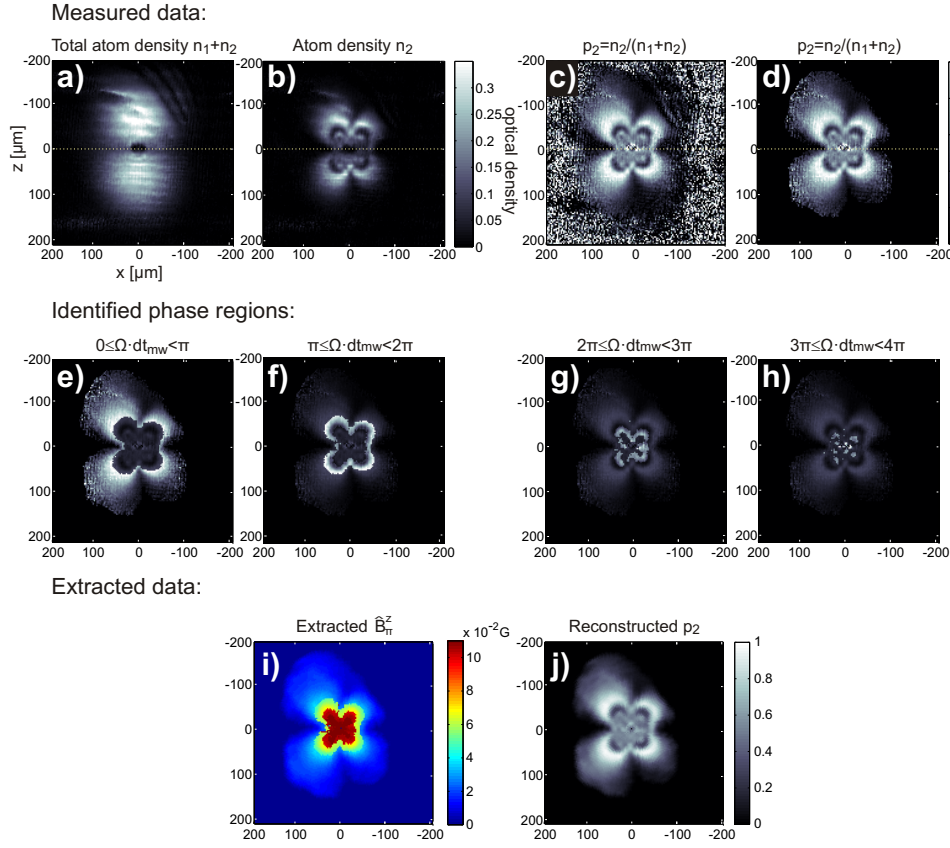
Figure 4.2.2: Demonstration of the ray-tracing method, here for the distribution of $\hat{B}^z_\pi(\mathbf{r})$. We take at least one image of the total atom number distribution $n_1(\mathbf{r}) + n_2(\mathbf{r})$, see panel (a), and of the number of atoms in $F = 2$, $n_2(\mathbf{r})$, see panel (b). From these we can calculate $p_2(\mathbf{r}) = \frac{n_2(\mathbf{r})}{n_1(\mathbf{r})+n_2(\mathbf{r})}$, panel (c), and remove the regions without atoms (d), because they disturb the peak finding algorithm. We send rays from the periphery to the center of the structure and identify the different positive and negative slope regions on $p_2(\mathbf{r})$ as well as their value of n. The different recognized slope regions for $n = 0$ (e,f) and $n = 1$ (g,h) are highlighted. Due to dephasing across a pixel caused by the strong near-field gradients, the proper recognition of the different slope regions complicates with increasing values of n. This problem could be avoided e.g. by taking two images with different dt_{mw}, one with small dt_{mw} for the region close to the CPW, and one with larger dt_{mw} for the outer regions. Using Eqs. (4.2.1) and (4.2.2) we calculate $\hat{B}^z_\pi(\mathbf{r})$ as shown in panel (i). From the reconstructed $\hat{B}^z_\pi(\mathbf{r})$ we again calculate $p_2(\mathbf{r})$ as shown in panel (j). Note that the reconstructed field corresponds to the same component that is shown in Figure 4.2.1 for an ideal CPW mode. The horizontal side lobes cannot be recognized because there are too few atoms in the respective regions.

103
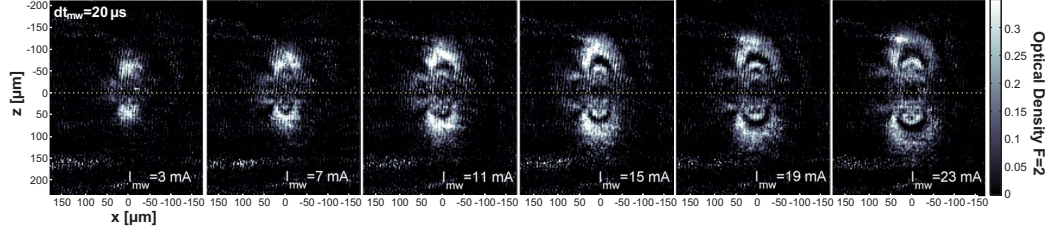
Figure 4.2.3: Imaging of $\hat{B}_\pi^x(\mathbf{r})$ using the movie method. We take series of k images, scanning either P_mw and/or dt_mw. Here, we only scan P_mw (and thereby I_mw) while keeping $dt_\mathrm{mw} = 20\,\mu$s fixed. From the images, we extract $\hat{B}_\pi^x(\mathbf{r})$ as described in the main text.

4.2.2 Movie method

In the movie method, we take series of k images, scanning either the microwave power P_mw and/or dt_mw, see Figure 4.2.3. k depends on the desired dynamic range, but can be as low as 10. The lowest value of P_mw and dt_mw should be such that $|\Omega_\gamma|\,dt_\mathrm{mw} \ll 1$ in the region of interest. For each image pixel, we thus obtain a sequence of k data points showing Rabi oscillations, see Figure 4.2.4a. We fit a function $\propto \sin^2\left[\frac{1}{2}\,|\Omega_\gamma(P_\mathrm{mw})|\,dt_\mathrm{mw}\right]$ to the data, where $|\Omega_\gamma(P_\mathrm{mw})| = a\sqrt{P_\mathrm{mw}}$, and a is the fit parameter. From the fit, we determine $|\Omega_\gamma(P_\mathrm{mw})|$ and thus via Eqs. (4.1.3) - (4.1.5), $\hat{B}_\gamma$ at this pixel for a given P_mw. As an example, Figure 4.2.4b shows an image of the Cartesian microwave field component $\hat{B}_x(\mathbf{r})$ near our on-chip CPW reconstructed in this way. We find that the fits can be improved by adding an exponential decay to the fit function, which accounts for dephasing due to microwave field gradients across the pixel or the optical resolution of the imaging system, whatever is greater.

4.2.3 Comparison between both extraction methods

Using the ray-tracing method, it is in principle possible to extract the microwave magnetic field distribution for one component $\hat{B}_\gamma$ using just one image of $n_2(\mathbf{r})$ and $n_1(\mathbf{r}) + n_2(\mathbf{r})$. To improve the data quality, we average over several images of $n_2(\mathbf{r})$ and $n_1(\mathbf{r}) + n_2(\mathbf{r})$.[2] A reliable recognition of the minima and maxima on a ray is not trivial. To improve the determination of minimas and maximas on a ray, we use smoothing and anti-aliasing[3] algo-

---

[2]In our experiment, the time to record one frame is 14 s, but could be reduced to below 3 s [33].

[3]In anti-aliasing, not just one but several rays are sent out, having a small divergence. This is a well-known method e.g. in computer graphics rendering, which avoids staircase-
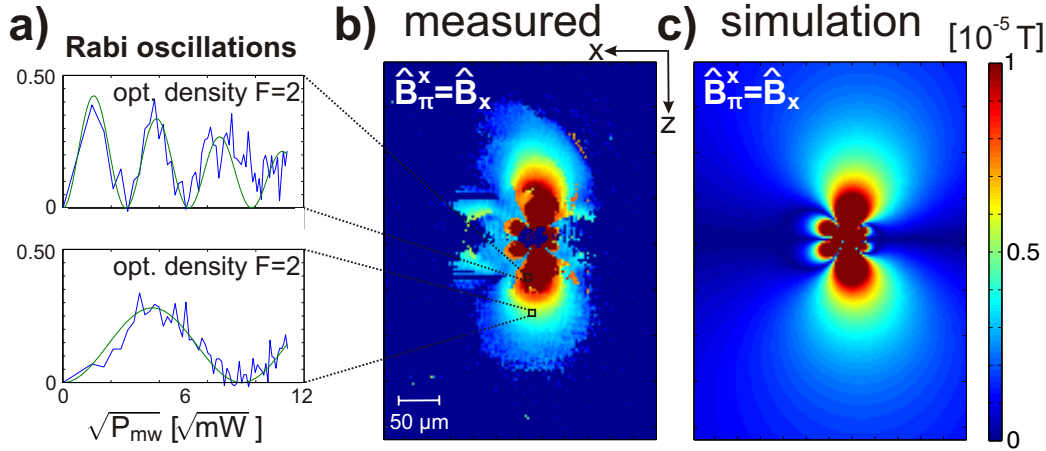
Figure 4.2.4: Movie method extraction of the microwave magnetic field component $\hat{B}_x(\mathbf{r})$ in the vicinity of the CPW and comparison to a simulation. The measurement is performed with $\omega = \omega_\pi$ and $\mathbf{B}_0$ along x. (a) Rabi-oscillations at two exemplary pixels of the image, recorded by varying P_{mw} at fixed $dt_{\mathrm{mw}} = 20\,\mu$s. The sinusoidal fits used to determine $|\Omega_\pi^x|$ and thus $\hat{B}_\pi^x$ as a function of $\sqrt{P_{\mathrm{mw}}}$ are shown. The observed decay of the oscillations is due to microwave field gradients across the pixel. (b) Image of $\hat{B}_\pi^x(\mathbf{r})$ at $P_{\mathrm{mw}} = 120\,$mW as obtained from the data. (c) Corresponding adjusted static simulation of $\hat{B}_\pi^x(\mathbf{r})$, which reproduces the measured field distribution best, see Section 4.3.

rithms in order not to mistake noise (like imaging or projection noise) as a minimum or maximum. This is a delicate task, because smoothing must not be too strong in order not to smooth out a true extremum. Furthermore, for the microwave near-field of complex structures, it might not be sufficient to send rays from all directions to the same center because there could be local extrema of the field.

Using the movie method on the other hand, we always need several images, but the data fitting procedure is relatively robust, as long as good starting values for the curve fitting are provided. In addition, with the movie method we typically achieve a higher dynamical range than with the ray-tracing procedure (see Figure 4.2.5). Therefore, for most tasks the movie method is more favorable than the ray-tracing method.

---

like sampling artifacts.
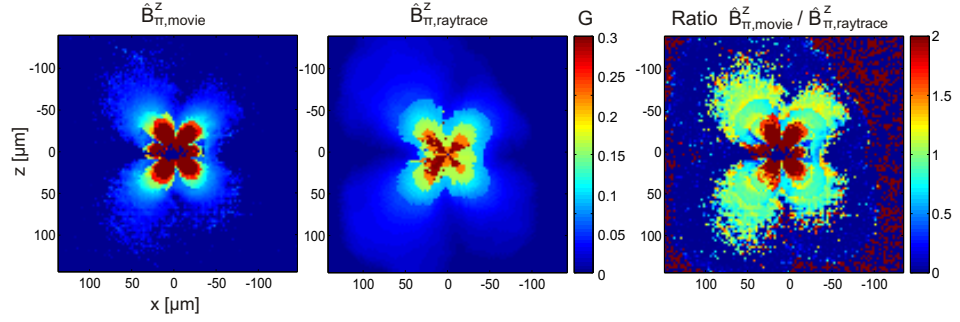
Figure 4.2.5: Comparison of the microwave magnetic field amplitudes $\hat{B}_\pi^z$ extracted using the movie method (left) and the ray-tracing method (center). The movie data is extracted from 25 shots with $P_{\mathrm{mw,i}} = (i+1) \times 1\,\mathrm{mW}$ and $dt_{\mathrm{mw}} = 20\,\mu\mathrm{s}$, while the ray-tracing data is extracted from the average of 60 shots imaging $n_2(\mathbf{r})$ and $n_1(\mathbf{r}) + n_2(\mathbf{r})$, at $P_{\mathrm{mw}} = 50\,\mathrm{mW}$ and $dt_{\mathrm{mw}} = 10\,\mu\mathrm{s}$. The plots shown are scaled to $\widetilde{P}_{\mathrm{mw}} = 120\,\mathrm{mW}$ for better comparison with Section 4.3. In the right panel, the ratio of the extracted magnetic fields is shown. In the outer regions, the extracted values from both methods agree very well. One can still recognize discontinuities from the ray-tracing method arising from the different recognized slope regions. In the center, where $\hat{B}_\pi^z$ is maximal, the data quality for both methods is not very good because of dephasing across the optical resolution caused by the strong microwave field gradient (pixel size 2.7 μm, optical resolution 10 μm in this set of measurements). In the case of the movie method, this causes strong damping of the sine oscillations which complicates the fitting, while for the ray-tracing method, it becomes increasingly difficult to properly determine $p_2(\mathbf{r})$ as well as the slope and the offset n of $|\Omega_\gamma(\mathbf{r})|$, see Eqs. (4.2.1) and (4.2.2).

4.2.4 Consistency check for extracted fields

It is possible to derive relations between the field components that allow one to check for validity of the extracted data. E.g. from Eqs. (4.1.6) and (4.1.8), one can derive the relation

$$\left(\hat{B}_{-}^{z'}\right)^2 + \left(\hat{B}_{+}^{z'}\right)^2 = \frac{1}{2}\left(\left(\hat{B}_{\pi}^{x'}\right)^2 + \left(\hat{B}_{\pi}^{y'}\right)^2\right) = \frac{1}{2}\left(\hat{B}_{x'}^2 + \hat{B}_{y'}^2\right). \qquad (4.2.3)$$

Using Eqs. (4.1.3) - (4.1.5) this can also be written as

$$\left|\Omega_{-}^{z'}\right|^2 + 6\left|\Omega_{+}^{z'}\right|^2 = 2\left|\Omega_{\pi}^{x'}\right|^2 + 2\left|\Omega_{\pi}^{y'}\right|^2. \qquad (4.2.4)$$

We test a subset of the movie-extracted data using Eq. (4.2.3), with $z' \equiv x$, $x' \equiv -z$ and $y' \equiv y$. The results are shown in Figure 4.2.6. We find that the extracted data reproduces Eq. (4.2.3) to within $\pm 25\%$ in regions with $|z| > 20\,\mu$m and which are well covered by atoms. More towards the center dephasing due to microwave field gradients across the optical resolution of $10\,\mu$m becomes strong and fitting is very difficult.

4.2.5 3D imaging

This near-field imaging technique can be extended to measure 3D distributions of $\hat{B}_\gamma(\mathbf{r})$ slice by slice, either by using a gradient of $B_0(\mathbf{r})$ such that only a slice of atoms is resonant with ω, or by using a light sheet detection technique [138], where slices perpendicular to the camera line of sight are imaged.

A further variant is to shape an atomic cloud either in the spatial atom number distribution or in the spatial hyperfine state population, prior to applying the microwave pulse, such that the atoms only undergo Rabi oscillations within a defined layer.

4.3 Characterization of the on-chip CPW

In this section, I exemplarily extract the microwave magnetic field components $\hat{B}_\pi^x(\mathbf{r})$ and $\hat{B}_\pi^z(\mathbf{r})$ around our single CPW structure with the movie method, and compare them to simulations (see Figures 4.3.1 - 4.3.3). In this way, the microwave current distribution on the atom chip wires, including induced currents in the metalization nearby, can be reconstructed.
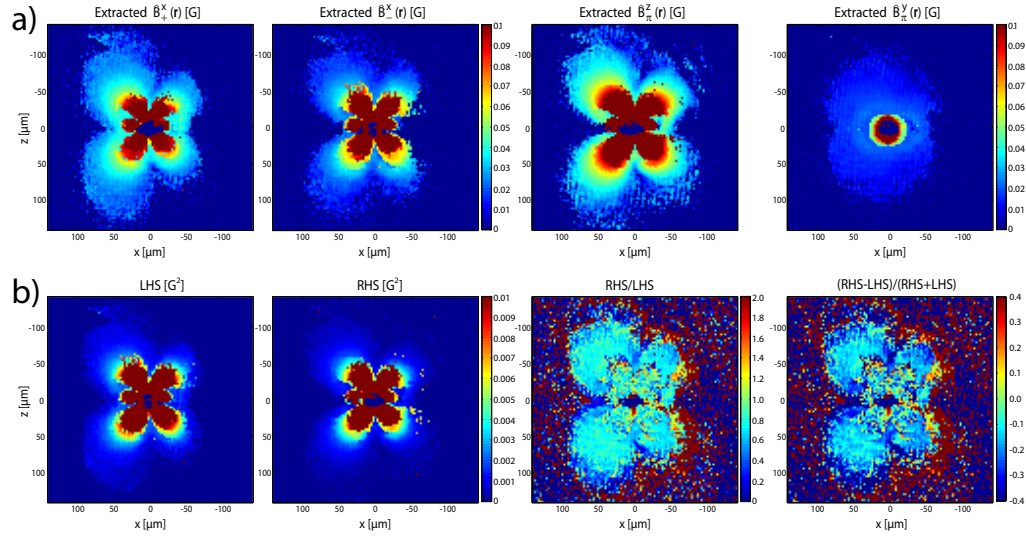
Figure 4.2.6: Consistency check for the data extracted using the movie method (reconstructed using 50 frames each). (a) Map of the extracted microwave magnetic field polarization components. In the center of the plots, near the CPW, microwave field gradients across the optical resolution lead to strong dephasing, which makes curve fitting very difficult. Therefore, for pixels whose fitted Rabi oscillation amplitude falls below a threshold, the magnetic field at the corresponding pixel is set to zero. (b) Calculation of the left-hand-side (LHS) and right-hand-side (RHS) of Eq. (4.2.3), as well as the ratio RHS/LHS and the normalized difference between RHS and LHS, (RHS − LHS)/(RHS + LHS). Regions which are well covered with atoms and where $|z| > 20\,\mu$m exhibit a normalized difference mostly below 25%.

Ideal CPW current distribution. We find that the measured field distributions $\hat{B}_\pi^x(\mathbf{r})$ and $\hat{B}_\pi^z(\mathbf{r})$ (Figure 4.3.1 left) do not agree with a static simulation for an ideal CPW mode (homogeneous planar currents I_{mw} on the signal wire and $-I_{\mathrm{mw}}/2$ on both grounds), see middle and right of Figure 4.3.1. The measured distribution extends much more along z than it does in the simulation.

Sonnet simulated current distribution. A refinement for the simulation drops the assumption of perfect and homogeneous CPW mode currents and uses the current distribution from Sonnet for the same structure (see Figure 4.3.2). Sonnet's current distribution shows induced currents in both DC wires next to the CPW grounds as well as currents induced in the lower wire layer. Interestingly, currents in a cut along x do not sum up to zero, which we attribute to surface charges due to the non-translational invariant structure.

The simulated fields with the current distribution from Sonnet ($I_{\mathrm{mw}} = 62\,\mathrm{mA}$) and comparison to the measurements are shown in the first two columns of Figure 4.3.3. We find that the current distribution from Sonnet reproduces the extracted fields much better than the perfect CPW mode before. Sonnet's current distribution produces microwave fields which extend much more along z, similar to the measured fields. Furthermore, the simulated field shows also a slight left/right asymmetry in $\hat{B}_\pi^x$, which is however less pronounced than what we measure. The origin of this asymmetry in the simulation is the asymmetry of the currents induced in the lower layer of the chip.

Adjusted static model. We adjust our static model to reproduce the measured fields as good as possible. The results are shown in the last two columns of Figure 4.3.3. We set the currents on the wires in the upper layer (including both DC wires next to the CPW) to the integrated values from Sonnet and allow for a 10% asymmetry in the currents in the wires left of the signal wire relative to those right of it (see top of third column in Figure 4.3.3). The results are shown in the third and fourth column of Figure 4.3.3. With this adjustment, we find the best agreement between measurements and simulation.
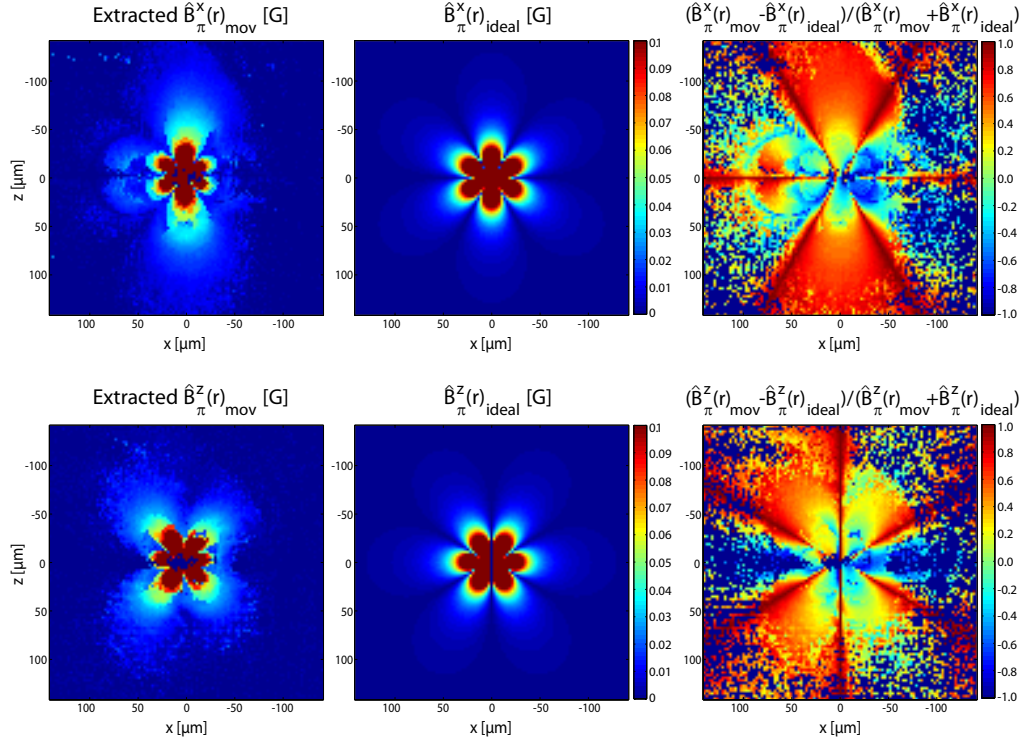
Figure 4.3.1: Measurements of $\hat{B}_\pi^x(\mathbf{r})$ and $\hat{B}_\pi^z(\mathbf{r})$ and comparison to a static simulation. The first column shows the measured values for $\hat{B}_\pi^x(\mathbf{r})$ and $\hat{B}_\pi^z(\mathbf{r})$, reconstructed with the movie method (using 50 frames each). The plots show the microwave magnetic field for $\widetilde{P}_{\mathrm{mw}} = 120\,\mathrm{mW}$. The field distribution for a perfect CPW mode, calculated with a static simulation, is shown in the center column ($I_{\mathrm{mw}} = 62\,\mathrm{mA}$ on the signal wire and $-I_{\mathrm{mw}}/2$ on each of both grounds). The rightmost column displays the normalized difference of the extracted microwave field and the simulated one. One can clearly recognize that the simulated field distribution does not adequately reproduce the measurements if one assumes an ideal CPW mode.
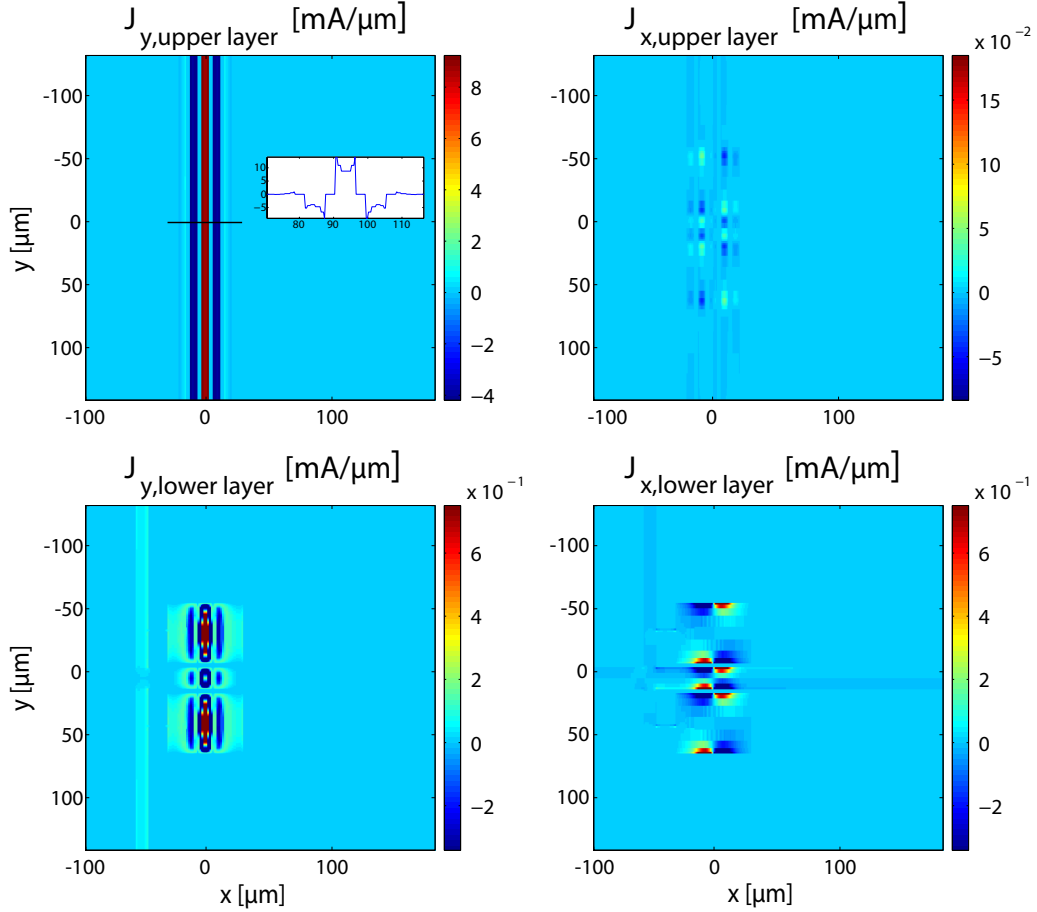
Figure 4.3.2: Illustration of the extracted current distribution from Sonnet. The upper row shows the current density in the upper layer of metalization (left: currents along y, right: along x), the lower row shows the currents in the lower layer. The inset in the upper left plot shows a cut along the black line indicated. The integrated current on the signal wire is equal to $I_{\mathrm{mw}} = 62\,\mathrm{mA}$.
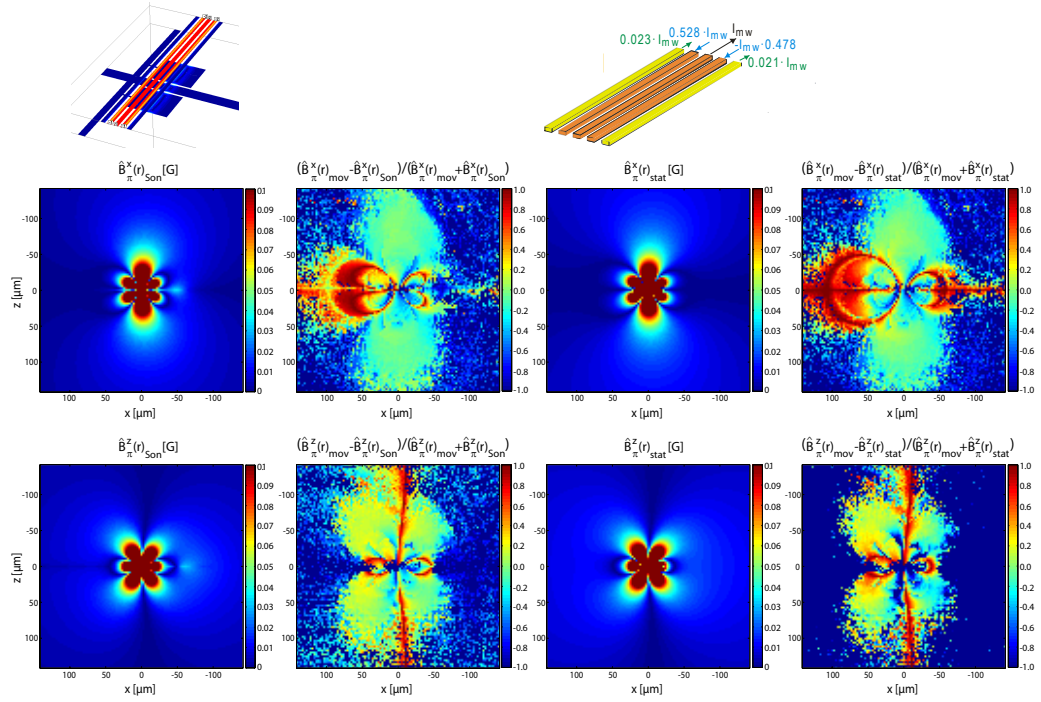
Figure 4.3.3: Comparison of the simulated microwave field distribution using Sonnets current distribution $\hat{B}^i_{\pi,\mathrm{Son}}$ to the one measured with the movie method $\hat{B}^i_{\pi,\mathrm{mov}}$ (left) and comparison to an adjusted static simulation $\hat{B}^i_{\pi,\mathrm{stat}}$ (right). The (integrated) current on the signal wire is equal to $I_{\mathrm{mw}} = 62\,\mathrm{mA}$. The description is given in the text.

4.4   Characterization of the microwave horn

This field imaging technique can also be used to characterize the field homogeneity from the microwave horn (that is used for internal state manipulation) at the position of the atoms. We release a cloud of atoms in state $|1\rangle$, while maintaining a magnetic field $\mathbf{B}_0 = 1.1\,\mathrm{G}$ along z. After waiting for $dt_{\mathrm{ho}} = 2.35\,\mathrm{ms}$ for the atom cloud to expand, we shine in a $40\,\mu\mathrm{s}$ pulse at frequency $\omega = \omega_+$ at a power of 1 W, that partly transfers the atoms to $|2, 0\rangle$. The atoms in $F = 2$ are then detected using state-selective absorption imaging. The result is shown in Figure 4.4.1. We do not observe a homogeneous field distribution, instead we find a nearly circularly symmetric intensity gradient, which is centered around the on-chip CPW. The observed field distribution is not primarily due to microwave power coupled into the CPW modes, as the coupling between the horn and the CPW is much too weak (see measurement in Section 3.3.2) and the measured field distribution corresponds to neither of both CPW modes. It is not entirely clear where the microwave currents are induced, but we speculate that currents induced in the gold mirrors on the chip may be involved in addition to currents on the CPW wires.

The field gradient results in spatial modulation of the Rabi oscillation frequencies for internal state manipulation. However, this modulation is still weak enough such that high contrast Rabi oscillations can be driven, see next chapter.

4.5   Reconstruction of the absolute microwave phase

While Section 4.1.2 describes the reconstruction of the relative phases $(\phi_y - \phi_x)$ and $(\phi_z - \phi_x)$ between the Cartesian components of $\hat{\mathbf{B}}$, it is also possible to reconstruct the spatial dependence of the global phase of $\hat{\mathbf{B}}$ using a Ramsey-type scheme. The procedure uses two microwave pulses. During the whole sequence, $\mathbf{B}_0$ remains constant. In the following, we assume $\mathbf{B}_0$ is pointing along the x-axis, so that $\phi_x(\mathbf{r})$ is measured. The other two phases, $\phi_y(\mathbf{r})$ and $\phi_z(\mathbf{r})$, can then be determined from the already known relative phases.

After releasing the atoms from the trap, they are prepared in an equal superposition of states $|1, -1\rangle$ and $|2, -1\rangle$ by application of a $\frac{\pi}{2}$-pulse at frequency $\omega = \omega_\pi$. This microwave pulse is applied from a well-characterized source, so that it has negligible (or at least known) intensity gradients and negligible (or known) phase gradients across the atomic cloud. This can be
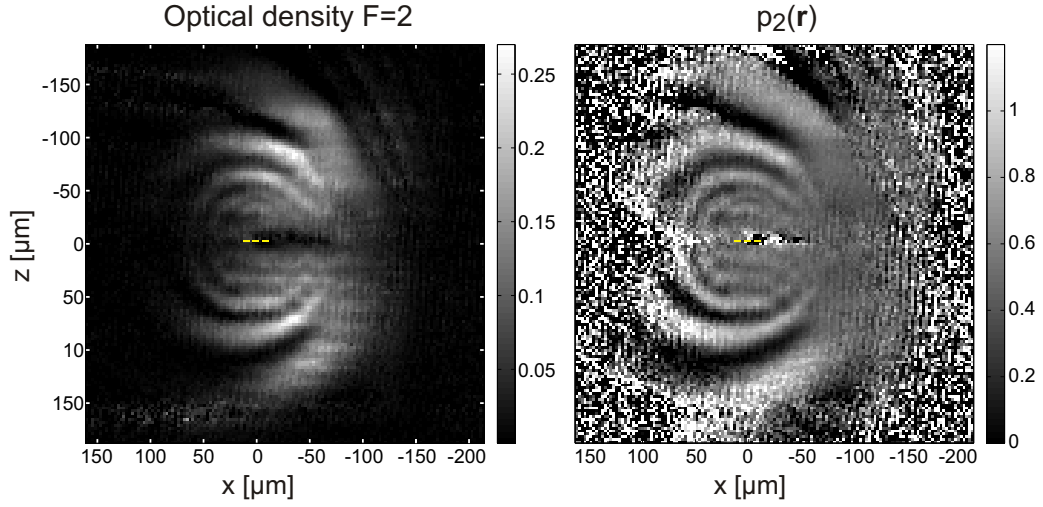
Figure 4.4.1: Distribution of Rabi frequencies $\Omega_+^z(\mathbf{r})$ from the microwave horn at the position of the atoms. See main text for the description of the experimental procedure. The left panel shows a measurement of $n_2(\mathbf{r})$, while in the right, a measurement of $p_2(\mathbf{r})$ is displayed. $n_2(\mathbf{r})$ and $n_1(\mathbf{r})$ are the average of 50 experimental runs. The CPW is indicated in yellow in both plots.

achieved by using an external microwave horn[4] [21]. The duration of the pulse is $dt_{\mathrm{mw},1} = \frac{\pi}{2|\Omega_{\pi,1}|}$, where $\Omega_{\pi,1} = |\Omega_{\pi,1}| \, e^{i\phi_{\pi,1}}$ is the Rabi frequency for the pulse. The state after this preparation pulse is (in the rotating wave approximation) [92]

$$|\psi_1\rangle = \tfrac{1}{\sqrt{2}} \left(|1,-1\rangle + i e^{-i\phi_{\pi,1}} |2,-1\rangle \right). \qquad (4.5.1)$$

Immediately after the end of this preparation pulse, the microwave in the device to be characterized is pulsed on at frequency $\omega_{\mathrm{mw},2} = \omega_\pi$ for a duration $dt_{\mathrm{mw},2}$. The Rabi frequency and phase of this second microwave pulse are denoted by $\Omega_{\pi,2}(\mathbf{r})$ and $\phi_{\pi,2}(\mathbf{r})$, respectively. After the second pulse, the state of an atom at position $\mathbf{r}$ is

$$
\begin{aligned}
|\psi_2(\mathbf{r})\rangle &= \tfrac{1}{\sqrt{2}} \left[\cos\left(\tfrac{|\Omega_{\pi,2}(\mathbf{r})| dt_{\mathrm{mw},2}}{2}\right) - e^{i\phi_{\pi,2}(\mathbf{r}) - i\phi_{\pi,1}} \sin\left(\tfrac{|\Omega_{\pi,2}(\mathbf{r})| dt_{\mathrm{mw},2}}{2}\right) \right] |1,-1\rangle \\
&+ \tfrac{i}{\sqrt{2}} \left[e^{-i\phi_{\pi,1}} \cos\left(\tfrac{|\Omega_{\pi,2}(\mathbf{r})| dt_{\mathrm{mw},2}}{2}\right) + e^{-i\phi_{\pi,2}(\mathbf{r})} \sin\left(\tfrac{|\Omega_{\pi,2}(\mathbf{r})| dt_{\mathrm{mw},2}}{2}\right) \right] |2,-1\rangle.
\end{aligned}
$$

The probability $p_2(\mathbf{r})$ of finding an atom at position $\mathbf{r}$ in state $F = 2$ is given

---

[4]I assume that the coupling into the microwave structure observed in the previous section can be calibrated out.

114

by

$$p_2(\mathbf{r}) = \frac{1}{2} + \frac{1}{2}\sin\left(|\Omega_{\pi,2}(\mathbf{r})|\, dt_{\mathrm{mw},2}\right) \cdot \cos\left(\phi_{\pi,1} - \phi_{\pi,2}(\mathbf{r})\right) \qquad (4.5.2)$$

To calculate $\phi_{\pi,2}(\mathbf{r})$, the quantities $|\Omega_{\pi,2}(\mathbf{r})|$ and $\phi_{\pi,1}$ have to be known. $|\Omega_{\pi,2}(\mathbf{r})|$ can be measured as described in Section 4.2. If $\mathbf{B}_0$ is pointing along the x-axis, then $\phi_x(\mathbf{r}) \equiv \phi_{\pi,2}(\mathbf{r})$.

The calculation above assumes that there is zero delay between the end of the first preparation pulse and the second microwave pulse. A similar calculation is also possible for non-zero delay between the two pulses.

4.6 Sensitivity and spatial resolution

In this section I estimate the maximum sensitivity of this technique for our set of experimental parameters. The microwave magnetic field sensitivity is mainly determined by the interaction time dt_{mw} of the atoms with the microwave pulse. A longer interaction time dt_{mw} leads to a higher microwave magnetic field sensitivity, because then a weaker microwave field can already drive a substantial fraction of a Rabi cycle. However, at the same time the effective spatial resolution $s_{\mathrm{eff}} \equiv 2\sigma_{\mathrm{eff}}$ decreases as the image blurs due to the movement of the atoms during dt_{mw}. In the following, the symbol σ always refers to an r.m.s. width. σ_{eff} is determined by the average moving distance σ_{mw} of the atoms during the microwave pulse, by the optical resolution of the imaging system $s_{\mathrm{opt}} \equiv 2\sigma_{\mathrm{opt}}$, and by the movement of the atoms during the imaging laser pulse, where thermal motion (σ_{tm}) and diffusive motion due to photon scattering (σ_{ps}) contribute. In the following, we will calculate σ_{mw}, σ_{tm}, σ_{ps}, and σ_{eff}.

Movement of atoms during the microwave pulse - σ_{mw}

A free-falling atom in a cloud at temperature T has a mean thermal velocity perpendicular to the line of sight of $v_{\mathrm{th}} = \sqrt{\frac{2k_B T}{m}}$ [1]. After releasing the atom from the trap and waiting for dt_{ho}, the atom has furthermore acquired a velocity $v_g = g \cdot dt_{\mathrm{ho}}$ along the direction of gravity. During the interaction with the microwave for a time dt_{mw}, the atom moves ballistically by an average distance

$$\sigma_{\mathrm{mw}} = g \cdot dt_{\mathrm{ho}} \cdot dt_{\mathrm{mw}} + \frac{1}{2}g \cdot dt_{\mathrm{mw}}^2 + \sqrt{\frac{2k_B T}{m}}dt_{\mathrm{mw}} \qquad (4.6.1)$$

For $T = 5\,\mu K$, $dt_{\mathrm{ho}} = 0$, and $dt_{\mathrm{mw}} = 80\,\mu\mathrm{s}$ we obtain $\sigma_{\mathrm{mw}} = 2.5\,\mu\mathrm{m}$. For short times, the last term in the equation above dominates (as it is the case

for our parameters). The displacement of the atoms during the microwave pulse can then be approximated by a Gaussian function f_{mw} of r.m.s. width σ_{mw}.

Movement of atoms during the imaging pulse - σ_{tm}

During the imaging pulse of duration dt_{im}, the atoms move ballistically by an average distance σ_{tm} given by

$$\sigma_{\mathrm{tm}} = g(dt_{\mathrm{ho}} + dt_{\mathrm{mw}})dt_{\mathrm{im}} + \frac{1}{2}g \cdot dt_{\mathrm{im}}^2 + \sqrt{\frac{2k_B T}{m}} \cdot dt_{\mathrm{im}} \qquad (4.6.2)$$

due to gravity and thermal motion. For $dt_{\mathrm{im}} = 40\,\mu\mathrm{s}$ we get $\sigma_{\mathrm{tm}} = 1.3\,\mu\mathrm{m}$. Again, for short times the atomic density distribution after the imaging pulse can be approximated by a Gaussian f_{tm} with r.m.s. width σ_{tm}.

Diffusive movement of atoms due to photon scattering - σ_{ps}

During the imaging laser pulse of duration dt_{im}, the atoms randomly scatter photons. The associated momentum recoils lead to a diffusive motion of the atoms, which leads at the end of the pulse to an average displacement perpendicular to the line of sight of [1]

$$\sigma_{\mathrm{ps}} = \sqrt{\frac{2}{3}} \cdot \sqrt{\frac{N_p}{3}} \cdot v_{\mathrm{rec}} \cdot dt_{\mathrm{im}},$$

where $v_{\mathrm{rec}} = \hbar k/m = 5.9\,\mathrm{mm/s}$ is the atomic recoil velocity for $^{87}\mathrm{Rb}$, and N_p the number of scattered photons, with $N_p = (\Gamma/2)\,dt_{\mathrm{im}}\,s/(1+s)$ and the natural line width $\Gamma = 2\pi \times 6.1$ MHz. For our experimental parameters (saturation parameter $s = I/I_{\mathrm{sat}} = 1$, $dt_{\mathrm{im}} = 40\,\mu\mathrm{s}$) we get $\sigma_{\mathrm{ps}} = 2.2\,\mu\mathrm{m}$.

Effective spatial resolution $s_{\mathrm{eff}} = 2\sigma_{\mathrm{eff}}$

The effective resolution can approximately be calculated by the convolution $f_{\mathrm{eff}} = f_{\mathrm{opt}} * [f_{\mathrm{ps}} * (f_{\mathrm{tm}} * f_{\mathrm{mw}})]$, where f_{opt} approximates the point spread function of the imaging system by a Gaussian f_{opt} with $\sigma_{\mathrm{opt}} = 2\,\mu m$. As a result, we get $\sigma_{\mathrm{eff}} = 4.1\,\mu\mathrm{m}$. We take as the effective resolution for our parameters $s_{\mathrm{eff}} = 2\sigma_{\mathrm{eff}} = 8.2\,\mu\mathrm{m}$.

Imaging noise

The noise on the absorption images is important for the sensitivity of our technique. It determines the minimum number of atoms $N_{2,\mathrm{min}}$ that has to be transferred by the microwave into the $F = 2$ manifold during dt_{mw} in order for the microwave field to be detectable. We currently use an *Andor iKon-M* camera with a quantum efficiency of 90% for absorption imaging. The optical resolution of our imaging system is $s_{\mathrm{opt}} = 4\,\mu\mathrm{m}$, the imaging pulse duration $dt_{\mathrm{im}} = 40\,\mu\mathrm{s}$, and we are imaging at saturation intensity ($s = I/I_{\mathrm{sat}} = 1$).[5] With these parameters, we calculate an uncertainty in the number of atoms detected in an area $A_{\mathrm{eff}} = \pi\sigma_{\mathrm{eff}}^2$ of 1.4 atoms r.m.s. We measure a value of $\sigma_{N,\mathrm{psn}} = 2.0$ atoms. The difference can be explained by interference fringes on the image. This additional noise could certainly be decreased further.

Quantum projection noise due to the probabilistic nature of the measurement process is an additional contribution of noise on the images. The measurement process projects the atomic superposition state onto the $F = 1$ and $F = 2$ states, resulting in a number of atoms of N_1 and N_2 in the two states, respectively. Even if the total number of atoms $N = N_1 + N_2$ is the same in each shot, N_1 and N_2 will show (anti correlated) fluctuations. This projection noise has an r.m.s. amplitude of $\sigma_{N_1} = \sigma_{N_2} = \sqrt{N \cdot p_2 \cdot (1 - p_2)}$, where σ_{N_i} denotes noise in N_i and $p_2 = N_2/N = N_2/(N_1 + N_2)$. The total noise on N_2 is thus $\sigma_{N,\mathrm{tot}} = \sqrt{\sigma_{N,\mathrm{psn}}^2 + \sigma_{N_2}^2}$. We find that in order to obtain a signal-to-noise-ratio $\mathrm{SNR} \equiv N_2/\sigma_{N,\mathrm{tot}} > 1$, we have to have $N_2 > N_{2,\mathrm{min}} = 3$.

Microwave field sensitivity

For the experimental data presented here, we trap about $N = 9 \times 10^3$ atoms in the magnetic trap. The trapping frequencies are $\omega_x = 2\pi \times 27\,\mathrm{Hz}$ and $\omega_y \approx \omega_z = 2\pi \times 680\,\mathrm{Hz}$. We calculate the average atomic density in the trap to $n = 2.2 \times 10^{11}\mathrm{cm}^{-3}$ [1]. The trapped cloud has a $1/e$ radius of $\rho = \sqrt{\frac{2k_B T}{m} \frac{1}{\omega_y}} = 7.2\,\mu m$ along the y-axis, which is the direction of the imaging beam. If we image the atoms with $dt_{\mathrm{ho}} = 0$, we have about $N = 170$ atoms inside a cylinder of radius σ_{eff} and height 2ρ. The microwave magnetic field which transfers on average $N_{2,\mathrm{min}} = 3$ atoms to $F = 2$ is obtained by requiring that

$$N_2 = N \sin^2\left[\frac{1}{2}|\Omega_\gamma|dt_{\mathrm{mw}}\right] \overset{!}{=} N_{2,\mathrm{min}}. \tag{4.6.3}$$

---

[5]The images evaluated in this chapter have been taken with a Princeton Instruments Coolsnap HQ, for which we measured a quantum efficiency of 41%. Furthermore the imaging system had a lower resolution of $s_{\mathrm{opt}} = 10\,\mu m$.

For the three transitions $\omega = \omega_-$, $\omega = \omega_\pi$, and $\omega = \omega_+$, this is equivalent to

$$N_{F=2} = N \sin^2 \left[\frac{1}{2} \left(\frac{\mu_B}{\hbar} \sqrt{3} \hat{B}_- \right) dt_{\text{mw}} \right] \approx N \left[\frac{1}{2} \left(\frac{\mu_B}{\hbar} \sqrt{3} \hat{B}_- \right) dt_{\text{mw}} \right]^2 \overset{!}{=} 3,$$

(4.6.4)

$$N_{F=2} = N \sin^2 \left[\frac{1}{2} \left(\frac{\mu_B}{\hbar} \sqrt{\frac{3}{4}} \hat{B}_\pi \right) dt_{\text{mw}} \right] \approx N \left[\frac{1}{2} \left(\frac{\mu_B}{\hbar} \sqrt{\frac{3}{4}} \hat{B}_\pi \right) dt_{\text{mw}} \right]^2 \overset{!}{=} 3,$$

(4.6.5)

$$N_{F=2} = N \sin^2 \left[\frac{1}{2} \left(\frac{\mu_B}{\hbar} \sqrt{\frac{1}{2}} \hat{B}_+ \right) dt_{\text{mw}} \right] \approx N \left[\frac{1}{2} \left(\frac{\mu_B}{\hbar} \sqrt{\frac{1}{2}} \hat{B}_+ \right) dt_{\text{mw}} \right]^2 \overset{!}{=} 3.$$

(4.6.6)

Solving the above equations with $dt_{\text{mw}} = 80\,\mu\text{s}$, we get $\hat{B}_- = \hat{B}_{-,\text{min}} = 2.2 \times 10^{-4}\,\text{G}$, $\hat{B}_\pi = \hat{B}_{\pi,\text{min}} = 4.4 \times 10^{-4}\,\text{G}$, and $\hat{B}_+ = \hat{B}_{+,\text{min}} = 5.4 \times 10^{-4}\,\text{G}$.

Note that the projection noise σ_{N_2} slowly increases with increasing N_2. Therefore, the absolute microwave magnetic field resolution of our method decreases with increasing values of $\hat{B}_\gamma$.

The consideration above relies on the assumption that we can achieve perfect resonance $\omega = \omega_\gamma$. Solving Eq. (4.6.3) for $N_{2,\text{min}}$, we obtain $|\Omega_\gamma|/2\pi = 0.53$ kHz for $N_2 = 3$. A change in $\omega_\gamma/2\pi$ of 0.53 kHz corresponds to a magnetic field instability of 2.5×10^{-4} G for Ω_-, 3.8×10^{-4} G for Ω_π and 7.6×10^{-4} G for Ω_+. Inside the magnetic shielding surrounding our experiment, we achieve a stability of B_0 of 2×10^{-4} G r.m.s., which could certainly be improved such that the effect can be neglected.

The sensitivity of our field imaging technique can be increased by using colder or denser clouds. Suitable techniques to reduce the temperature further are adiabatic relaxation of the trap or further forced evaporative cooling.

4.7 Measurement of microwave fields with trapped atoms

Our microwave field imaging method can be modified in different ways to get better spatial or field resolution. In the following I will outline some of those ideas.

4.7.1 Magnetically trapped atoms

For measuring the microwave magnetic field on a small region of investigation, it is possible to hold a BEC in a magnetic trap and optionally scan its position spatially from shot to shot (cf. Section 3.9). Such scanning can be done

on a sub-μm length scale [23], and the trap position can be scanned in all three dimensions. A typical step size is given by twice the Thomas-Fermi radius r_{TF} of the BEC in the trap. For example, for 1000 atoms in a trap with trap frequencies $f_i = 500\,\mathrm{Hz}$ ($i = x, y, z$), the Thomas-Fermi radius is $r_{\mathrm{TF}} = 1.2\,\mu\mathrm{m}$. Because $|2, m_2\rangle$ with $m_2 = -2, -1, 0$ are magnetically non-trappable states, transitions are measured by detecting atom loss from the trap. The magnetic field sensitivity is limited by atom loss not caused by the microwave. If initially $N = 1000$ atoms in a BEC in state $|1, -1\rangle$ are trapped in a spherical magnetic trap with $f_i = 500\,\mathrm{Hz}$, 500 ± 16 atoms are lost during a trap holding time of 3 s due to three body recombination and background gas collisions.[6] An additional loss of ~ 20 atoms due to the microwave can be recognized (at a signal-to-noise-ratio $\gtrsim 1$). The corresponding microwave magnetic field $\hat{B}_\gamma$ is estimated by

$$N_{F=2} = \tilde{N}\left(1 - e^{-\Gamma_\gamma(\hat{B}_\gamma)\cdot dt_{\mathrm{mw}}}\right) \overset{!}{=} 20. \qquad (4.7.1)$$

Γ_γ is the outcoupling rate, taking into account that $\Omega_\gamma \ll \mu_c$, and therefore only a fraction of the atoms is effectively resonant with ω, which leads to incoherent coupling. Γ_γ is given by $\Gamma_\gamma = -\frac{15\pi}{8}\frac{\hbar\Omega_\gamma^2}{\mu_c}(r_c - r_c^3)$, $r_c = \sqrt{\hbar\delta_\gamma/\mu_c}$ [78], where $\delta_\gamma = \omega - \omega_\gamma$ is the detuning in the trap center. Γ_γ is maximized for $r_c = \sqrt{3}$ [78]. Solving Eq. (4.7.1) with $\tilde{N} = \frac{N_{\mathrm{initial}} + N_{\mathrm{final}}}{2} = 750$ and $\mu_c = h \cdot 2\,\mathrm{kHz}$ we get a sensitivity of $B_- = 1.6 \times 10^{-7}\,\mathrm{G}$, $B_\pi = 3.1 \times 10^{-7}\,\mathrm{G}$ and $B_+ = 3.8 \times 10^{-7}\,\mathrm{G}$.

In this consideration, fluctuations of B_0 have not been taken into account. Fluctuations of B_0 are tolerable as long as $|(m_{F=2}g_{F=2} - m_{F=1}g_{F=1})\mu_B\Delta B_0| < \mu_c$. For $m_{F=2} = 0$ and $m_{F=1} = -1$ we get $\Delta B_0 = 2.9 \times 10^{-3}\,\mathrm{G}$.

4.7.2 Optically trapped atoms

If instead of a magnetic trap, a far-detuned crossed optical dipole trap is used (with the same trap frequencies of $f_i = 500\,\mathrm{Hz}$), the sensitivity can be increased further. This increase is due to two reasons. Firstly, all hyperfine states are trapped, therefore a transfer of 10 atoms into $F = 2$ is detectable using state selective imaging. Secondly, not only a fraction $\propto \frac{\Omega_\gamma}{\mu_c}$ of the atoms in the trap are coupled incoherently by the microwave magnetic field, as it is the case for magnetically trapped atoms, but all atoms are coupled in a coherent way (neglecting the small differences in the relevant scattering lengths). Therefore the maximum microwave magnetic field sensitivity, estimated by

$$N_{F=2} = \tilde{N} \cdot \sin^2\left[\frac{1}{2}|\Omega_\gamma|\,dt_{\mathrm{mw}}\right] \overset{!}{=} 10, \qquad (4.7.2)$$

---

[6] assuming a background collisional life time of 8 s.
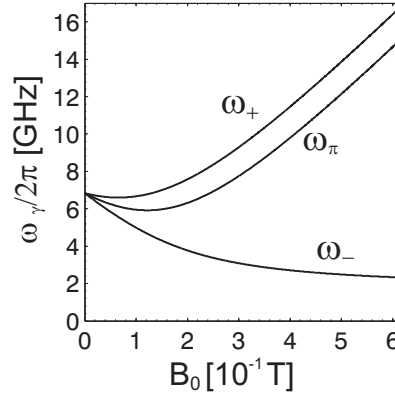
Figure 4.8.1: Transition frequencies ω_-, ω_π, and ω_+ for ^{87}Rb as a function of B_0. The individual transition frequencies can be tuned by up to 10 GHz with magnetic fields of up to 5000 G.

for $dt_{\mathrm{mw}} = 3\,\mathrm{s}$ and $\tilde{N} = 750$ atoms, is $B_- = 5 \times 10^{-9}\,\mathrm{G}$, $B_\pi = 1 \times 10^{-8}\,\mathrm{G}$ and $B_+ = 1.2 \times 10^{-8}\,\mathrm{G}$. Here, stability of the static magnetic field B_0 limits the achievable microwave field sensitivity in the same way as described in Section 4.6.

By using an optical lattice, not only one trap is formed, but many. In this way, the field distribution is measured in 2D, which is substantially faster than the optical scanning method.

4.8 Tunability of frequencies ω_-, ω_π and ω_+

The transition frequencies ω_-, ω_π, and ω_+ between the initial state $|1, -1\rangle$ and the target states $|2, m_2\rangle$ ($m_2 = -2, -1, 0$) for ^{87}Rb, can be adjusted by change of the static magnetic field B_0. For small magnetic fields ($B_0 < 500\,\mathrm{G}$) the transition frequencies are approximately given by $\omega_- = \omega_0 - 3\omega_L$, $\omega_\pi = \omega_0 - 2\omega_L$ and $\omega_+ = \omega_0 - \omega_L$, where $\omega_0 = 2\pi \times 6834.682610$ MHz and $\omega_L = \mu_B B_0 / 2\hbar$.

For larger values of B_0, the above formula is not valid anymore, and the Breit-Rabi formula has to be used, see Section 1.4.

For ^{87}Rb, the transition frequencies $\omega_\gamma/2\pi$ can be tuned over a range of more than 10 GHz using technically feasible magnetic fields of up to 5000 G (see Figure 4.8.1). Note that for $B_0 > 10^4\,\mathrm{G}$, we start entering the Paschen-Back regime, where the matrix elements of Eqs. (4.1.3) - (4.1.5) change and the theory has to be modified.

By using atomic species other than ^{87}Rb, different frequency ranges become

accessible, e.g. $9.2\,\mathrm{GHz}$ for Cs or $1.7\,\mathrm{GHz}$ for Na.

4.8.1 Using a two-photon transition

Instead of using a one-photon Rabi transition, it is also possible to use a two-photon transition, where two microwave fields or a microwave and a radio frequency field are applied to the atoms (see Section 1.6). This widens the accessible frequency range for imaging. The first field (frequency ω_1) is applied externally with known spatial distribution, while the other field (frequency ω_2) is the field to be imaged. Resonant Rabi oscillations occur for $\omega_1 + \omega_2 - E_{\mathrm{ls}}/\hbar = \omega_\gamma$, where E_{ls} denotes the level shift from the off-resonant electromagnetic fields (see Section 1.6).

4.9 Ramsey interferometry and off-resonant probing

Instead of having ω resonant with a hyperfine transition frequency, it is also possible to probe an off-resonant microwave or light-field (or anything else that causes a differential energy shift between the involved hyperfine levels) using a scheme based on Ramsey interferometry [139]. In Ramsey interferometry, the interaction with the off-resonant microwave field of duration T_{int} is enclosed by two resonant $\frac{\pi}{2}$-pulses. The first pulse prepares the atoms in an equal superposition of two hyperfine states such as

$$|\psi_1\rangle(t=0) = \tfrac{1}{\sqrt{2}}\left(|1,-1\rangle + ie^{-i\phi_{\mathrm{mw}}}|2,m_2\rangle\right). \qquad (4.9.1)$$

During time T_{int} both states accumulate a differential phase shift $\Delta\phi = \int_0^{T_{\mathrm{int}}} \frac{E_{\mathrm{diff}}}{\hbar}dt$. E_{diff} is the differential potential between the two hyperfine levels involved and is in general state-dependent, see next chapter. The state after this interaction is

$$|\psi_1\rangle(t=T_{\mathrm{int}}) = \tfrac{1}{\sqrt{2}}\left(|1,-1\rangle + ie^{-i\Delta\phi-i\phi_{\mathrm{mw}}}|2,m_2\rangle\right). \qquad (4.9.2)$$

After applying the second $\frac{\pi}{2}$-pulse, the state is

$$|\psi_2\rangle = \tfrac{1}{2}\left[\left(1-e^{-i\Delta\phi}\right)|1,-1\rangle + ie^{-i\phi_{\mathrm{mw}}}\left(e^{-i\Delta\phi}+1\right)|2,m_2\rangle\right], \qquad (4.9.3)$$

where ϕ_{mw} is the phase of the resonant microwave in a frame rotating at the atomic transition frequency. The probabilities to detect an atom in state $|1,-1\rangle$ and $|2,m_2\rangle$, respectively, show Ramsey oscillations of the form

$$p_1(\mathbf{r}) = \tfrac{1}{2}\left(1-\cos(\Delta\phi)\right), \qquad (4.9.4)$$
$$p_2(\mathbf{r}) = 1-p_1(\mathbf{r}) = \tfrac{1}{2}\left(1+\cos(\Delta\phi)\right). \qquad (4.9.5)$$

121

By measuring the relative populations $p_1(\mathbf{r})$ and $p_2(\mathbf{r})$ after the second $\frac{\pi}{2}$ pulse, it is possible to determine the value of $\Delta\phi$ and thereby E_{diff}. Details on the effect of an off-resonant microwave field are discussed in Section 1.8 and in the next chapter.

Chapter 5

Trapped-atom interferometry on a chip

Applications of ultracold neutral atoms in quantum information processing [34], quantum simulations [140] and quantum-enhanced metrology [141, 142, 36] rely on the coherent control of internal states, motional states and collisional interactions. Coherent manipulation of internal [9] and motional [15, 16, 17, 18, 19, 20] states on atom chips has been demonstrated in separate experiments. The combined coherent manipulation of internal and motional states with a state-dependent potential on a chip was shown for the first time in the experiments reported in this chapter [21]. We use a state-dependent microwave potential to implement a trapped-atom interferometer with internal-state labeling of the interferometer paths. In combination with collisional interactions, it is a crucial ingredient for entanglement generation and at the heart of recently proposed schemes for atom-chip quantum gates [40, 43] and for producing spin squeezed states on an atom chip [46], as has recently been demonstrated in our experiment, see [47] and Chapter 6.

The state-selective potential is generated by the on-chip microwave near-fields. We entangle atomic internal state and motional state in a controlled and reversible way, as required for the gate of [40, 43].

Microwave potentials generated by far-field radiation were already studied in the 1990s [49, 50]. Hundreds of kilowatts of circulating microwave power inside a cavity were necessary, because the centimeter wavelength prevents tight focusing and thus limits the attainable potential gradients. Using microwave near-fields generated by micrometer-sized waveguides on atom chips, it is possible to realize much stronger gradients with only milliwatts of power, because the near-field gradients do not depend on the wavelength, but instead on the transverse waveguide dimensions and the distance from the waveguide (see Chapter 2).

In this chapter, I first report on coherent internal state manipulation and present the performance of the state-selective near-field potentials, before I cover an experiment where we implement a trapped-atom interferometer with internal state labeling. We show combined coherent control of both internal and motional degrees of freedom [21].

5.1   Coherent internal-state manipulation

For all measurements in this chapter, we use a quasi-pure condensate in state $|1\rangle$ (with spatial wave function $\psi_{|1\rangle}$) containing up to 1000 atoms. We transfer it into the experiment trap, which is a cigar-shaped harmonic trap $V_Z(\mathbf{r})$ with measured trap frequencies $f_x = 109\,\text{Hz}$ ($f_\perp = 500\,\text{Hz}$) in the axial (radial) direction, and measured static magnetic field in the trap center $B_0(\mathbf{r}_\text{m}) = 3.23\,\text{G}$, pointing along x (see Table 3.1). The trap is at a distance of $44\,\mu\text{m}$ from the surface, the position $\mathbf{r}_\text{m}$ of the minimum of $V_Z(\mathbf{r})$ is indicated in Figure 5.2.2 below.

To prepare the BEC in a superposition of states $|1\rangle$ and $|2\rangle$, we coherently couple both states with a two-photon transition (see Figure 5.2.1), which is the combination of a blue detuned microwave (detuning $\Delta = 2\pi \times 360\,\text{kHz}$ from the intermediate state), radiated by the microwave horn, and a red detuned radio-frequency, applied to the atoms using the rf-antenna (see Section 1.6). This results in a two-photon Rabi frequency $\Omega_\text{2P}/2\pi = 2.1\,\text{kHz}$, and the efficiency of a π-pulse is $(96 \pm 1)\%$ in the experiment presented here. Such two-photon Rabi oscillations are shown in Figure 5.1.1a. A slight dephasing ($1/e$ dephasing time $\tau = 11.5\,\text{ms}$) is caused by the microwave field gradients from the horn at the position of the atoms, in qualitative agreement with the findings in Section 4.4.

For measuring atomic coherence properties, we use Ramsey's separated oscillatory fields method [139], where we vary the delay time T_R between two $\pi/2$ pulses. We observe Ramsey oscillations at frequency $\Omega_\text{Ramsey}/2\pi = 7.6\,\text{kHz}$, which show a contrast of $(96\pm1)\%$ after 12.7 ms (see Figure 5.1.1b). While the pulses are applied, the two-photon resonance frequency is shifted by $\nu_\text{ls} = E_\text{ls}/h = 7.6\,\text{kHz}$ with respect to the undriven system, which is caused by the detuned microwave of the two-photon drive (see Section 1.6). We always adjust the frequency of the two-photon drive such that the detuning from the two-photon resonance is zero while the pulse is applied. In between the pulses, the phase of the atomic superposition state thus evolves at a rate $-2\pi\nu_\text{ls}$ with respect to the two-photon drive, which determines Ω_Ramsey [47].
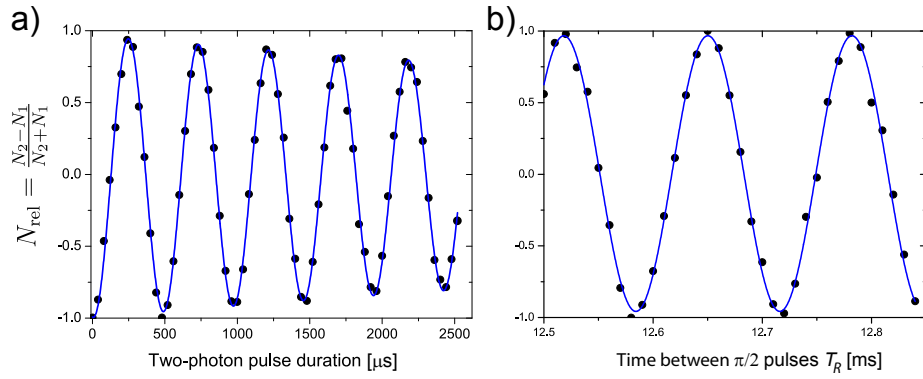
Figure 5.1.1: Rabi and Ramsey oscillation in the relative atom number $N_{\rm rel}$ for a BEC with in total 1000 atoms. (a) Rabi oscillations resulting from the resonant two-photon drive, with measured frequency $\Omega_{\rm 2P}/2\pi = 2.1\,{\rm kHz}$. The observed decay is due to microwave field gradients across the BEC, see main text. (b) Measured Ramsey interference fringes between $|1\rangle$ and $|2\rangle$ as a function of the delay T_R between both $\pi/2$ pulses, with frequency $\Omega_{\rm Ramsey} = 2\pi \times 7.6\,{\rm kHz}$, and a contrast of $(96 \pm 1)\%$ after 12.7 ms. Both measurements have been carried out with the Andor iKon-M camera, which allows to take out fluctuations in the prepared total atom number (see Section 3.7.1).
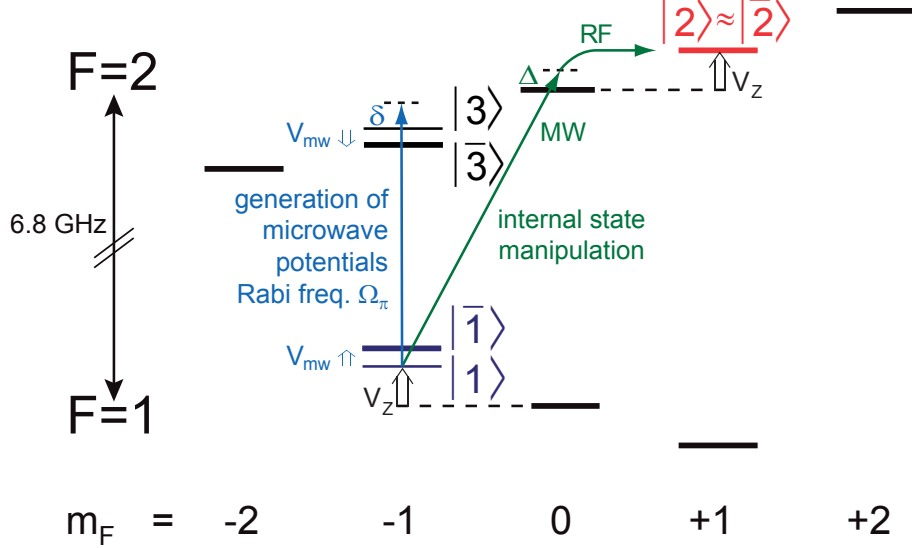
Figure 5.2.1: Coherent internal-state manipulation and generation of state-dependent microwave potentials. Hyperfine structure of the ^{87}Rb ground state in the static magnetic field of the microtrap. The clock states $|1\rangle$ and $|2\rangle$ experience nearly identical Zeeman energy shifts V_Z. To generate state-dependent potentials, the microwave near-field of the CPW couples $|1\rangle$ to the auxiliary state $|3\rangle$ with Rabi frequency Ω_π and detuning $\delta = \Delta_{1,-1}^{2,-1}$. The resulting dressed state $|\bar{1}\rangle$ is shifted in energy by V_{mw} with respect to $|1\rangle$. State $|2\rangle$ is nearly unperturbed by the microwave near-field, because all transitions connecting to $|2\rangle$ are far off resonance.

5.2 State-selective splitting of a BEC

To generate the state-selective potentials, we launch a microwave at frequency ω into the single CPW structure, which is blue detuned by $\delta = \Delta_{1,-1}^{2,-1}$ with respect to the transition $|1\rangle \leftrightarrow |F = 2, m_F = -1\rangle \equiv |3\rangle$ (see Figure 5.2.1). The detuning δ is chosen such that the microwave primarily couples $|1\rangle$ to the auxiliary state $|3\rangle$, with position-dependent Rabi frequency $\Omega_\pi(\mathbf{r}) = -\sqrt{3/4}(\mu_B/\hbar)B_\pi(\mathbf{r})$. All transitions other than $|1\rangle \leftrightarrow |3\rangle$ are much further off resonance and therefore have only minor effects (i.e. $\left|\Delta_{1,-1}^{2,-1}\right| \ll \left|\Delta_{1,j}^{2,i}\right|$, $[i,j] \neq [-1,-1]$). The coupling results in a dressed state $|\bar{1}\rangle$ that is shifted in energy by $V_{\mathrm{mw}}(\mathbf{r})$ with respect to $|1\rangle$; the overall potential seen by $|\bar{1}\rangle$ is thus $V_{|\bar{1}\rangle} = V_Z + V_{\mathrm{mw}}$. In contrast, state $|2\rangle$ and its potential remain essentially unchanged, $|\bar{2}\rangle \approx |2\rangle$ and $V_{|\bar{2}\rangle} \approx V_{|2\rangle} = V_Z$ (see Figure

5.2.1), because the microwave is very far off resonance from all transitions connecting to this state. In the experiments described in this chapter, we focus on the regime $|\Omega_\pi|^2 \ll |\delta|^2$, where $|\bar{1}\rangle$ contains only a small admixture of state $|3\rangle$, which is important because $|3\rangle$ has opposite magnetic moment, and a large admixture would spoil the good coherence properties of our state pair. In this limit, $V_{\mathrm{mw}}(\mathbf{r}) \approx \hbar |\Omega_\pi(\mathbf{r})|^2 / 4\delta(\mathbf{r})$ and $|\bar{1}\rangle \approx |1\rangle + \Omega_\pi(\mathbf{r})/2\delta(\mathbf{r})|3\rangle$.

To demonstrate state-selective splitting, we prepare BECs in our experiment trap in an equal superposition of states $|1\rangle$ and $|2\rangle$. Here and in the following, the two-photon microwave intermediate state detuning $\Delta/2\pi = 280\,\mathrm{kHz}$ and $\Omega_{\mathrm{2P}}/2\pi = 1.47\,\mathrm{kHz}$.

5.2.1 Adiabatic splitting

We prepare BECs containing $N = 400$ atoms in an equal superposition of states $|1\rangle$ and $|2\rangle$ by applying a $\pi/2$ pulse of 170 μs duration on the two-photon transition. Right after this pulse, which is fast compared with the trap oscillation periods, the motional wave functions of $|1\rangle$ and $|2\rangle$, $\psi_{|1\rangle}$ and $\psi_{|2\rangle}$, overlap completely. Then, within 150 ms, we smoothly ramp up the microwave power in the CPW to a final value $P_{\mathrm{mw}} = 120\,\mathrm{mW}$, at fixed detuning $\delta(\mathbf{r}_{\mathrm{m}}) = \delta_{\mathrm{m}} = 2\pi \times 150\,\mathrm{kHz}$. This corresponds to a ramp of V_{mw} that is adiabatic with respect to the dynamics of the internal state, ensuring population of only state $|\bar{1}\rangle$, but not $|\bar{3}\rangle$, as well as adiabatic to the motion, enabling the BEC wave function $\psi_{|\bar{1}\rangle}$ to follow the potential. At the end of the ramp, we switch off the combined static and microwave potential within 0.3 ms and image the atomic density distributions quasi *in situ*, using state-selective absorption imaging [48]. Figure 5.2.3a shows images taken in this way. We observe that the BEC is state-selectively split along x by a distance $s = 9.4\,\mu\mathrm{m}$, which is 3.9 times the radius of each of the two trapped clouds [143].

The splitting is due to the strong near-field gradient in $|\Omega_\pi(\mathbf{r})|$ around $\mathbf{r} = \mathbf{r}_{\mathrm{m}}$ (see Figure 5.2.2). By comparison, the spatial dependence of $\delta(\mathbf{r})$ is weak. Although $|\Omega_\pi(\mathbf{r})|$ has gradients of similar magnitude along x and z (see Figure 5.2.2b), the spatial splitting is nearly one-dimensional because $f_\perp^2 \gg f_x^2$. Figure 5.2.3b shows the measured s as a function of P_{mw}/δ for different values of δ. The data points lie on top of each other as expected from the scaling $V_{\mathrm{mw}} \sim |\Omega_\pi|^2 / \delta \sim P_{\mathrm{mw}}/\delta_{\mathrm{m}}$ in the regime $|\Omega_\pi|^2 \ll |\delta^2|$. The maximally applied $P_{\mathrm{mw}} = 120\,\mathrm{mW}$ corresponds to $|\Omega_\pi(\mathbf{r}_{\mathrm{m}})| = 2\pi \times 122\,\mathrm{kHz}$, which we measure independently by driving resonant Rabi oscillations with the microwave near-field. Note that for $\delta > 0$, the repulsive microwave potential pushes state $|\bar{1}\rangle$ into regions where $|\Omega_\pi(\mathbf{r})| \ll |\Omega_\pi(\mathbf{r}_{\mathrm{m}})|$ so that $|\Omega_\pi|^2 \ll |\delta|^2$ is always satisfied.
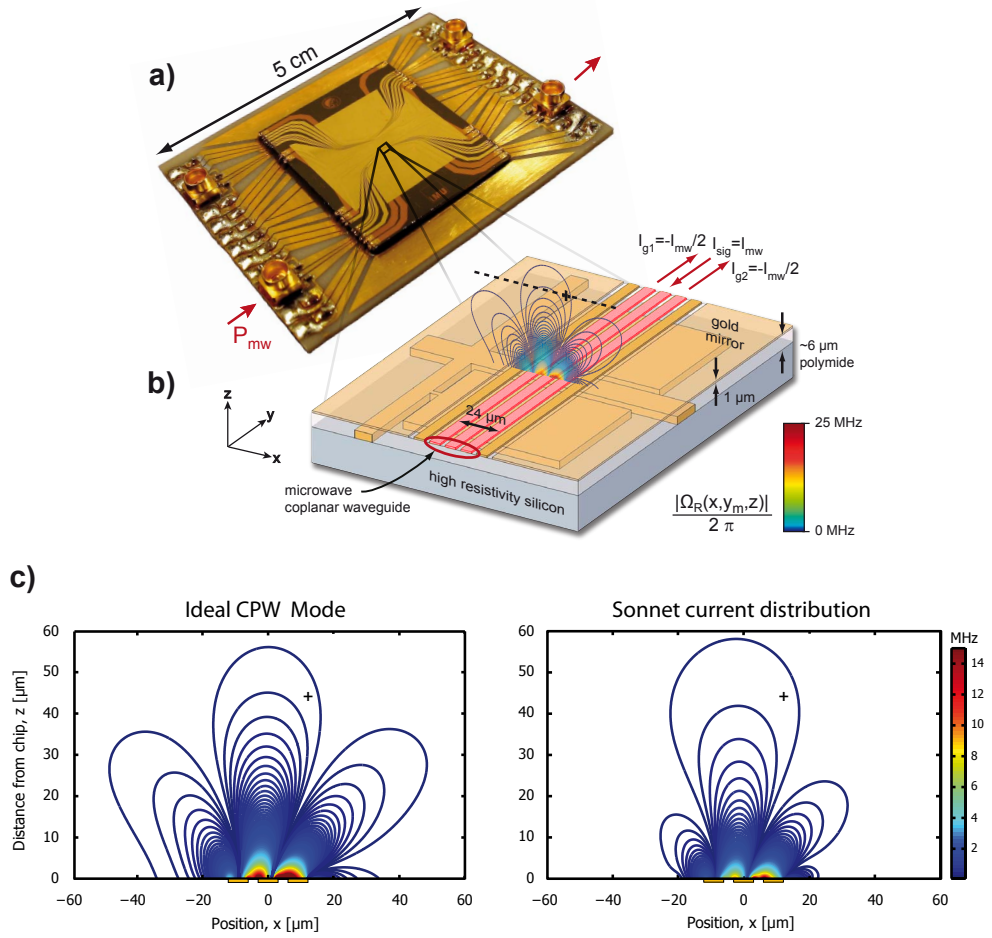
Figure 5.2.2: Visualization of the near-field gradients in the experiment region. (a) Photograph of the atom chip and (b) close up of the experimental region. The position $\mathbf{r}_{\mathrm{m}} = (x_{\mathrm{m}}, y_{\mathrm{m}}, z_{\mathrm{m}}) = (12, 0, 44)\,\mu\mathrm{m}$ of the minimum of the static trap $V_Z(\mathbf{r})$ is indicated by the black cross ($\mathbf{r} = 0$ corresponds to the top surface of the wire in the center of the CPW). An ideal CPW mode with microwave current amplitudes $I_{\mathrm{sig}} = I_{\mathrm{mw}}$ on the signal wire and $I_{\mathrm{g1}} = I_{\mathrm{g2}} = -I_{\mathrm{mw}}/2$ on each of both grounds is indicated. Equipotential lines of $|\Omega_{\pi}|/2\pi$ are indicated for $I_{\mathrm{mw}} = 76\,\mathrm{mA}$ (line spacing 70 kHz). The asymmetry in $|\Omega_{\pi}|/2\pi$ with respect to $x = 0$ is due to the spatial dependence of the static magnetic field $B_0(\mathbf{r})$, that gives rise to $V_Z(\mathbf{r})$. (c) Comparison between the calculated distribution of $|\Omega_{\pi}|/2\pi$ for an ideal CPW mode (left) and for Sonnet's current distribution, see Section 4.3. Both distributions are calibrated by the measured Rabi frequency $|\Omega_{\pi}(\mathbf{r}_{\mathrm{m}})|/2\pi = 122\,\mathrm{kHz}$. Even though both distributions differ significantly, the field gradients at the position of the trap are very similar.
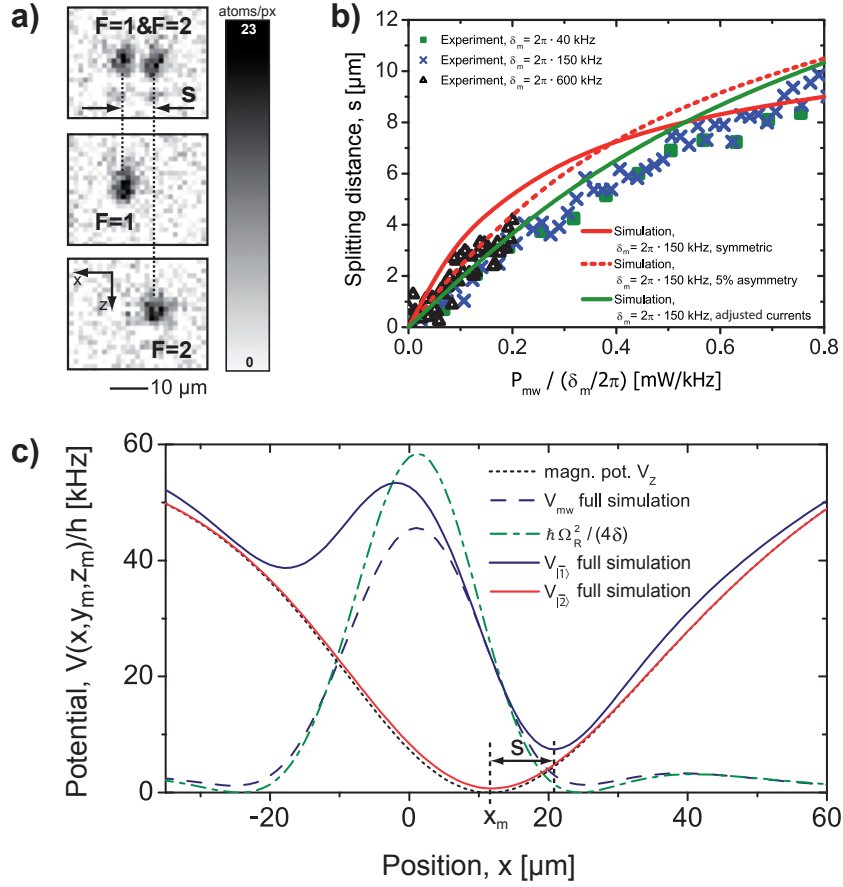
Figure 5.2.3: State-selective splitting of a BEC. (a) Absorption images of the adiabatically split BEC ($P_{\mathrm{mw}} = 120\,\mathrm{mW}$, $\delta_{\mathrm{m}} = 2\pi \times 150\,\mathrm{kHz}$). By imaging both hyperfine states simultaneously (top), only $F = 1$ (middle) or only $F = 2$ (bottom), the state-selectivity of the splitting is demonstrated. (b) Measured splitting distance as a function of $P_{\mathrm{mw}}/\delta_{\mathrm{m}}$ for different values of δ_{m} as indicated. The solid red line is the result of a static simulation assuming an ideal CPW mode; the dashed line assumes a slightly asymmetric mode ($I_{g1} = -0.45 \times I_{\mathrm{mw}}$, $I_{g2} = -0.55 \times I_{\mathrm{mw}}$). The green line shows the splitting resulting from the adjusted static current distribution, which reproduced the measured microwave field distribution best in Section 4.3. Notice that even though the measured field distribution shows a significant deviation from the ideal CPW mode for $z \geq 50\mu m$ (see Chapter 4), the field gradients along x are of similar magnitude near $\mathbf{r}_{\mathrm{m}}$. (c) Simulated potentials along the splitting direction (see the dashed line in Figure 5.2.2b), for an ideal CPW mode and $I_{\mathrm{mw}} = 76\,\mathrm{mA}$, corresponding to the parameters of a). The potential minimum of $V_{|\bar{1}\rangle}$ is shifted by the microwave, whereas $V_{|\bar{2}\rangle} \approx V_Z$. The full microwave potential V_{mw} (dashed blue) and the approximation $V_{\mathrm{mw}} \approx \hbar |\Omega|^2 / 4\delta$ for $|\Omega|^2 \ll |\delta|^2$ (dash dotted green) are shown in comparison.

129
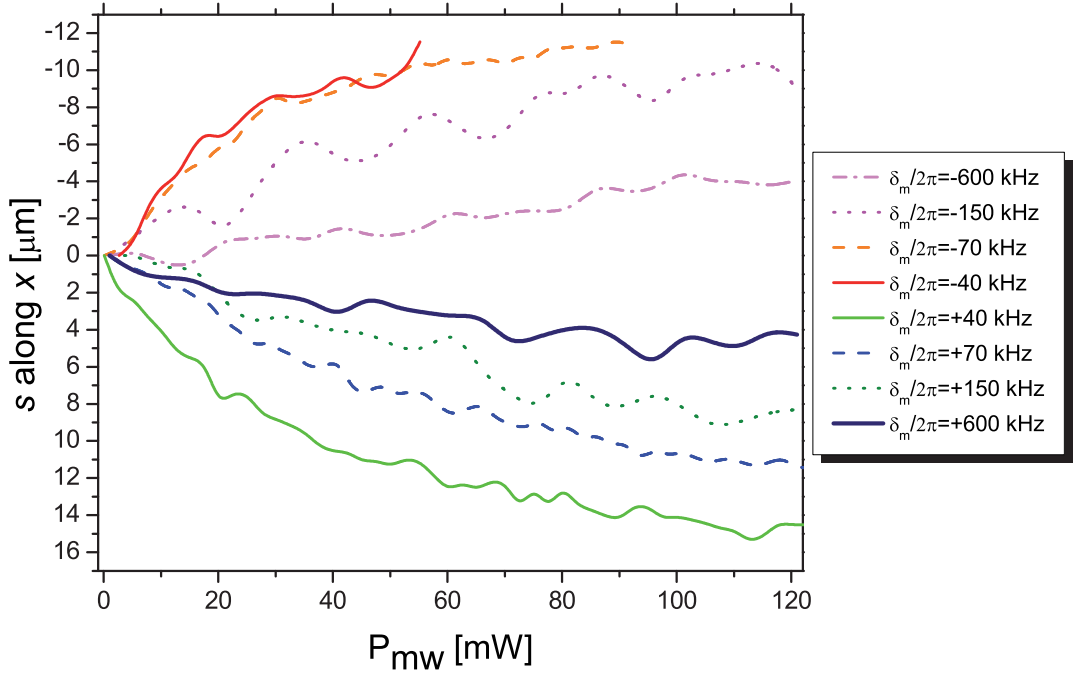
Figure 5.2.4: Measurement of the splitting s along x as a function of P_{mw} and δ_m with BECs. For $s > 11\,\mu$m the atoms are lost because the trap opens. The displacement along z is below the resolution of our imaging system.

The observed splitting is reproduced by our static simulation of $V_{|\bar{1}\rangle}$ and $V_{|\bar{2}\rangle}$ that takes the full 8-level system into account (see Section 1.8), where the microwave current amplitude I_{mw} is calibrated using the measured $|\Omega_\pi(\mathbf{r}_m)|$. Figure 5.2.3c shows a slice through the simulated potentials along the splitting direction, assuming an ideal CPW mode. In agreement with the experiment, the simulation shows that we can selectively displace the wave function of state $|\bar{1}\rangle$ with the microwave potential gradient.

**Sign of detuning δ_m** By changing the sign of the detuning δ_m from blue to red, the microwave potential can be changed from repulsive to attractive for $|\bar{1}\rangle$. Measurements of s along x for various positive and negative values of δ_m are shown in Figure 5.2.4. We observe that the trapped atoms are lost for small negative values of δ_m and $s > 11\,\mu$m because the trap opens.

5.3 BEC interferometry

In the following, we demonstrate the coherence of the splitting process by carrying out trapped-BEC interferometry with internal state labeling of the interferometer arms. Our interferometer consists of a Ramsey $(\pi/2)$-$(\pi/2)$ sequence on the $|1\rangle \leftrightarrow |2\rangle$ transition in combination with state-dependent splitting and recombination of the motional wave functions between the pulses. We use a non-adiabatic splitting and recombination scheme, see Figure 5.3.1a, which is motivated by the sequence required for the atom chip controlled phase gate in [43]. By choosing $\delta_{\mathrm{m}} = 600\,\mathrm{kHz}$, we ensure that the admixture of state $|3\rangle$ is small enough so that decoherence due to magnetic field noise is not a problem on the timescale of our experiment. After the first $\pi/2$ pulse, which prepares the atoms in an equal coherent superposition of $|1\rangle$ and $|2\rangle$, the microwave on the CPW is switched on within $50\,\mu\mathrm{s}$ to $P_{\mathrm{mw}} = 120\,\mathrm{mW}$, which corresponds to a sudden displacement of the potential minimum for state $|\bar{1}\rangle$ by $4.3\,\mu\mathrm{m}$. After a variable delay, we switch off the microwave within $50\,\mu\mathrm{s}$, followed by the second $\pi/2$ pulse and state-selective detection (after a time-of-flight of 4 ms) to determine the number of atoms N_1 (N_2) in state $|1\rangle$ ($|2\rangle$). The time between the $\pi/2$ pulses, T_{R}, corresponds to the overall time the microwave was turned on. In this scheme, the switching of V_{mw} is adiabatic with respect to the internal-state dynamics, but fast compared to the trap oscillation period. The wave function $\psi_{|\bar{1}\rangle}$ is thus set into oscillation in the shifted potential $V_{|\bar{1}\rangle}$. We can record these oscillations by varying T_{R} and imaging the atoms without applying the second $\pi/2$ pulse, see Figure 5.3.1b. The wave function $\psi_{|\bar{1}\rangle}$ oscillates with a peak-to-peak amplitude of 8.5 μm and a frequency of $\tilde{f}_x = 116\,\mathrm{Hz}$. Small deviations of the oscillation frequency $\tilde{f}_x$ from the trap frequency f_x arise due to additional mean field effects from the resting wave function $\psi_{|2\rangle}$. Periodically $\psi_{|\bar{1}\rangle}$ comes back to its initial position, when T_{R} is an integer multiple of $1/\tilde{f}_x = 8.6\,\mathrm{ms}$. At these times, it overlaps with the wave function $\psi_{|2\rangle}$. Note that owing to collisions, $\psi_{|2\rangle}$ starts to oscillate as well.

If we apply both $\pi/2$ pulses and vary T_{R}, we observe Ramsey interference fringes, see Figure 5.3.2. The interference contrast is modulated by the wave function overlap of the two states and thus periodically vanishes and reappears again owing to the oscillation of state $\psi_{|\bar{1}\rangle}$. As a measure of the wave function overlap, we plot $\sigma(N_2)/\bar{N}_2$ as a function of T_{R}, where $\sigma(N_2)$ is the standard deviation and $\bar{N}_2$ is the mean of N_2 obtained from a running average over one period of the Ramsey fringes (15 measured datapoints for each state), see Figure 5.3.2a. This measure of the overlap has the advantage that it is largely insensitive to noise on the Ramsey fringes. Corresponding fringe
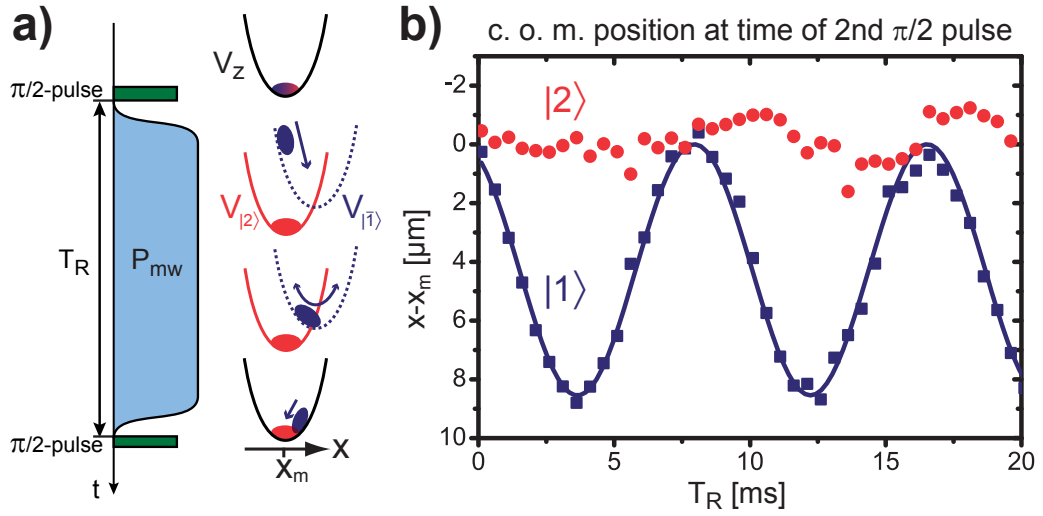
Figure 5.3.1: Dynamical splitting and recombination scheme used for BEC interferometry. (a) Timing sequence of the interferometer. In between the two $\pi/2$-pulses of a Ramsey sequence on the $|1\rangle \leftrightarrow |2\rangle$ transition, the microwave on the CPW is pulsed on for a duration T_R, resulting in a sudden displacement of the potential minimum of $V_{|\bar{1}\rangle}$. This sets the wave function $\psi_{|\bar{1}\rangle}$ into oscillation. (b) Oscillation of the atoms, recorded with the sequence of (a), but with the second $\pi/2$ pulse omitted. The center-of-mass (c.o.m.) position of the atoms at the end of the sequence is shown as a function of T_R. $\psi_{|1\rangle}$ oscillates whereas $\psi_{|2\rangle}$ remains initially at rest. Each time the wave functions overlap in the trap, energy is transferred between the states.

data and *in situ* images of the atoms at specific times T_R are shown in Figure 5.3.2b+c. Precisely at the time when the wave function $\psi_{|\bar{1}\rangle}$ has carried out a full oscillation in $V_{|\bar{1}\rangle}$, a sharp recurrence of the contrast is observed. The recurrence of the interference proves that the combined evolution of internal and motional state is coherent. The relatively high contrast of the first recurrence (Michelson contrast 50%) shows that the collisional interactions between the atoms observable in Figure 5.3.1b lead only to a relatively small distortion of the wave functions $\psi_{|i\rangle}$. Wave function distortion can be reduced to negligible levels by optimal control of the splitting process as discussed in [43].

For the second (and subsequent) recurrences, we observe substantial phase noise on the Ramsey fringe data. In contrast, when we take Ramsey fringes without splitting the BEC, comparable noise is visible only for T_R beyond several hundred milliseconds. Fundamental as well as technical sources of this noise are discussed in Section 5.5.

5.4 Role of atomic collisions

Collisional interactions play an important role during splitting and merging of the different states. Furthermore, spin-squeezing arises as a result of collisions when the spatial wave functions $\psi_{|1\rangle}$ and $\psi_{|2\rangle}$ are not overlapping completely, see [47] and Section 6.1.

In the following, I present some experimental findings on collisional effects in our system and compare them to simulations.

In the diabatic splitting scheme, where the wave function $\psi_{|\bar{1}\rangle}$ oscillates and overlaps with $\psi_{|2\rangle}$ periodically, momentum is transferred each time they meet, as can be seen in Figure 5.3.1b. Our collaborators Li Yun and Alice Sinatra from Paris (LKB/ENS) performed a 3D Gross-Pitaevskii (GP) simulation for our set of parameters (i.e. $N = 400$ atoms). The simulated dynamics (Figure 5.4.1a) is similar to the measured one (Figure 5.3.1b). One can recognize in the simulation that collisions do not only influence center of mass oscillations of both BECs, but also lead to excitations within their spatial wave functions $\psi_{|i\rangle}$. Such excitations decrease the wave function overlap at the recurrences, which results in a decreased Ramsey contrast (see Figure 5.4.1b).

For splitting distances s which are large compared to the radii r_x of $\psi_{|i\rangle}$, the recurrence times $k \cdot \tilde{\tau}_x = k/\tilde{f}_x$ $(k = 1, 2, \ldots)$ are approximately multiples of $\tau_x = 1/f_x$, since the states experience the mean-field repulsion of the other state only for a relatively short period of time compared to $\tilde{\tau}_x$. As the splitting distances s get smaller and become comparable to or less than r_x,

a) Time between $\pi/2$-pulses, T_R [ms]

$\dfrac{\sigma(N_2)}{\bar{N}_2}$

b) $\dfrac{N_1 - N_2}{N_1 + N_2}$

c) In-situ images
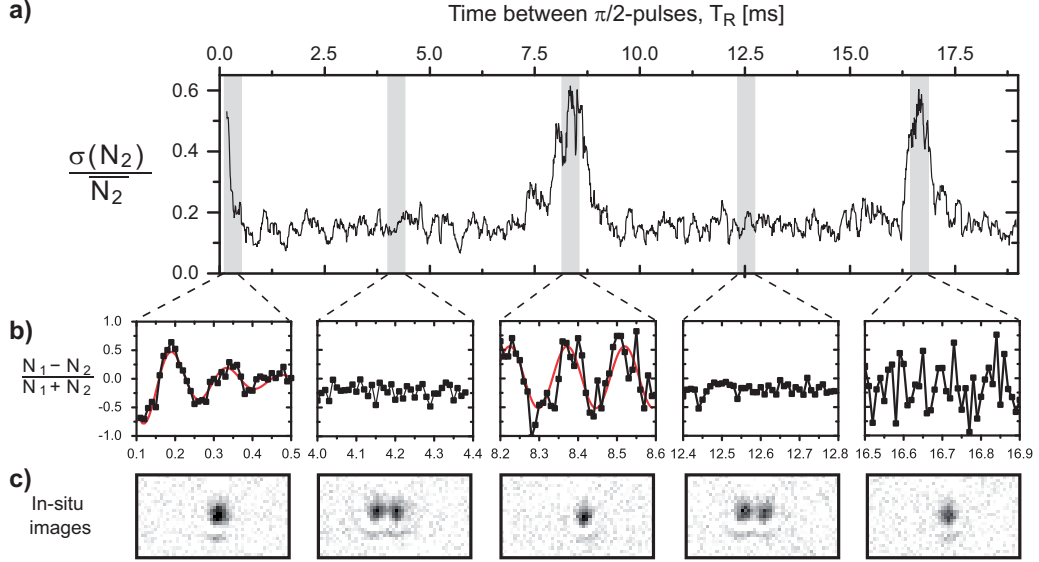
Figure 5.3.2: Periodic recurrences of Ramsey interference contrast in the BEC interferometer. The contrast of the Ramsey fringes on the $|1\rangle \leftrightarrow |2\rangle$ transition is modulated owing to the periodic splitting and recombination of the motional wave functions $\psi_{|i\rangle}$. (a) As a measure of the wave function overlap, we show $\sigma(N_2)/\bar{N}_2$ as a function of T_R, where $\sigma(N_2)$ is the standard deviation and $\bar{N}_2$ is the mean of N_2 obtained from a running average over a time interval $[T_R - 75\,\mu\text{s}, T_R + 75\,\mu\text{s}]$, corresponding to one period of the Ramsey fringes. The width of the recurrence is influenced by nonlinear wave function dynamics due to mean-field interactions. (b) Corresponding Ramsey fringe data for selected values of T_R. Each data point is determined from two consecutive runs of the experiment, in which either N_1 or N_2 is detected. The surplus of atoms in state $|2\rangle$ at times when the contrast has vanished (second and fourth graph) is probably due to the intensity gradients of the microwave used to drive the two-photon transition. The data shown here is taken with the *CoolSnap* camera, which only images one state per experimental cycle. The data thus includes fluctuations in the prepared total atom number, which cannot be taken out. (c) *In situ* images of the atomic density distribution of $|1\rangle$ and $|2\rangle$, for T_R corresponding to the center of the windows in (b).
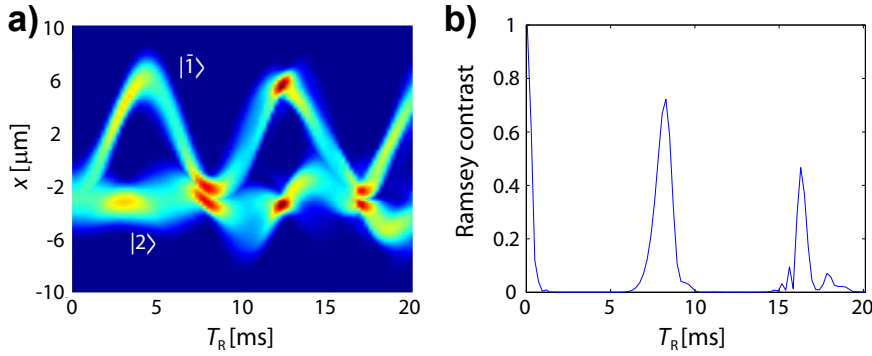
Figure 5.4.1: 3-dimensional Gross-Pitaevskii (GP) simulation for our experimental parameters ($N = 400$ atoms) including atom loss, performed by Li Yun from Alice Sinatra's group. (a) Axial density distribution as a function of T_R. At time $T_R = 0$ the atoms are prepared in an equal superposition of $|1\rangle$ and $|2\rangle$. 10 μs later, the potential minimum for state $|\bar{1}\rangle$ is shifted during 50 μs by 4.3 μm along x. The spatial wave function $\psi_{|\bar{1}\rangle}$ oscillates in the shifted trap while the wave function $\psi_{|2\rangle}$ remains at rest. At the recurrences, the oscillating wave function $\psi_{|\bar{1}\rangle}$ kicks the wave function $\psi_{|2\rangle}$, which affects center of mass motion as well as excitations within $\psi_{|i\rangle}$. (b) Wave function overlap of $\psi_{|\bar{1}\rangle}$ and $\psi_{|2\rangle}$ as a function of T_R, which is equal to the expected Ramsey contrast in the absence of technical noise. The wave function overlap at the time of the first recurrence is 75% and the one at the second recurrence is 50%.
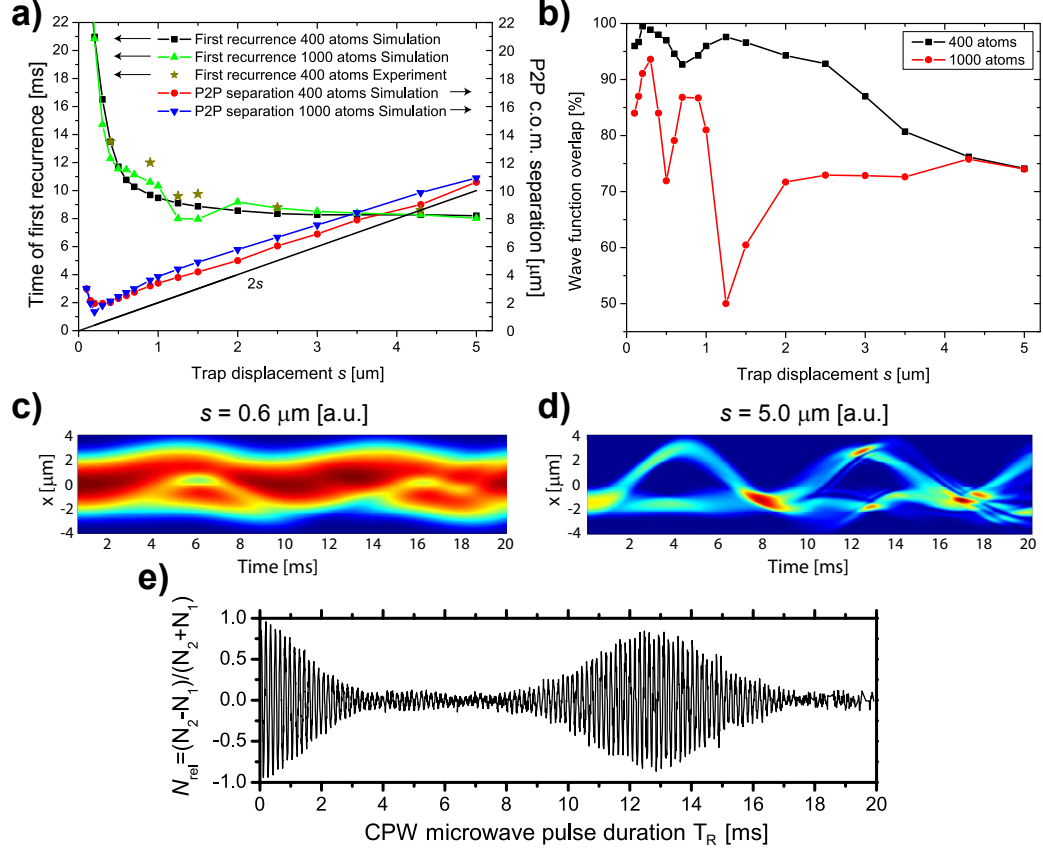
Figure 5.4.2: Splitting dynamics from 1-dimensional GP simulations, where the splitting distance s is varied, for 400 and 1000 atoms. (a) shows the time of the first recurrence $\tilde{\tau}_x$ and the peak-to-peak splitting between $\psi_{|\bar{1}\rangle}$ and $\psi_{|2\rangle}$ as a function of the trap displacement s (see main text). (b) Wave function overlap between both states at the time of the first recurrence for 400 and 1000 atoms. (c) and (d) show the axial atomic densities from the GP simulation for $s = 0.6\,\mu$m and $s = 5\,\mu$m ($N = 400$, each colormap is arbitrarily scaled). In d) the time of maximum splitting (first recurrence) is 4.3 ms (8.6 ms), while in c), the times are 6 ms (10.8 ms). (e) For comparison a complete experimental scan, with $\delta_m = 2\pi \times 12$ MHz and $N = 1250$ atoms, where both potential minima for $|1\rangle$ and $|2\rangle$ are shifted in opposite directions along x by in total $s = 0.52\,\mu$m. Here the time of the first recurrence ($\tilde{\tau}_x = 12.7$ ms) is significantly longer than τ_x. This data has been taken with the iKon-M camera, which allows to correct for the total prepared atom number. The fringes can be fitted by a continuous, amplitude-modulated sine function.
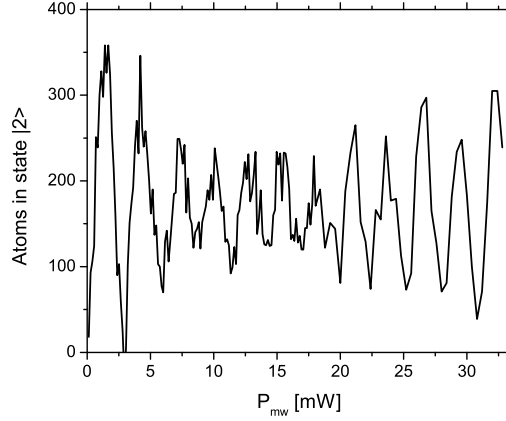
Figure 5.4.3: Collapse and recurrence by varying P_{mw} at fixed pulse duration T_R =8.6 ms and fixed $\delta_m = 2\pi \times 150\,\text{kHz}$.

the dynamics becomes increasingly influenced by the presence of the other wave function. This effect is illustrated in Figure 5.4.2a-d, where I performed a 1D Gross-Pitaevskii (GP) simulation (using a MATLAB program written by Philipp Treutlein) for two different atom numbers and variable splitting distances s. One can see that with decreasing s the time of the first recurrence $\tilde{\tau}_x$ increases, in agreement with our experimental findings. The peak-to-peak (P2P) separation between $\psi_{|\bar{1}\rangle}$ and $\psi_{|2\rangle}$, which in the non-interacting case would be $2s$, is a little larger than $2s$ due to mean-field repulsion, and for $s \to 0$ saturates at finite values comparable to the Thomas-Fermi radii of the clouds. In fact, a small displacement s can trigger a component separation, as has been observed in [89, 47].

Figure 5.4.2b shows the simulated wave function overlap between $\psi_{|\bar{1}\rangle}$ and $\psi_{|2\rangle}$ at the time of the first recurrence. For 1000 atoms, it is much more modulated by mean-field repulsion effects and the excitation of breathing modes. Panels c) and d) show the simulated axial atomic density distribution as a function of time for $s = 0.6\,\mu\text{m}$ and $s = 5\,\mu\text{m}$.

We also observe collapses and revivals of the Ramsey contrast when scanning the microwave power P_{mw} while keeping the time T_R fixed. This is due to the time dependence of the recurrences as a function of $s(P_{mw})$ (see Figure 5.4.2a).

Experimental results are shown in Figure 5.4.3, where a microwave pulse duration of $T_R = 8.6\,\text{ms} \approx \tau_x$ is chosen.

5.5   Phase noise

In this section, I discuss sources of phase fluctuations $\delta\varphi$ between states $|1\rangle$ and $|2\rangle$. They show up as noise in the Ramsey measurement shown in Figure 5.3.2.

5.5.1   Technical phase noise

Magnetic field fluctuations   The magnetic moment of state $|\overline{1}\rangle$ is slightly different than that of $|2\rangle$, which makes their relative phase sensitive to magnetic field fluctuations. We directly measure the magnetic field sensitivity of the Ramsey fringes in Figure 5.3.2 by scanning $B_0(\mathbf{r}_\mathrm{m})$ in the experiment with T_R fixed, and find that a magnetic field change of 16 mG leads to a phase shift of 2π at the time of the first recurrence. We measure r.m.s. magnetic field fluctuations inside the magnetic shielding of 225 μG (see Section 3.2), which corresponds to r.m.s. phase fluctuations of $\delta\varphi_B = 0.03\pi$ at the first recurrence ($T_\mathrm{R} = 8.6\,\mathrm{ms}$) and $\delta\varphi_B = 0.06\pi$ at the second (because the characteristic time scale of magnetic field fluctuations is many seconds and therefore much longer than $2 \times \tilde{\tau}_x$).

Surface effects, such as loss and decoherence due to thermal magnetic near-field noise [7], are negligible in the present experiments because of the thin metallic chip layers and relatively large atom-surface distances.

Fluctuations of P_mw   We also measure the sensitivity of the Ramsey phase on changes of P_mw, and use it to estimate that the measured r.m.s. fluctuations of $\delta P_\mathrm{mw} = 60\,\mu$W result in phase fluctuations of $\delta\varphi_{P_\mathrm{mw}} = 0.01\pi$ at the first recurrence and $\delta\varphi_{P_\mathrm{mw}} = 0.02\pi$ at the second.

Current source fluctuations   The energy difference between states $|\overline{1}\rangle$ and $|2\rangle$ is very sensitive to fluctuations of the homogeneous magnetic bias field B_y. The strong dependence arises because fluctuations in B_y change the position of the trapped atoms in the inhomogeneous microwave near-field potential, resulting in a change of the differential energy shift of the two states.

In the experiment, we measure fluctuations on the current which generates B_y corresponding to a magnetic field fluctuation of 10 mG peak-to-peak, which are synchronous with the 50 Hz AC power line (B_y=5.2 G during the relevant experiment phase). At the time when we performed these experiments, we only synchronized the start of the experimental sequence with the line phase, such that at the time of the relevant experimental phase the

line phase was randomly about $\pm\pi/6$ out of phase with the experiment, due to instabilities of the power line frequency. We measured r.m.s. fluctuations of the mean of B_y of 570 μG in a 8.6 ms window and 810 μG for 17.2 ms windows at the relevant time in the experimental sequence.

A simulation shows that a change in B_y of 1 mG results in a change of the differential energy between the trap minima for $|\bar{1}\rangle$ and $|2\rangle$ of $h \cdot 30$ Hz/mG.

Therefore, the fluctuations in B_y lead to an r.m.s. phase uncertainty of $\delta\varphi_{B_y} = 0.29\pi$ at the first revival and $\delta\varphi_{B_y} = 0.81\pi$ at the second.

Fluctuations of the prepared total atom number   We prepare 400 atoms with r.m.s. fluctuations in the total atom number of $\delta N = 21$ (including imaging noise). The measurements in Figure 5.3.2 were performed with the *Coolsnap HQ* camera, which can only image one state per experimental cycle. Therefore, fluctuations in the detected atom number due to imaging noise and imperfect atom number preparation appear as apparent phase noise. This corresponds to a phase uncertainty of $\delta\varphi_N \sim 0.03\pi$ on the slope of a Ramsey fringe.

5.5.2   Quantum noise

Projection noise for a spin-squeezed state   The internal state of a BEC of N two-level atoms can be described by a collective spin $\mathbf{S} = \sum_{i=1}^{N} \mathbf{s}_i$, the sum of the individual spins $1/2$ of each atom. Its component $S_z = (N_2 - N_1)/2$ is half the atom number difference between states $|2\rangle$ and $|1\rangle$. The first $\pi/2$ pulse prepares the BEC in a coherent spin state $\psi_{\text{css}} = \frac{1}{2^{N/2}}\left(|1\rangle + |2\rangle\right)^{\otimes N}$ with mean spin $\langle S_x \rangle = N/2$ and $\langle S_y \rangle = \langle S_z \rangle = 0$. In this state, the quantum noise is evenly distributed among the spin components orthogonal to the mean spin, $\sigma_{S_y} = \sigma_{S_z} = \sqrt{N}/2$, satisfying the Heisenberg uncertainty relation $\sigma_{S_y}\sigma_{S_z} = |\langle S_x \rangle|/2$ [47].

During the state-selective splitting the wave function of the initial state ψ_{css} evolves into a spin-squeezed state ψ_{sss} [47, 46]. In our sequence, this squeezing shows up as increased projection noise because the second $\pi/2$ pulse rotates ψ_{sss} such that the anti-squeezed spin component is nearly oriented along the poles of the Bloch sphere, which leads to strongly increased projection noise [21] (see illustration in Figure 5.5.1 and the squeezing experiments in Chapter 6.1 for details).

A two-mode simulation from Li Yun and Alice Sinatra (LKB/ENS Paris) that includes atom loss suggests that for our experimental parameters, the long axis of the squeezed state ψ_{sss} at the time of the first recurrence is 9 times longer than that of the initial state ψ_{css}. After the second $\pi/2$ pulse the anti-squeezed axis of ψ_{sss} has an angle of $\sim 10°$ with the axis of the Bloch
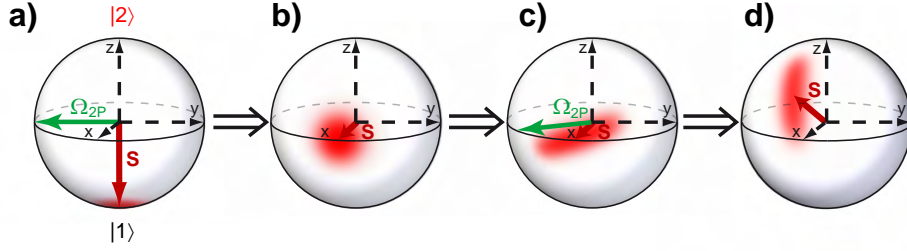
Figure 5.5.1: Effect of spin squeezing in our experiment, visualized on a Bloch sphere. (a) Initially we prepare a condensate with 400 atoms in state $|1\rangle$. (b) A $\pi/2$ pulse prepares the BEC in a coherent spin state ψ_{css}. The uncertainties in the plane perpendicular to the mean spin **S** are equal $\sigma_{S_y} = \sigma_{S_z} = \sqrt{N}/2$. (c) During the process of splitting and recombining, ψ_{css} evolves into a spin squeezed state ψ_{sss}. At the time of the first revival, the long semi-axis is about $9 \times \sigma_{S_y}$, while the short semi-axis has a width of $\sim \sigma_{S_z}/5$. The long axis is now nearly oriented along the equator of the Bloch sphere, with an angle of $\sim 10°$ in between. (d) The second $\pi/2$ pulse rotates ψ_{sss} on the Bloch sphere such that the anti-squeezed axis of ψ_{sss} has an angle of $\sim 10°$ with the axis of the Bloch sphere. In the experiment this is detected as a 8.9-fold increase in the measured projection noise. All numbers were calculated by Li Yun and Alice Sinatra in a two-mode simulation for our experimental parameters (including atom loss).

sphere, thus we expect an 8.9-fold increased projection noise.

We estimate that the increased projection noise due to spin squeezing corresponds to a phase uncertainty of $\delta\varphi_{ss} = 0.14\pi$ at the first recurrence and $\delta\varphi_{ss} = 0.28\pi$ at the second.

Furthermore, slight phase noise arises due to the discreteness of particle loss from the trap when $\psi_{|1\rangle}$ and $\psi_{|2\rangle}$ are separated. Each lost particle changes the chemical potential $\mu_{c,|i\rangle}$ in the respective state $|i\rangle$ which leads to a change in the phase evolution. This contribution to the total phase noise $\delta\varphi$ is very small and is not quantified here.

Putting all noise sources into a Ramsey-sequence simulation, where we assume perfect spatial wave function overlap of $\psi_{|1\rangle}$ and $\psi_{|2\rangle}$, we expect a Ramsey signal with a Michelson contrast of 68% at the first recurrence and $\sim 0\%$ at the second (calculated using the average of 100 simulations, see Figure 5.5.2a+b). If we include the simulated wave function overlap of 75% at the first recurrence and 50% at the second (see Section 5.4), then we get
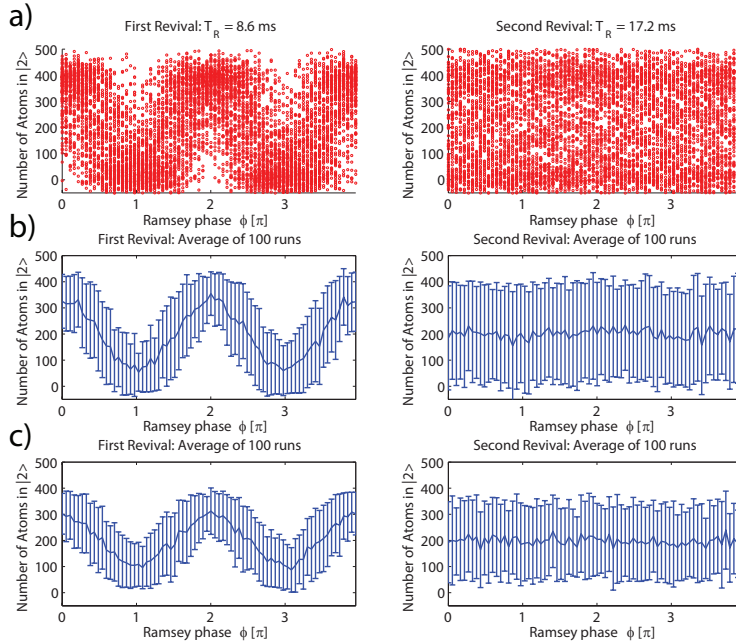
Figure 5.5.2: Effect of technical and quantum noise as well as finite wave function overlap on a Ramsey signal at the first revival (left column) and second revival (right column). (a) Simulation of 100 Ramsey scans including technical and quantum noise for on average $N = 400$ atoms, assuming perfect spatial wave function overlap of $\psi_{|1\rangle}$ and $\psi_{|2\rangle}$ and (b) statistical average of the scans. The Michelson contrast from the simulation is 68% at the first recurrence and $\sim 0\%$ at the second. (c) If we also take the simulated spatial wave function overlap into account (75% at the first recurrence and 50% at the second, see Section 5.4), we get a Ramsey contrast of 52% at the first and $\sim 0\%$ at the second recurrence, which is very similar to the measured values.

a Ramsey contrast of 52% at the first recurrence and still none at the second (Figure 5.5.2c), very similar to the experimentally measured values (50% and 0%, c.f. Figure 5.3.2b).

Since the phase noise is dominated by technical noise, we are very confident that the observed noise level could be lowered significantly with an optimized setup.

141

5.6 Advantages of microwave near-field potentials

Internal-state labeling of the interferometer paths [52], as demonstrated here, offers several advantages for trapped-atom interferometry. Compared with state-insensitive beam splitters, which operate by ramping up a barrier in the potential, the splitting and recombination can be controlled much more accurately by driving the internal-state transition. The interferometer paths can be closed inside the trap without the excitation of solitons, which subsequently decay into vortices [20, 144]. Furthermore, readout is greatly simplified, because it does not require spatially resolving interference patterns. Instead, only N_1 and N_2 have to be determined, which can be done with high accuracy. Many-body effects in the interferometer could either be suppressed by adjusting the trap frequencies for operation at lower density, or used beneficially to increase measurement precision with spin-squeezed states (see next chapter).

The oscillation of $\psi_{|\bar{1}\rangle}$ results in periodic entanglement and disentanglement of internal and motional states of the atoms. This mechanism is at the heart of the quantum phase gate proposed in [43, 40], see Section 6.2.

Microwave near-field potentials could be used to trap neutral atoms in internal states that cannot be trapped with static fields [49, 50], or to realize electrodynamic traps for ultracold molecules or electrons. An extension to multiple microwave frequencies seems promising and is technically straightforward.

Further applications of microwave near-field potentials on atom chips are discussed in the following chapter.

Chapter 6

Entanglement generation with microwave potentials

In the following, I discuss ways of using state-dependent microwave near-field potentials to generate multi-particle entanglement via collisional interactions.

Entanglement of atoms has been generated in a similar way in state-dependent optical lattice potentials [97]. The advantage of our system is that it is adaptable to a large range of atom numbers, ranging from large ensembles (as required for metrology with spin-squeezed states) over mesoscopic atom numbers (for example, for experiments on entangled number states) in principle down to individual atoms [145, 146, 12, 147] (as required for quantum information processing).

6.1 Spin-squeezing and multi-particle entanglement

Today's best atomic clocks are limited by the "standard quantum limit" of interferometric measurement [148], which arises from the quantum noise inherent in measurements on a finite number of uncorrelated particles. The emerging field of quantum metrology investigates the use of multi-particle entangled states, such as spin squeezed states, to improve the measurement precision beyond the standard quantum limit [36].

The *one-axis twisting scheme* [149] in principle allows the creation of a huge amount of atomic entanglement in a two-component BEC [46, 47]. In this scheme, a coherent spin state ψ_{css} dynamicaly evolves into a spin-squeezed state ψ_{sss} where the condensate atoms are entangled, which is due to atomic interactions that provide a nonlinear term in the Hamiltonian for the BEC internal state [47].

As mentioned in Section 5.5.2, the internal state of a BEC of N two-level atoms can be described by a collective spin $\mathbf{S} = \sum_{i=1}^{N} \mathbf{s}_i$ with z-component $S_z = (N_2 - N_1)/2$. For a BEC in a coherent spin state ψ_{css}, the atoms are uncorrelated and the quantum noise is evenly distributed among the spin components orthogonal to the mean spin. For $\mathbf{S}$ along x, $\sigma_{S_y}\sigma_{S_z} = |\langle S_x\rangle|/2$. This gives rise to the *standard quantum limit* if ψ_{css} is used in a Ramsey interferometer, where the Ramsey phase φ can be measured with quantum noise $\sigma_\varphi = 1/\sqrt{N}$.

Quantum correlations between the atoms can reduce the noise of one spin quadrature in the $y - z$ plane at the cost on increasing the noise in the orthogonal one, resulting in a spin squeezed state. Its usefulness in metrology is quantified by the squeezing parameter [39]

$$\xi^2 = N\sigma^2_{S_{\perp,\min}}/\langle S_x\rangle^2, \tag{6.1.1}$$

where $\sigma^2_{S_{\perp,\min}}$ is the minimal variance of the spin in the y-z plane. With entangled states, a lower bound of the Ramsey phase uncertainty is $\sigma_\varphi = 1/N$, known as the Heisenberg limit [150].

Spin squeezing is produced via the one-axis twisting Hamiltonian [149]

$$H/\hbar = \beta S_z + \Omega_{2\mathrm{P}}S_\varphi + \chi S_z^2, \tag{6.1.2}$$

which describes our BEC in good approximation. The first two terms in Eq. (6.1.2) are linear and describe rotations of the spin on the Bloch sphere. The third, nonlinear term with coefficient χ arises due to elastic collisional interactions in the condensate. It "twists" the state on the Bloch sphere, which results in spin squeezing and entanglement (see Figure 6.1.1). The parameter χ is given by

$$\chi = \frac{1}{2\hbar}\left(\partial_{N_1}\mu_1 + \partial_{N_2}\mu_2 - \partial_{N_2}\mu_1 - \partial_{N_1}\mu_2\right)_{\langle N_1\rangle\langle N_2\rangle}, \tag{6.1.3}$$

and depends on the derivatives of the chemical potentials

$$\mu_j = \langle\phi_j|h_j|\phi_j\rangle + \sum_{k=0,1} U_{ij}N_k\int\mathbf{dr}\,|\phi_j|^2\,|\phi_k|^2 \tag{6.1.4}$$

of the two BEC components evaluated at the mean atom numbers $\langle N_1\rangle = \langle N_2\rangle = N/2$ [47]. Here, h_j is the single-particle Hamiltonian including kinetic energy and the trapping potential, and $\phi_j(\mathbf{r})$ is the spatial mode function of state $|j\rangle$. The interaction strengths U_{jk} are given in Section 1.7.1.
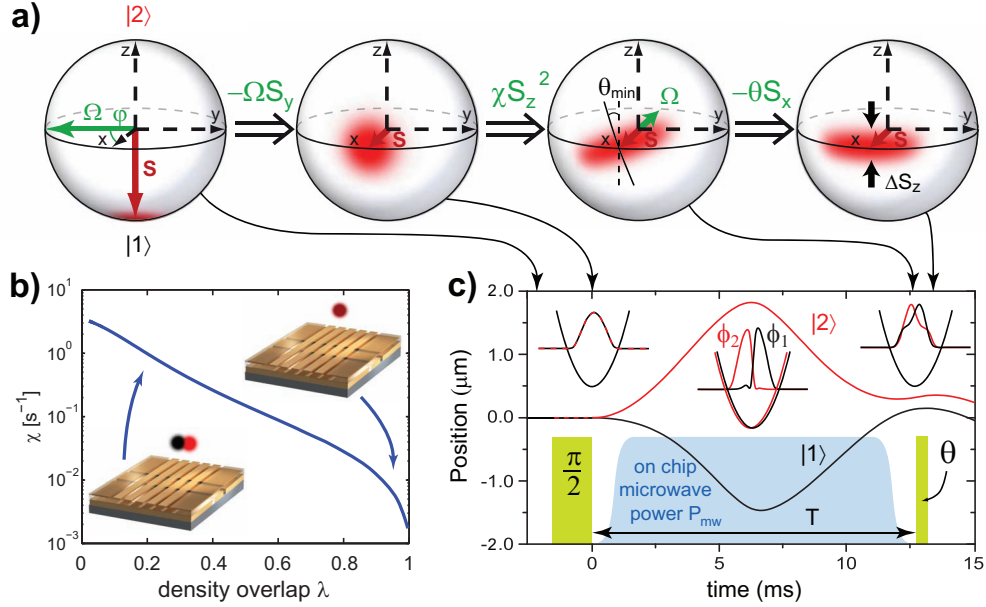
Figure 6.1.1: Spin squeezing through controlled collisional interactions. (a) Evolution of the BEC internal state on the Bloch sphere ($\beta = 0$ for illustration). Starting with all atoms in $|1\rangle$, a $\pi/2$ pulse prepares a coherent spin state ψ_{css} with mean spin $\langle \mathbf{S} \rangle$ along x and isotropic quantum noise in the y-z plane (fuzzy red circle). Subsequent nonlinear evolution with χS_z^2 deforms the noise circle into an ellipse, creating a spin-squeezed state ψ_{sss} with reduced noise at an angle θ_{min}. We turn the state ψ_{sss} with a second pulse by different angles θ around $-x$ and measure σ_{S_z}. (b) Control of the nonlinearity χ with the state dependent potentials. Its dependence on the normalized density overlap λ of the two BEC components is shown, calculated from stationary mode functions in potentials of increasing separation. The insets represent situations with little overlap ($\lambda \ll 1$, left) and large overlap ($\lambda \approx 1$, right). (c) Experimental sequence and motion of the two BEC components corresponding to (a). In between the pulses for internal-state manipulation (green), the state-dependent microwave potential ($\delta = 2\pi \times 12\,\mathrm{MHz}$, $P_{mw} = 120$ mW) is turned on (blue, pulse durations and microwave ramp times are exaggerated). It dynamically splits and recombines the wave functions $\psi_{|1\rangle}$ and $\psi_{|2\rangle}$, so that $\chi > 0$ during the time T. The simulated center-of-mass motion of the two states $|1\rangle$ (black) and $|2\rangle$ (red) is shown as a function of time. A slight asymmetric splitting of the potentials results in an asymmetric oscillation. Insets, corresponding BEC mode functions ϕ_1 and ϕ_2 along the splitting direction at the beginning (left), in the middle (center) and at the end (right) of the sequence.

If the spatial modes of both BEC components overlap completely, $\phi_1 = \phi_2$, then $\chi \approx 0$ because the crossed terms with the minus signs compensate the direct terms with the plus sign in Eq. (6.1.3). We can control the value of χ by controlling the overlap of ϕ_1 and ϕ_2 with our state-selective near-field potentials. By spatially separating atoms in states $|1\rangle$ and $|2\rangle$ the crossed terms in Eq. (6.1.3) vanish and $\chi > 0$. This is illustrated in Figure 6.1.1b, where we plot χ as a function of the density overlap $\lambda = \left(\int \mathbf{dr} \, |\phi_1|^2 \, |\phi_2|^2 \right) / \sqrt{\int \mathbf{dr} \, |\phi_1|^4 \int \mathbf{dr} \, |\phi_2|^4}$, calculated from stationary mode functions in traps of increasing separation for our experimental parameters [47].

We recently performed such an experiment [47], where we split and recombine a two-component BEC during 12.7 ms ($P_{\mathrm{mw}} = 120\,\mathrm{mW}$ and $\delta = 2\pi \times 12\,\mathrm{MHz}$, resulting in a splitting of both potential minima of $s = 0.52\,\mu\mathrm{m}$ [47]), see schematic in Figure 6.1.1c. We then perform tomography of the squeezed state by rotating ψ_{sss} around itself by an angle θ and measuring the projection noise $\sigma_{S_z}(\theta)$. We measure a reduction in the detected projection noise $\sigma^2_{S_{\perp,\mathrm{min}}} = \sigma^2_{S_z}(\theta = 6°)$ of $-3.7 \pm 0.4\,\mathrm{dB}$ compared with $\sigma^2_{S_z}$ for a coherent spin state ψ_{css}. Together with the measured Ramsey contrast after splitting and recombining of $C = (88 \pm 3)\%$ we get a squeezing parameter $\xi^2 = -2.5 \pm 0.6\,\mathrm{dB}$ [47], proving that the state is a useful resource for quantum enhanced metrology. Furthermore, ξ^2 is an entanglement witness with $\xi^2 < 1$ indicating at least bipartite entanglement between the atoms in the condensate [45].

6.2   Controlled phase gate

Atom chips are very promising for applications in quantum information processing (QIP) [34, 42]. They combine the exquisite coherence properties of neutral atoms [9, 31] with the tailorability of micropotentials and the scalability through microfabrication. The chip allows interfacing to photons ("flying qubits") through optical cavities on the chip [12, 151] as well as to solid-state quantum devices [78, 152]. Furthermore, two-dimensional magnetic microtrap arrays ("qubit storage registers") have already been realized on a chip [14].

Recently, a controlled phase gate for single atoms was proposed [43, 40] which relies on state-dependent microwave near-field potentials as investigated in this thesis [43]. In this proposal, the truth table of a controlled phase gate is realized (which results in entanglement) by means of state-selective collisional interactions between single atoms (see Figure 6.2.1).
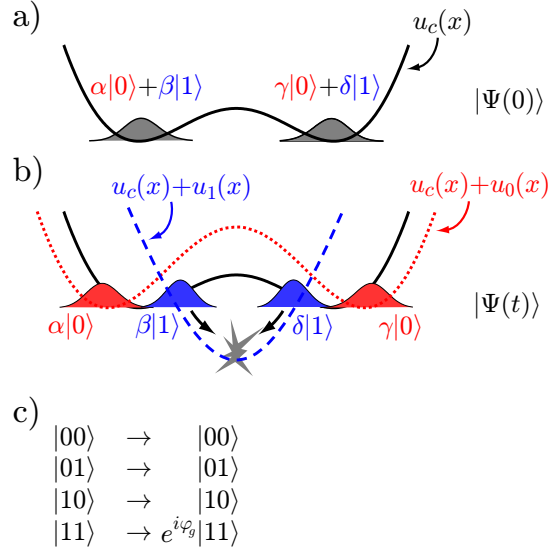
Figure 6.2.1: Working principle of the collisional phase gate. (a) Initially both qubit wave functions reside in their parts of the double well potential u_c, which is created by DC currents on chip wires. Notice that the state labeling in this figure follows standard QIP conventions; $|F = 2, m_F = 1\rangle \equiv |0\rangle$ and $|F = 1, m_F = -1\rangle \equiv |1\rangle$ (b) Qubit wave functions during gate operation. The microwave near-field generates a potential u_0 (u_1) for states $|0\rangle$ ($|1\rangle$), which removes the barrier for state $|1\rangle$ so that the wave functions $\psi_{|1\rangle}$ start to oscillate in the resulting single-well potential. After an integer number of oscillation periods, during which the oscillating states pick up a collisional phase shift φ_g, the microwave potentials are switched off again and the oscillating parts of the wave functions are brought back to rest again. (c) Resulting truth table of the collisional phase gate. The collisional phase shift φ_g of the two-qubit basis state $|11\rangle$ results in entanglement. For $\varphi_g = \pi$, we get the truth table of a controlled phase gate. The figure is taken from [69].

For an experimental realization of [43] the following ingredients are required:

- Control of atomic collisions in a double well potential with state-dependent barrier

- Single atom detection, ideally on-chip

- Deterministic single atom preparation in the vibrational ground state of the trap

Our collaborating group in Paris lead by J. Reichel has very recently succeeded in demonstrating single atom detection and preparation by using an on-chip optical fiber cavity [12, 153]. The coherent manipulation of motional states shown in the previous chapter gives us confidence that we can realize a double well potential with a state-dependent barrier, as required for the gate of [43]. While we do not yet have single atom preparation ready in our experiment, collisional interactions in a state-dependent double well potential could already be investigated with small condensates in our experiment.

The next step would be to design a new chip, which combines our near-field potentials with on-chip fiber cavities in order to realize the gate.

Conclusion

In this thesis, I studied the coherent interaction of ultracold atoms with microwave near-fields provided by a waveguide structure integrated on an atom chip.

The microwave field imaging method presented in this thesis offers an interesting combination of high spatial resolution and excellent microwave magnetic field sensitivity, allowing full microwave field reconstruction [55]. The microwave field can be probed on a large region of interest at once, which makes this method time efficient. It might e.g. be used in the atom clock community to characterize the microwave field homogeneity in the interaction region. Furthermore, since it is sensitive to frequencies used in communication technology, it could find commercial applications, e.g. in prototype testing of MMICs. One could imagine that in a commercial application, the device under test does not have to be locked into a vacuum chamber which is time consuming, but rather the microwave device could be separated from the cloud of atoms by a thin membrane through which the field distribution is measured [56].

The state-selective microwave near-field potentials have been used for coherent manipulation of the motional wave function of mesoscopic BECs [21]. We reversibly entangled internal and motional states to implement a trapped-atom interferometer with internal state labeling of the interferometer arms. Such an interferometer might be used for portable inertial force sensing systems [59, 32, 33].

The state-selectivity can also be used for the generation of multi-particle entanglement. We already used a scheme similar to the one for trapped-atom interferometry for the production of spin-squeezed states, where we measured a spin noise reduction of $-3.7 \pm 0.4\,\mathrm{dB}$ ($-2.5 \pm 0.6\,\mathrm{dB}$ *useful* squeezing) implying four-partite entanglement [47]. Spin-squeezed states are useful for quantum metrology to surpass the "standard quantum limit" in interferometric measurements [39]. The atom interferometer dynamics is also very similar to the one required for the implementation of a controlled phase gate for single atoms [43]. We foresee that the phase gate, which requires coherent

149

state-selective manipulation of the motional wave functions in combination with single atom preparation and detection, could be implemented by combining our state-selective microwave near-field potentials with the on-chip fiber cavities from Jakob Reichel's group, which were already used for deterministic single atom preparation and detection [153]. A natural next step towards the realization of the gate would be to simulate the collisional phase shift with small BECs, which we can readily produce with our setup.

The same effect that produces the squeezing can also be used for the generation of Schrödinger phase cat states [154, 155]. The phase spreading mechanism will refocus the phase of the BEC after a time $t_{\mathrm{rev}} = 2/\chi$ due to the discreteness of the atom number (for our parameters, $\chi_{\mathrm{max}} = 3\,\mathrm{Hz}$ for $N = 1250$, we get $t_{\mathrm{rev}} = 660\,\mathrm{ms}$). In between, at time $t_{\mathrm{rev}}/2$, the system is in a Schrödinger phase cat state [154]. Such a state is easily destroyed (and its formation is inhibited) by decoherence phenomena such as particle loss and technical phase noise [154]. In our current setup, atom loss would limit us to $N = 14$ [156], for which we would get a revival after $t_{\mathrm{rev}} = 5.4\,\mathrm{ms}$. However, such small atom numbers are hard to prepare reproducibly in our current setup. We envisage that the deterministic preparation of such small atom numbers could be achieved using on-chip optical fiber cavities [12, 153].

On-chip microwave near-fields are currently also investigated for the implementation of compact and robust chip-based atomic clocks [30] with long interrogation times, where the near-fields allow for well-defined and stable Ramsey pulses.

Microwave near-field potentials could be used to trap neutral atoms in internal states that cannot be trapped with static fields [49, 50], or to realize electrodynamic traps for ultracold molecules and electrons. Experiments to guide and manipulate electrons with microwave near-field potentials are currently in preparation [157].

Finally, microwave near-fields around superconducting coplanar waveguide resonators are also discussed as a way to reach strong coupling between a hyperfine excitation in an atomic ensemble and a single photon in the superconducting resonator [152].

I am convinced that the state-selective microwave near-field potentials demonstrated in this work are a versatile tool which will pave the way to a lot of very exciting experiments yet to come.

Appendix A

Chip design

Here I present the design of the different chips of the atom chip package. Figure A.0.1 shows the structures on the base chip (green) together with the structures on the science chip, where the color yellow (red) indicates structures on the lower (upper) layer of the science chip. The three gold mirrors and the science chip substrate (blue) are plotted semi-transparent to show the structures below. The labeling of the base chip wires corresponds to the labeling on the patch board used to connect the chip wires with current sources.

The base chip alone is shown in Figure A.0.2. Most wires on the chip are just lead wires to the science chip. The current *IUBasisMOT2* (up to 9.2 A) is used to generate the quadrupole magnetic field in the last MOT stage, the MOT close to the chip surface.

The science chip is shown in Figures A.0.3 and A.0.4. Figure A.0.3 shows a schematic of both chip layers together with a photograph of a chip (the picture shows the chip before cutting away the unnecessary parts of the Si substrate, see Section 2.2.2). On the photo, one can recognize the bumps on the on-chip mirror due to the structures in the lower chip layer. To avoid such bumps of the CPW close to the atoms where the CPW crosses the *Long-Ioffe* wire (see Figure 3.8.1), we designed "pedestals" for the CPW on the lower layer, close to the *Long-Ioffe* wire (see the magnified insets in the upper part of the Figure). The 5 μm broad gap between the pedestals and the *Long-Ioffe* wire is well planarized out by the three polyimide layers between both metalization layers (see the inset on the photograph).

Figure A.0.4 shows the structures in the lower layer of the science chip, which are used for magnetic trapping. The currents indicated correspond to the ones from Section 3.8.
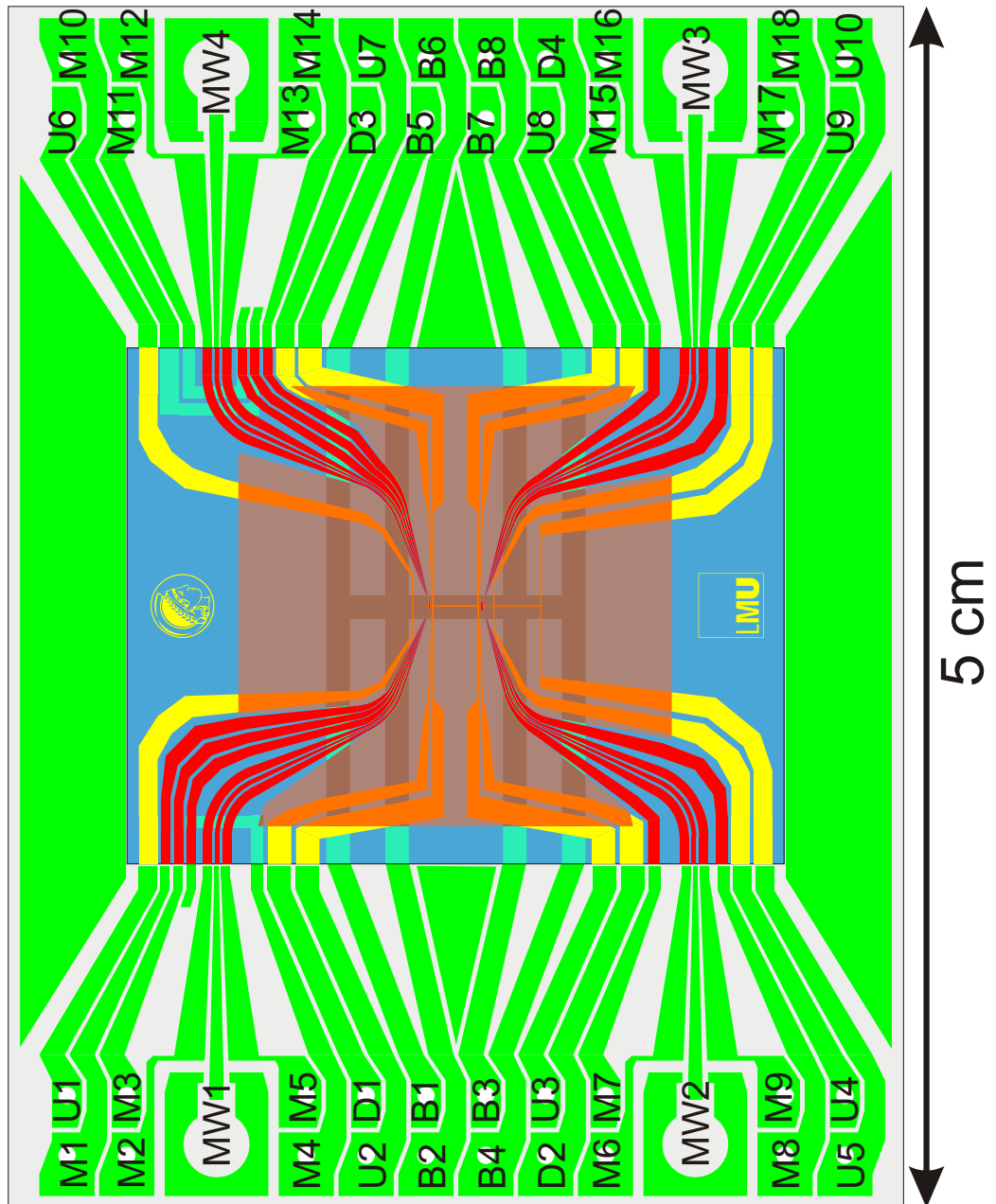
Figure A.0.1: Schematic of the structures on the base and the science chip.
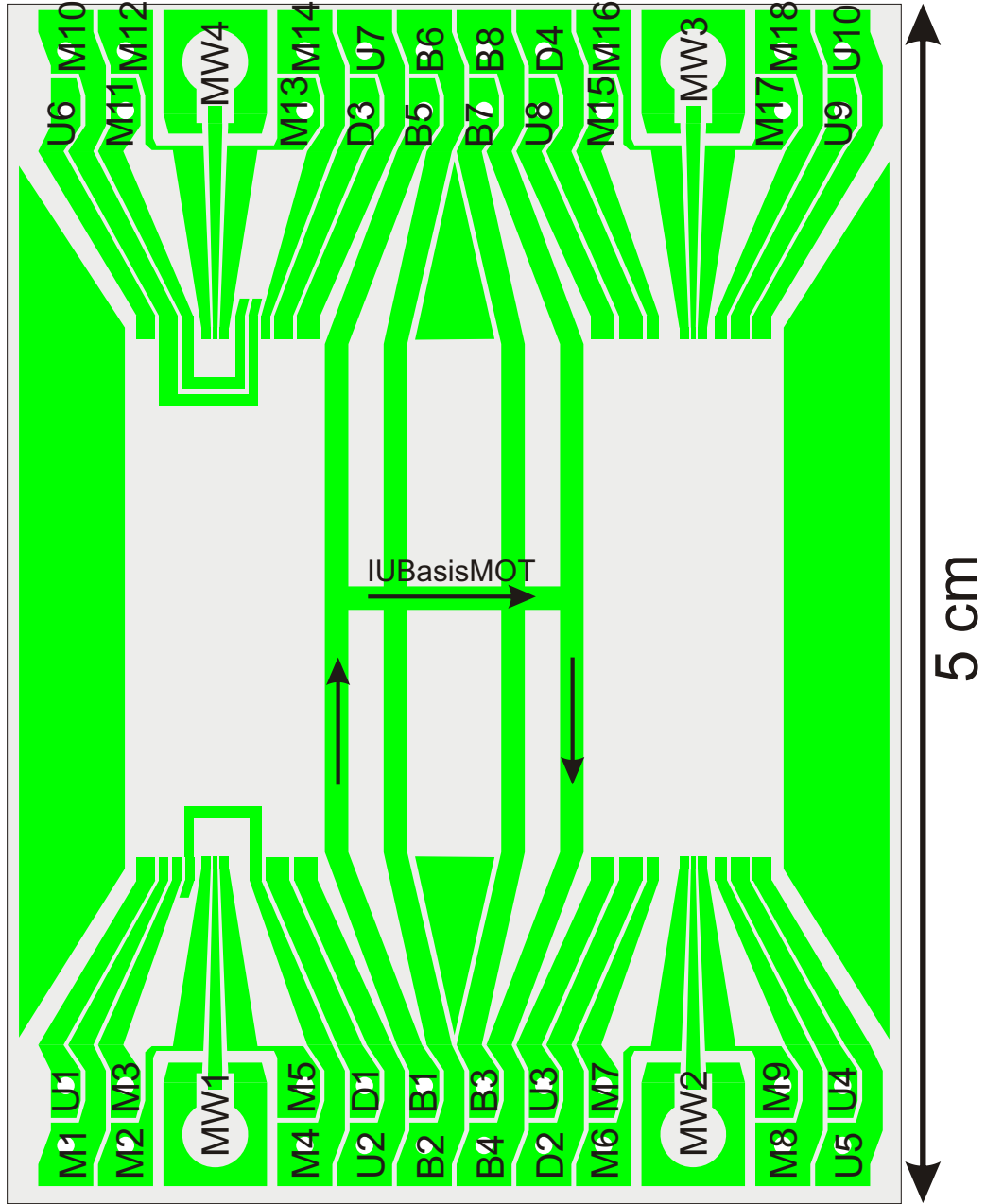
Figure A.0.2: Structures on the base chip.
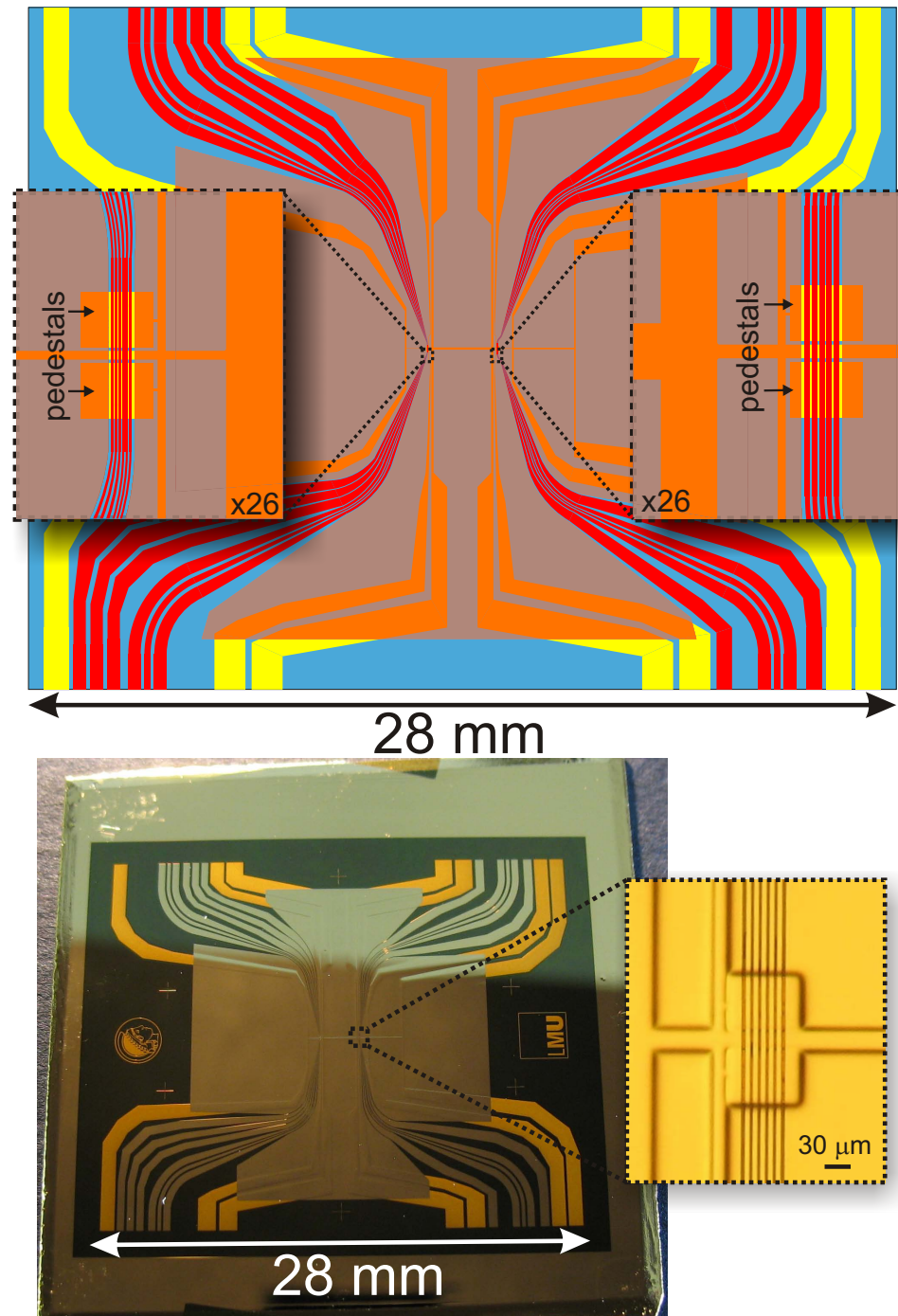
Figure A.0.3: Overview of the structures on both layers of the science chip.
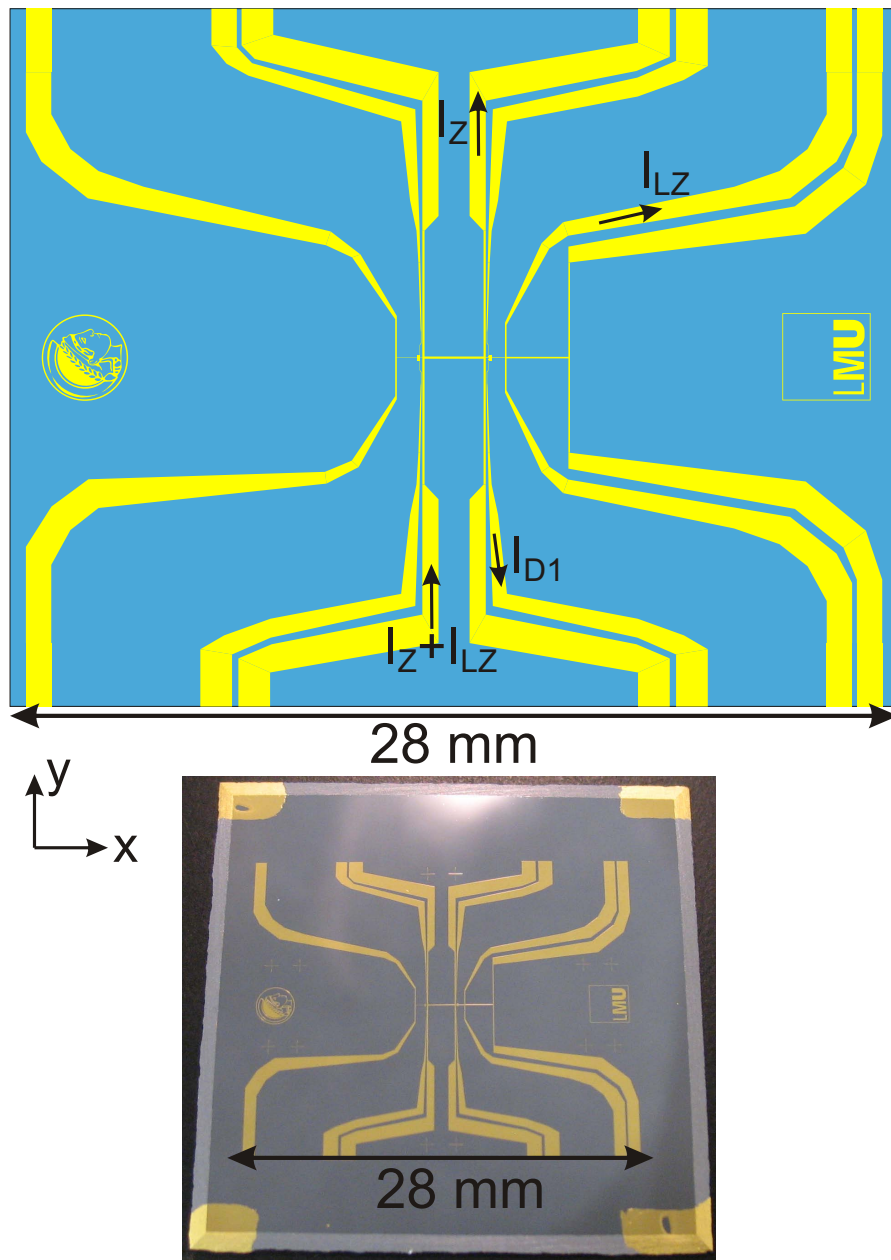
Figure A.0.4: Schematic and photograph of the structures on the lower science chip layer.

Appendix B

Fundamental constants and ^{87}Rb data

Fundamental constants

Planck's constant	h	$6.626\,068\,96(33) \times 10^{-34}$ Js
Bohr magneton	μ_B	$9.274\,009\,15(23) \times 10^{-24}$ J/T
		$h \cdot 1.399\,624\,604(35)$ MHz/G
Bohr radius	a_0	$0.529\,177\,208\,59(36) \times 10^{-10}$ m

Rubidium-87 data

Atomic mass	m	$1.443\,160\,648(72) \times 10^{-25}$ kg
Nuclear spin	I	$3/2$

D$_2$ transition (5^2S$_{1/2} \leftrightarrow 5^2P_{3/2}$) optical properties

Wavelength (vacuum)	λ	$780.241\,209\,686(13)$ nm
Frequency	ω_0	$2\pi \cdot 384\,230\,484\,468\,5(62)$ THz
Natural line width	Γ	$2\pi \cdot 6.0666(18)$ MHz
Saturation intensity $\vert F = 2, m_F = \pm 2\rangle \leftrightarrow \vert F' = 3, m'_F = \pm 3\rangle$ cycling transition ($\sigma^\pm$ polarized light)	I_{sat}	$1.669(2)$ mW/cm^2

$5^2\mathrm{S}_{1/2}$ ground state porperties

Hyperfine structure constant	A_{hfs}	$h \cdot 3.417\,341\,305\,452\,15(5)$ GHz
Zero-field hyperfine splitting	$\Delta E_{\mathrm{hfs}} = 2A_{\mathrm{hfs}}$	$h \cdot 6.834\,682\,610\,904\,29(9)$ GHz
Electron spin g-factor	g_J	$2.002\,331\,13(20)$
Nuclear spin g-factor	g_I	$-0.000\,995\,141\,4(10)$
Static polarizability	α_0	$h \cdot 0.0794(16)\,\mathrm{Hz}/(\mathrm{V/cm})^2$
S-wave scattering lengths		from [95]
$\lvert 1,-1\rangle - \lvert 1,-1\rangle$	a_{11}	$100.40\,a_0 = 5.3129\,\mathrm{nm}$
$\lvert 2,1\rangle - \lvert 1,-1\rangle$	a_{21}	$97.66\,a_0 = 5.1679\,\mathrm{nm}$
$\lvert 2,1\rangle - \lvert 2,1\rangle$	a_{22}	$95.00\,a_0 = 5.0272$ nm

Loss rate constants

Two-body collisions	$K_{\lvert 2,1\rangle} \equiv K_2$	$1.194(19) \times 10^{-13}\,\mathrm{cm}^3\mathrm{s}^{-1}$ [95]
	$K_{\lvert 1,-1\rangle - \lvert 2,1\rangle} \equiv K_{12}$	$0.780(19) \times 10^{-13}\,\mathrm{cm}^3\mathrm{s}^{-1}$ [95]
Three-body collisions	$L_{\lvert 1,-1\rangle} = L_1$	$5.8(19) \times 10^{-30}\mathrm{cm}^6\mathrm{s}^{-1}$ [96]

Data has been taken from [66] where not indicated otherwise.

Appendix C

Angular momentum matrix elements

In this chapter I give the matrix elements for magnetic dipole transitions between hyperfine states $|F, m_F\rangle$. I follow [69] to which the reader is referred for more details.

The strength of magnetic dipole transitions between hyperfine states $|F, m_F\rangle \equiv |J, I, F, m_F\rangle$ is related to the corresponding angular momentum matrix elements. The total angular momentum is $\mathbf{F} = \mathbf{J} + \mathbf{I}$, where $\mathbf{J}$ is the electron angular momentum and $\mathbf{I}$ is the nuclear spin. Within the ground state hyperfine manifold of ^{87}Rb, $J = 1/2$ and $I = 3/2$ have fixed values, which can be combined to $F = 1$ and $F = 2$. In terms of Cartesian components, $\mathbf{F} = (F_x, F_y, F_z)$, we define $F_\pm \equiv F_x \pm iF_y$. Similar definitions are used for $I_\pm$ and $J_\pm$.

In this appendix, $|F, m_F\rangle$ refers to the eigenstates of the operators $\mathbf{F}^2$ and F_z. Note that in the main text of this thesis, $|F, m_F\rangle$ refers more generally to the eigenstates of the full Breit-Rabi Hamiltonian, Eq. (1.4.1), which are a function of the external magnetic field B. Both definitions are equivalent for $B \to 0$.

The matrix elements $\langle F', m'_F|F_\gamma|F, m_F\rangle$ ($\gamma = +, -, z$) between states with $F' = F$ are

$$\langle F, m'_F|F_z|F, m_F\rangle = m_F \delta_{m'_F, m_F} \tag{C.0.1}$$

$$\langle F, m'_F|F_\pm|F, m_F\rangle = \sqrt{(F \mp m_F)(F \pm m_F + 1)}\delta_{m'_F, m_F \pm 1}. \tag{C.0.2}$$

Matrix elements of $\mathbf{F}$ between states with $F' \neq F$ vanish, $\langle F' \neq F, m'_F|F_\gamma|F, m_F\rangle = 0$. Using $F_\gamma = I_\gamma + J_\gamma$, we find

$$\langle F', m'_F | I_\gamma | F, m_F \rangle = -\langle F', m'_F | J_\gamma | F, m_F \rangle \text{ for } F' \neq F.$$

In the calculation of the microwave potentials (Section 1.8) and the Rabi frequencies for microwave field imaging (Section 4.1.1), we neglected the coupling of the microwave to the nuclear spin $\mathbf{I}$ and encounter the matrix elements

$$\langle 2, m_2 | \boldsymbol{\epsilon} \cdot \mathbf{J} | 1, m_1 \rangle,$$

where $\boldsymbol{\epsilon} = (\epsilon_x, \epsilon_y, \epsilon_z)$ is a unit polarization vector, whose components may be complex. Using $J_x = \frac{1}{2}(J_+ + J_-)$ and $J_y = -\frac{i}{2}(J_+ - J_-)$, we express $\boldsymbol{\epsilon} \cdot \mathbf{J}$ as

$$\boldsymbol{\epsilon} \cdot \mathbf{J} = \epsilon_x J_x + \epsilon_y J_y + \epsilon_z J_z = \tfrac{1}{2}(\epsilon_x - i\epsilon_y)J_+ + \tfrac{1}{2}(\epsilon_x + i\epsilon_y)J_- + \epsilon_z J_z.$$

The non-vanishing matrix elements are:

$$
\begin{aligned}
\langle 2, 2 | J_+ | 1, 1 \rangle &= \sqrt{\frac{3}{4}} \\
\langle 2, 1 | J_+ | 1, 0 \rangle &= \sqrt{\frac{3}{8}} \\
\langle 2, 0 | J_+ | 1, -1 \rangle &= \sqrt{\frac{1}{8}}
\end{aligned}
\tag{C.0.3}
$$

$$
\begin{aligned}
\langle 2, 0 | J_- | 1, 1 \rangle &= -\sqrt{\frac{1}{8}} \\
\langle 2, -1 | J_- | 1, 0 \rangle &= -\sqrt{\frac{3}{8}} \\
\langle 2, -2 | J_- | 1, -1 \rangle &= -\sqrt{\frac{3}{4}}
\end{aligned}
\tag{C.0.4}
$$

$$
\begin{aligned}
\langle 2, 1 | J_z | 1, 1 \rangle &= -\sqrt{\frac{3}{16}} \\
\langle 2, 0 | J_z | 1, 0 \rangle &= -\sqrt{\frac{1}{4}} \\
\langle 2, -1 | J_z | 1, -1 \rangle &= -\sqrt{\frac{3}{16}}
\end{aligned}
\tag{C.0.5}
$$

Bibliography

[1] W. Ketterle, D. Durfee, and D. Stamper-Kurn, *Making, probing and understanding Bose-Einstein condensates*, in *Bose-Einstein condensation in atomic gases, Proceedings of the International School of Physics "Enrico Fermi", Course CXL*, edited by M. Inguscio, S. Stringari, and C. Wieman, pages 67–176, Amsterdam, 1999, IOS Press.

[2] A. Migdall, J. Prodan, W. Phillips, T. Bergeman, and H. Metcalf, *First Observation of Magnetically Trapped Neutral Atoms*, Phys. Rev. Lett. **54**, 2596 (1985).

[3] R. Grimm, M. Weidemüller, and Y. B. Ovchinnikov, *Optical dipole traps for neutral atoms*, Adv. At. Mol. Opt. **42**, 95 (2000).

[4] J. Reichel, W. Hänsel, and T. W. Hänsch, *Atomic Micromanipulation with Magnetic Surface Traps*, Phys. Rev. Lett. **83**, 3398 (1999).

[5] R. Folman, P. Krüger, J. Schmiedmayer, J. Denschlag, and C. Henkel, *Microscopic Atom Optics: From Wires to an Atom Chip*, Adv. At. Mol. Opt. Phys. **48**, 263 (2002).

[6] J. Reichel, *Microchip traps and Bose-Einstein condensation*, Appl. Phys. B **74**, 469 (2002).

[7] J. Fortágh and C. Zimmermann, *Magnetic microtraps for ultracold atoms*, Rev. Mod. Phys. **79**, 235 (2007).

[8] W. Hänsel, J. Reichel, P. Hommelhoff, and T. W. Hänsch, *Magnetic Conveyor Belt for Transporting and Merging Trapped Atom Clouds*, Phys. Rev. Lett. **86**, 608 (2001).

[9] P. Treutlein, P. Hommelhoff, T. Steinmetz, T. W. Hänsch, and J. Reichel, *Coherence In Microchip Traps*, Phys. Rev. Lett. **92**, 203005 (2004).

[10] B. Lev, *Fabrication of micro-magnetic traps for cold neutral atoms*, Quant. Inf. Comput. **3**, 450 (2003).

[11] S. Groth, P. Krüger, S. Wildermuth, R. Folman, T. Fernholz, J. Schmiedmayer, D. Mahalu, and I. Bar-Joseph, *Atom chips: Fabrication and thermal properties*, Appl. Phys. Lett. **85**, 2980 (2004).

[12] Y. Colombe, T. Steinmetz, G. Dubois, F. Linke, D. Hunger, and J. Reichel, *Strong atom-field coupling for Bose-Einstein condensates in an optical cavity on a chip*, Nature **450**, 272 (2007).

[13] S. Hofferberth, I. Lesanovsky, B. Fischer, T. Schumm, and J. Schmiedmayer, *Non-equilibrium coherence dynamics in one-dimensional Bose gases*, Nature **449**, 324 (2007).

[14] S. Whitlock, R. Gerritsma, T. Fernholz, and R. Spreeuw, *Two-dimensional array of microtraps with atomic shift register on a chip*, New J. Phys. **11**, 23021 (2009).

[15] Y.-J. Wang, D. Z. Anderson, V. M. Bright, E. A. Cornell, Q. Diot, T. Kishimoto, M. Prentiss, R. A. Saravanan, S. R. Segal, and S. Wu, *Atom Michelson Interferometer on a Chip Using a Bose-Einstein Condensate*, Phys. Rev. Lett. **94**, 090405 (2005).

[16] T. Schumm, S. Hofferberth, L. M. Andersson, S. Wildermuth, S. Groth, I. Bar-Joseph, J. Schmiedmayer, and P. Krüger, *Matter-wave interferometry in a double well on an atom chip*, Nat. Phys. **1**, 57 (2005).

[17] A. Günther, S. Kraft, M. Kemmler, D. Koelle, R. Kleiner, C. Zimmermann, and J. Fortágh, *Diffraction of a Bose-Einstein Condensate from a Magnetic Lattice on a Microchip*, Phys. Rev. Lett. **95**, 170405 (2005).

[18] A. Günther, S. Kraft, C. Zimmermann, and J. Fortágh, *Atom Interferometer Based on Phase Coherent Splitting of Bose-Einstein Condensates with an Integrated Magnetic Grating*, Phys. Rev. Lett. **98**, 140403 (2007).

[19] G.-B. Jo, Y. Shin, S. Will, T. A. Pasquini, M. Saba, W. Ketterle, D. E. Pritchard, M. Vengalattore, and M. Prentiss, *Long Phase Coherence Time and Number Squeezing of Two Bose-Einstein Condensates on an Atom Chip*, Phys. Rev. Lett. **98**, 030407 (2007).

[20] G.-B. Jo, J.-H. Choi, C. Christensen, T. Pasquini, Y.-R. Lee, W. Ketterle, and D. Pritchard, *Phase Sensitive Recombination of Two Bose-Einstein Condensates on an Atom Chip*, Phys. Rev. Lett. **98**, 180401 (2007).

[21] P. Böhi, M. F. Riedel, J. Hoffrogge, J. Reichel, T. W. Hänsch, and P. Treutlein, *Coherent manipulation of Bose-Einstein condensates with state-dependent microwave potentials on an atom chip*, Nat. Phys. **5**, 592 (2009).

[22] Y. Lin, I. Teper, C. Chin, and V. Vuletić, *Impact of the Casimir-Polder Potential and Johnson Noise on Bose-Einstein Condensate Stability Near Surfaces*, Phys. Rev. Lett. **92**, 050404 (2004).

[23] D. Hunger, S. Camerer, T. W. Hänsch, D. König, J. P. Kotthaus, J. Reichel, and P. Treutlein, *Resonant Coupling of a Bose-Einstein Condensate to a Micromechanical Oscillator*, Phys. Rev. Lett. **104**, 143002 (2010).

[24] D. Cano, B. Kasch, H. Hattermann, R. Kleiner, C. Zimmermann, D. Koelle, and J. Fortágh, *Meissner Effect in Superconducting Microtraps*, Physical Review Letters **101**, 183006 (2008).

[25] S. Wildermuth, S. Hofferberth, I. Lesanovsky, E. Haller, L. M. Andersson, S. Groth, I. Bar-Joseph, P. Krüger, and J. Schmiedmayer, *Microscopic magnetic-field imaging*, Nature **435**, 440 (2005).

[26] S. Wildermuth, S. Hofferberth, I. Lesanovsky, S. Groth, P. Krüger, and J. Schmiedmayer, *Sensing electric and magnetic fields with Bose-Einstein condensates*, Appl. Phys. Lett. **88**, 264103 (2006).

[27] S. Aigner, L. D. Pietra, Y. Japha, O. Entin-Wohlman, T. David, R. Salem, R. Folman, and J. Schmiedmayer, *Long-Range Order in Electronic Transport through Disordered Metal Films*, Science **319**, 1226 (2008).

[28] M. P. A. Jones, C. J. Vale, D. Sahagun, B. V. Hall, and E. A. Hinds, *Spin coupling between cold atoms and the thermal fluctuations of a metal surface*, Phys. Rev. Lett. **91**, 080401 (2003).

[29] D. M. Harber, J. M. McGuirk, J. M. Obrecht, and E. A. Cornell, *Thermally Induced Losses in Ultra-Cold Atoms Magnetically Trapped Near Room-Temperature Surfaces*, J. Low Temp. Phys. **133**, 229 (2003).

[30] P. Rosenbusch, *Magnetically trapped atoms for compact atomic clocks*, Applied Physics B **95**, 227 (2009).

[31] C. Deutsch, F. Ramirez-Martinez, C. Lacroûte, F. Reinhard, T. Schneider, J. Fuchs, F. Piéchon, F. Laloë, J. Reichel, and P. Rosenbusch, *Spin self-rephasing and very long coherence times in a trapped atomic ensemble*, preprint arXiv:1003.5925 [physics.atom-ph] (2010).

[32] A. Vogel, M. Schmidt, K. Sengstock, K. Bongs, W. Lewoczko, T. Schuldt, A. Peters, T. van Zoest, W. Ertmer, E. Rasel, T. Steinmetz, J. Reichel, T. Könemann, W. Brinkmann, W. Göklü, C. Lämmerzahl, H. J. Dittus, G. Nandi, W. P. Schleich, and R. Walser, *Bose-Einstein condensates in microgravity*, Appl. Phys. B **84**, 663 (2006).

[33] D. M. Farkas, K. M. Hudek, E. A. Salim, S. R. Segal, M. B. Squires, and D. Z. Anderson, *A Compact, Transportable, Microchip-Based System for High Repetition Rate Production of Bose-Einstein Condensates*, Appl. Phys. Lett. **96**, 093102 (2010).

[34] D. P. DiVincenzo, *The Physical Implementation of Quantum Computation*, Fortschr. Phys. **48**, 771 (2000).

[35] E. Jané, G. Vidal, W. Dür, P. Zoller, and J. I. Cirac, *Simulation of quantum dynamics with quantum optical systems*, Quant. Inf. and Comp. **3**, 15 (2003).

[36] V. Giovannetti, S. Lloyd, and L. Maccone, *Quantum-Enhanced Measurements: Beating the Standard Quantum Limit*, Science **306**, 1330 (2004).

[37] V. Giovannetti, S. Lloyd, and L. Maccone, *Quantum Metrology*, Phys. Rev. Lett. **96**, 010401 (2006).

[38] J. J. Bollinger, W. M. Itano, D. J. Wineland, and D. J. Heinzen, *Optimal frequency measurements with maximally correlated states*, Phys. Rev. A **54**, 4649 (1996).

[39] D. J. Wineland, J. J. Bollinger, W. M. Itano, and D. J. Heinzen, *Squeezed atomic states and projection noise in spectroscopy*, Phys. Rev. A **50**, 67 (1994).

[40] T. Calarco, E. A. Hinds, D. Jaksch, J. Schmiedmayer, J. I. Cirac, and P. Zoller, *Quantum gates with neutral atoms: Controlling collisional interactions in time-dependent traps*, Phys. Rev. A **61**, 022304 (2000).

[41] A. Negretti, T. Calarco, M. A. Cirone, and A. Recati, *Performance of quantum phase gates with cold trapped atoms*, Eur. Phys. J. D **32**, 119 (2005).

[42] P. Treutlein, T. Steinmetz, Y. Colombe, B. Lev, P. Hommelhoff, J. Reichel, M. Greiner, O. Mandel, A. Widera, T. Rom, I. Bloch, and T. W. Hänsch, *Quantum information processing in optical lattices and magnetic microtraps*, Fortschr. Phys. **54**, 702 (2006).

[43] P. Treutlein, T. Hänsch, J. Reichel, A. Negretti, M. Cirone, and T. Calarco, *Microwave potentials and optimal control for robust quantum gates on an atom chip*, Phys. Rev. A **74**, 022312 (2006).

[44] E. Charron, M. A. Cirone, A. Negretti, J. Schmiedmayer, and T. Calarco, *Theoretical analysis of a realistic atom-chip quantum gate*, Phys. Rev. A **74**, 012308 (2006).

[45] A. Sørensen, L.-M. Duan, J. Cirac, and P. Zoller, *Many-particle entanglement with Bose-Einstein condensates*, Nature **409**, 63 (2001).

[46] Y. Li, P. Treutlein, J. Reichel, and A. Sinatra, *Spin squeezing in a bimodal condensate: spatial dynamics and particle loss*, Eur. Phys. J. B **68**, 365 (2009).

[47] M. F. Riedel, P. Böhi, Y. Li, T. Hänsch, A. Sinatra, and P. Treutlein, *Atom-chip-based generation of entanglement for quantum metrology*, Nature **464**, 1170 (2010).

[48] M. Matthews, D. Hall, D. Jin, J. Ensher, C. Wieman, E. Cornell, F. Dalfovo, C. Minniti, and S. Stringari, *Dynamical Response of a Bose-Einstein Condensate to a Discontinuous Change in Internal State*, Phys. Rev. Lett. **81**, 243 (1998).

[49] C. C. Agosta, I. F. Silvera, H. T. C. Stoof, and B. J. Verhaar, *Trapping of Neutral Atoms with Resonant Microwave Radiation*, Phys. Rev. Lett. **62**, 2361 (1989).

[50] R. J. C. Spreeuw, C. Gerz, L. S. Goldner, W. D. Phillips, S. L. Rolston, C. I. Westbrook, M. W. Reynolds, and I. F. Silvera, *Demonstration of Neutral Atom Trapping with Microwaves*, Phys. Rev. Lett. **72**, 3162 (1994).

[51] R. E. Collin, *Foundations for Microwave Engineering*, John Wiley & Sons, Hoboken, 2nd edition, 2001.

[52] C. J. Bordé, *Atomic interferometry with internal state labelling*, Phys. Lett. A **140**, 10 (1989).

[53] A. D. Cronin, J. Schmiedmayer, and D. E. Pritchard, *Optics and interferometry with atoms and molecules*, Rev. Mod. Phys. **81**, 1051 (2009).

[54] B. Dubetsky and M. A. Kasevich, *Atom interferometer as a selective sensor of rotation or gravity*, Phys. Rev. A **74**, 023615 (2006).

[55] P. Böhi, M. F. Riedel, T. W. Hänsch, and P. Treutlein, *Imaging of microwave fields using ultracold atoms*, to appear in Appl. Phys. Lett. (2010).

[56] P. Böhi, M. F. Riedel, T. W. Hänsch, and P. Treutlein, *Method and device for sensing microwave magnetic field polarization components*, U.S. patent pending .

[57] A. S. Sørensen and K. Mølmer, *Entanglement and Extreme Spin Squeezing*, Phys. Rev. Lett. **86**, 4431 (2001).

[58] R. C. Böhm, C. and E. Kubalek, *Contactless electrical characterization of MMICs by device internal electrical sampling scanning-force-microscopy*, Microwave Symposium Digest IEEE MTT-S International, San Diego (1994).

[59] C. Westbrook, *Atom chips: Read the labels*, Nature Physics **5**, 538 (2009).

[60] T. Gustavson, P. Bouyer, and M. Kasevich, *Precision Rotation Measurements with an Atom Interferometer Gyroscope*, Phys. Rev. Lett. **78**, 2046 (1997).

[61] M. de Angelis, A. Bertoldi, L. Cacciapuoti, A. Giorgini, G. Lamporesi, M. Ptevedelli, G. Saccorotti, F. Sorrentino, and G. M. Tino, *Precision gravimetry with atomic sensors*, Meas. Sci. Technol. **20**, 022001 (2009).

[62] J. Reichel, W. Hänsel, P. Hommelhoff, and T. W. Hänsch, *Applications of integrated magnetic microtraps*, Appl. Phys. B **72**, 81 (2001).

[63] V. Bagnato, G. Lafyatis, A. Martin, E. Raab, R. Ahmad-Bitar, and D. Pritchard, *Continuous Stopping and Trapping of Neutral Atoms*, **58**, 2194 (1987).

[64] R. van Roijen, J. Berkhout, S. Jaakkola, and J. Walraven, *Experiments with Atomic Hydrogen in a Magnetic Trapping Field*, **61**, 931 (1988).

[65] H. F. Hess, G. P. Kochanski, J. M. Doyle, N. Masuhara, D. Kleppner, and T. Greytak, *Magnetic trapping of spin-polarized atomic hydrogen*, Phys. Rev. Lett. **59** (1987).

[66] D. Steck, *Rubidium 87 D Line Data*, http://steck.us/alkalidata/ , version 2.1.2 (2009).

[67] W. Wing, *On neutral particle trapping in quasistatic electromagnetic fields*, Prog. Quant. Electr. **8**, 181 (1984).

[68] J. Schmiedmayer, *Guiding and trapping a neutral atom on a wire*, Phys. Rev. A **52** (1995).

[69] P. Treutlein, *Coherent manipulation of ultracold atoms on atom chips*, PhD thesis, Ludwig-Maximilians-Universität München and Max-Planck-Institut für Quantenoptik, 2008, published as MPQ report 321.

[70] D. Pritchard, *Cooling Neutral Atoms in a Magnetic Trap for Precision Spectroscopy*, Phys. Rev. Lett. **51**, 1336 (1983).

[71] C. Sinclair, E. Curtis, I. Llorente Garcia, J. Retter, B. Hall, S. Eriksson, B. Sauer, and E. Hinds, *Bose-Einstein condensation on a permanent-magnet atom chip*, Phys. Rev. A **72**, 031603 (2005).

[72] T. Mukai, C. Hufnagel, A. Kasper, T. Meno, A. Tsukada, K. Semba, and F. Shimizu, *Persistent Supercurrent Atom Chip*, Phys. Rev. Lett. **98**, 260407 (2007).

[73] G. Breit and I. Rabi, *Measurement of Nuclear Spin*, Phys. Rev. **38**, 2082 (1931).

[74] D. Harber, H. Lewandowski, J. McGuirk, and E. Cornell, *Effect of cold collisions on spin coherence and resonance shifts in a magnetically trapped ultracold gas*, Phys. Rev. A **66**, 053616 (2002).

[75] W. Hänsel, P. Hommelhoff, T. Hänsch, and J. Reichel, *Bose-Einstein condensation on a microelectronic chip*, Nature **413**, 498 (2001).

[76] T. Müller, B. Zhang, R. Fermani, K. Chan, Z. Wang, C. Zhang, M. Lim, and R. Dumke, *Trapping of ultra-cold atoms with the magnetic field of vortices in a thin film superconducting micro-structure*, **1**, 2 (2009).

[77] A. Shevchenko, M. Korppi, K. Lindfors, M. Heilio, M. Kaivola, E. Il'yashenko, and T. H. Johansen, *All-optical reversible switching of local magnetization*, Applied Physics Letters **91**, 041916 (2007).

[78] P. Treutlein, D. Hunger, S. Camerer, T. Hänsch, and J. Reichel, *Bose-Einstein Condensate Coupled to a Nanomechanical Resonator on an Atom Chip*, Phys. Rev. Lett. **99**, 140403 (2007).

[79] H.-J. Miesner, D. M. Stamper-Kurn, M. R. Andrews, D. S. Durfee, S. Inouye, and W. Ketterle, *Bosonic Stimulation in the Formation of a Bose-Einstein Condensate*, Science **279**, 1005 (1998).

[80] C. Pethick and H. Smith, *Bose-Einstein Condensation in Dilute Gases*, Cambridge University Press, Cambridge, 2002.

[81] W. Ketterle and N. van Druten, *Bose-Einstein condensation of a finite number of particles trapped in one or three dimensions*, Phys. Rev. A **54**, 656 (1996).

[82] A. J. Dalfovo, S. Giorgini, L. P. Pitaevskii, and S. Stringari, *Theory of Bose-Einstein condensation in trapped gases*, Rev. Mod. Phys. **71**, 463 (1999).

[83] A. J. Leggett, *Bose-Einstein condensation in the alkali gases: Some fundamental concepts*, Rev. Mod. Phys. **73**, 307 (2001).

[84] A. M. Mateo and V. Delgado, *Ground-state properties of trapped Bose-Einstein condensates: Extension of the Thomas-Fermi approximation*, Phys. Rev. A **75**, 063610 (2007).

[85] A. M. Mateo and V. Delgado, *Extension of the Thomas-Fermi approximation for trapped Bose-Einstein condensates with an arbitrary number of atoms*, Phys. Rev. A **74**, 065602 (2006).

[86] T. Gentile, B. Hughey, D. Kleppner, and T. Ducas, *Experimental study of one- and two-photon Rabi oscillations*, Phys. Rev. A **40**, 5103 (1989).

[87] C. Myatt, E. Burt, R. Ghrist, E. Cornell, and C. Wiemann, *Production of Two Overlapping Bose-Einstein Condensates by Sympathetic Cooling*, Phys. Rev. Lett. **78**, 586 (1997).

[88] D. Hall, M. Matthews, C. Wieman, and E. Cornell, *Measurements of Relative Phase in Two-Component Bose-Einstein Condensates*, Phys. Rev. Lett. **81**, 1543 (1998).

[89] D. Hall, M. Matthews, J. Ensher, C. Wieman, and E. Cornell, *Dynamics of Component Separation in a Binary Mixture of Bose-Einstein Condensates*, Phys. Rev. Lett. **81**, 1539 (1998).

[90] H. Lewandowski, J. McGuirk, D. Harber, and E. Cornell, *Decoherence-Driven Cooling of a Degenerate Spinor Bose Gas*, Phys. Rev. Lett. **91**, 240404 (2003).

[91] J. M. McGuirk, H. J. Lewandowski, D. M. Harber, T. Nikuni, J. E. Williams, and E. A. Cornell, *Spatial Resolution of Spin Waves in an Ultracold Gas*, Phys. Rev. Lett. **89**, 090402 (2002).

[92] M. Scully and M. Zubairy, *Quantum Optics*, Cambridge University Press, Cambridge, U.K., 1997.

[93] J. Javanainen and M. Wilkens, *Phase and Phase Diffusion of a Split Bose-Einstein Condensate*, Phys. Rev. Lett. **78**, 4675 (1997).

[94] M. R. Matthews, *Two-Component Bose-Einstein Condensation*, PhD thesis, University of Colorado, 1999.

[95] K. Mertes, J. Merrill, R. Carretero-González, D. Frantzeskakis, P. Kevrekidis, and D. Hall, *Nonequilibrium Dynamics and Superfluid Ring Excitations in Binary Bose-Einstein Condensates*, Phys. Rev. Lett. **99**, 190402 (2007).

[96] E. A. Burt, R. W. Ghrist, C. J. Myatt, M. J. Holland, E. A. Cornell, and C. E. Wieman, *Coherence, Correlations, and Collisions: What One Learns about Bose-Einstein Condensates from Their Decay*, Phys. Rev. Lett. **79**, 337 (1997).

[97] O. Mandel, M. Greiner, A. Widera, T. Rom, T. W. Hänsch, and I. Bloch, *Controlled collisions for multiparticle entanglement of optically trapped atoms*, Nature **425**, 937 (2003).

[98] A. Peters, K. Chung, and S. Chu, *High-precision gravity measurements using atom interferometry*, Metrologia **38**, 25 (2001).

[99] P. Krüger, X. Luo, M. W. Klein, K. Brugger, A. Haase, S.Wildermuth, S. Groth, I. Bar-Joseph, R. Folman, and J. Schmiedmayer, *Trapping and Manipulating Neutral Atoms with Electrostatic Fields*, Phys. Rev. Lett. **91**, 233201 (2003).

[100] D. Heine, M. Wilzbach, T. Raub, B. Hessmo, and J. Schmiedmayer, *An integrated atom detector: single atoms and photon statistics*, Phys. Rev. A **79**, 021804 (2009).

[101] S. Eriksson, M. Trupke, H. Powell, D. Sahagun, C. Sinclair, E. Curtis, B. Sauer, E. Hinds, Z. Moktadir, C. Gollasch, and M. Kraft, *Integrated optical components on atom chips*, Eur. Phys. J. D **35**, 135 (2005).

[102] S. Pollock, J. Cotter, A. Laliotis, and E. Hinds, *Integrated magneto-optical traps on a chip*, preprint arXiv:0905.0771 [physics.atom-ph] .

[103] C. Cohen-Tannoudji, J. Dupont-Roc, and G. Grynberg, *Atom-Photon Interactions*, Wiley-VCH, Berlin, 1998.

[104] J. D. Jackson, *Classical Electrodynamics*, Wiley, New York, 1st edition, 1962.

[105] C. P. Wen, *Coplanar Waveguide: A Surface Strip Transmission Line Suitable for Nonreciprocal Gyromagnetic Device Applications*, IEEE Transactions on Microwave Theory and Techniques **17** (1969).

[106] M.-A. R. Riaziat, M. and I.-J. Feng, *Propagation Modes and Dispersion Characteristics of Coplanar Waveguides*, IEEE Transactions on Microwave Theory and Techniques **38**, 245 (1990).

[107] J. Leib and M. Töpper, *New Wafer-Level-Packaging Technology using Silicon-Via-Contacts For Optical and Other Sensor Applications*, Electronic Components and Technology Conference , 843 (2004).

[108] R. M. Simons, *Coplanar Waveguide Circuits, Components, and Systems*, Wiley & Sons, New York, 2001.

[109] W. Heinrich, *Quasi-TEM description of MMIC coplanar lines including conductor-loss effects*, IEEE Trans. Microwave Theory Tech. **41**, 45 (1993).

[110] H. Klingbeil and W. Heinrich, *Calculation of CPW A.C. Resistance and Inductance Using a Quasi-Static Mode-Matching Approach*, IEEE Transactions on Microwave Theory and Techniques **42**, 1004 (1994).

[111] S. Matthes, *Koplanare Kopplerstrukturen für den Einsatz im Mikrowellen- und Millimeterwellenbereich*, Master's thesis, Universität Kassel, 2005.

[112] G. Ghione and C. U. Naldi, *Coplanar Waveguides for MMIC Applications: Effect of Upper Shielding, Conductor Backing, Finite-Extend Ground Planes, and Line-to-Line Coupling*, IEEE Transactions on Microwave Theory and Techniques **35**, 260 (1987).

[113] G. E. Ponchak, L. P. B. Katehi, and E. M. Tentzeris, *Finite Ground Coplanar (FGC) Waveguide: Its Characteristics and Advantages For Use In RF and Wireless Communication Circuits*, in *3rd International Wireless Communications Conference (WCC 1998) Digest, San Diego, CA, Nov. 1, 1998*, pages 75–83, 1998.

[114] P. Treutlein, *Lossy microwave transmission lines*, unpublished (2005).

[115] *S-Parameter Design*, Agilent Application Notes **154**, http://cp.literature.agilent.com/litweb/pdf/5952 (2006).

[116] F. G. Yost, *Soldering to Gold Films*, Gold Bulletin **10**, 94 (1977).

[117] L. D. Pietra, S. Aigner, C. von Hagen, S. Groth, I. Bar-Joseph, H. J. Lezec, and J. Schmiedmayer, *Designing potentials by sculpturing wires*, Phys. Rev. A **75**, 063604 (2007).

[118] A. Leanhardt, T. Pasquini, A. S. M. Saba, Y. Shin, D. Kielpinski, D. Pritchard, and W. Ketterle, *Cooling Bose-Einstein Condensates Below 500 Picokelvin*, Science **301**, 1513 (2003).

[119] S. Du, M. B. Squires, Y. Imai, L. Czaia, R. A. Saravanan, V. Bright, J. Reichel, T. W. Hänsch, and D. Z. Anderson, *Atom-chip Bose-Einstein condensation in a portable vacuum cell*, Phys. Rev. A **70**, 053606 (2004).

[120] H. J. Lewandowski, D. M. Harber, D. L. Whitaker, and E. A. Cornell, *Simplified System for Creating a Bose-Einstein Condensate*, J. Low Temp. Phys. **132**, 309 (2003).

[121] J. Hoffrogge, *Mikrowellen-Nahfelder auf Atomchips*, Master's thesis, Ludwig-Maximilians-Universität München, 2007.

[122] V. Mahal, A. Arie, M. A. Arbore, and M. Fejer, *Quasi-phase-matched frequency doubling in the waveguide of a 1560-nm diode laser and locking at the rubidium D_2 absorption line*, Optics Letters **21**, 1217 (1996).

[123] L. Ricci, M. Weidemüller, T. Esslinger, A. Hemmerich, C. Zimmermann, V. Vuletic, W. König, and T. W. Hänsch, *A compact grating-stabilized diode laser system for atomic physics*, Opt. Comm. **117**, 541 (1995).

[124] Z. W. G. Reinaudi, T. Lahaye and D. Guéry-Odelin, *Strong saturation absorption imaging of dense clouds of ultracold atoms*, Optics Letters **32**, 3143 (2007).

[125] W. Hänsel, *Magnetische Mikrofallen für Rubidiumatome*, PhD thesis, Ludwig-Maximilians-Universität München and Max-Planck-Institut für Quantenoptik, 2001, published as MPQ report 263.

[126] P. Hommelhoff, *Bose-Einstein-Kondensate in Mikrochip-Fallen*, PhD thesis, Ludwig-Maximilians-Universität München and Max-Planck-Institut für Quantenoptik, 2002, published as MPQ report 280.

[127] L. DiCarlo, J. M. Chow, J. M. Gambetta, L. S. Bishop, B. R. Johnson, D. I. Schuster, J. Majer, A. Blais, L. Frunzio, S. M. Girvin, and R. J. Schoelkopf, *Demonstration of two-qubit algorithms with a superconducting quantum processor*, Nature **469**, 240 (2009).

[128] I. D. Robertson and S. Lucyszyn, editors, *RFIC and MMIC design and technology*, The Institution of Electrical Engineers, London, 1st edition, 2001.

[129] C. Böhm, F. Saurenbach, P. Taschner, C. Roths, and E. Kubalek, *Voltage contrast in integrated circuits with 100 nm spatial resolution by scanning force microscopy*, J. Phys. D.: Appl. Phys. **26**, 1801 (1993).

[130] S. Sayil, D. Kerns, and S. Kerns, *A survey of contactless measurement and testing techniques*, Potentials, IEEE **24**, 25 (2005).

[131] G. David, P. Bussek, U. Auer, F. J. Tegude, and D. Jäger, *Electro-optic probing of RF signals in submicrometre MMIC devices*, Electronic Letters **31**, 2188 (1995).

[132] R. Black, F. Wellstood, E. Dantsker, A. H. Miklich, D. Nemeth, D. Koelle, F. Ludwig, and J. Clarke, *Imaging radio-frequency fields using a scanning SQUID microscope*, Appl. Phys. Lett. **66**, 1267 (1995).

[133] T. Budka, S. Waclawik, and G. Rebeiz, *A Coaxial 0.5-18 GHz Near Electric Field Measurement System for Planar Microwave Circuits Using Integrated Probes*, IEEE Trans. on Microwave Theory and Techniques **44**, 2174 (1996).

[134] S. Dutta, C. P. Vlahacos, D. E. Steinhauer, A. Thanawalla, B. J. Feenstra, F. C. Wellstood, S. Anlage, and H. Newman, *Imaging microwave electric fields using a near-field scanning microwave microscope*, Appl. Phys. Lett. **74**, 156 (1999).

[135] Y. Gao and I. Wolff, *A miniature magnetic field probe for measuring fields in planar high-frequency circuits*, Microwave Symposium Digest, IEEE MTT-S International **3**, 1159 (1995).

[136] Y. Gao and I. Wolff, *Miniature Electric Near-Field Probes for Measuring 3-D Fields in Planar Microwave Circuits*, IEEE Trans. on Microwave Theory and Techniques **46**, 907 (1998).

[137] T. Dubois, S. Jarrix, A. Penarier, and P. Nouvel, *Near-Field Electromagnetic Characterization and Perturbation of Logic Circuits*, IEEE Trans on Instrumentation and Measurement **57**, 2398 (2008).

[138] R. Bücker, A. Perrin, S. Manz, T. Betz, C. Koller, T. Plisson, J. Rottmann, T. Schumm, and J. Schmiedmayer, *Single-particle-sensitive imaging of freely propagating ultracold atoms*, New Journal of Physics **11** (2009).

[139] N. F. Ramsey, *Molecular Beams*, Clarendon Press, Oxford, 1956.

[140] S. Lloyd, *Universal Quantum Simulators*, Science **273**, 1073 (1996).

[141] J. A. Dunningham, *Using quantum theory to improve measurement precision*, Contemp. Phys. **47**, 257 (2006).

[142] A. M. Childs, J. Preskill, and J. Renes, *Quantum information and precision measurement*, J. Mod. Opt. **47**, 155 (2000).

[143] A. M. Mateo and V. Delgado, *Ground-state properties of trapped Bose-Einstein condensates: Extension of the Thomas-Fermi approximation*, Phys. Rev. A **75**, 063610 (2007).

[144] R. G. Scott, T. E. Judd, and T. M. Fromhold, *Exploiting Soliton Decay and Phase Fluctuations in Atom Chip Interferometry of Bose-Einstein Condensates*, Phys. Rev. Lett. **100**, 100402 (2008).

[145] R. B. Diener, B. Wu, M. G. Raizen, and Q. Niu, *Quantum Tweezer for Atoms*, Phys. Rev. Lett. **89**, 070401 (2002).

[146] B. Mohring, M. Bienert, F. Haug, G. Morigi, W. P. Schleich, and M. G. Raizen, *Extracting atoms on demand with lasers*, Phys. Rev. A **71**, 053601 (2005).

[147] A. Dudarev, M. Raizen, and Q. Niu, *Quantum many-body culling: Production of a Definite Number of Ground-State Atoms in a Bose-Einstein Condensate*, Phys. Rev. Lett. **98**, 063001 (2007).

[148] G. Santarelli, P. Laurent, P. Lemonde, A. Clairon, A. G. Mann, S. Chang, A. N. Luiten, and C. Salomon, *Quantum Projection Noise in an Atomic Fountain: A High Stability Cesium Frequency Standard*, Phys. Rev. Lett. **82**, 4619 (1999).

[149] M. Kitagawa and M. Ueda, *Squeezed spin states*, Phys. Rev. A **47**, 5138 (1993).

[150] C. Gross, T. Zibold, E. Nicklas, J. Estève, and M. Oberthaler, *Nonlinear atom interferometer surpasses classical precision limit*, Nature **464**, 1165 (2010).

[151] T. Aoki, B. Dayan, E. Wilcut, W. Bowen, A. S. Parkins, H. J. Kimble, T. J. Kippenberg, and K. J. Vahala, *Observation of Strong Coupling between One Atom and a Monolithic Microresonator*, Nature **443**, 671 (2006).

[152] J. Verdú, H. Zoubi, C. Koller, J. Majer, H. Ritsch, and J. Schmiedmayer, *Strong magnetic coupling of an ultracold gas to a superdonducting waveguide cavity*, Phys. Rev. Lett. **103**, 043603 (2009).

[153] R. Gehr, J. Volz, G. Dubois, T. Steinmetz, and Y. Colombe, *Cavity-based single atom preparation and high-fidelity hyperfine state readout*, preprint arXiv:1002.4424 [quant-ph] .

[154] Y. Castin, *Coherent Atomic Matter Waves*, in *Les Houches Session LXXII*, edited by R. Kaiser, C. Westbrook, and F. David, pages 1–136, Springer-Verlag, Berlin, 2001.

[155] A. Micheli, D. Jaksch, J. I. Cirac, and P. Zoller, *Many-particle entanglement in two-component Bose-Einstein condensates*, Phys. Rev. A **67**, 013607 (2003).

[156] Y. Li and A. Sinatra, *private communication.*

[157] J. Hoffrogge and P. Hommelhoff, *private communication.*

Danksagung

Ich möchte mich an dieser Stelle bei all denjenigen bedanken, die zum Gelingen dieser Arbeit beigetragen haben.

An erster Stelle bedanke ich mich bei Herrn Prof. Hänsch für die Aufnahme in seine Arbeitsgruppe und für die Möglichkeit, in einer solch aussergewöhnlichen Gruppe mitarbeiten zu dürfen.

Besonderer Dank gebührt meinem Gruppenleiter Prof. Philipp Treutlein für die Betreuung dieser Arbeit, die vertrauensvolle und konstruktive Zusammenarbeit sowie für seine ständige Bereitschaft zur Diskussion von physikalischen Fragestellungen. Ich danke ihm auch für das präzise Korrekturlesen dieser Arbeit.

Ebenso danke ich meinem Mitstreiter Max Riedel für die gute und produktive Teamarbeit, für die heiteren Stunden im Labor sowie die Exkurse in die Welt jenseits der Physik.

Weiter danke ich Johannes Hoffrogge für die gute und produktive Zusammenarbeit in der Aufbauphase des Experiments.

Ich danke den übrigen Gruppenmitgliedern David Hunger, Stephan Camerer, Maria Korppi, Jad Halimeh, Andreas Jöckel, Roman Schmied und Matthias Mader für die äusserst angenehme Gruppenatmosphäre, deren Hilfsbereitschaft und für gemeinsame Aktivitäten.

Bei Prof. Jörg Kotthaus und seinem Team bedanke ich mich für den grosszügigen Zugang zum Reinraum sowie für die Einführung in die Benutzung der verschiedenen dort vorhandenen Geräte. Hier danke ich besonders Stefan Schöffberger und Philipp Altpeter.

Das freundschaftliche Klima auf unserem Gang hat die Arbeitsatmosphäre sehr positiv beeinflusst. Ich bedanke mich insbesondere bei den teils ehemaligen Kollegen Matthias Taglieber, Arne Voigt, Louis Costa, Hannes Brachmann, Wolfgang Wieser, Christoph Eigenwillig, Daniel Schlenk, Jürgen Volz, Michael Krug, Florian Henkel, Markus Weber, Wenjamin Rosenfeld und Martin Fürst.

Dank gebührt Gabriele Gschwendtner und Nicole Schmidt für deren zügige Hilfe bei administrativen oder logistischen Fragestellungen.

Ich bedanke mich bei Toni Scheich für seine Hilfe in der Welt der Elektronik.

Ich bin meinen Eltern und meiner Freundin Sveta sehr dankbar für deren fortwährende Unterstützung. Ich danke Sveta für ihr grosses Verständnis und ihre grosse Geduld, wenn es im Labor mal wieder später geworden ist.